

DISS. ETH NO. 23792

Nanostructured electrode materials for rechargeable batteries

A thesis submitted to obtain the degree of
DOCTOR OF SCIENCES of ETH ZURICH
(Dr. sc. ETH Zurich)

presented by
MARC DOMINIK WALTER
MSc ETH Chemistry, ETH Zurich

born on 02.09.1988
citizen of the Federal Republic of Germany

accepted on the recommendation of
Prof. Dr. Maksym V. Kovalenko, examiner
Prof. Dr. Markus Niederberger, co-examiner

2016

Vun nix kütt nix.

– Kölsches Sprichwort

Declaration

I hereby confirm that I am the sole author of the written work herein enclosed and that I have compiled it in my own words. Parts excepted are corrections of form and content by the supervisor.

Title of work:

Nanostructured electrode materials for rechargeable batteries

With my signature I confirm:

- I have committed none of the forms of plagiarism.
- I have documented all methods, data and processes truthfully.
- I have not manipulated any data.
- I have mentioned all persons who were significant contributors to this work, as described below.
- I have obtained copyright permissions from the journal for reproducing the text and figures in this thesis, where needed.
- I am aware that the work may be screened electronically for plagiarism.

Place, date

Signature(s)

Dr. Rolf Erni (Empa) performed STEM characterization in Chapter 3.

Simon Doswald (ETH Zurich, Empa) carried out parts of the synthetic work in Chapters 4 and 5.

Dr. Frank Krumeich (ETH Zurich) performed EDX-STEM mapping in Chapter 5.

Tanja Zünd (ETH Zurich, Empa) carried out parts of the electrochemical measurements in Chapter 6.

Dr. Maryna Bodnarchuk (ETH Zurich, Empa) synthesized and characterized the metal phosphide nanocrystals used in Chapter 7.

Dr. Kostiantyn Kravchyk (ETH Zurich, Empa) carried out the Li-ion half-cells tests with metal phosphide nanocrystals in Chapter 7.

Cornelia Böfer (ETH Zurich, Empa) carried out parts of the electrochemical measurements in Chapter 9.

Beatrice Fischer (Empa) carried out GPC measurements presented in Chapter 9.

Acknowledgements

First and foremost, I thank Prof. Dr. Maksym V. Kovalenko for the great opportunity to join his group and work in an exciting field. Throughout my PhD studies his guidance, support and encouragement, when things did not work out immediately, were extremely valuable. I especially want to thank him for giving me the freedom to always tackle new challenging projects.

I thank Prof. Dr. Markus Niederberger for his kind willingness to co-examine this thesis.

I thank Dr. Kostiantyn V. Kravchyk, who taught me most experimental skills ranging from synthesis of monodisperse nanocrystals to battery assembly, for his continuous help and advice.

I want to express my gratitude to the entire Kovalenko Group for their support.

Especially, I would like to thank Georgian Nedelcu, Dr. Loredana Protesescu and Dr. Maryna I. Bodnarchuk, who were always very helpful, whenever I visited the labs at Höggerberg, and Claudia Salameth-Ott and Chantal Hänni for support with administrative matters.

Special thanks go also to all the master students, who I had the pleasure to supervise, for their contributions.

I also want to thank our collaborators from Belenos Clean Power Holding Ltd. for very helpful discussions and the members of the Empa Electron Microscopy Center for their support.

Finally, I thank my family: For Everything.

Table of contents

Summary	i
Zusammenfassung	iii
Chapter 1. Introduction	1
1.1. Rechargeable batteries	1
1.2. Nanomaterials as electrode materials for electrochemical energy storage	11
1.3. Scope and outline of the dissertation	14
Chapter 2. Methods and techniques	18
2.1. Synthesis of nanocrystals	18
2.2. Characterization	20
2.3. Electrochemical measurements	24
Chapter 3. Inexpensive antimony nanocrystals and their composites with red phosphorus as high-performance anode materials for Na-ion batteries	28
3.1. Introduction	28
3.2. Experimental section	30
3.3. Results and discussion	31
3.4. Conclusion	42
Chapter 4. Inexpensive colloidal SnSb nanoalloys as efficient anode materials for Li- and Na-ion batteries	44
4.1. Introduction	44
4.2. Experimental section	46
4.3. Results and discussion	47
4.4. Conclusion	58
Chapter 5. Oxidized Co-Sn nanoparticles as long-lasting anode materials for Li-ion batteries	59
5.1. Introduction	59
5.2. Experimental section	60
5.3. Results and discussion	62
5.4. Conclusion	71
Chapter 6. Pyrite (FeS ₂) nanocrystals as inexpensive high-performance Li-ion cathode and Na-ion anode materials	72
6.1. Introduction	72
6.2. Experimental section	74
6.3. Results and discussion	75
6.4. Conclusion	84
Chapter 7. Evaluation of metal phosphide nanocrystals as anode materials for Na-ion batteries	86
7.1. Introduction	86
7.2. Experimental section	88
7.3. Results and discussion	89
7.4. Conclusion	94
Chapter 8. Efficient and inexpensive Na/Mg hybrid battery	95
8.1. Introduction	95
8.2. Experimental section	99
8.3. Results and discussion	100
8.4. Conclusion	104

Chapter 9. Pyrene-based polymers as high-performance cathode materials for Al-ion batteries.....	107
9.1. Introduction	107
9.2. Experimental section	108
9.3. Results and discussion	109
9.4. Conclusion	118
Chapter 10. Conclusions and outlook	119
10.1. Conclusions	119
10.2. Outlook	121
References	123
Appendix A. Abbreviation list	134
Appendix B. Curriculum Vitae	135
Appendix C. List of publications	136
Appendix D. List of patents	138
Appendix E. List of presentations	139

Summary

Novel rechargeable batteries are urgently required for the next generation of portable electronics, electric vehicles and stationary energy storage. Irrespectively of whether the goal is to improve present day Li-ion batteries in terms of energy or power density or to develop potentially low-cost battery systems based on Na-, Mg- or Al-ions, the development of novel electrode materials is essential for major breakthroughs in the field. Particularly, nanostructured materials offer potentially superior electrochemical properties due to faster reaction kinetics and better reversibility of the alloying/conversion reaction with the respective metal ions. Thus, in this thesis nanomaterials were explored as novel electrode materials for rechargeable room-temperature batteries ranging from already established Li-ion batteries to potentially more inexpensive batteries based, for instance, on Na- or Mg-ions.

In detail, Sb nanocrystals (NCs) were synthesized using a novel, simple and inexpensive procedure. Such Sb NCs not only show outstanding rate performance and cycling stability as Na-ion anode materials with capacities close to the theoretical value of 660 mAh g^{-1} , but allow the fabrication of a P/Sb/Cu composite by simple mixing of bulk red phosphorus and copper nanowires, which delivers capacities of $> 1100 \text{ mAh g}^{-1}$ for more than 50 cycles at a current of 125 mA g^{-1} . The same simple reaction procedure for synthesizing Sb NCs was further extended to intermetallic nanoalloys of SnSb and Co-Sn. SnSb NCs, while showing excellent capacity retention as Na-ion anode material, only reached capacities close to the theoretical value for Li-ion storage. In detail, SnSb NCs delivered capacities of 760 mAh g^{-1} for 100 cycles (at 1000 mA g^{-1}) in Li-ion half-cells and $\sim 600 \text{ mAh g}^{-1}$ for 60 cycles (at 400 mA g^{-1}) with an average discharge voltage of 3.0 V in Li-ion full-cells with LiCoO_2 as cathode material. Further, CoSn_2O_x nanoparticles (NPs), prepared by ball-milling of inexpensively synthesized Sn and Co NPs in air, are demonstrated as very stable Li-anode material with only 8% capacity loss over 1500 cycles at a high cycling rate of 1984 mA g^{-1} .

Apart from nanostructured Sb-based electrode materials, numerous metal sulfide and metal phosphides NCs were explored for the first time as potential anode materials for Na-ion batteries, due to their very high theoretical capacities (typically in the range of $\sim 1000 \text{ mAh g}^{-1}$). In particular, nanostructured sulfides FeS_2 , NiS_2 , CoS_2 , PbS , SnS , CuS , ZnS and $\text{Cu}_2\text{ZnSnS}_4$ and metal phosphides FeP , CoP , NiP_2 and CuP_2 were investigated, with FeS_2 NCs clearly arising as the most promising candidate delivering capacities of more than 500 mAh g^{-1} for 400 cycles at a current density of 1000 mA g^{-1} .

Such FeS₂ NCs were used further as cathode material in combination with a metallic magnesium anode for the first demonstration of a Na/Mg hybrid battery. This proof-of-principle battery showed promising electrochemical properties with a cathodic capacity of ~190 mAh g⁻¹ and a discharge voltage of ~1.0 V over 40 cycles (at 200 mA g⁻¹). Based on earth-abundant elements only such Na/Mg hybrid battery can be of potential interest as future low-cost solution for stationary large-scale energy storage.

In the context of developing novel, inexpensive batteries, finally an Al-ion battery is presented using pyrene-based polymers as high-performance cathode materials. Particularly, poly(nitropyrene-*co*-pyrene) showed electrochemical properties comparable to the present state-of-the-art material pyrolytic graphite with a high discharge voltage of ~1.7 V, a stable capacity of ~100 mAh g⁻¹ and energy efficiency of ~86% for at least 1000 cycles at a current of 200 mA g⁻¹.

Zusammenfassung

Neue, wiederaufladbare Batterien werden dringend benötigt für die nächste Generation von tragbaren Elektronikgeräten, Elektrofahrzeuge und stationäre Energiespeicherung. Unabhängig davon, ob das Ziel ist heutige Li-Ionen-Batterien hinsichtlich von Energie- oder Leistungsdichte zu verbessern oder potentiell kostengünstige Batteriensysteme basierend auf Na-, Mg- oder Al-Ionen zu entwickeln, die Entwicklung neuer Elektrodenmaterialien ist essentiell für bedeutende Durchbrüche auf dem Gebiet.

Insbesondere nanostrukturierte Materialien bieten potentiell verbesserte elektrochemische Eigenschaften aufgrund von schnellerer Reaktionskinetik und besserer Reversibilität der Legierungs-/Umwandlungsreaktion mit den jeweiligen Metallionen. Folglich wurden in dieser Arbeit Nanomaterialien als neuartige Elektrodenmaterialien für wiederaufladbare Raumtemperaturbatterien, reichend von bereits etablierten Li-Ionen-Batterien bis zu möglicherweise kostengünstigeren Batterien basierend auf beispielsweise Na- oder Mg-Ionen, erforscht.

Im Einzelnen, wurden Sb Nanokristalle unter Verwendung einer neuen, einfachen und preisgünstigen Methode synthetisiert. Derartige Sb Nanokristalle zeigen nicht nur aussergewöhnliche Entladegeschwindigkeit und Zyklenstabilität als Na-Ionen-Anodenmaterialien mit Kapazitäten nahe dem theoretischen Wert von 600 mAh g^{-1} , sondern erlauben die Herstellung eines P/Sb/Cu-Komposits durch einfaches Mischen mit rotem Phosphor und Kupfer-Nanodrähten, welches Kapazitäten von $> 1100 \text{ mAh g}^{-1}$ für mehr als 50 Zyklen bei einem Strom von 125 mA g^{-1} liefert. Dasselbe einfache Reaktionsverfahren für Sb Nanokristalle wurde überdies ausgeweitet auf intermetallische Nanolegierungen von SnSb und Co-Sn. Obwohl SnSb Nanokristalle ausgezeichnete Retention der Kapazität als Na-Ionen-Anodenmaterialien zeigen, wurden Kapazitätswerte nahe dem theoretischen Wert nur für Li-Ionen-Speicherung erreicht. Im Einzelnen, lieferten SnSb Nanokristalle Kapazitäten von 760 mAh g^{-1} für 100 Zyklen (bei 1000 mA g^{-1}) in Li-Ionen-Halbzellen und $\sim 600 \text{ mAh g}^{-1}$ für 60 Zyklen (bei 400 mA g^{-1}) mit einer durchschnittlichen Entladespannung von 3.0 V in Li-Ionen-Batterien mit LiCoO_2 als Kathodenmaterial. Des Weiteren werden CoSn_2O_x Nanopartikel, hergestellt durch Kugelmahlen an Luft von kostengünstig synthetisierten Sn und Co Nanopartikeln, als sehr stabiles Li-Ionen-Anodenmaterial vorgestellt mit nur 8% Kapazitätsverlust über 1500 Zyklen bei einer hohen Lade-/Entladerate von 1984 mA g^{-1} .

Neben nanostrukturierten Sb-basierten Elektrodenmaterialien, wurde eine Vielzahl an Metallsulfid- und Metallphosphid-Nanokristallen zum ersten Mal als potentielle Anodenmaterialien für Na-Ionen-Batterien, aufgrund ihrer sehr hohen theoretischen Kapazitäten (typischerweise im Bereich von $\sim 1000 \text{ mAh g}^{-1}$), untersucht. Insbesondere wurden die nanostrukturierten Sulfide FeS_2 , NiS_2 , CoS_2 , PbS , SnS , CuS , ZnS und $\text{Cu}_2\text{ZnSnS}_4$ sowie die Metallphosphide FeP , CoP , NiP_2 und CuP_2 untersucht, wobei FeS_2 Nanokristalle eindeutig als vielversprechendste Kandidaten hervorgingen mit Kapazitäten von mehr als 500 mAh g^{-1} für 400 Zyklen bei einer Stromdichte von 1000 mA g^{-1} .

Derartige FeS_2 Nanokristalle wurde überdies als Kathodenmaterial in Kombination mit einer metallischen Magnesium-Anode für die erste Demonstration einer Na/Mg-Hybridbatterie verwendet. Diese Proof-of-Principle-Batterie zeigte vielversprechende elektrochemische Eigenschaften mit einer kathodischen Kapazität von $\sim 190 \text{ mAh g}^{-1}$ und einer Entladespannung von $\sim 1.0 \text{ V}$ über 40 Zyklen (bei 200 mA g^{-1}). Eine derartige Na/Mg-Hybridbatterie, basierend nur auf reichlich vorhandenen Elementen, kann von möglichem Interesse sein als zukünftige kostengünstige Lösung für stationäre Energiespeicher.

Im Zusammenhang mit neuen, kostengünstigen Batterien, wird schlussendlich eine Al-Ionen Batterie vorgestellt mit Pyrene-basierten Polymeren als Kathodenmaterialien. Insbesondere Poly(Nitropyrene-*co*-Pyrene) zeigte elektrochemische Eigenschaften vergleichbar zum derzeitigen State-of-the-art-Material pyrolytischem Graphit mit einer hohen Entladespannung von $\sim 1.7 \text{ V}$, einer stabilen Kapazität von $\sim 100 \text{ mAh g}^{-1}$ und einer Energieeffizienz von $\sim 86\%$ für mindestens 1000 Zyklen bei einem Strom von 200 mA g^{-1} .

Chapter 1. Introduction

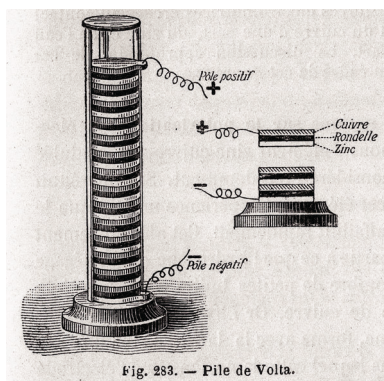


Fig. 283. — Pile de Volta.

Courtesy of Éditions Vuibert

1.1. Rechargeable batteries

Fundamental considerations for batteries. Since the development of the first battery by Alessandro Volta more than 200 years ago,¹ rechargeable batteries have conquered most areas of everyday life ranging from watches to laptops and further widespread application, for instance, for electromobility or stationary storage, is expected.²⁻⁴ Despite difficulties to understand all the electrochemical processes taking place, the general working principle of a rechargeable battery is relatively simple. During discharge of the battery a redox reaction between a “reductant” material (negative electrode, anode) and “oxidant” material (positive material, cathode), which are spatially separated, yet connected electrically through an external electrical circuit, takes place. The negative electrical charge (electrons) moving from the “reductant” to the “oxidant” is balanced by the removal of positively charged ions (*e.g.*, Li-ions) from the “reductant” and their insertion into the “oxidant” material. Thus, both materials need to be connected ionically through an ion-conducting electrolyte, *e.g.*, a liquid containing the respective positively charged ions in dissociated form. The driving force for the redox reaction expressed as Gibbs free energy ΔG is related to the potential difference between the two electrode materials ΔE and accordingly the voltage U .⁵

$$\frac{-\Delta G}{zF} = \Delta E = U \quad (1.1.)$$

z = number of electrons exchanged, F = Faraday’s constant

Importantly, the potential E of each half-cell can be in principle calculated using the Nernst Equation:⁶

$$E = E^0 + \frac{RT}{zF} \ln \frac{a_{\text{Ox}}}{a_{\text{Red}}} \quad (1.2.)$$

E^0 = standard electrode potential, R = gas constant, T = temperature, a = activity

During discharge of the battery the voltage decreases, since the driving force for the reaction is diminished by the continuous redox reaction. Upon charging the battery the processes are reversed and both previously intercalated positively charged ions and electrons are removed from the cathode and reinserted into the anode material. In a thermodynamically perfect system the voltage required for charging would be the same as the one observed during discharging, which is not the case in real systems. The deviation of the potential E from the thermodynamic value E_{thd} is the so called overpotential η .⁷

$$\eta = E - E_{\text{thd}} \quad (1.3.)$$

This overpotential is the necessary extra potential required for the redox reaction to take place due to kinetic limitations of the system. As a result of overpotential effects in a real battery the charging voltage is somewhat higher and the discharging voltage lower, leading to energy efficiencies $< 100\%$. In order to recharge the battery an obvious requirement is for the redox reaction to be reversible, which is not the case for all battery types. In terms of the nomenclature rechargeable batteries are coined as secondary, whereas non-rechargeable batteries are named primary batteries.⁸ In particular, one of the most widely used rechargeable battery technology are lithium(Li)-ion batteries (LIBs) with LiCoO_2 as cathode and graphite as anode material. Importantly, it should be noted that commercial rechargeable LIBs typically do not contain metallic Li as anode material, since lithium is prone to form branchlike structures (dendrites) during cycling, which can lead to short-circuiting of the cell and consequently even explosion of the battery.^{9, 10} In case of such a battery based on LiCoO_2 /graphite – and LIBs in general – the charge transfer is accompanied by the removal and insertion of Li-ions as illustrated in Figure 1.1.

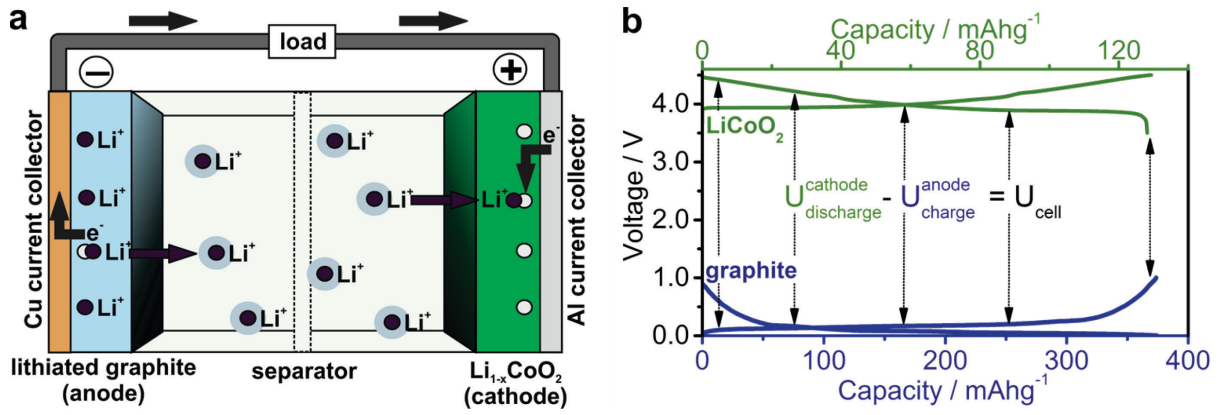
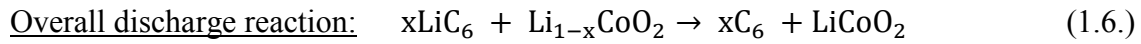
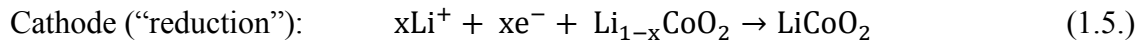
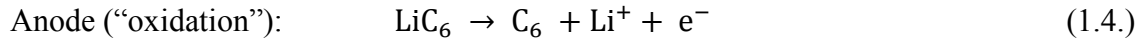


Figure 1.1. (a) Schematic working principle of a Li-ion battery with a graphite anode and LiCoO_2 cathode. (b) Charge/discharge curves of graphite and LiCoO_2 in Li-ion half-cells.

The reactions taking place during discharge of the battery are as follows:¹¹



An important value is the amount of charge Q , which can be calculated by integration of the current I over the time t :¹²

$$\int_{t_1}^{t_2} I(t) dt = Q = nzF \quad (1.7.)$$

n = amount of substance, z = number of electrons exchanged, F = Faraday's constant

It should be noted that in real batteries not the entire charge is used for the reversible redox reaction, but a certain fraction is consumed by irreversible side reactions, such as the decomposition of the electrolyte at very high or low voltages.

A measure for the extent to which such irreversible processes are consuming charge is the coulombic efficiency (CE):¹²

$$\text{CE} = \frac{Q_{\text{discharge}}}{Q_{\text{charge}}} \cdot 100\% \quad (1.8.)$$

For combinations of electrolytes and electrode materials, where the electrochemical potential of the anode μ_a lies above the LUMO or the electrochemical potential of the cathode μ_c lies below the HOMO of the electrolyte, reductive/oxidative electrolyte decomposition is

thermodynamically favored.¹³ However, the electrolyte decomposition does in the most desirable case not continue indefinitely, because an electronically insulating, yet ionically conducting interface is formed between electrolyte and electrode material. This interface composed of decomposition products of the electrolyte is the so called solid electrolyte interface (SEI) and can block further electrolyte decomposition.¹⁴

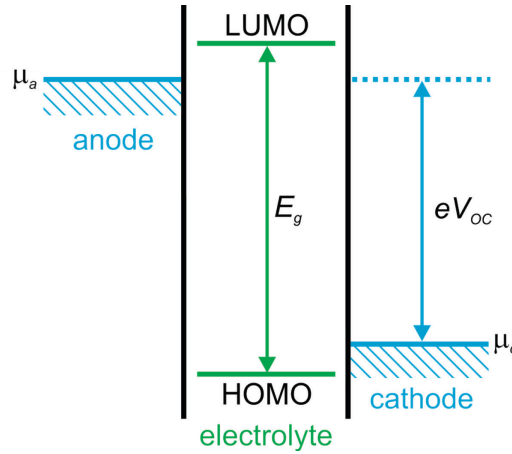


Figure 1.2. Schematic representation of the relative energies of electrolyte and electrodes. The stability window of the electrolyte is given by E_g with the LUMO above the electrochemical potential of the anode μ_a and the HOMO below the electrochemical potential μ_c of the cathode meaning that decomposition of the electrolyte is thermodynamically not favored. Reproduced with modifications from Goodenough et al.¹³

Relating the charge Q to the mass of the electrode material m gives the specific capacity C_s , which can be converted into the volumetric density C_v , if the density ρ is known:

$$C_s = \frac{Q}{m} = \frac{nzF}{m} \quad (1.9.)$$

$$C_v = C_s \cdot \rho \quad (1.10.)$$

Accordingly the theoretical capacity $C_{s,th}$ of a given electrode material can be calculated according to:

$$C_{s,th} = \frac{zF}{M} \quad (1.11.)$$

For instance, in case of LiCO_2 the theoretical specific capacity is 137 mAh g^{-1} based on $z = 0.5$ and $M = 97.87 \text{ g mol}^{-1}$.¹⁵ The important electrochemical parameters which determine the energy density W of such a battery are not only the specific/volumetric capacities C_a of the anode and C_c cathode material as they give the number of how much charge can be

extracted from the electrode materials per unit of mass/volume, but also the voltage U at which electrons are extracted from the anode and transferred to the cathode material according to:¹⁶

$$W = U \cdot C_{\text{cell}} = U \cdot \frac{C_a C_c}{C_a + C_c} \quad (1.12.)$$

$$W_s = U \cdot \frac{C_{s,a} C_{s,c}}{C_{s,a} + C_{s,c}} \quad (1.13.)$$

$$W_v = U \cdot \frac{C_{v,a} C_{v,c}}{C_{v,a} + C_{v,c}} \quad (1.14.)$$

Relating the energy density to the unit of time t during which the energy is released leads to the power density P :

$$P = \frac{W}{t} = \frac{U \cdot C_{\text{cell}}}{t} \quad (1.15.)$$

Besides power and energy density, there are numerous important electrochemical key values that have to be considered such as long-term cycling performance (cycle life), calendrical life, coulombic efficiency (measure for charge loss due to irreversible side reactions, *e.g.*, electrolyte decomposition), energy efficiency and the performance at different charge/discharge rates or at different temperatures. Moreover, since values such as energy or power density are related to the mass/volume of the electrode materials, for practical cells one has to consider the mass/volume of all cell parameters such as electrolyte, casing and separator. For instance, whereas the theoretical capacity of a graphite/LiCoO₂ cell is $\sim 400 \text{ Wh kg}^{-1}$, the practical energy density is with $\sim 200 \text{ Wh kg}^{-1}$ approximately 50% lower.¹⁷

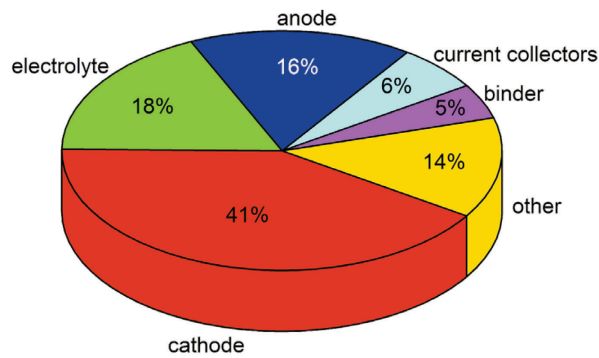


Figure 1.3. Weight distribution of different battery components in a typical (high-energy) Li-ion battery. Derived from Gaines et al.¹⁸

Especially, for practical cells further equally important factors to consider are safety, environmental friendliness and cost both in absolute numbers as well as related to cycle life and energy density. The great challenge to develop new batteries is to find systems that fulfill this multitude of parameters satisfactorily.

Emerging battery technologies. Notably, in terms of energy and power density LIBs outperform all other mature rechargeable battery technologies such as Ni-MH, Ni-Cd or Pb-acid (see Figure 1.4.).

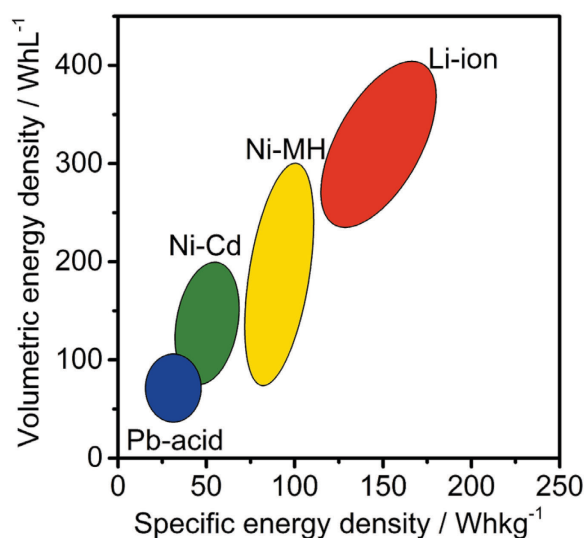


Figure 1.4. Comparison of volumetric and specific energy densities of the commercially four most important rechargeable (room-temperature) batteries. Derived from Tarascon et al.⁹

However, the superior performance of LIBs has not led to the complete replacement of the aforementioned alternatives, due to the fact that depending on the application – which can range from small batteries for watches to large scale energy storage systems as uninterrupted power supply for entire cities^{19, 20} – factors such as cost or safety can be more important than solely energy and power density. Particularly, Pb-acid and primary batteries continue to play a major role accounting for ~50% of the revenue with batteries (see Figure 1.5.).

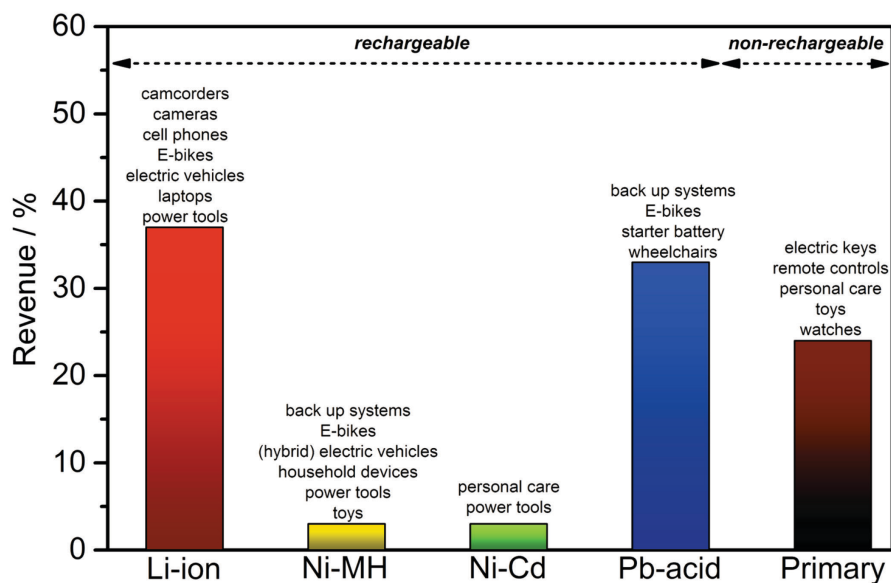


Figure 1.5. Global revenue distribution of 2009 (total 47.5 billion USD) and typical applications of different batteries.²¹

Presently, three main fields for batteries with somewhat different requirements can be identified: portable electronics, electric vehicles and large scale energy storage. Whereas, portable electronics powered by batteries are ubiquitous, their use for the latter two applications remains rather the exception. The motivation to use batteries as energy storage devices for vehicles and large scale system mainly stems from the need to lower carbon dioxide emissions. Instead of burning either fossil fuels in vehicles or power plants for energy generation, the ultimate idea is to use the energy stored in efficient batteries produced from intermittent renewable sources such as wind or solar power. However, for electric vehicles the main issue up to date is that even the best Li-ion battery technology cannot compete in terms of energy density with the established combustion engine/gasoline and is rather expensive.²² It is also rather the cost factor, which has hampered the widespread use of batteries for large scale energy storage.² Notably, the cost of batteries depends largely on the materials involved, for instance, in case of LIBs 96% of the overall cost is due to the materials (see Figure 1.6.). Particularly, the Li-ion containing electrolyte and cathode material LiCoO_2 , which also contains relatively expensive cobalt, are responsible for almost 70% of the overall cost of such a battery. In light of the relatively high cost of Li-salts and issue of supply security as result of their limited abundance, batteries based on sodium (Na),²³⁻³⁵ magnesium (Mg)³⁶⁻⁴⁰ or aluminum(Al)^{39, 41} are gaining increasing attention due to the high earth-abundance of their elements and therefore potentially lower cost (see also Figure 1.7.). However, replacing Li-ions with Na-, Mg- or Al-ions has drastic

effects on the electrochemistry and different challenges are encountered requiring the development of new electrode materials and electrolyte formulations.

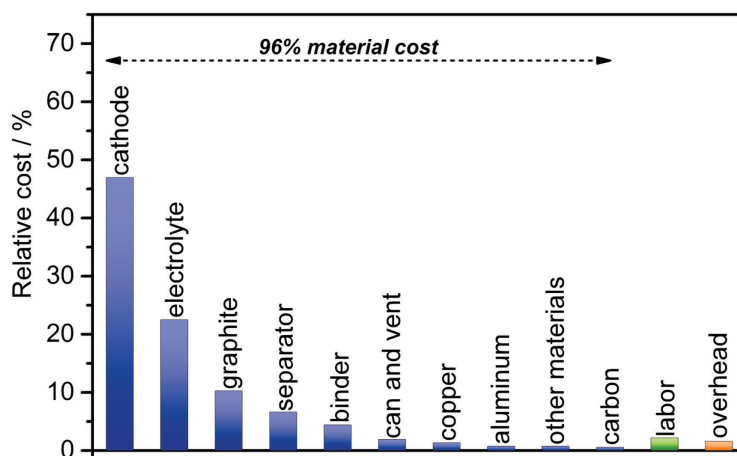


Figure 1.6. Cost structure of different battery components in a typical Li-ion battery. Derived from Gaines *et al.*¹⁸

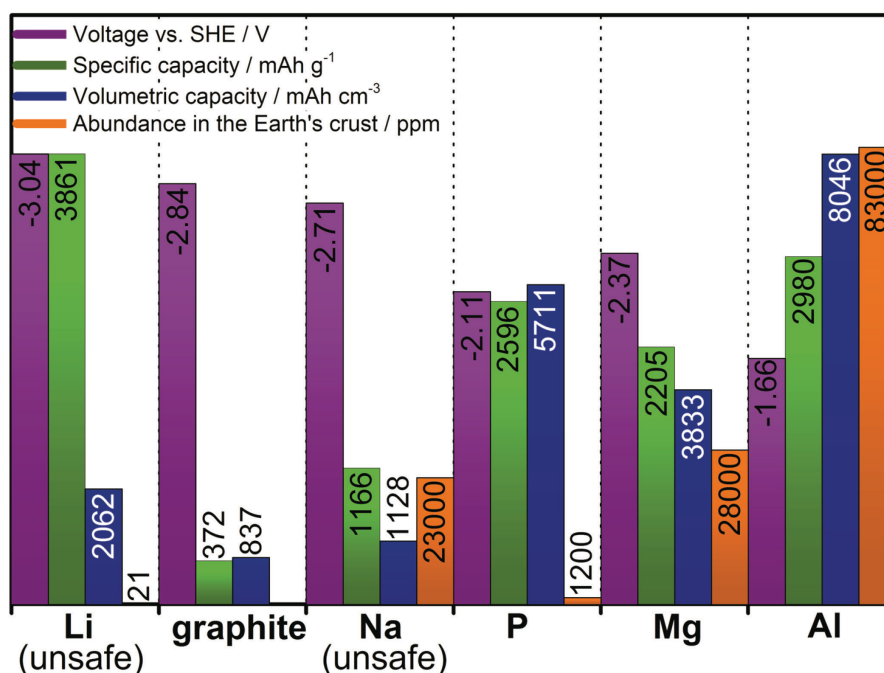


Figure 1.7. Comparison of the voltage vs. SHE (standard hydrogen electrode), specific and volumetric capacities and earth-abundance for anode materials. Since elemental lithium and sodium cannot be used safely in rechargeable batteries due to dangerous dendrite formation, graphite (for Li-ion storage) and phosphorus (for Na-ion storage) are listed as potential substitutes.^{39, 42}

Na-ion batteries (SIBs) are conceptually identical to their Li-ion counterparts. However, despite the proximity in the periodic table, the electrochemistry of Li- and Na-ions is often very different due to the ~50% larger radius of the Na-ion compared to Li. For instance, the direct Na-ion analogue to LiCoO_2 – NaCoO_2 – shows poorer electrochemical performance

characterized by significantly lower discharge voltage.⁴³ Nevertheless, in terms of Na-ion cathode materials, very efficient electrode materials have been developed such as $\text{Na}_{1.5}\text{VPO}_{4.8}\text{F}_{0.7}$ ⁴⁴ or $\text{Na}_4\text{Co}_3(\text{PO}_4)_2\text{P}_2\text{O}_7$ ⁴⁵ with electrochemical performances comparable to the best Li-ion cathodes. In fact, for Na-ion batteries the great remaining challenge lies in developing a suitable anode material. Similar to metallic Li using elemental Na as anode material is, because of dendrite formation, not advisable for rechargeable batteries.⁴⁶ In addition, graphite, which serves as anode material for Li-ion batteries by intercalating Li-ions between the graphene layers, struggles to insert Na-ions in conventional electrolytes simply due to the larger size of the ions.⁴⁷ Thus, the development of high-performance SIBs largely depends on the development on suitable high-energy density anode materials.

Contrary, to both LIBs and SIBs, where the elemental metals cannot be used as anode materials because of dendrite formation during cycling, which can lead to short-circuiting (and explosion) of the battery,^{9, 10, 46} the great advantages of Mg-ion batteries (MIBs) and Al-ion batteries (AIBs) are that elemental Mg and Al can be deposited smoothly and are therefore safe to use as anode materials in rechargeable batteries.^{37, 39}

Importantly, metallic Mg and Al combine many important properties such as safety, low cost, non-toxicity, very high storage capacities (2205 mAh g⁻¹ / 3833 mAh cm⁻³ for Mg, 2980 mAh g⁻¹ / 8046 mAh cm⁻³ for Al, see also Figure 1.7.) making them ideal anode materials.^{37, 39, 48} Unlike many other anode materials for LIBs or SIBs such as Si or Sn, which would require the fabrication of electrodes with conductive additives and polymeric binders or even nanostructuring of the active material, metallic Mg and Al can be used readily as anode materials and are easy to handle. However, despite all the advantages of metallic Mg and Al as anode material, commercialization of such batteries has been mainly hindered by the lack of efficient cathode materials and – especially in case of MIBs – limitations caused by the electrolyte.

In case of MIBs the difficulty lies in reversibly inserting and removing Mg-ions (at reasonably high charge/discharge rates at room temperature) as result of the typically stronger coulomb interactions of the Mg-ions (small radius and divalent charge) with the host lattice of “classical” cathode materials compared to Li- or Na-ions. One of the few examples where efficient Mg-insertion/removal has been demonstrated successfully is Chevrel phase Mo_6S_8 ($\text{Mo}_6\text{S}_8 + 2\text{Mg}^{2+} + 4\text{e}^- \leftrightarrow \text{Mg}_2\text{Mo}_6\text{S}_8$) enabled by relatively weak interactions between Mg-ions and the host lattice.³⁶ In addition to finding suitable cathode materials, developing Mg-ion batteries is complicated by the electrolyte chemistry.^{49, 50} One important consideration for all batteries is that due to the either very negative or positive potential at the

electrodes the electrolyte is prone to reduction or oxidation, leading to the formation of a layer of the decomposition products on the electrodes inhibiting further electrolyte decomposition. Whereas in case of LIBs or SIBs, typically this SEI layer is still ionically conducting because of the high diffusivity/mobility of Li/Na-ions, in case of Mg-ions such layer immediately blocks Mg-diffusion and therefore inhibits the cell reaction.³⁹ To overcome this issue Grignard and borohydrides have been demonstrated as efficient Mg-electrolytes. However, such compounds are not only possibly too reactive to be used in practical cells, but because of their high reactivity the maximal cell voltage of MIBs is usually limited to ca. 2 V, if non-noble metal current collectors are used.^{37, 51} In conclusion, the greatest challenges for Mg-ion batteries lie in both finding electrolytes with higher electrochemical stability and to develop cathode materials which can efficiently and quickly insert/remove Mg-ions with high capacities and at high potentials.

Al offers theoretically even higher volumetric capacities than Li (four times higher) or Mg (two times higher), as result of its low mass and the fact that each Al-atom can “release” three electrons per formula unit.³⁹ However, the potential for the Al^{3+}/Al reaction is far more shifted towards positive values (-1.66 vs. SHE, see also Figure 1.7.), meaning that for a given cathode material, the obtained voltage with Al-anodes will always be lower compared to for instance Li (-3.04 V vs. SHE). Additional complications are the fact that Al-plating and stripping is typically achieved using mixtures of AlCl_3 and ionic liquids, which tend to corrosion and often limit the accessible potential range to values below ~ 2.5 V.³⁹ Moreover, finding suitable cathode materials with high capacity and high operating voltage remains a great challenge. One of the few examples, where a relatively efficient Al-ion battery has been reported, is by using pyrolytic graphite as cathode material.⁴¹ However, it should be noted that the working principle of such a battery is different from “classical” Li-ion batteries. Rather than reversibly inserting/removing Al^{3+} – which would be very difficult because of the strong coulombic interaction of such trivalent ion with any host lattice – the species that is inserted between the graphene layers is AlCl_4^- .⁴¹ Whereas the insertion of Al^{3+} would be accompanied by the “reduction” of the respective electrode material, in case of AlCl_4^- insertion the direction of the current is reversed. In fact, since for present day Al-ion batteries the electrolyte is majorly involved in the electrode reactions and therefore a limiting factor, one additional challenge for Al-ion batteries will be to minimize the amount of electrolyte used and therefore maximize the whole battery system in terms of energy per volume and mass.

In summary, the development of potentially less expensive batteries for large scale energy storage such as SIBs, MIBs and AIBs and potential improvement of present day LIBs in terms of power or energy density largely depends on the development of suitable high-performance electrode materials.

1.2. Nanomaterials as electrode materials for electrochemical energy storage

Nanomaterials – meaning any kind of material with sizes below 100 nm – have in the recent years become of major interest for the field of electrochemical energy storage, due to potential advantages resulting from their nanoscale dimensions.⁵²⁻⁵⁴ Nanostructuring of the active material can enhance reaction kinetics and accordingly allow charging/discharging at higher rates, since, due to the higher surface area of nanomaterials, the contact area with the electrolyte and other electrode components (such as conductive carbons) is larger. In addition, reaction kinetics can be enhanced as result of the short diffusion lengths within the nano-sized material. In particular, the diffusion time constant τ is given by the square of the diffusion length L divided by the diffusion constant D :⁵⁵

$$\tau = \frac{L^2}{D} \quad (1.16.)$$

Whereas most potential advantages of nanomaterials arise from the higher surface area, it is likewise the source of most disadvantages.⁵⁶ The irreversible charge loss by formation of the SEI *via* decomposition of the electrolyte is typically much higher for nano-sized materials because of their larger surface area. Since the charge needs to be balanced by the opposing electrode (*e.g.*, LiCoO_2), this phenomenon lowers the energy density of a practical cell significantly. In addition, parasitic side reactions of the electrolyte are typically more pronounced for electrodes with higher surface areas leading to potentially poorer long-term stability. Further disadvantages of nano-sized materials are their often relatively complicated and expensive preparation and the fact that the nano-sized materials show typically lower densities compared to bulk materials.⁵⁶ Nevertheless, interest in nanomaterials has remained strong, due to the fact that numerous potentially promising high capacity electrode materials (shown in Figure 1.8.) – practically unusable as bulk materials – show only reasonable performance for Li- and Na-ion storage in nanostructured form.^{53, 57-61}

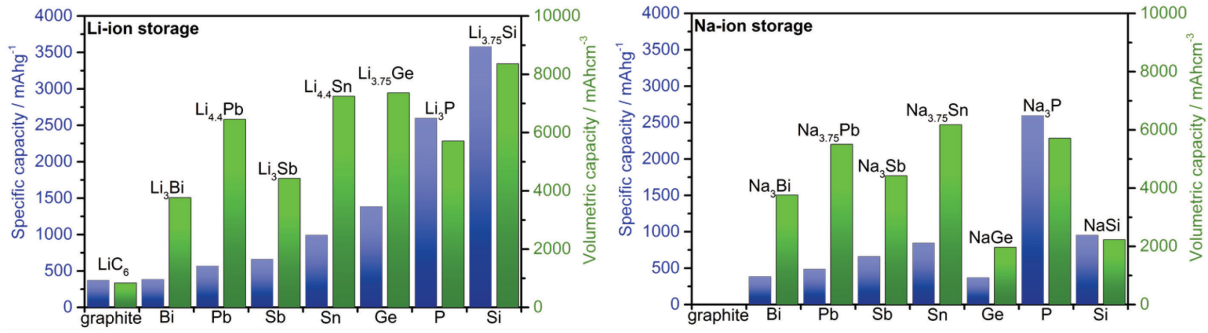


Figure 1.8. Specific and volumetric capacities for potential Li- and Na-ion anode materials taking into account the highest lithiated or sodiated phase at room temperature (based on values from the database <http://materials.springer.com>).

However, the alloying reactions these materials undergo with Li or Na typically involve massive volumes changes in the range of 400-100%, calculated on basis of the change of molar volume ΔV between the final (*e.g.*, fully lithiated) phase V_m and the initial phase V_m^0 (Figure 1.9.):

$$\Delta V = 100\% \cdot \frac{(V_m - V_m^0)}{V_m^0} \quad (1.17.)$$

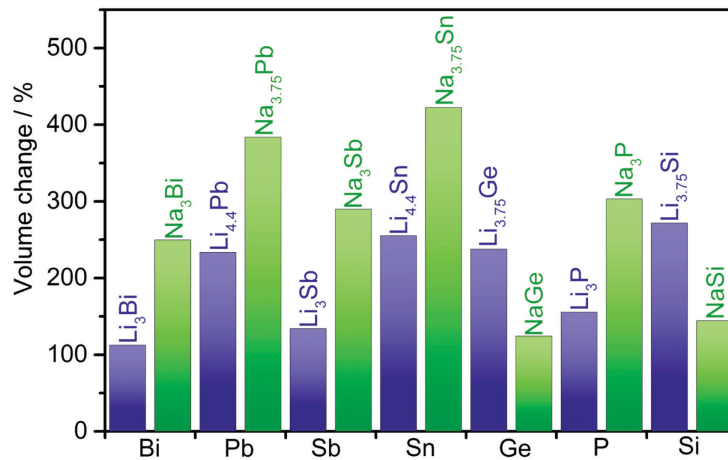


Figure 1.9. Calculated molar volume change for potential anode materials for Li- and Na-ion storage taking into account the highest lithiated or sodiated phase at room temperature (based on values from the database <http://materials.springer.com>).

Such massive volume changes during charging/discharging typically lead to such large mechanical stress, that the electrode material cracks and crumbles. This pulverization of the materials subsequently causes loss of electrical contacts and hence rapid decrease of the capacity. Importantly, numerous reports indicate that this issue can be mitigated by the use of nano-sized materials.^{16, 19, 26, 29, 53, 54, 56-58, 61-76} The underlying principle is that nanometer-sized particles can exhibit different mechanical properties than their bulk

counterparts. For instance, for Si NPs as Li-ion anode materials, it was shown that below a particle size of 150 nm Si NPs expand elastically leading to superior cycling performance compared to the larger-sized particles, which crack upon expansion.⁷⁷

Finally, apart from the two main advantages of nanomaterials – potentially improved reaction kinetics and cycling stability – the use of nanostructured materials can lead to different reaction pathways or higher reversibility, if the electrochemical reaction for instance involves phase separation as it is the case for many conversion type materials.⁵⁶

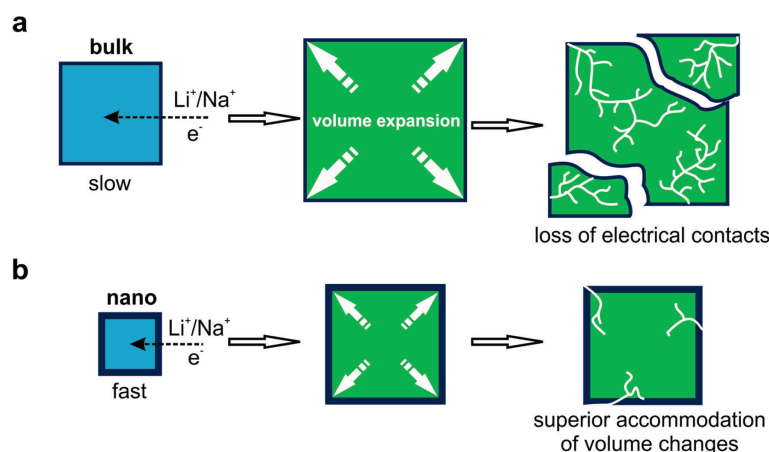


Figure 1.10. Schematic representation of the advantages of nanostructured materials compared to their bulk counterparts.

1.3. Scope and outline of the dissertation

In summary, this PhD project was dedicated to the synthesis of nanostructured materials and their application as electrode materials for rechargeable, room-temperature batteries. This chapter provided background on rechargeable batteries and the possible benefits of employing nanomaterials as electrode materials and is followed by details on the used experimental methods and techniques (Chapter 2). In the following seven chapters (Chapter 3-9) the results of this thesis are presented corresponding to five first-author publications and two patent applications of the Aspirant. The final chapter (Chapter 10) concludes the thesis and provides an outlook on future directions. The full list of publications, including all coauthored publications from collaborative projects, and list of filed patents can be found in the appendices (Appendix C and D).

Inexpensive antimony nanocrystals and their composites with red phosphorus as high-performance anode materials for Na-ion batteries (Chapter 3). Despite the fact that Na-ion batteries had been conceptually studied already in the 1980s,^{78, 79} just around 2011 the field started to gain momentum with an ever increasing number of publications per year to the point that just in the years 2014/2015 more articles were published than in all previous years combined (based on <http://www.scopus.com>, search term “sodium ion batteries”). Whereas at around the time this PhD project had started the performance of Na-ion cathode materials was already comparable to its Li-ion counterparts,⁴⁴ it had become clear that the Achilles heel of Na-ion batteries is the lack of suitable anode materials due to the poor performance of graphite and silicon – the two most prominent Li-ion anode materials.^{80,81} Based on the pioneering work of Darwiche *et al.*⁸² on bulk Sb as anode material for Na-ion batteries, the Kovalenko Group had reported unprecedented rate capability and excellent cycling stability for monodisperse 20 nm Sb NCs as Na-ion anode material.⁵⁷ However, despite the fact that such monodisperse NCs can serve as model systems to study size-dependent properties and can show excellent electrochemical properties, they are unlikely materials to be used on the industrial scale. Due to the relatively high cost for precursors, solvents and multiple purification steps including removal of organic ligands – especially when considering reaction yield – the synthesis of monodisperse NCs is too expensive to allow commercialization of such materials. Therefore, the question, which triggered the first part of this chapter, was, if it is possible to develop an inexpensive synthetic procedure to produce Sb NCs with the same average size (sacrificing size

uniformity to a certain extent) and how their performance as Na-ion anode materials would differ from monodisperse Sb NCs. In light of the fact that red phosphorus theoretically shows one of the highest Na-ion storage capacities (2596 mAh g^{-1}),^{27, 28} the aim of the second part of this chapter was to explore the possibilities of improving cycling stability and rate capability by forming a composite of red phosphorus and inexpensively synthesized Sb NCs.

Inexpensive colloidal SnSb nanoalloys as efficient anode materials for Li- and Na-ion batteries (Chapter 4); Oxidized Co-Sn nanoparticles as long-lasting anode materials for Li-ion batteries (Chapter 5). Based on the work presented in Chapter 3 on inexpensively synthesized Sb NCs by simple reduction of antimony chloride with sodium borohydride in N-methylpyrrolidone, the goal of the work presented in these chapters was to investigate to what extent this inexpensive synthetic procedure can be applied to other metallic nanocrystals, particularly intermetallic nanoalloys of tin (Sn). Sn-based alloys are of particular interest, due to the fact that (together with Si) Sn is one of the few anode materials potentially capable of improving the energy and power density of practical Li-ion batteries^{58, 83-86} Previous reports have hinted at the superior performance of intermetallic Sn alloys compared to pure phase Sn anodes, especially in terms of cycling stability.^{64, 87-89} The two anode materials investigated (mainly for Li-ion storage) were SnSb – as example of an intermetallic compound with two active materials – and Co-Sn based materials – as example of an alloy with an active (Sn) and inactive (Co) material. Apart from half-cell tests, the goal was also to evaluate these materials with regards to their applicability for full-cells by carrying out electrochemical tests with LiCoO_2 (for Li-ion batteries) or $\text{Na}_{1.5}\text{VPO}_{4.8}\text{F}_{0.7}$ (for Na-ion batteries) as cathode materials. This development of inexpensive, upscalable procedures to produce high-performance anode materials for Li-ion batteries was a particular goal of the collaboration of the Kovalenko Group with Belenos Clean Power Holding Ltd. as part of the CTI project “*Precisely Engineered Nanocrystals and their Superstructures for Advanced Li-ion Batteries*”.

Pyrite (FeS_2) nanocrystals as inexpensive high-performance Li-ion cathode and Na-ion anode materials (Chapter 6); Evaluation of metal phosphide nanocrystals as anode materials for Na-ion batteries (Chapter 7). Despite their theoretically very high specific capacities based on conversion reactions,⁹⁰ numerous metal sulfides and phosphides had never been studied as potential anode materials for Na-ion batteries. In fact, when the two projects presented in Chapters 6 and 7 were conceived in 2014, only sulfides of

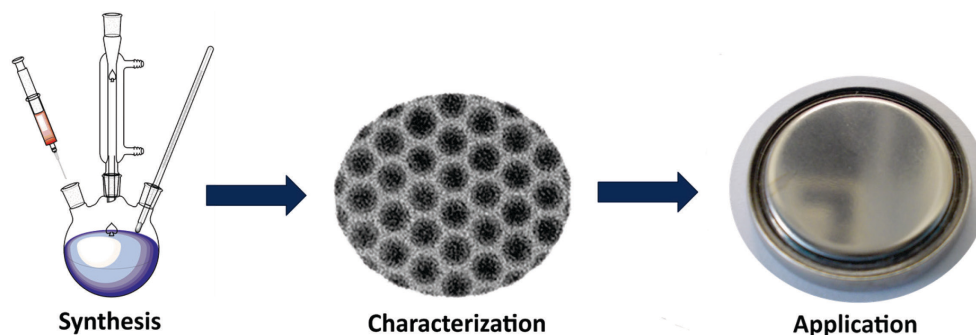
Mo,^{29, 91-94} W,⁹⁵ Sn⁹⁶⁻⁹⁹ and Sb¹⁰⁰ had been investigated. In case of metal phosphides even less was known about the Na-ion storage properties of this class of materials with the report of Li *et al.*¹⁰¹ on FeP being the only prior publication. Hence, the main goal of the work presented was to investigate and compare nanostructured metal sulfides (FeS₂, NiS₂, CoS₂, PbS, SnS, CuS, ZnS, Cu₂ZnSnS₄) and metal phosphides (FeP, CoP, NiP₂, CuP₂) as potential anode materials for Na-ion batteries. Given the commercial application of FeS₂ as cathode material in primary Li-ion batteries (*e.g.*, by Energizer[®]), application of FeS₂ NCs as cathode material for rechargeable Li- and Na-ion batteries is also considered in Chapter 6.

Efficient and inexpensive Na/Mg hybrid battery (Chapter 8). Since the pioneering work of Aurbach and coworkers in 2000,³⁶ Chevrel-phase Mo₆S₈ has remained the benchmark material for Mg-ion batteries, despite intensive efforts to identify superior cathode materials.¹⁰²⁻¹¹⁰ Due to the difficulty to develop suitable Mg-ion cathode materials, a new strategy that has been proposed in several proof-of-principle publications starting from 2014 is to use Li/Mg hybrid batteries.^{48, 111-116} In such a battery the metallic Mg-anode is combined with a Li-ion cathode material to circumvent the issue of slow kinetics typical Mg-ion cathodes are suffering from. However, the practical energy density of such battery is limited by the oxidative stability window of the electrolyte on the one hand and the fact that large volumes of electrolyte are necessary to store the Li/Mg-ions. Hence, it is highly unlikely that this kind of battery can outperform state-of-the-art Li-ion batteries in terms of practical energy density. However, since for applications such as large-scale energy storage rather cost than energy density are the major requirement, the goal of the work presented in this chapter was to develop a hybrid battery that is particularly inexpensive. It was aimed at combining a Na-ion rather than a Li-ion cathode material with the metallic Mg-anode, because of the significantly higher abundance and hence lower cost of sodium salts in comparison to lithium. The question which triggered this work was not only whether it is possible to design such a Na/Mg hybrid battery (which had never been demonstrated before), but, if it is possible using an inexpensive and environmentally friendly cathode material, namely FeS₂.

Pyrene-based polymers as high-performance cathode materials for Al-ion batteries (Chapter 9). In 2015 Lin *et al.* published in *Nature* the concept of a non-aqueous Al-ion battery based on a pyrolytic graphite cathode with unprecedented cycling stability, rate performance and energy efficiency.⁴¹ Accordingly, the question, which motivated the work presented in this chapter, was, if molecular compounds composed similarly to graphite

of sp^2 -hybridized carbons, yet only few condensed aromatic rings, can serve in analogy as cathode material. In particular, the aim was to investigate the molecule pyrene ($C_{16}H_{10}$) in monomeric and polymeric form, because of its reported p-type redox-activity at relatively high voltages for Li- and Na-ion batteries.^{117, 118} This class of materials is especially interesting, since, unlike cathode materials based on relatively costly transition metals (*e.g.*, Co, Ni), pyrene is inexpensively available by distillation of coal tar and used already commercially in large quantities for dyes and dye precursors.¹¹⁹ A potential advantage of such polymers over graphite are the numerous possibilities to tune the electrochemical properties by variation of the chemical composition. Therefore, the aim of this work was to synthesize not only homopolymers of pyrene, but copolymers with pyrene carrying substituents (*e.g.*, 1-nitropyrene) and to evaluate the effects of this compositional variation on the electrochemical behavior.

Chapter 2. Methods and techniques



2.1. Synthesis of nanocrystals

In this work NCs were typically synthesized colloiddally based on the “hot-injection” method.¹²⁰ This method is based on the rapid addition of one precursor (reagent A) to a hot solution of another precursor (reagent B) (Figure 2.1.).

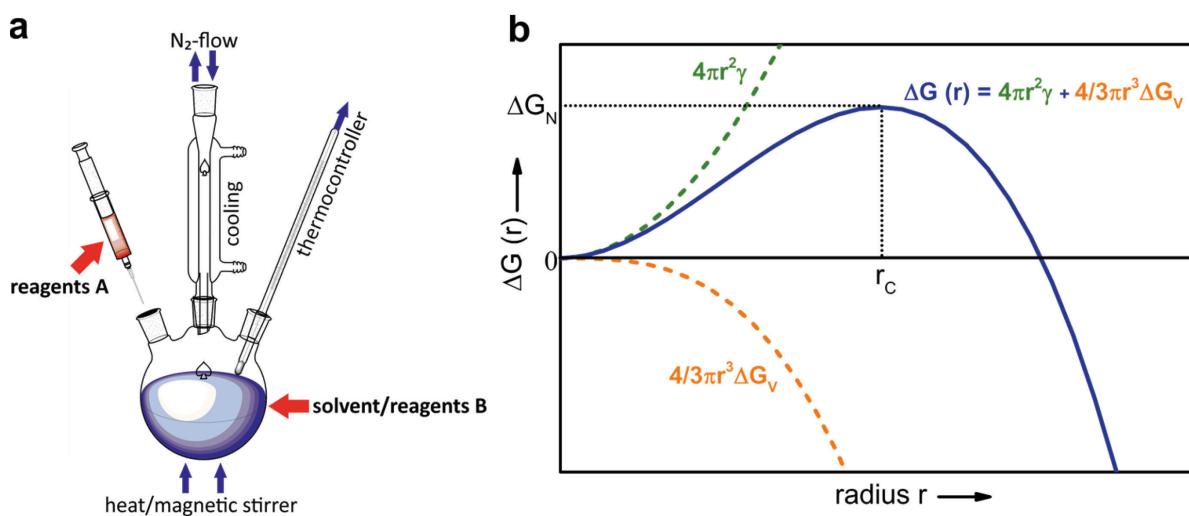


Figure 2.1. (a) Schematic representation of the experimental set-up for synthesis of colloidal nanocrystals. (b) Total free energy of a spherical nucleus $\Delta G(r)$ with the contributions of the surface energy and free energy of bulk crystal formation. Derived from Kwon et al.¹²¹

As result of the typically high concentrations of the precursors and high temperature, the activation barrier for nucleation can be overcome easily resulting in the formation of many small crystal nuclei contrary to few large ones. The underlying thermodynamic considerations are the following:^{121, 122}

The total free energy $\Delta G(r)$ of a spherical nucleus with radius r is given by the sum of the surface energy γ (positive value) and the free energy of the bulk crystal formation ΔG_V (volume energy; negative value for supersaturations $S > 1$).

$$\Delta G(r) = 4\pi r^2 \gamma + \frac{4}{3}\pi r^3 \Delta G_V \quad (2.1.)$$

$$\text{with } \Delta G_V = \frac{-RT \ln S}{V_m} \quad (2.2.)$$

$$\text{and } S = \frac{[M]}{[M]_0} \quad (2.3.)$$

R = gas constant, T = temperature, V_m = molar volume, $[M]$ = monomer concentration, $[M]_0$ = monomer concentration of the bulk solid

For small particles the positive contribution from the surface energy leads to overall positive values of $\Delta G(r)$. Differentiation of $\frac{d\Delta G(r)}{dr}$ gives the critical radius a particle needs to have to stay stable in solution and not be dissolved again, expressed as r_C .

$$r_C = \frac{2\gamma V_m}{RT \ln S} \quad (2.4.)$$

Vice versa r_C reveals the requirements for obtaining small nuclei, which is high supersaturation S and high temperature T .

It should be noted that typically the hot-injection method is used for synthesizing not only small nano-sized particles, but monodisperse ones, meaning particles with very narrow size distributions. To obtain such high degree of uniformity important considerations are the stages of size-focusing during the NC growth and ultimately Ostwald ripening, once the monomer concentration is sufficiently depleted,¹²³ which are, however, not discussed here, since obtaining monodisperse particles was not a particular goal of this work.

The general experimental set-up for synthesizing NCs is schematically shown in Figure 2.1.a. In a typical experiment NCs were synthesized by heating a solution of a specific precursor in a round-bottom flask equipped with a condenser using a heating-mantle and digital thermocontroller as well as a magnetic stirrer. To exclude air and humidity synthesis was carried out under N_2 flow *via* Schlenk-line. Upon reaching the desired reaction temperature additional reagents were injected with a syringe and needle through a septa into the flask and kept at the reaction temperature for the desired amount of time.

2.2. Characterization

Transmission electron microscopy (TEM). TEM is a highly useful technique for obtaining information about morphology and size of nanomaterials down to resolutions of less than 1 nm (in case of HR-TEM). The working principle of a TEM is the following.¹²⁴ A focused electron beam generated by an emission source (*e.g.*, tungsten filament) hits the specimen (thin film on conducting substrate). A fraction of the electrons will be fully transmitted, whereas some are elastically or inelastically scattered as result of the interaction with the sample. The extent to which the electrons are scattered depends on the thickness and composition of the materials and ultimately generates the contrast of the final image, which is observed on a fluorescent screen. Namely, in bright-field TEM the darker areas correspond to higher thickness/heavier atoms, as can be also seen in Figure 2.2. as example of a TEM image of Sn NCs. TEMs are typically operated with voltages of 300-100 kV under ultrahigh vacuum. Unless noted otherwise, herein TEM images were obtained with a Philips CM30 TEM microscope at 300 kV using carbon-coated Cu grids as substrates (Ted-Pella).

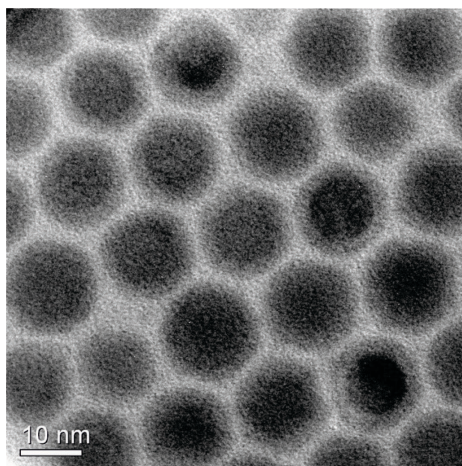


Figure 2.2. TEM-image of 10 nm Sn NCs.

Scanning electron microscopy (SEM). For SEM the sample is scanned with a beam of electrons with typical acceleration voltages of 30-1 kV of the electron beam.¹²⁵ Near the surface of the sample secondary or backscattered electrons are generated by the electron beam. Since the extent to which electrons are detected depends on the distance to the detector, SEM allows revealing the topography of a sample as shown in Figure 2.3.b as example. It should be noted that samples for SEM either need to be conducting or surface-coated with a conducting material. SEM was performed using a NanoSEM 230.

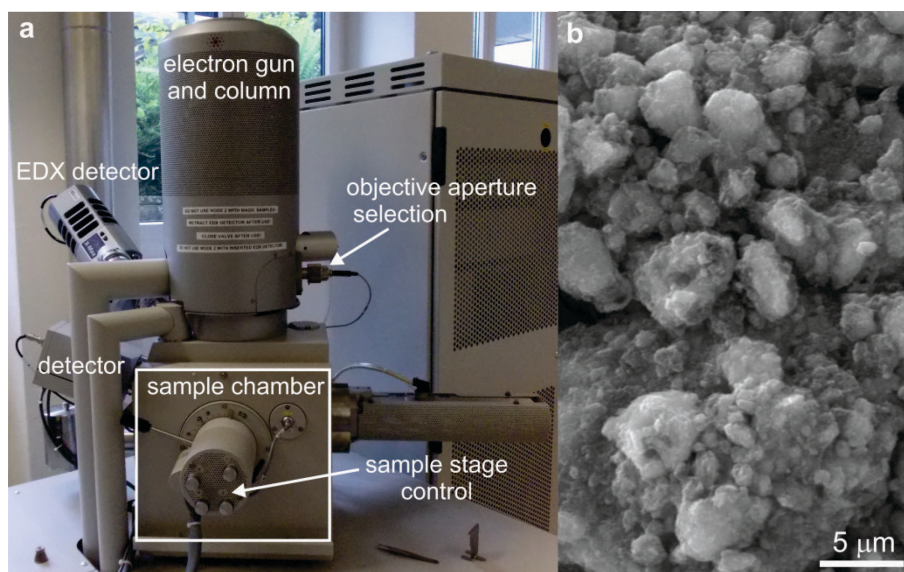


Figure 2.3. (a) Photograph of NanoSEM 230 at the Empa Electron Microscopy Center. (b) SEM-image of carbon coated $\text{Na}_{1.5}\text{VPO}_{4.8}\text{F}_{0.7}$.

Energy dispersive X-ray spectroscopy (EDX). EDX can be used to (rather qualitatively) determine the elemental composition of materials. With an electron beam electrons in the inner shell of the respective elements are excited and ejected. Consequently electrons from outer shells fall back to the unoccupied inner shell emitting the difference in energy as X-rays (see also Figure 2.4.).¹²⁶ Since elements have unique atomic energy levels, detection of the emitted X-rays can be used to reveal the elemental composition. EDX was performed using a NanoSEM 230.

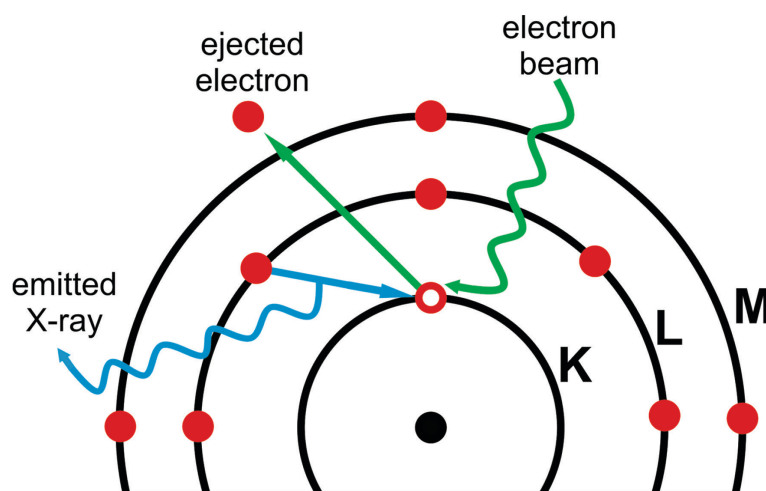


Figure 2.4. Schematic representation of the principle of EDX. Derived from Goldstein et al.¹²⁶

Powder X-ray diffraction (XRD). XRD can be used for identifying the crystals structure(s) present in a material. X-rays, used for irradiating the sample, will be scattered by the crystalline phases. Constructive interference will occur, if the following condition applies (Bragg's Law; see also Figure 2.5.):¹²⁷

$$n\lambda = 2d\sin\theta \quad (2.5.)$$

n = integer number, λ = wavelength, d = lattice spacing, θ = scattering angle

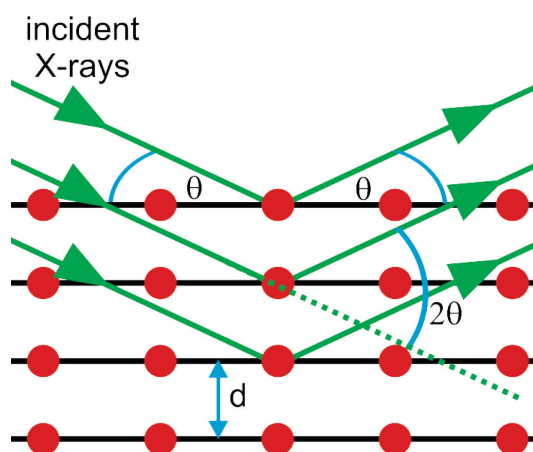


Figure 2.5. Graphical representation of Bragg's Law. Derived from Massa.¹²⁸

Based on the detected intensities as function of the scattering angle a diffractogram, as shown in Figure 2.6. for Sn NCs, is obtained, which can be compared to reported structures for phase identification.

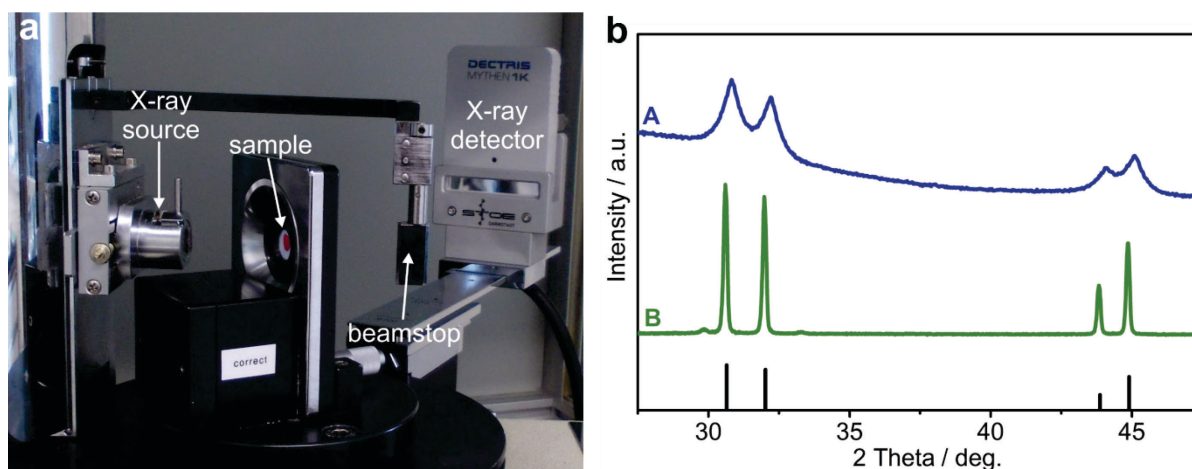


Figure 2.6. (a) Photograph of a STOE STADI P powder X-ray diffractometer. (b) XRD patterns of Sn NCs with sizes of (A) 10-5 nm (see also Chapter 5) and (B) < 150 nm (commercial Sn nanopowder from Sigma-Aldrich).

For materials with sizes of less than 100 nm the XRD-pattern can also be used to gain information about the crystallite domain size, which can be correlated with the line broadening according to:¹²⁹

$$L = \frac{K\lambda}{\beta \cos\theta} \quad (2.6.)$$

L = mean size of crystalline domains, K = shape factor,
 β = width at half the maximum intensity

Powder XRD was measured on a STOE STADI P powder X-ray diffractometer (Cu- $K\alpha_1$ irradiation, $\lambda = 1.540598 \text{ \AA}$, germanium monochromator).

Attenuated total reflection Fourier transform infrared (ATR-FTIR) spectroscopy. For ATR-FTIR measurements first the sample is pressed onto a crystal with high refractive index (*e.g.*, diamond). Then an incident infrared beam undergoes multiple reflections inside the crystal before reaching the detector (see also Figure 2.7.).¹³⁰

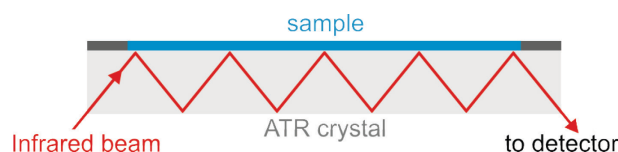


Figure 2.7. Working principle of an ATR-FTIR-spectrometer. Derived from Smith.¹³¹

Based on the different intensities of the incident and reflected infrared light measured by the detector a spectrum as shown in Figure 2.8 is obtained.

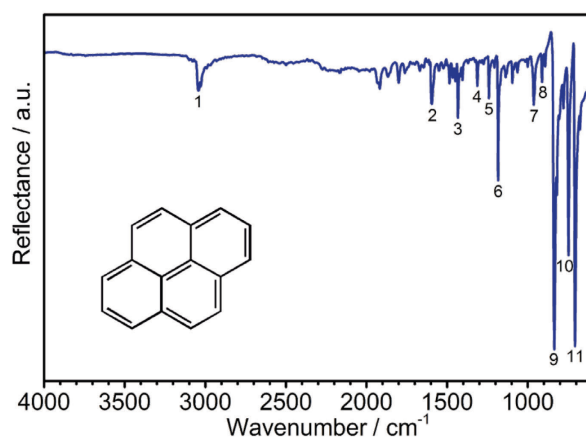


Figure 2.8. Example of a FTIR-spectrum obtained for the molecule pyrene.

Since the energy of IR-active vibrations depends on the nature of the chemical bonds, FTIR spectroscopy can be used to quickly obtain information about the molecules in a sample, in particular, about the presence/absence of functional groups with signals at very characteristic wavenumbers.¹³² For instance, for the molecule pyrene – as shown in Figure 2.8. – the vibrations at $\sim 3050\text{ cm}^{-1}$ (1) can be assigned to $\text{sp}^2\text{-C-H}$ stretching, vibrations at $1600\text{-}1300\text{ cm}^{-1}$ (2-4) to ring vibration and vibrations at $750\text{-}700\text{ cm}^{-1}$ to C-H deformation modes (10,11). The vibrations between $1300\text{-}800\text{ cm}^{-1}$ (5-9) can correspond to various C-H deformation, C-H bending or ring deformation modes.¹³³ ATR-FTIR spectroscopy measurements were carried out on a Nicolet iS5 FT-IR spectrometer (Thermo Scientific).

2.3. Electrochemical measurements

Electrode preparation and cell assembly. For electrochemical testing electrodes were prepared by mixing the active material with carbon black (amorphous carbon particles with sizes of 30-50 nm) as conductive additive, a polymeric binder and a solvent for the latter. Mixing of the components was carried out typically using a Fritsch Pulverisette 7 classic line ball-mill operated for 1 hour at 500 rpm with a ZrO_2 beaker and 50 ZrO_2 balls with a diameter of 5 mm (see also Figure 2.9).

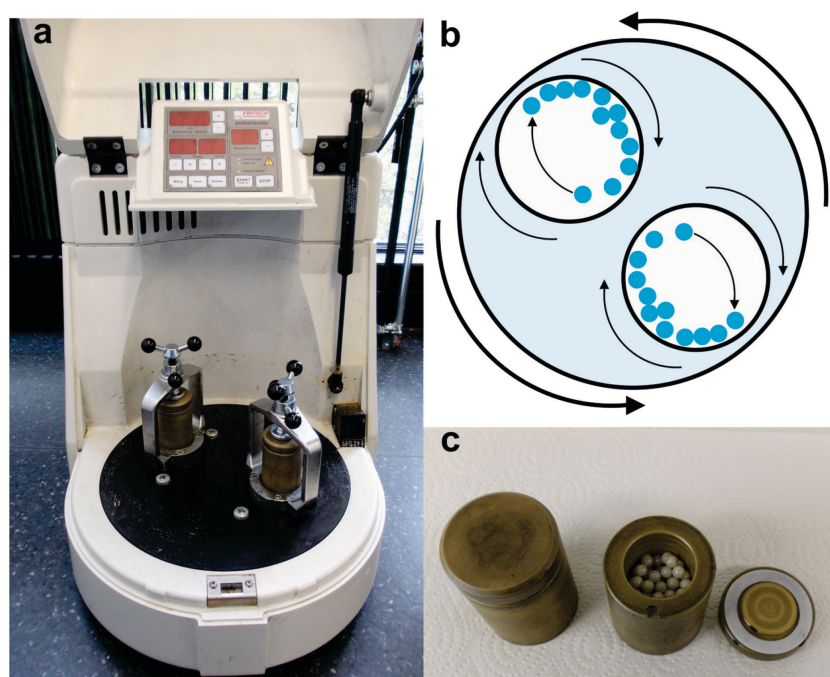


Figure 2.9. (a) Photograph of a Fritsch Pulverisette 7 classic line ball-mill with (c) the respective ZrO_2 ball-milling beakers. (b) Working principle of a ball-mill: Materials are ground or homogenized by the impact of the balls.

The resulting homogeneous slurries were coated onto metallic current collectors (typically Cu or Al) and dried at elevated temperatures under vacuum. Typical electrode loadings were $\sim 0.5 \text{ mg cm}^{-2}$. Herein, the electrochemical performance was typically assessed using stainless steel coin cells (20 mm diameter) with all the components, except the electrolyte, shown in Figure 2.10.

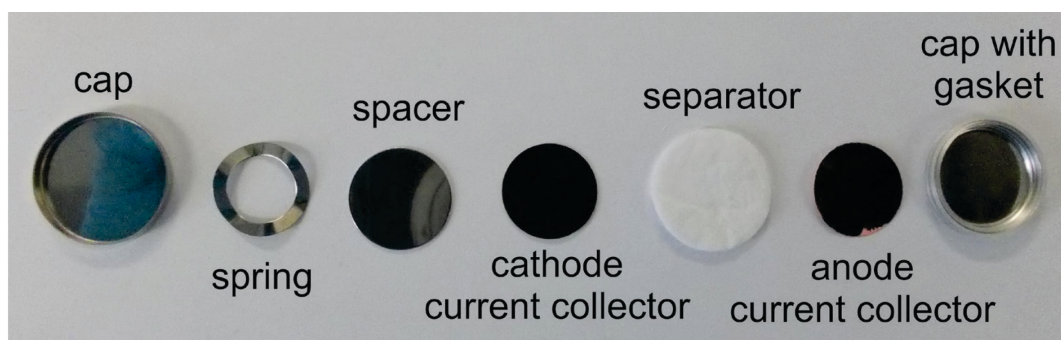


Figure 2.10. Coin cell components of a full-cell. For half-cells the cathode or anode material is replaced by the respective elemental metal (e.g., Li, Na, Mg, Al).

For half-cell tests one of the current collector materials was the respective elemental metal (e.g., elemental Li for Li-ion half-cell tests). Cells were assembled in an Ar-filled glovebox ($[\text{O}_2] < 0.1 \text{ ppm}$, $[\text{H}_2\text{O}] < 0.1 \text{ ppm}$).

Cyclic voltammetry. For cyclic voltammetry (CV) measurements the potential is varied using a defined scan rate v (unit: mV s^{-1}) within a certain potential range:

$$v = \frac{\Delta E}{\Delta t} \quad (2.7.)$$

The observed current reveals at which potential the electrochemical processes take place and, to a certain extent, if such processes are reversible. For instance, in Figure 2.11.a the CV of CoSn_2 NCs (see also Chapter 5) in a Li-ion half-cells is shown.

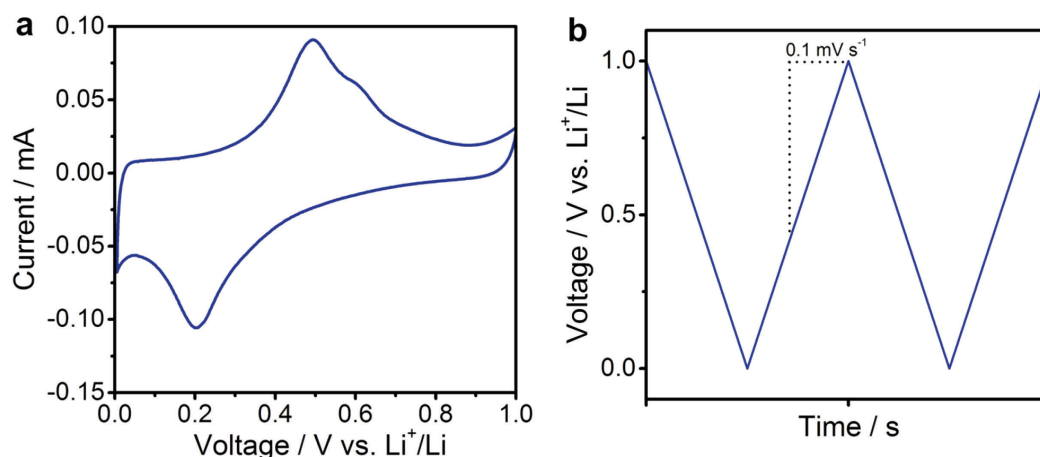


Figure 2.11. (a) CV of CoSn_2 NCs in a Li-ion half-cell with (b) the corresponding change of voltage over time (the slope corresponds to the scan rate v).

The peak upon discharge (negative current) at 0.2 V vs. Li^+/Li can be identified as main lithiation process with the corresponding delithiation process takes place at approximately 0.5 V vs. Li^+/Li (positive current). For instance, no corresponding process can be identified for the relatively high current close to 0 V vs. Li^+/Li , indicating its irreversible nature, most likely corresponding to electrolyte decomposition.

Galvanostatic cycling measurements. Contrary to CV measurements galvanostatic cycling measurements are useful to assess the electrochemical performance of the material under more practical conditions. Batteries are cycled within a defined potential range using a constant current rate (thus galvanostatic). For discharging a negative current is applied. Once the lower cut-off voltage is reached, the sign of the current is changed to the respective positive value and the battery is charged. As discussed in Chapter 1.1., for a given current rate and measured time for charging/discharging the charge can be calculated, and hence the capacity taking into account the mass of the electrode material. Important information about the electrochemistry can be further derived from the profile of the galvanostatic charge/discharge curves (shown in Figure 2.12. for $\text{Na}_{1.5}\text{VPO}_{4.8}\text{F}_{0.7}$, see Chapter 4 for details.)

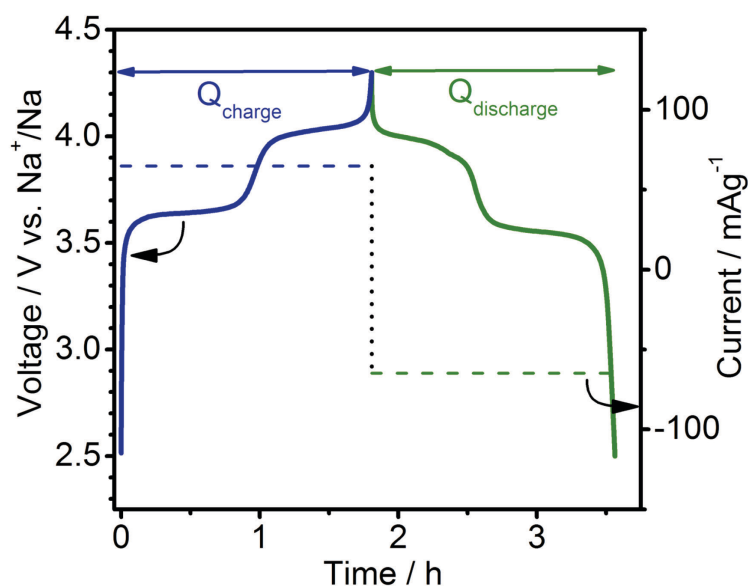
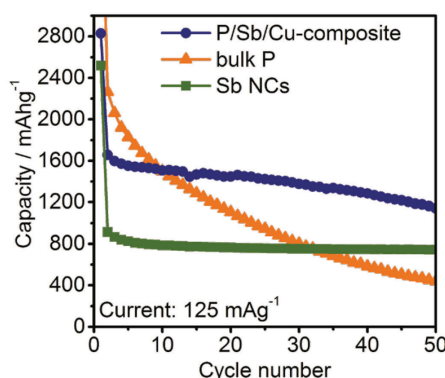


Figure 2.12. Voltage as function of time for galvanostatic charging and discharging of $\text{Na}_{1.5}\text{VPO}_{4.8}\text{F}_{0.7}$ in a Na^+ half-cell.

Similar to the peaks observed in CV measurements, plateau-like areas in the galvanostatic charge/discharge curves, reveal at which potential the main electrochemical processes take place. Importantly, the shift of the plateaus for charging/discharging indicates to a certain extent kinetic hindrance. Large shifts of the potential for charging/discharging ultimately illustrate how good the energy efficiency for the tested battery is. Apart from energy efficiency, another important value for galvanostatic measurements is the coulombic efficiency, the ratio of charging and discharging capacity, as discussed in Chapter 1.1.

Chapter 3. Inexpensive antimony nanocrystals and their composites with red phosphorus as high-performance anode materials for Na-ion batteries



3.1. Introduction

Rechargeable batteries – which can store electricity of any origin in the form of chemical bond energy – are increasingly required to offer higher energy density, long cycle life and safety, all at sufficiently low cost of production. Na-ion batteries (SIBs) have long been neglected in favor of Li-ion batteries (LIBs), mainly due to the successful commercialization of LIBs early in the 1990s. However, in light of the limited abundance and geographically uneven distribution of lithium salts (with main reserves in South America) concerns are raising regarding security of supply and cost of Li in the near future. Hence, for the growing need for batteries for electrical mobility and large-scale energy storage, conceptually identical SIBs are gaining attention as an economically viable alternative to LIBs.^{23-25, 134} While SIB cathodes have now reached similar performance to LIB cathodes,^{34, 44, 135-140} the development of stable high-energy-density anode materials for SIBs still lacks well behind the Li-ion counterparts. In particular, silicon as well as graphite – which are the two most successful LIB anode materials – have been reported to possess a negligible capacity for Na-ion storage.^{80,81} Thus an extensive exploration of novel Na-ion anode materials has been launched in the recent years.^{27, 28, 30, 100, 141-154}

Low cost and high Na-ion storage capacity are the major considerations for pre-selection of promising materials, whereas long cycle life has to be achieved *via* smart engineering of the electrodes at micro/nanoscale. In this regard, red phosphorus (P) is both cheap and offers one of the highest known theoretical capacities for Na-ion storage (2596 mAh g⁻¹ for P \leftrightarrow Na₃P transition). However, achieving such high capacities with acceptable cycling stability is hampered by massive increase of volume upon sodiation ($\Delta V = 291\%$)²⁷ leading to the formation of cracks, loss of electrical contacts and fast capacity fading after several charge/discharge cycles. These difficulties are also commonplace for Si-based and other alloying anode materials in LIBs and are usually mitigated by nanostructuring of the active material.^{19, 54, 56, 59, 62, 63, 155-167} Another common problem of P is the rather poor electronic conductivity and low diffusivity of Na-ions. Red P is a rather soft material with a low melting point and can be processed into a micro/nanostructured battery anode by hand- or ball-milling with amorphous carbon nanoparticles (NPs).^{27, 28, 146, 154} Such composites do show record-breaking near-theoretical capacities, but suffer from capacity fading due to both inherent instability of P and far from optimal performance of present-day Na-ion electrolytes. The second most promising Na-ion anode material is Sb (and Sb-based compounds), with a theoretical capacity of 660 mAh g⁻¹ (for Sb \leftrightarrow Na₃Sb conversion) and good cycling stability.^{30, 82, 147-153} Recently, monodisperse Sb nanocrystals (NCs), produced *via* organometallic synthesis in nonpolar organic solvents, with excellent cycling stability and rate capability were introduced (retention of > 80% of theoretical capacity at 20C-rate for charge and discharge, 1C-rate being current density of 660 mA g⁻¹).⁵⁷ Yet the fundamental drawback of organometallically prepared Sb NCs is the high cost of their synthesis and purification in organic solvents, using coordination compounds as precursors and expensive reducing agents.

For the work presented in this chapter it was thought to combine the best of P and Sb – much higher capacity of P and fast and stable cycling of Sb – into a functional synergy through the design of an inexpensive P-Sb composite. The insights gained from previous work on monodisperse Sb NCs was used; in particular, the fact that the performance of Sb NCs is only moderately size-dependent as long as NCs are in 20-100 nm size range.⁵⁷ Hence, for the present work a facile low-cost synthesis of Sb NCs was developed, which, despite broader size distribution, exhibit even better performance than organometallically-synthesized Sb NCs. The motivation was to find whether good electrochemical properties of Sb-P composite can be achieved without nanostructuring by high-energy mechanical milling, but simply by

one-pot mixing the commercial red P with Sb NCs, solvent, binder and conductive additive. Further, through the addition of copper nanowires (Cu NWs) the importance of tailoring the electronic conductivity and mechanic stability for enhancing electrochemical performance is demonstrated. The as-prepared P/Sb/Cu-composite delivers a capacity of $> 1300 \text{ mAh g}^{-1}$ for 30 cycles corresponding to $> 80\%$ of its theoretical capacity. Moreover, the P/Sb/Cu-composite shows outstanding rate capability retaining a capacity of $> 900 \text{ mAh g}^{-1}$ at a current of 2000 mA g^{-1} .

3.2. Experimental section

Synthesis of Sb NCs. To synthesize $\sim 20 \text{ nm}$ Sb NCs, NaBH_4 (48 mmol, 98%, ABCR) was dissolved in anhydrous N-methyl-2-pyrrolidone (NMP, 51 mL, 99.8%, Fluorochem Ltd) in a three-necked flask under nitrogen and heated to 60°C . SbCl_3 (12 mmol, 99%, ABCR) dissolved in NMP (9 mL) was quickly injected *via* syringe. The reaction mixture instantly turned black and was cooled down immediately using a water-ice bath. After cooling to room-temperature, Sb NCs were separated from the solution by centrifugation (8000 rpm, 4 min) and washed three times with deionized water (30 mL) to remove unreacted NaBH_4 and water-soluble side products such as NaCl. The reaction product was finally dried in the vacuum oven at room temperature, yielding 1.2 g of Sb NCs (82% reaction yield).

Synthesis of Cu NWs. Cu NWs were synthesized according to a procedure published by Guo *et al.*¹⁶⁸

Electrode fabrication, cell assembly and electrochemical measurements. The following battery components were used: carbon black (Super C65, TIMCAL), carboxymethyl cellulose (CMC, Daicel Fine Chem Ltd.), NaClO_4 (98%, Alfa Aesar, additionally dried), propylene carbonate (BASF, battery grade), fluoroethylene carbonate (FEC, Hisunny Chemical, battery grade), glass microfiber separator (GF/D, Whatman), and Cu-foil ($9 \mu\text{m}$, MTI Corporation).

In a typical electrode preparation, the respective materials were combined with deionized water and mixed in a Fritsch Pulverisette 7 classic planetary mill for 1 hour at 500 rpm. Mixing weight ratios were Sb:CB:CMC = 64%:21%:15% for pure Sb NCs, and P/Sb:CB:CMC = 40%:40%:20% or P/Sb:CB:Cu:CMC = 40%:30%:10%:20%. The aqueous slurries were coated onto Cu current collectors and then dried overnight at 80°C under vacuum prior to use. All electrochemical measurements were conducted in homemade, reusable and air-tight coin-type cells assembled in an Ar-filled glove box ($\text{O}_2 < 1 \text{ ppm}$, $\text{H}_2\text{O} < 1 \text{ ppm}$). Elemental sodium was employed as both reference and counter electrode. As

electrolyte 1M NaClO₄ in propylene carbonate with 10% fluoroethylene carbonate was used. Glass fiber was used as separator. Galvanostatic cycling tests were carried out at room temperature on MPG2 multi-channel workstation (BioLogic). Capacities were normalized by the mass of active material.

Materials characterization. Transmission Electron Microscopy (TEM) images were obtained with a Philips CM30 TEM microscope at 300 kV using carbon-coated Cu grids as substrates (Ted-Pella). Scanning transmission electron microscopy (STEM) and EDX mapping were performed on a JEOL 2200FS TEM/STEM microscope. Scanning electron microscopy (SEM) was performed using a NanoSEM 230. Powder X-ray diffraction (XRD) was measured on a STOE STADI P powder X-ray diffractometer (Cu-K α ₁ irradiation, $\lambda = 1.540598$ Å).

3.3. Results and discussion

Inexpensive synthesis and electrochemical performance of Sb NCs. Colloidal NCs make for an ideal battery material: they can be safely and conveniently produced and handled as stable dispersions in common solvents. Using monodisperse Sb NCs, it was recently reported that 20 nm NCs exhibit higher Li-ion and Na-ion storage capacities and improved cycling stability, especially at higher rates of charge and discharge, than both smaller ~10 nm particles and (sub)micron-sized Sb.⁵⁷ However, the synthesis of monodisperse Sb NCs involved expensive organic and coordination compounds (precursors, solvents, surfactants and reducing agents), as well as multiple steps of washing and removal of surface capping ligands. Yet a very important conclusion was obtained: mean particle size has a very modest effect on the electrochemical characteristics of Sb NCs, as long as it lies within the range of 20-100 nm, in striking contrast to, for instance, Li-ion storage in Sn NCs, showing satisfactory performance only at sizes of 10 nm and below.⁵⁸ Such intrinsic tolerance of Sb to crystallite size has prompted to search for an inexpensive synthetic route, even if the “precision” of the synthesis is somewhat sacrificed. For this work, a much simpler and cheaper (~1 USD g⁻¹) synthesis of Sb NCs *via* reduction of SbCl₃ with NaBH₄ at 60 °C was developed (for details, see the Experimental Section), yielding NCs of similar size as in the previous study, but at a cost that is lower by factor of ~100. The main features of this synthesis are the gram-scale and further up-scalable production with above 80% reaction yield, simple isolation of Sb NCs by centrifuging and convenient recycling of the solvent. The absence of surfactants obviates lengthy purification and surfactant-removal procedures.

The only post-synthetic treatment is washing with water to remove the reaction byproducts (sodium chloride and borates). Figure 3.1. shows Sb NCs with the mean size of ~20 nm. The X-ray diffraction (XRD) pattern shows phase-pure, highly crystalline Sb NCs (space group $N166$, $R-3m$, $a = b = 0.4306$ nm, $c = 1.1288$ nm; calculated crystallite size of 22 nm; see Figure 3.1. and Table 3.1. for Rietveld refinement), without any detectable traces of Sb oxides or reaction byproducts.

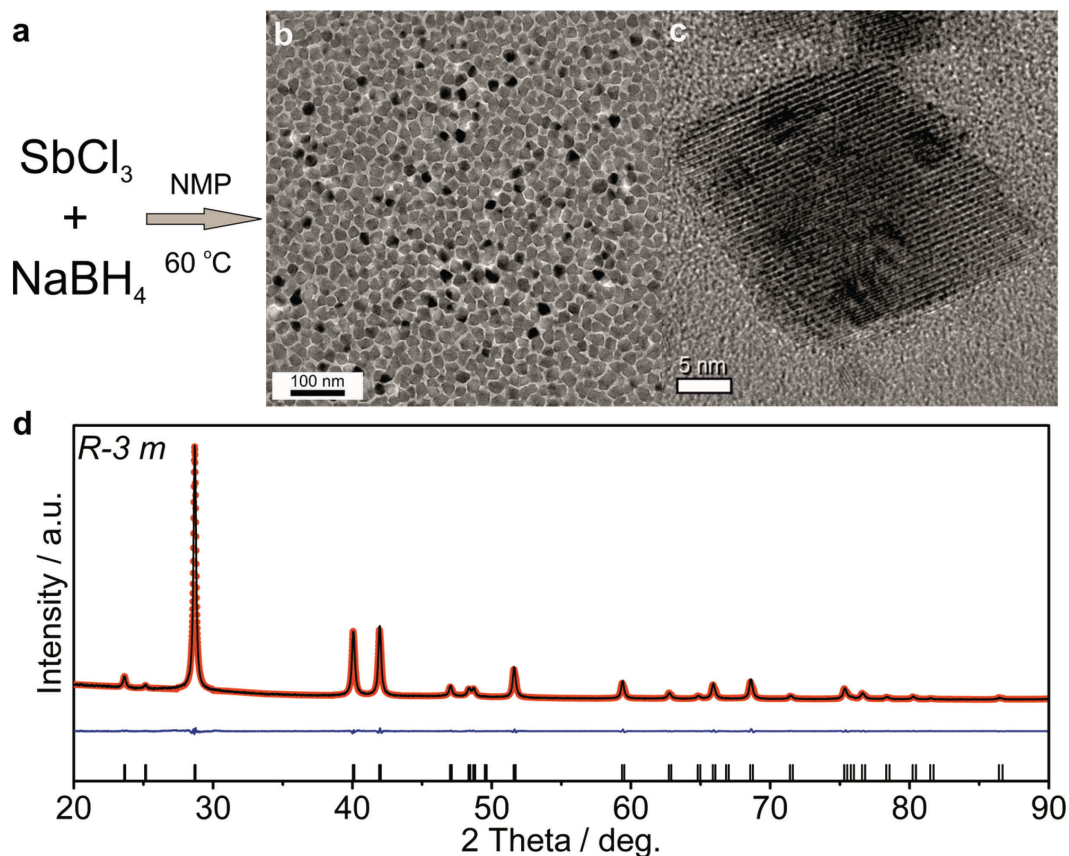


Figure 3.1. Synthesis and characterization of Sb NCs. (a) Reaction scheme. (b) TEM image. (c) High-resolution TEM image. (d) X-ray diffraction (XRD) pattern indexed to pure-phase hexagonal Sb (ICDD database, PDF Entry No.: 00-071-1173) with Rietveld refinement shown as black curve.

Table 3.1. Rietveld refinement parameters for Sb NCs corresponding to the black curve in Figure 3.1. Rietveld refinement was carried out using FullProf Suite (<https://www.ill.eu/sites/fullprof/>).

Pattern				Phase	
Chi2	Rp	Rwp	Rexp	Rbragg	RF-factor
2.396	12.9	11.3	7.29	0.954	1.81

Preparation and electrochemical performance of Sb-P nanocomposites.

Electrochemical performance of Sb NCs and of all other materials in this study has been tested in coin-type half-cells with metallic Na as counter electrode. Working electrodes were prepared by mixing Sb NCs (64 wt%), with carbon black (CB) as conductive additive (21 wt%) and carboxymethyl cellulose (CMC, 15 wt%) as a water soluble polymeric binder, followed by doctor-blade casting of the slurry onto Cu-foil. 1M NaClO₄ in propylene carbonate was used as electrolyte and fluoroethylene carbonate (FEC) was used as electrolyte additive for stabilizing the solid-electrolyte interface (SEI).¹⁶³ In spite of the broader size distribution compared to organometallically-synthesized Sb NCs,⁵⁷ inexpensive Sb NCs developed in this study exhibit same or even better electrochemical characteristics (Figure 3.2.).

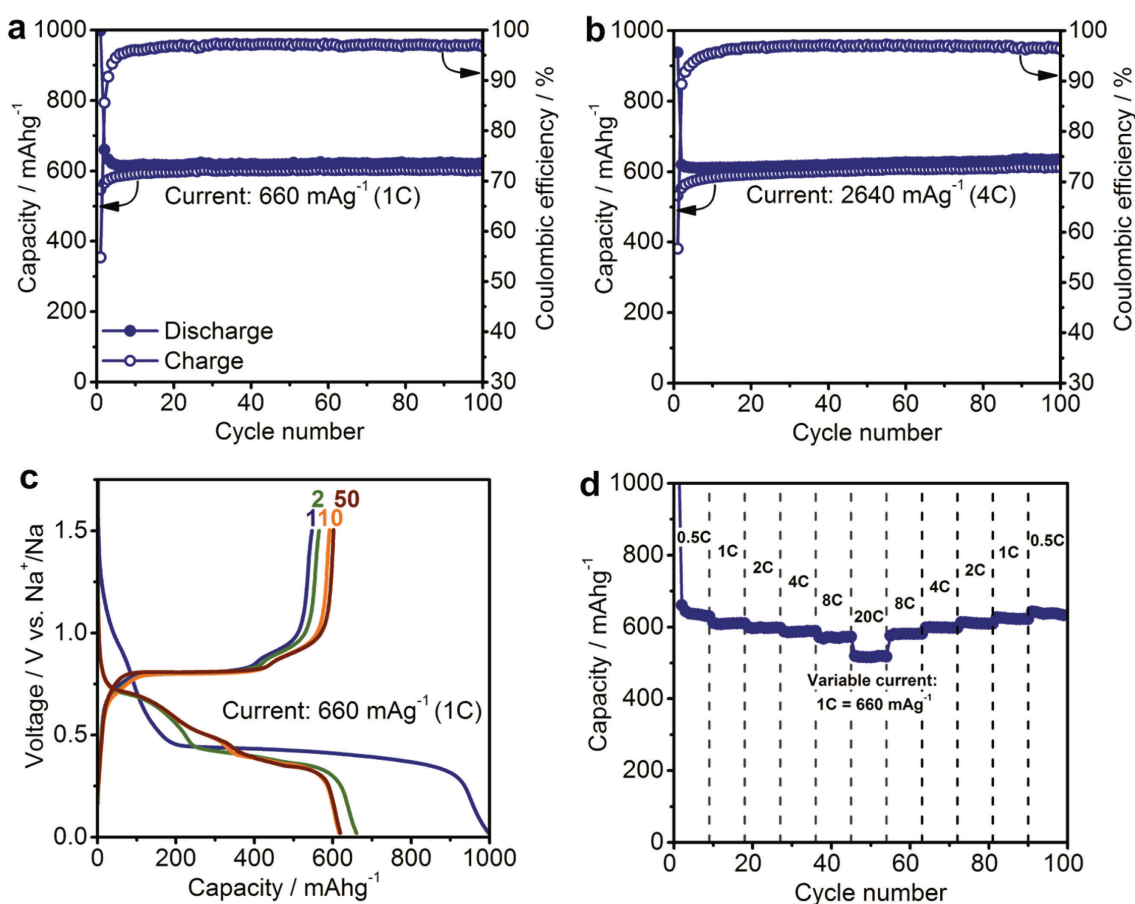


Figure 3.2. Electrochemical performance of Sb NCs in Na-ion half-cells. Capacity retention of Sb NCs cycled at a current of (a) 660 mA g⁻¹ and (b) 2640 mA g⁻¹. (c) Galvanostatic charge/discharge curves at a rate of 660 mA g⁻¹. (d) Rate capability tests at different current rates. All batteries were cycled in the potential range 0.02-1.5 V vs. Na⁺/Na.

Namely, near-theoretical capacity is obtained at 0.5-1C rates (1C corresponds to current density of 660 mA g^{-1}) without noticeable deterioration in the first 100 cycles. The small increase of the charge capacity observed in the charge/discharge curves might be due to the fact that not all of the electrode material is fully active during the first cycles because of kinetic limitations. Considering the massive volume changes for the sodiation/desodiation reaction most likely the electrodes undergo restructuring in the first cycles leading to slightly better ionic and electronic conductivity, which explains the small increase of the charge capacity. Rate capability tests indicate retention of at least 85% of capacity at a high rate of 20C (13.2 A g^{-1}) and full recovery of the capacity after decrease of the cycling rate to 0.5C. The rate capability of Sb is unprecedented for Na-ion anodes, and is comparable to fastest Li-ion anode materials such as graphite,¹⁶⁹ and Li-titanates.¹⁷⁰ In addition, at a relatively high current density of 660 mA g^{-1} Sb NC anodes show excellent cycling stability for at least 250 cycles, when the charge capacity is limited to 550 mAh g^{-1} (Figure 3.3.).

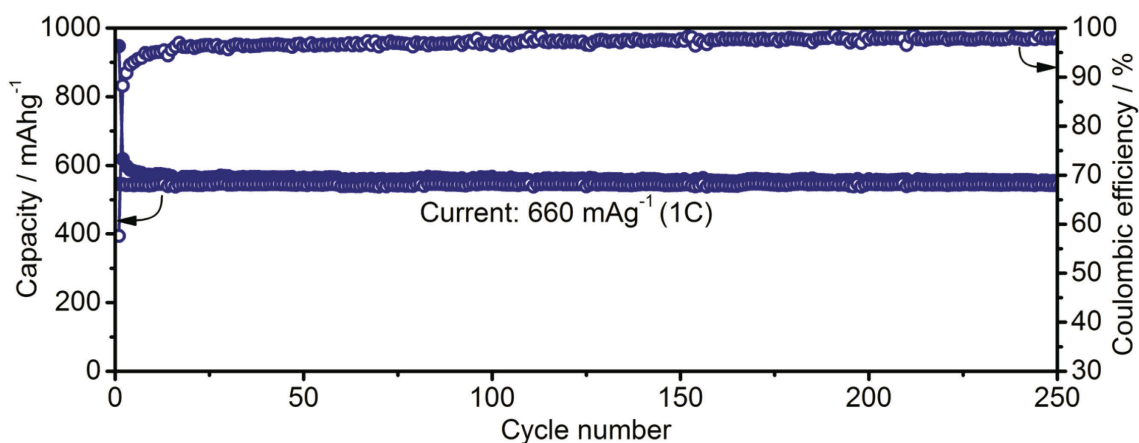


Figure 3.3. Long-term cycling stability for Sb NCs in Na-ion half-cells. Cells were cycled with a current of 660 mA g^{-1} and limitation of the charge capacity to 550 mAh g^{-1} in the potential range 0.02-1.5 vs. Na^+/Na .

Such impressively fast and stable operation of Sb anodes can be attributed to the synchronous effect of several properties. First, Sb is a good electronic conductor due to its semimetallic nature. Second, its crystalline structure is characterized by the low atomic packing factor of just 39%¹⁷¹ and the crystal structure comprised of puckered layered planes with large channels for diffusion of alkali-ions. Insertion of Na-ions into Sb involves only one crystalline (Na_3Sb) and several amorphous phases, including amorphous Sb.⁸² De-insertion primarily occurs as direct $\text{Na}_3\text{Sb}_{\text{hex}} \rightarrow \text{Sb}_{\text{amorphous}}$ transition. Such reduced number of intermediate crystalline phases can greatly enhance the conversion kinetics. The theoretical value for volumetric expansion upon full sodiation to hexagonal Na_3Sb can be estimated from

the difference in the molar volumes between the final (Na_3Sb) and the initial metallic (Sb) phases: $\Delta V = [V_m(\text{Na}_x\text{Sb}) - V_m(\text{Sb})]/V_m(\text{Sb}) = 290\%$. Possibly isotropic, nearly strain-free expansion/contraction of amorphous phases can explain the tolerance of Sb to such drastic volumetric changes.

Fundamentally, the formation of composites opens up multiple new opportunities for tuning the electronic and ionic transport, surface chemistry, porosity and mean particle size with strong implications for rate capability and cycling stability. The initial goal of this study was to obtain a compelling combination of the two materials: functional synergy of higher capacity of P with high-rate capability and high cyclability of Sb.

P undergoes very similar to Sb volumetric changes of $\sim 290\%$ upon full sodiation to Na_3P .¹⁴⁶ At the same time, P shows much faster capacity fade,^{27, 28, 146, 154} which can be attributed to poorer electronic and ionic conductivity or higher reactivity towards the electrolyte. Replacing some of the P with Sb NCs might give rise to improved electrochemical properties as (sub)micron-sized P particles are more diluted in a conductive nanoscopic matrix of Sb and CB. For 1:1 mixture of Sb and P, one can expect capacities up to theoretical weighed average of 1628 mAh g^{-1} .

Figure 3.4. captures the main result of the work in this chapter – significant enhancement in reversibility of Na-ion storage by combining Sb NCs, “bulk” P and Cu NWs. Electrodes containing either Sb NCs, commercial red P or 1:1 mixtures thereof, with or without Cu NWs, were prepared with an overall mass ratio active-material:CB:CMC = 40%:40%:20%. Such relatively high fraction of conductive carbons such as CB are generally used for P-based electrodes in Na-ion batteries to provide sufficient electronic conductivity and mechanical stability of the electrodes.^{27, 28, 146, 154} Currents and capacities were related to the active mass without CB. As shown in Figure 3.4., electrodes comprising 40% of pure Sb NCs deliver stable capacities and excellent rate capability.

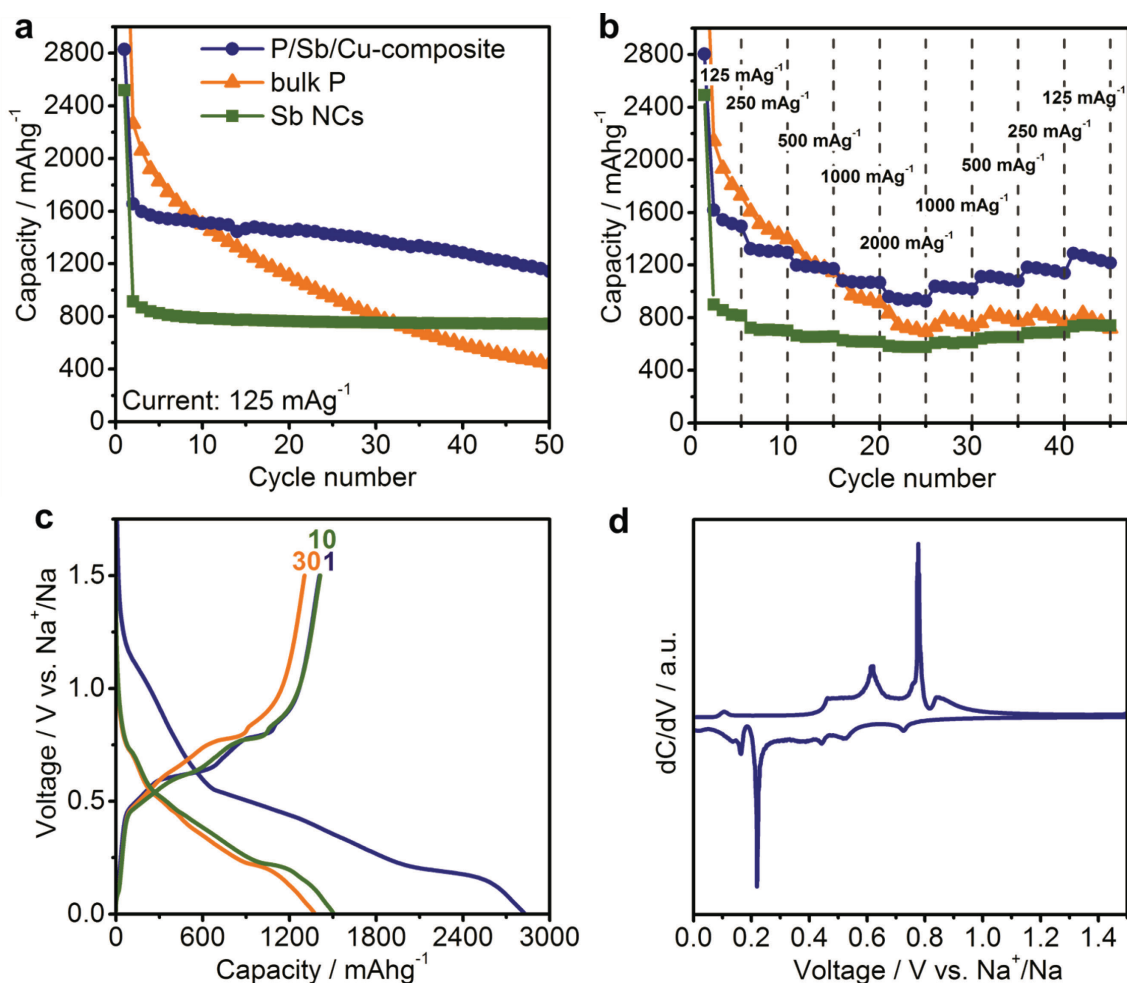


Figure 3.4. Electrochemical performance of the P/Sb/Cu composite electrodes in comparison to Sb NCs and red P: (a) Cycling stability at a current density of 125 mA g⁻¹. (b) Rate capability tests. (c) Galvanostatic charge and discharge curves and (d) differential capacity plot for the 10th cycle at a current density of 125 mA g⁻¹ for the P/Sb/Cu composite.

The fact that at a current of 125 mA g⁻¹ the apparent capacity of Sb NCs exceeds the theoretical value of 660 mAh g⁻¹ can be explained by the contribution from CB (Figure 3.5.). At this current density CB exhibits stable capacity of ca. 100 mAh g⁻¹, and thus may be contributing ~100 mAh g⁻¹ in its 1:1 mixture with Sb (or Sb/P).

Electrodes composed of “bulk” P do show theoretical capacities in the first cycles, indicating that electronic connectivity is satisfactory in the as-prepared electrode, but undergo severe capacity fading to 440 mAh g⁻¹ after 50 cycles. This result is fully consistent with the available literature on mechanically produced P/carbon electrodes.^{146, 154} Experiments using 1:1 mixtures of “bulk” P and Sb NCs indicate electrochemical performance which exceeds the mathematic sum of the individual contributions, leading to retention of more than 800 mAh g⁻¹ of capacity after 30 cycles (Figure 3.6.).

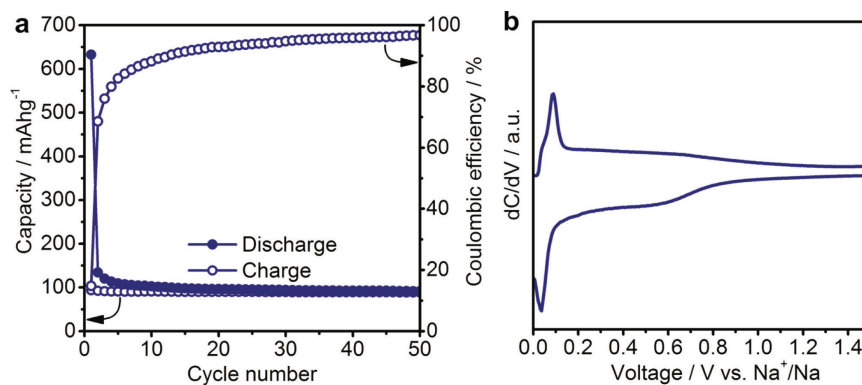


Figure 3.5. (a) Galvanostatic cycling of electrodes composed of 80% CB and 20% CMC at 125 mA g⁻¹ in the voltage range of 0-1.5 V. (b) Differential capacity plot for the 10th cycle.

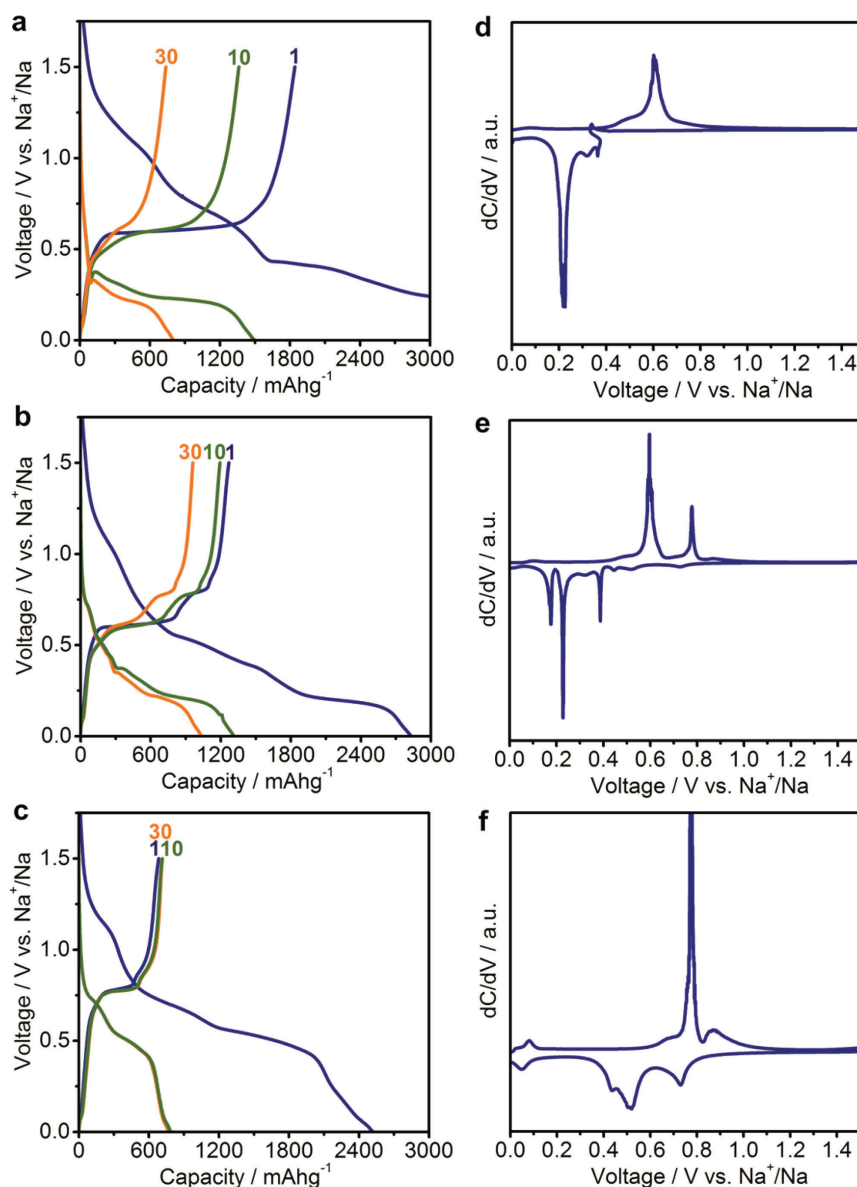


Figure 3.6. Galvanostatic charge/discharge curves for electrodes composed of (a) "bulk" P, (c) Sb NCs and (b) 1:1 mixtures thereof for cycling at a current of 125 mA g⁻¹ in the potential range 0-1.5 V. Differential capacity plots for the 10th cycle for electrodes composed of (d) "bulk" P, (f) Sb NCs and (e) 1:1 mixtures thereof for cycling at a current of 125 mA g⁻¹ in the potential range 0-1.5 V.

This improved capacity retention observed for electrodes of Sb/P electrodes can be explained by the lower content of P. Due to the higher “dilution” of P particles in a matrix of Sb NCs and CB the volume changes can be buffered more effectively and electrodes are suffering from less mechanical stress leading to better cycling stability. Further major improvement has been attained by replacing some CB with Cu NWs. Cu NWs were synthesized according to a previously published procedure by Guo *et al.* (Figure 3.7).¹⁶⁸ It should be noted that Cu NWs are becoming comparably inexpensive. For instance, during this project, Li *et al.* reported facile synthesis of Cu NWs at a cost of 4.20 USD g⁻¹.¹⁷² Further, it is generally well known that the cost of synthesis may further go down by up to an order of magnitude when material is produced on the industrial scale. Electrodes comprising 1:1 mixtures of “bulk” P/Sb NCs with 10 wt% Cu NWs (i.e. 25% of CB was replaced with Cu NWs) delivered capacity of > 1300 mAh g⁻¹ for 30 cycles, corresponding to > 80% of the theoretical capacity for this mixture (1628 mAh g⁻¹). After 50 cycles still a capacity of > 1100 mAh g⁻¹ is retained, by 60% higher than in Cu-free samples and almost three times the value for “bulk” P, clearly manifesting the synergy between P and nanoscopic Sb and Cu.

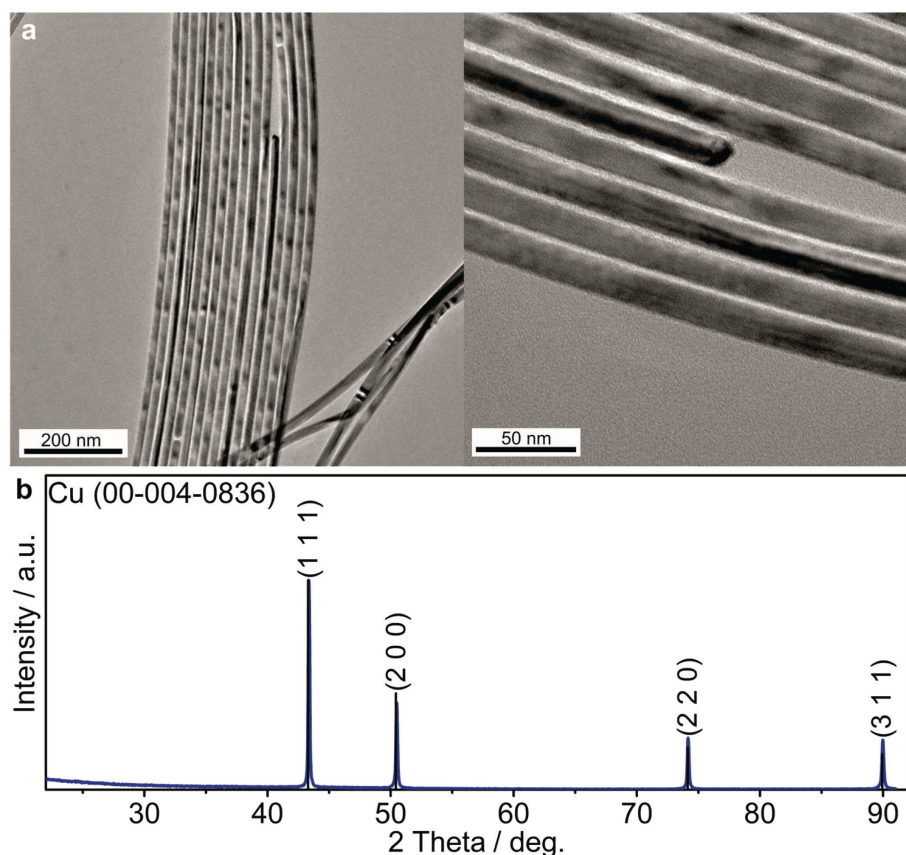


Figure 3.7. (a) TEM images and (b) XRD pattern of Cu NWs

An obvious benefit of the P/Sb/Cu formulation is seen also in the rate capability tests (Figure 3.4.b). For comparison, all formulations of electrodes were subjected first to stepwise increase of the current density to 2000 mA g⁻¹, and then to stepwise reduction of the current. Whereas electrodes of “bulk” P fail to recover their capacity, the P/Sb/Cu-composite is able to retain the same capacity level as after the continuous cycling at 125 mA g⁻¹. In addition, the P/Sb/Cu-composite shows excellent rate capability with capacities of > 900 mAh g⁻¹ at 2000 mA g⁻¹ current density.

An advantage of P is its lower electrode potential compared to Sb, potentially giving rise to higher energy density – that is higher voltage×capacity product of a full cell battery – when combined with a high-voltage cathode. Figure 3.4.c presents galvanostatic charge (desodiation) and discharge (sodiation) curves for P/Sb/Cu-composite, showing that sodiation and desodiation occurs at an average voltage of 0.5 V, highly suitable for anode applications. Additional hints can be found from differential capacitance plots (dC/dV, Figure 3.4.d), derived from the charge/discharge curves, presented for the 10th cycle (within the regime of stable cycling). In the first cycle (not shown here), two desodiation features at 0.6 and 0.8 V indicate individual contributions from P and Sb, as observed in reference electrodes comprising red P and Sb NCs (see Figure 3.6.). However, in the subsequent cycles an additional broad component in 0.4-0.8V range is built up, not present in Cu-free P/Sb electrodes. Further, it was observed that P/Sb electrodes exhibit an additional sodiation process at 0.16 V, not seen for electrodes composed of only P or Sb (see Figure 3.6.). All other processes correspond to the individual contributions from P and Sb.^{82, 146} Temporal separation of electrochemical processes due to the spread of sodiation (desodiation) features over the broad voltage range may in fact have a stabilizing effect. In a recent study on Sn-Ge nanocomposites as LIB anodes,¹⁷³ as well as in numerous other reports on LIBs, stepwise lithiation and delithiation in composites of several electrode materials has been shown to enhance the mechanical stability, as compared to instant expansion of the whole electrode.

The coulombic efficiency – the ratio between the amounts of electrical charge spent for sodiation and desodiation processes in each cycle – provides an important insight into the reversibility of the charging/discharging processes. Due to the formation of the solid-electrolyte interface (SEI) the coulombic efficiency for the first cycle with P/Sb/Cu electrodes is only 60%, but reached 95% in the subsequent cycles at a current of 125 mA g⁻¹. This initially low coulombic efficiency can be explained by the small size of Sb NCs and Cu NWs, which provides a large surface area for the irreversible electrolyte decomposition during the

first discharge. During cycling at a relatively high current of 2000 mA g^{-1} the coulombic efficiency increased to 98%. As commonly reported for conversion anode materials with large volume changes during cycling, the cracking of SEI layer leads to continuous decomposition of the electrolyte on the freshly exposed surfaces. This constant reformation of the SEI lowers the coulombic efficiency and long-term cycling stability due to degradation of both the electrodes and electrolytes.

Figure 3.8. depicts the proposed stabilizing effect present in P/Sb/Cu electrodes. Cu NWs are assumed to cause better mechanic stability and improved electronic connectivity, slowing down the loss of electric contact due to pulverization of P particles. Cu NWs can trap fractured material to a degree that zero-dimensional CB particles cannot provide. Overall, dilution of the (sub)micron-sized P particles, when mixed with Sb NCs and Cu NWs, most likely improves the overall mechanical stability of the electrode leading to retarded cracking and crumbling during cycling.

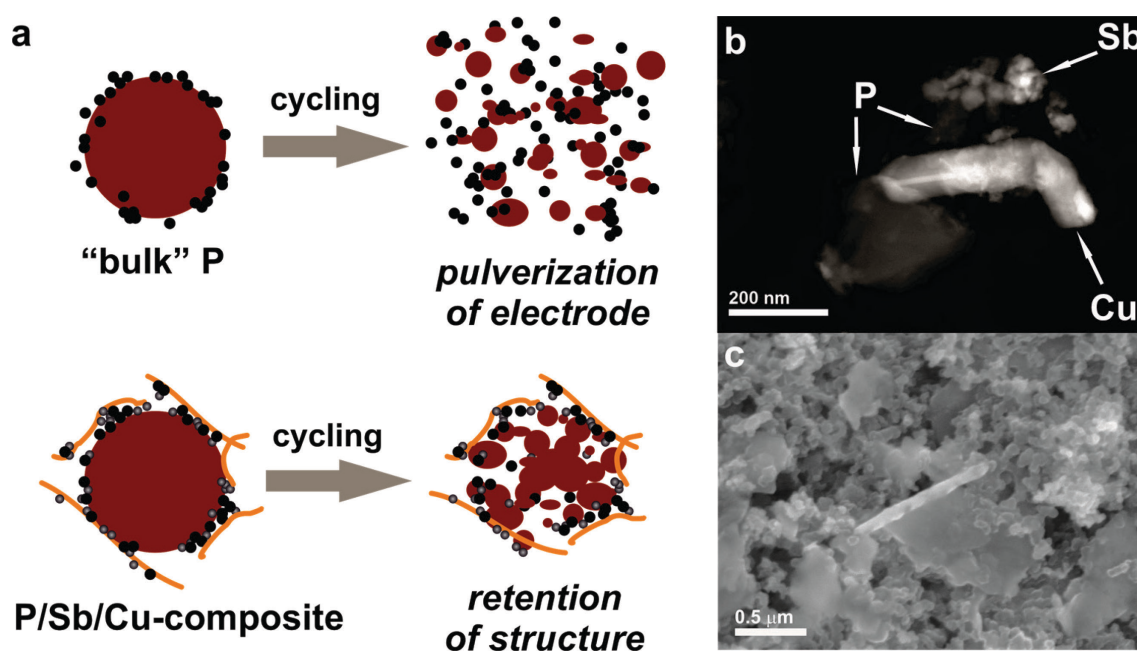


Figure 3.8. Schematics and characterization of the P/Sb/Cu composite: (a) Schematic depiction of the proposed stabilizing effect of Cu NWs (with P in red, CB in black, Sb NCs in grey and Cu NWs in yellow). (b) HAADF-STEM image. (c) SEM image.

High-angle angular dark field-scanning transmission electron images (HAADF-STEM), bright-field STEM images, elemental mapping by energy-dispersive X-ray spectrometry (EDX-map, Figure 3.9.) and scanning electron microscopy images (SEM) clearly evidence intimate intermixing in P/Sb/Cu electrodes. Thus, the herein presented outstanding

electrochemical properties of the P/Sb/Cu-composite can be attributed to the effective embedding of “bulk” P in a Sb/Cu/CB matrix.

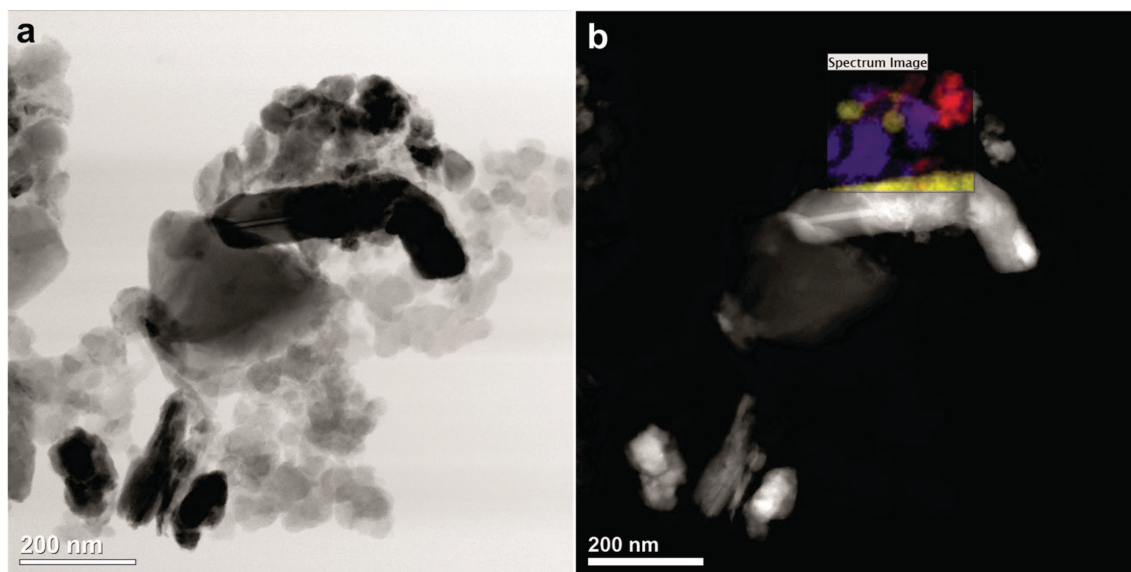


Figure 3.9. BF and HAADF-STEM images of the P/Sb/Cu-composite with an EDX-map as a colored inset (violet = P, red = Sb, yellow = Cu).

It is important to point out that of all measured electrodes only the ones comprising “bulk” P and Sb NCs with 10 wt% Cu NWs had clearly emerged as champion devices. Replacing Sb NCs with micrometer-sized commercial Sb led to significantly poorer performance (Figure 3.10.b), very similar to purely P-based electrodes. Similarly, whereas electrodes containing both “bulk P” and Cu NWs exhibit higher cycling stability than in the absence of Cu NWs, they fall well behind the P/Sb/Cu-composite (Figure 3.10.c). In addition, increasing the content of Cu NWs from 10 to 20 wt% did not improve the cycling stability further, but rather led to lower capacities (Figure 3.10.a). Considering that electrodes are composed of particles with very different size, this observation indicates that in order to obtain the optimal electrical contact in the electrodes and therefore highest capacity the ratio between CB particles and Cu NWs needs to be sufficiently balanced.

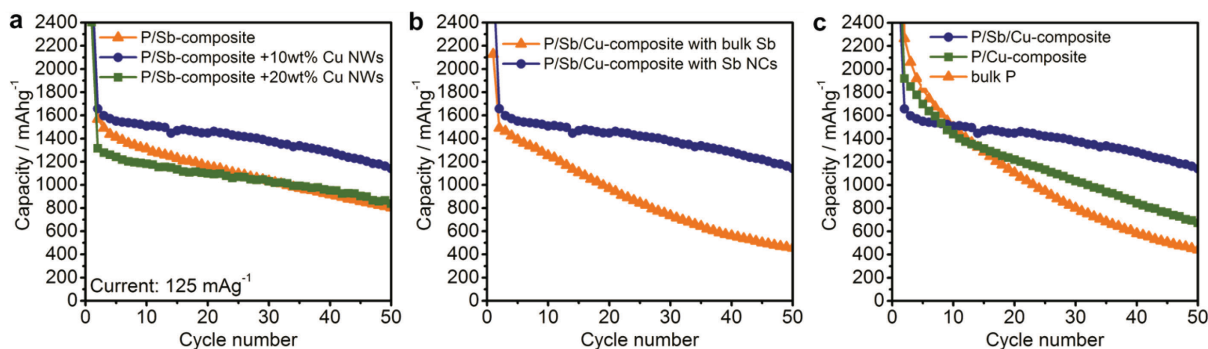


Figure 3.10. (a) Galvanostatic cycling of electrodes composed of "bulk P" and Sb NCs (1:1) with and without 10% or 20% Cu NWs. (b) Galvanostatic cycling of P/Sb/Cu-composite prepared from Sb NCs or from microcrystalline Sb. (c) Galvanostatic cycling of electrodes composed of either "bulk P", "bulk P" with 10 wt% Cu NWs, or "bulk" P/Sb NCs (1:1) with 10 wt% Cu NWs. Cell were cycled with a current of 125 mA g⁻¹ in the potential range 0-1.5 V.

A great deal of work still has to be focused on improving the long-term cycling stability of the electrodes. Besides the effect of the active storage material, the cycling stability is a complex function of the electrode formulation (chemistry and amounts of binder and conductive additive), porosity, electrode thickness, electrolyte, temperature *etc.* In particular, coulombic efficiencies of ~92%, ~95%, and 97-98% for P, P/Sb/Cu and Sb electrodes respectively, indicate a continuous consumption of electrolyte for side anodic reactions, reformation of unstable SEI layer after each cycle and, very likely, high reactivity of Na₃P towards the electrolyte.¹⁴⁶ Smart engineering of the electrodes, for instance, by designing secondary structures combined with judicious choice of electrolytes and electrolyte additives will enable higher stability of SEI layer in future studies. It should be noted that in the field of SIBs the problems of optimizing the chemistry of electrolytes and understanding of SEI formation had so far received much less attention as compared to 30 years of research on LIBs, and the knowledge are not necessarily interchangeable between these two fields.

3.4. Conclusion

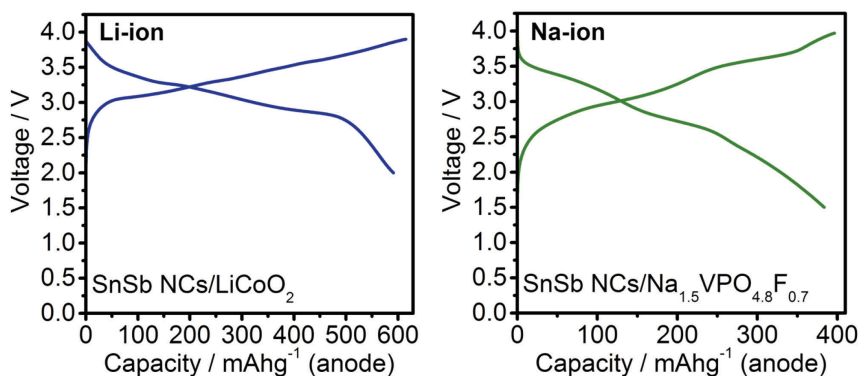
In summary, the work presented in this chapter showcases a strategy for constructing a composite Na-ion anode material, which combines several active materials with functional synergy between them. First, a facile low-cost synthesis of Sb NCs that exhibit outstanding high-rate capability and long cycling life as anode material in SIBs was presented. Compared to previous syntheses of Sb nanostructures,¹⁷⁴⁻¹⁷⁶ the advantages are the use of inexpensive reagents, the absence of any surfactants, simple washing procedure, high reaction yield and scalability. In fact, all that needs to be done for the synthesis is injecting the Sb precursor solution at very moderate temperature (60 °C) to the solution of NaBH₄, which can easily be

done on the industrial scale with both either a batch or a continuous flow reactor. All used reagents can be easily and safely handled and the resulting material can be washed just with water for purification, therefore, this procedure can be readily applied on the industrial scale. A compelling P/Sb/Cu composite anode was then devised by simple mechanic mixing of Sb NCs with “bulk” red P and Cu NWs. In this composite, larger (sub)micron-sized P particles are embedded into a nanoscopic matrix of intimately intermixed Sb NCs, Cu NWs and nanoparticulate CB. Electrodes composed of 1:1 mixtures of “bulk” P/Sb NCs with 10 wt% Cu NWs delivered $> 1300 \text{ mAh g}^{-1}$ for 30 cycles and $> 1100 \text{ mAh g}^{-1}$ after 50 cycles at 125 mA g^{-1} . Furthermore, reversible capacities of $> 900 \text{ mAh g}^{-1}$ at high current density of 2000 mA g^{-1} have been obtained as well.

Reproduced with modifications from:

M. Walter, R. Erni and M. V. Kovalenko. *Inexpensive Antimony Nanocrystals and Their Composites with Red Phosphorus as High-Performance Anode Materials for Na-ion Batteries*. Sci. Rep., **2015**, 5, 8418.

Chapter 4. Inexpensive colloidal SnSb nanoalloys as efficient anode materials for Li- and Na-ion batteries



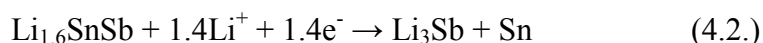
4.1. Introduction

Li-ion batteries (LIBs) with higher energy and power densities are actively sought to increase the competitiveness and widespread deployment of electric cars and stationary energy storage units, and for enabling new portable electronic devices.^{134, 177} Great hopes have been extended to conceptually similar Na-ion batteries (SIBs)²³⁻²⁵ due to the much greater natural abundance of Na and the possibility of replacing copper anode current collectors with aluminum foils. The eventual success of SIBs will require this technology to have the same energy density as LIBs.

The energy density of a battery is primarily determined by the charge storage capacity of the electrode materials and the overall voltage of the battery. In this regard, SIBs face a critical challenge: a lack of efficient anode materials. For instance, graphite, the commercialized anode material for LIBs, shows only a negligible Na-ion capacity,⁸⁰ causing a recent surge of research on Na-ion anode materials.^{27, 28, 30, 141-153} Certain metals and metalloids that alloy with Na and Li are especially promising, such as Sb and Sn which both show 2-3 times higher gravimetric and volumetric energy densities than graphite (*e.g.*, 992 mAh g⁻¹ or ~7300 mAh cm⁻³ for the reversible formation of Li_{4.4}Sn). However, alloying leads to a much more intense reconstruction of the host material, as compared to intercalation. Such anode materials undergo massive volume changes of 100-300% upon lithiation (even greater for Na-ions), causing fast capacity fading due the formation of cracks, loss of electrical contacts and eventual disintegration of the electrode. Nanostructuring of the electrode

material has been demonstrated to efficiently mitigate the effects of mechanical stress in many systems.^{16, 19, 26, 54, 56, 58, 61, 63, 65, 66, 75, 76} In this chapter it is focused on SnSb as a promising anode material and a facile and inexpensive solution-based synthesis of nanocrystals (NCs) of this compound with a mean size of 10-30 nm is presented, and their efficient performance for Na-ion and Li-ion storage demonstrated.

The choice of the SnSb system stems from several advantages of this compound. First, both components of this alloy contribute to its high theoretical capacity of 824 mAh g⁻¹.¹⁷⁸



Similarly, the theoretical maximum capacity for Na-ion storage in SnSb is 752 mAh g⁻¹ based on the formation of Na₃Sb and Na_{3.75}Sn; however, the exact mechanism of this reaction is not fully understood, except that it does not occur in analogy to Li and is not a mere combination of the separate processes taking place for Sb and Sn.¹⁴⁸ Secondly, alloying/dealloying reactions of Sn and Sb occur at different potentials, which smoothens the mechanical stress somewhat. Finally, Sn and Sb are at least as inexpensive as common cathode materials comprising transition metals (*e.g.*, Co and V). Notable examples of SnSb-based anode materials for both Li- and Na-ion storage are monodisperse SnSb NCs,⁶⁴ SnSb-C nanofibers,¹⁷⁹ CNT-Sn-Sb nanorods,¹⁸⁰ and SnSb-C composites.^{147, 181, 182}

A specific goal of this study was to develop a new synthesis route to SnSb NCs that is orders of magnitude cheaper than the previously published procedure for monodisperse particles by the Kovalenko Group.⁶⁴ That previous synthesis route involved the use of expensive, air-sensitive organic and coordination compounds (alkylamides as precursors, alkylamines as solvents, long-chain surfactants and reducing agents), as well as multiple steps of washing and removal of surface capping ligands, with a very low overall atomic economy.⁶⁴ Here a surfactant-free synthesis is presented that is at least 1000 times cheaper, by utilizing metal chlorides as precursors and NaBH₄ as a reducing agent, and which does not require any post-synthetic purification other than rinsing in water. It is demonstrated that these SnSb NCs exhibit electrochemical performance which is the same as or better than the “expensive” NCs from the previous study.⁶⁴ Also results from full-cell experiments are presented. Under anode-limiting operation, SnSb NCs retain Li-ion capacities of 600 mAh g⁻¹ at an average voltage

of 3.0 V when paired with a LiCoO₂ cathode, and a Na-ion capacity of 400 mAh g⁻¹ at an average voltage of 2.7 V when paired with a Na_{1.5}VPO_{4.8}F_{0.7} cathode.

4.2. Experimental section

Synthesis of SnSb NCs. A solution of NaBH₄ (32 mmol, 98%, ABCR) in anhydrous N-methyl-2-pyrrolidone (NMP, 17 mL, 99.5%, Fisher BioReagents) was heated to 60 °C under nitrogen. Upon reaching 60 °C, a solution of SnCl₂ (1 mmol, ≥ 99%, Alfa Aesar) dissolved in anhydrous NMP (1.5 mL) was injected, followed immediately by the injection of SbCl₃ (1 mmol, 99%, ABCR) and cooling down to room temperature using a water-ice bath. The resulting black precipitate was separated from the solution by centrifugation and washed three times with water (30 mL) to remove side products such as NaCl or borates. After drying under vacuum at room temperature a fine black powder was obtained with a yield of ~0.2 g (83%).

Synthesis of bulk SnSb. Micrometer-sized SnSb particles were synthesized by heating a mixture of Sn (1 mmol, 99.8%, Sigma-Aldrich) and Sb powder (1 mmol, 99.5%, Alfa Aesar) above their respective melting points to 700 °C under inert atmosphere. After 5 min at 700 °C the material was cooled naturally to room temperature and the resulting product was ground using a mortar and pestle.

Assembly and testing of half- and full-cells. The following battery components were used: carbon black (CB, Super C65, TIMCAL), carboxymethyl cellulose (CMC, Grade: 2200, Daicel Fine Chem. Ltd.), NaClO₄ (98%, Alfa Aesar, additionally dried), propylene carbonate (PC, BASF, battery grade), fluoroethylene carbonate (FEC, Solvay, battery grade), 1M LiPF₆ in a mixture of ethyl carbonate and dimethyl carbonate (EC:DMC, 1:1 by volume, Merck, battery grade), glass microfiber separator (GF/D, Whatman), and Cu-foil (9 µm thick, MTI Corporation). SnSb-containing electrodes were prepared by mixing SnSb (NCs or bulk), CB and CMC (64%:21%:15%) with water using a Fritsch Pulverisette 7 classic planetary mill (500 rpm, 1 hour). The resulting slurries were coated onto Cu-foil and dried at 80 °C for 12 hours under vacuum. The typical loading was ~0.5 mg cm⁻². Electrochemical measurements were conducted in air-tight coin-type cells assembled in an Ar-filled glove box (O₂ < 0.1 ppm, H₂O < 0.1 ppm). Elemental lithium and sodium were employed as both the reference and counter electrode in half-cells. LiCoO₂ (MTI Corporation) coated onto Al-foil was used as the Li-ion cathode for full-cells (the loading of active material was ~20 mg cm⁻²). For Na-ion full-cell experiments, Na_{1.5}VPO_{4.8}F_{0.7} was prepared according to Park *et al.*⁴⁴ as the cathode. Prior to electrode preparation, Na_{1.5}VPO_{4.8}F_{0.7} was carbon-coated by ball-milling with CB (20 wt%) and annealing at 450 °C for 12 hours.¹⁸³ Before the assembly of Na-ion

full-cells, SnSb electrodes were charged/discharged for 5 cycles vs. elemental Na in the potential range of 0.005-2.0 V at a current of 200 mA g⁻¹. As the electrolyte, 1M LiPF₆ in EC:DMC with 3% FEC was used for LIBs and 1M NaClO₄ in PC with 10% FEC was used for SIBs in this work. One layer of glass microfiber served as the separator in all cases. Galvanostatic cycling experiments were carried out at room temperature on a MPG2 multi-channel workstation (BioLogic). For Li-ion full-cell experiments, the batteries were cycled in the potential range of 2.0-3.9 V at a current of 400 mA g⁻¹. Na-ion full-cell experiments were conducted within a limited charge and discharge capacity window of 400 mAh g⁻¹, in the potential range of 1.5-4.3 V at a current density of 200 mA g⁻¹. All capacities reported in this work correspond to the content of SnSb.

Materials characterization. Transmission electron microscopy (TEM) images were obtained using a Philips CM30 microscope operated at 300 kV using carbon-coated Cu grids as substrates (Ted-Pella). Powder X-ray diffraction (XRD) was measured on a STOE STADI P diffractometer (Cu-Kα₁ irradiation, λ = 1.540598 Å). Scanning electron microscopy (SEM) and energy-dispersive X-ray spectroscopy (EDX) measurements were carried out using a NanoSEM 230 microscope.

4.3. Results and discussion

In the novel synthesis route to SnSb NCs (Figure 4.1.) developed herein, a solution of NaBH₄ in N-methyl-2-pyrrolidone (NMP) was heated under nitrogen to 60 °C, followed by the consecutive injections of SnCl₂ and then SbCl₃ dissolved in the same solvent. As in the previously reported “expensive” organometallic synthesis of SnSb NCs,⁶⁴ Sb is introduced last to prevent the formation of Sb NCs. As seen in TEM images (Figure 4.1.b) the resulting SnSb NCs have a size distribution between 10-30 nm. XRD measurements confirm that the sole crystalline product is cubic SnSb compound (space group *Fm-3m* (225), *a* = 6.13 Å, COD entry 9008724), without any traces of Sn, Sb or their respective oxides (Figure 4.1.c).

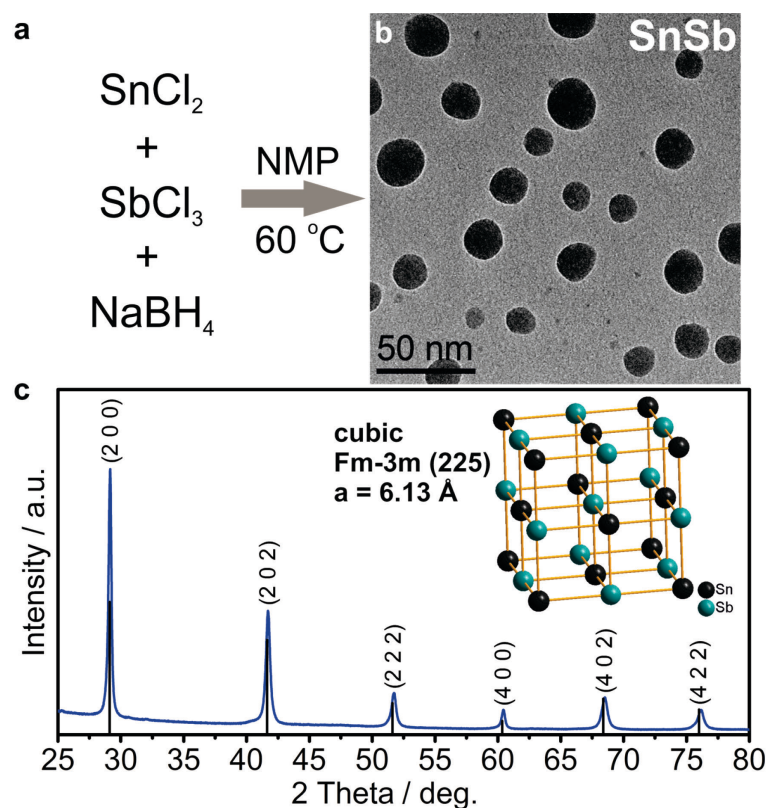


Figure 4.1. Synthesis and characterization of SnSb NCs. (a) Reaction scheme. (b) Transmission electron microscopy (TEM) image. (c) X-ray diffraction (XRD) pattern of SnSb NCs indexed to cubic SnSb (COD entry 9008724).

Notably, even for storage of eight months under ambient conditions no formation of crystalline oxides can be detected (Figure 4.2.).

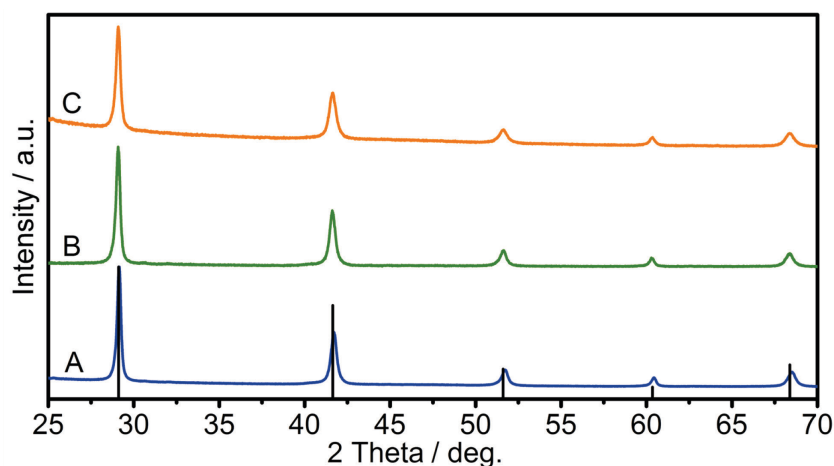


Figure 4.2. XRD patterns for (A) pristine SnSb NCs, (B) SnSb NCs after storage under ambient conditions for eight months and (C) electrode material containing SnSb NCs, carbon black and CMC (indexed to cubic SnSb, COD entry 9008724).

Efficient removal of the main side product NaCl and potentially unreacted NaBH₄, SnCl₂ or SbCl₃ is further evidenced by the absence of signals corresponding to sodium and chlorine in the energy dispersive X-ray (EDX) spectra of the purified SnSb NCs (Figure 4.3.).

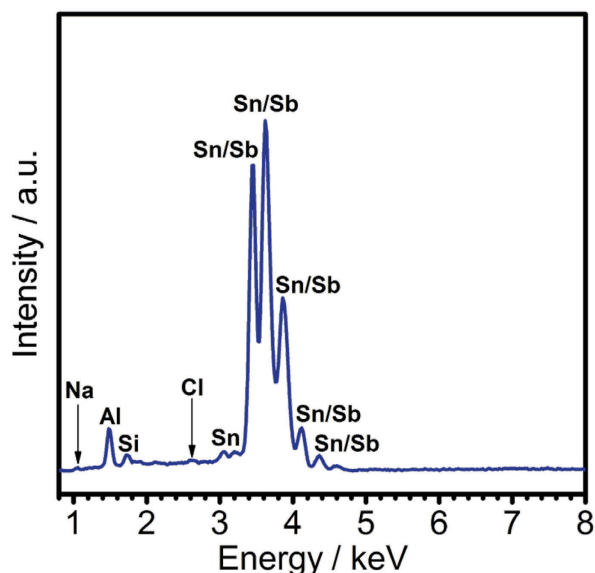


Figure 4.3. EDX spectrum of SnSb NCs indicating complete removal of the main side product NaCl. The Al/Si signal originates from the substrate.

Together, the use of inexpensive reagents, absence of surfactants, recycling of the solvent (NMP), high reaction yield and the non-essentiality of purification of the final product with organic solvents all lead to the low estimated overall cost of this synthesis of not more than 0.3 USD per gram of SnSb (which is essentially only the cost of the starting salts and reducing agent). In stark contrast to hydrothermal/solvothermal procedures^{184, 185} the synthesis presented herein is carried out at low temperatures, under ambient pressure and with short, sub-minute reaction times, ideal for up-scaling.

Li- and Na-ion half-cell tests. Half-cell experiments serve to shed initial light on the capacity, energy density and rate capability of the anodes investigated in this work (Figure 4.4.). Working electrodes were prepared by mixing the SnSb NCs with carbon black (CB) and carboxymethyl cellulose (CMC) as a binder in water and coating the resulting slurry onto Cu-foil (for Li- and Na-ion cells, respectively). In this regard it should be noted that SnSb NCs retain their cubic structure after electrode preparation without the formation of crystalline oxides (Figure 4.2.). Standard liquid electrolyte formulations were used: LiPF₆ in EC:DMC for Li-ion and NaClO₄ in PC for Na-ion cells. In both cases, FEC was added to the electrolyte because of its known beneficial effect on cycling stability due to the stabilization of the solid-electrolyte interface (SEI).^{163, 179, 186, 187}

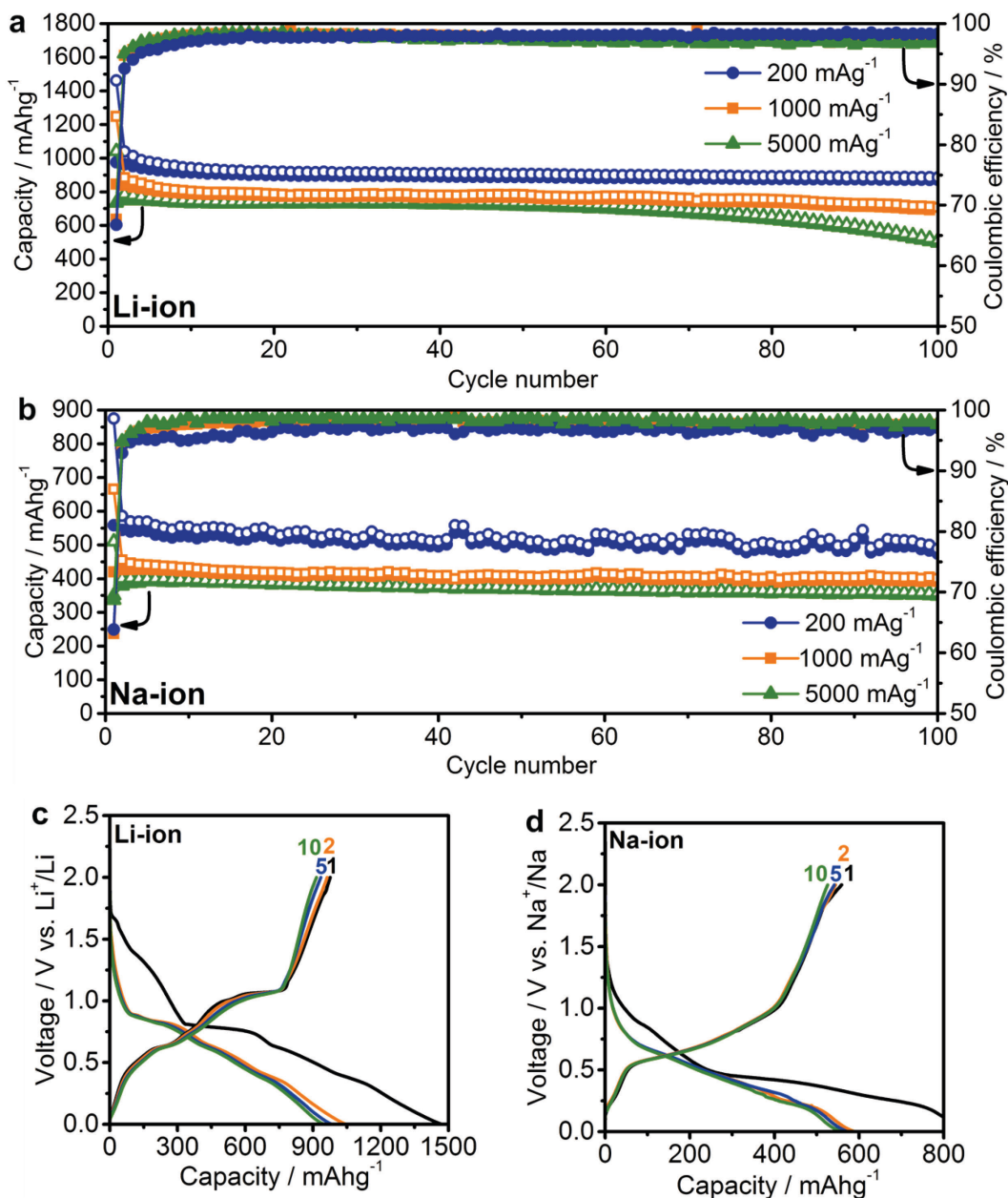


Figure 4.4. Electrochemical performance of SnSb NCs. Capacity retention for SnSb NCs in (a) Li-ion and (b) Na-ion half-cells at a current of 200, 1000 and 5000 mA g⁻¹. Galvanostatic charge and discharge curves for SnSb NCs in (c) Li-ion and (d) Na-ion half-cells at a current of 200 mA g⁻¹. All measurements were performed in the potential range of 0.005-2.0 V.

As is apparent in Figure 4.4., SnSb NCs deliver initial capacities close to the theoretical maximum at all tested current densities, with values of 980, 850 and 730 mAh g⁻¹ at 200, 1000, and 5000 mA g⁻¹, respectively, and retain 90%, 80% and 70% of these initial capacities after 100 cycles. The observation of capacities that are higher than the theoretical capacity (by up to 10%) may arise from the contribution of amorphous carbon of ~100-200 mAh per gram of carbon and also, possibly, due to reversible interfacial lithium storage mechanisms as previously reported for conversion-type materials^{188, 189} or even reversible Li-ion storage by a

polymeric gel-like layer formed by the electrolyte.¹⁹⁰ A significant irreversible capacity is observed in the first few cycles, resulting in an initial coulombic efficiency of just 63-70% for both Li-ion and Na-ion cells. This irreversible capacity can be attributed to the formation of an SEI layer over the large surface area of the nanostructured electrode. During subsequent cycles, the coulombic efficiency rises to ~97-98%, indicating that side reactions such as SEI reformation or electrolyte decomposition continue to occur, causing the remaining 2-3% deficit.

Despite only a minor difference in theoretical capacity between Na₃Sb and Na_{3.75}Sn, significantly lower capacities were observed for SnSb NC Na-ion anodes, as in previous reports.^{64, 191} In particular, at currents of 200, 1000 and 5000 mA g⁻¹, initial capacities of only 560, 420 and 380 mAh g⁻¹ were obtained, respectively. However, contrary to Li-ion half-cells, a much higher fraction of the initial capacity was retained (~90-95%) after 100 cycles at these current densities. This result is clearly an improvement over previous reports of Na-ion storage in SnSb (for a detailed comparison with existing literature reports, see Table 4.1. and 4.2.).^{64, 147, 165, 178-182, 191-195}

Table 4.1. Comparison of the electrochemical performance of SnSb NCs as a Li-ion anode material (present work) with previously reported results.

Anode material	Current density (mA g ⁻¹)	Initial capacity (mAh g ⁻¹)	Retained capacity (mAh g ⁻¹)	Cycle number	Reference
SnSb NCs	200	980	870	100	Present work
	1000	850	710	100	
	5000	730	520	100	
nano-SnSb/MCMB/carbon composite	100	506	423	100	165
nano-Sn-Sb-Cu	100	~450	390	30	194
nano-SnSb/CNT	160	950	860	40	178
SnSb NPs on SnO ₂ /Sn/C	50	886	515	40	191
SnSb/amorphous carbon	100	~550	620	50	182
SnSb-C	100	915	672	120	181
SnSb/CNT	100	680	480	50	192
CNT-Sn-Sb nanorods	180	708	672	80	180
monodisperse SnSb NCs	330	~800	680	100	64
	2640	605	615	100	

Table 4.2. Comparison of the electrochemical performance of SnSb NCs as a Na-ion anode material (present work) with previously reported results.

Anode material	Current density (mA g ⁻¹)	Initial capacity (mAh g ⁻¹)	Retained capacity (mAh g ⁻¹)	Cycle number	Reference
SnSb NCs	200 1000 5000	560 420 380	500 400 360	100 100 100	Present work
SnSb NPs on SnO ₂ /Sn/C	50	385	305	40	191
SnSb-carbon nanofibers	100	347	345	205	179
nano-SnSb/C	100	544	435	50	147
monodisperse SnSb NCs	660	~350	~350	100	64

The small size of SnSb NCs enhances the kinetics of the charge/discharge reactions due to fast ionic and electronic transport, and also leads to improved cycling stability by more effectively accommodating the impact of volume changes during cycling.^{16, 56} The importance of downsizing of the active material is further evidenced by comparison to electrochemical experiments using micrometer-sized SnSb particles prepared by melting elemental Sn and Sb powders (Figure 4.5.).

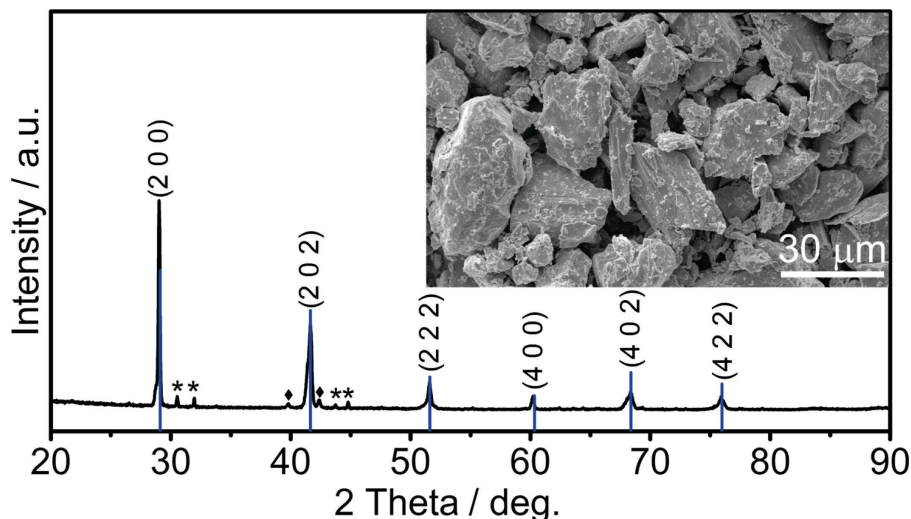


Figure 4.5. XRD pattern of bulk SnSb prepared by melting elemental Sn and Sb indexed to cubic SnSb (COD entry 9008724) with the corresponding SEM image as inset. The small additional peaks most likely correspond to impurities of elemental Sn(*) and Sb(♦).

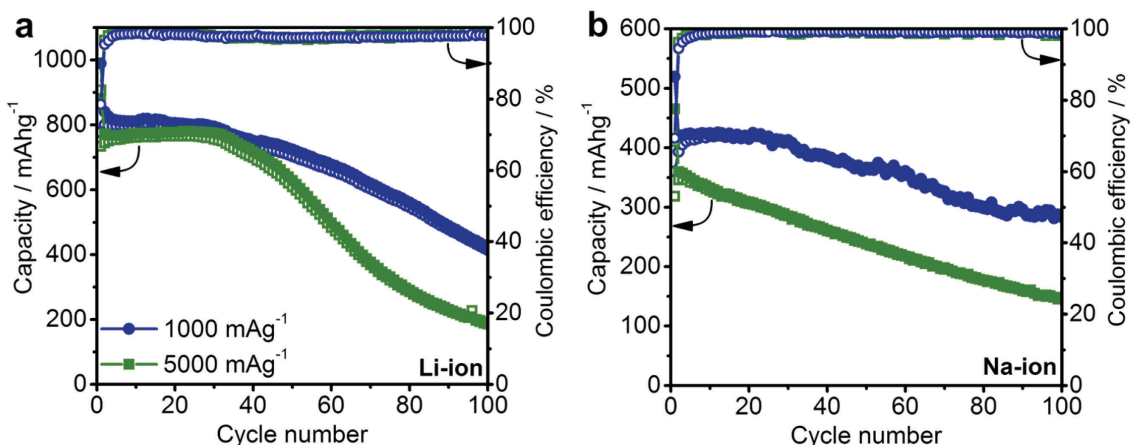


Figure 4.6. Capacity retention for bulk SnSb in (a) Li-ion and (b) Na-ion half-cells using a current of 1000 and 5000 mA g⁻¹. All batteries were measured in the 0.005-2.0 V potential range.

Such bulk SnSb particles show much poorer capacity retention both for Li- and Na-ion half-cells (Figure 4.6.), despite similar reaction mechanisms as indicated by the similarities of the charge/discharge curves (Figure 4.7.).

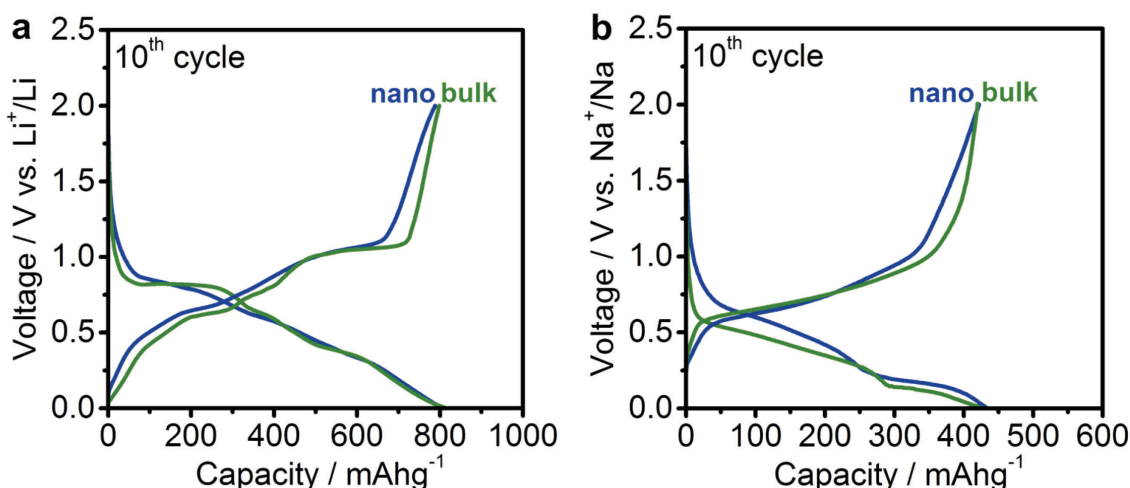


Figure 4.7. Comparison of the galvanostatic charge/discharge curves (10th cycle) for SnSb-based electrodes in (a) Li-ion and (b) Na-ion half-cells at a current of 1000 mA g⁻¹. All batteries were measured in the potential range of 0.005-2.0 V.

Notably, compared to monodisperse 20 nm particles,⁶⁴ the herein presented SnSb NCs, show the same or even better electrochemical performance, indicating that narrow size distributions are not crucial for obtaining good electrochemical performance. Moreover, the absence of any surfactants during the reaction most likely leads to higher capacity levels compared to monodisperse 20 nm SnSb NCs, since remaining insulating ligands on the surface can decrease the storage capacity.

Apart from their high storage capacities, SnSb NCs show relatively low delithiation and desodiation potentials (Figure 4.4.c and d), making them highly attractive materials for full-

cell applications. It should also be noted that whereas for Li-ion storage the galvanostatic charge/discharge curves are essentially comprised of a combination of the features of the pure phase compounds (the delithiation of Sn occurring between 0.8-0.4 V and Sb at ~ 1.1 V), the alloying reaction of SnSb NCs with Na is clearly different.¹⁴⁸ The same conclusion can be made from cyclic voltammetry measurements, which are fully consistent with previous reports on SnSb (Figure 4.8).^{178, 179}

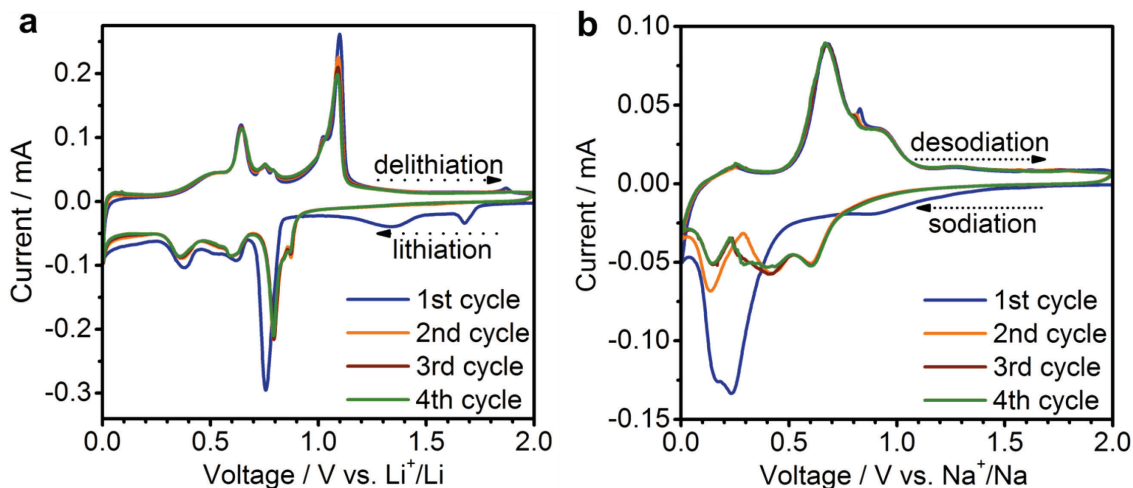
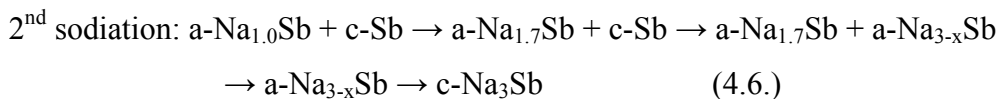
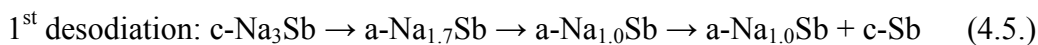
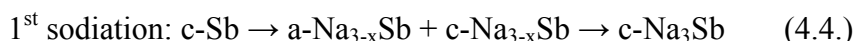
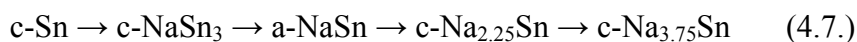


Figure 4.8. Cyclic voltammograms of SnSb NCs tested in (a) Li-ion or (b) Na-ion half-cells using a scan rate of 0.1 mV s^{-1} in the potential range 0.005-2.0 V.

Whereas the reaction mechanism of SnSb with Na is not fully clarified due to difficulties to analyze the amorphous intermediates and products,¹⁹⁶ the reaction mechanism of Sb has been elucidated to proceed *via* the following steps (where c - crystalline, a - amorphous):¹⁹⁷



Transition through amorphous phases, helping in mitigating volumetric changes, has been hypothesized as one of the reasons for the relatively high cycling stability of Sb-based electrodes.¹⁹⁷ In the case of Sn, the sodiation mechanism was proposed to take place according to the following sequence:¹⁹⁸



However, it should be noted that this sequence was obtained at low current rates (C/50) with an additional potentiostatic step at 5 mV vs. Na^+/Na . Under more practical cycling conditions at higher rates full sodiation of Sn to $\text{Na}_{3.75}\text{Sn}$ might in fact not occur,¹⁹⁹ as supported by significantly lower capacities reported for Sn-based electrodes.²⁰⁰⁻²⁰² Notably, whereas in the case of SnSb electrodes Na_3Sb could be crystallized at elevated temperatures, Sn environments remain incompletely sodiated, as reported by Baggetto *et al.*¹⁹⁶ Thus, the generally lower capacity of SnSb-based anodes for Na-ion compared to Li-ion storage^{64, 191} – which is also observed for the herein presented SnSb NCs – might be attributed to not fully sodiated Sn-phases.

Li- and Na-ion full-cell tests. To evaluate the practical utility of SnSb nanomaterials as anodes, Li- and Na-ion full-cells were assembled using standard cathode materials (Figure 4.9. and 4.10.). Anode-limited operation of a full-cell allows the assessment of the behavior of the anode in more practically relevant conditions. As in half-cell experiments, all specific currents and capacities correspond to the mass of the SnSb active material in the anode.

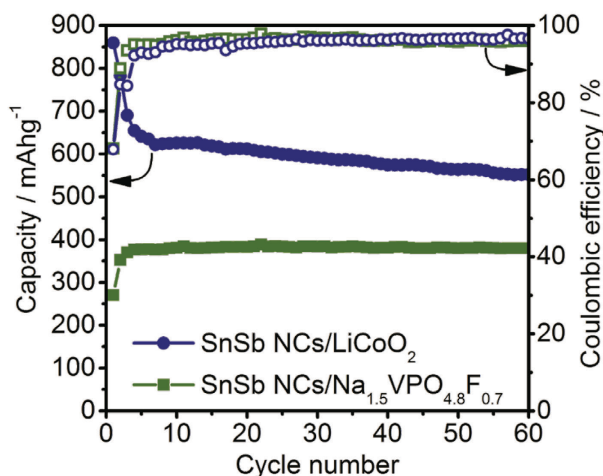


Figure 4.9. Electrochemical performance of SnSb NCs Li-ion and Na-ion full-cells using LiCoO_2 or $\text{Na}_{1.5}\text{VPO}_{4.8}\text{F}_{0.7}$ as cathode material. Capacity retention for SnSb NCs at a current of 400 mA g^{-1} in Li-ion and at 200 mA g^{-1} in Na-ion full cells. Li-ion cells were cycled in the potential range 2.0-3.9 V. Na-ion cells were cycled with limitation of charge and discharge capacity to 400 mAh g^{-1} . Displayed capacities and currents are related to the mass of SnSb NCs.

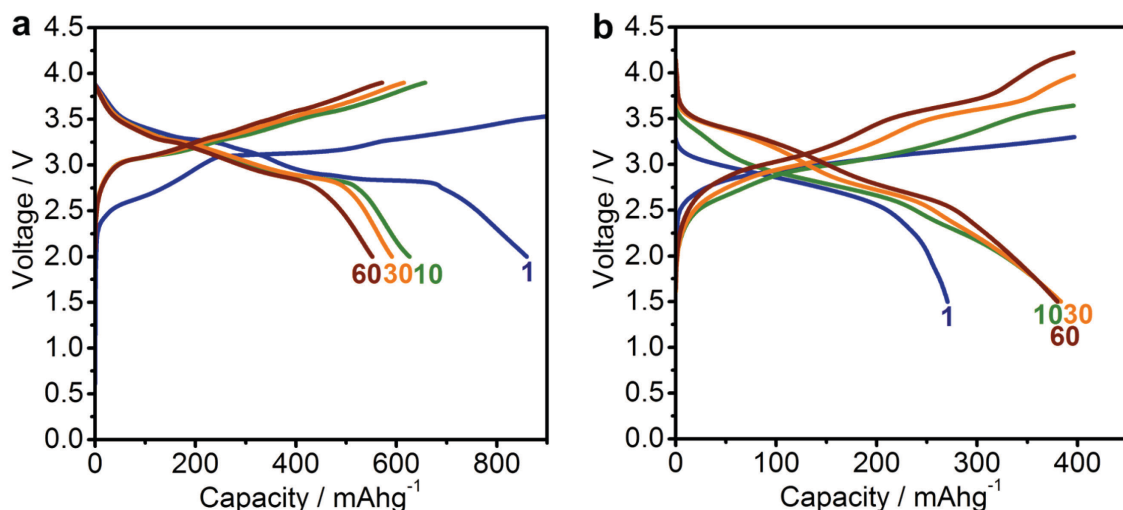


Figure 4.10. Galvanostatic charge/discharge curves for SnSb NCs in (a) Li-ion and (b) Na-ion full-cells using LiCoO_2 or $\text{Na}_{1.5}\text{VPO}_{4.8}\text{F}_{0.7}$ as cathode material. Li-ion cells were cycled with a current of 400 mA g^{-1} in the potential range 2.0-3.9 V. Na-ion cells were cycled with a current of 200 mA g^{-1} and limitation of charge and discharge capacity to 400 mAh g^{-1} . Displayed capacities and currents are related to the mass of SnSb NCs.

Li-ion full-cells were assembled using commercial LiCoO_2 cathodes and then cycled in the potential range of 2.0-3.9 V with a current density of 400 mA g^{-1} (anode). For at least 60 cycles SnSb NCs deliver an average Li-ion storage capacity of 600 mAh g^{-1} with an average discharge voltage of 3.0 V. Na-ion full-cells were assembled using $\text{Na}_{1.5}\text{VPO}_{4.8}\text{F}_{0.7}$ as the cathode, synthesized according to Park *et al.*⁴⁴ and characterized by powder XRD (Figure 4.11.a, Table 4.3.) This cathode material exhibits high cycling stability and a high sodiation potential ($\sim 3.8 \text{ V vs. Na}^+/\text{Na}$, Figure 4.11.b).⁴⁴

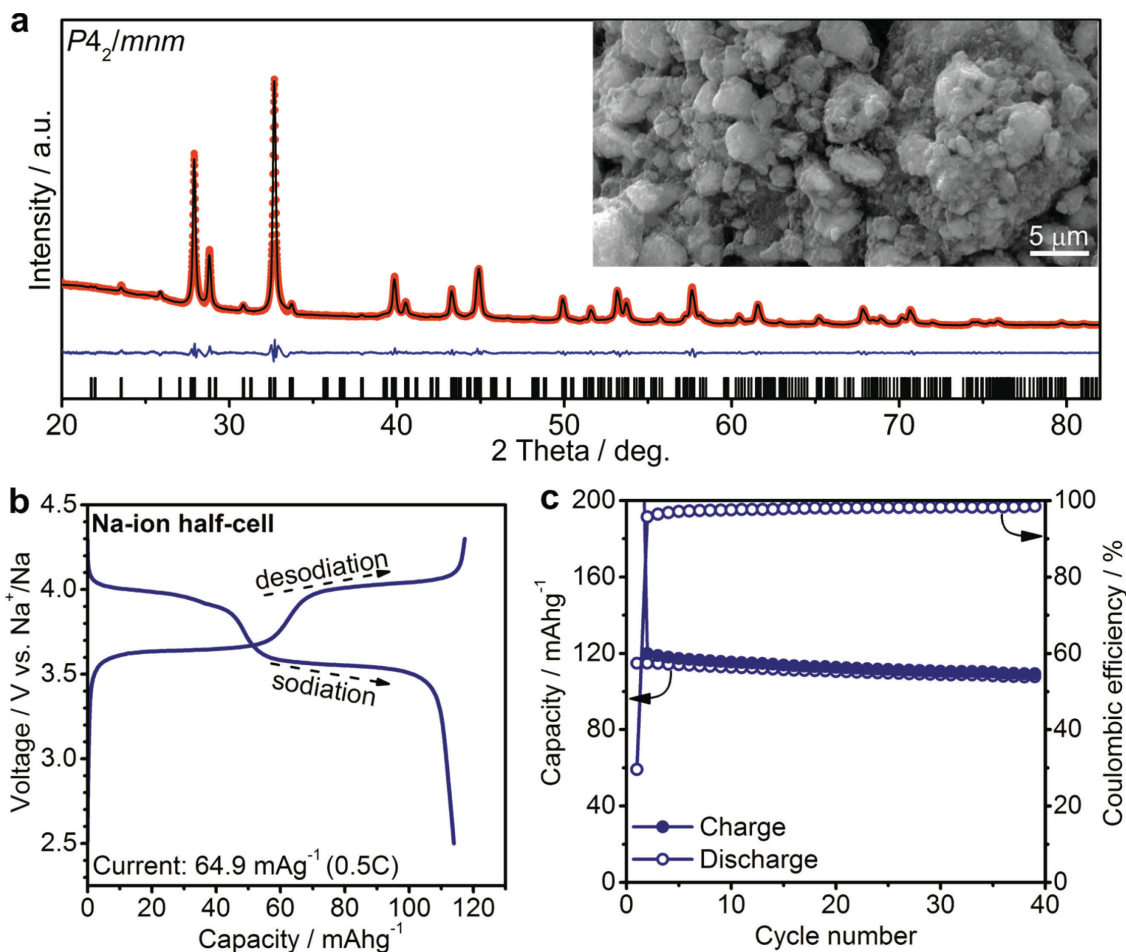


Figure 4.11. (a) X-ray diffraction (XRD) pattern of $Na_{1.5}VPO_{4.8}F_{0.7}$ and Rietveld refinement with the observed pattern (red dots), the calculated pattern (black curve), difference between observed and calculated pattern (blue line) and Bragg positions (black bars) (space group $P4_2/mnm$, $a = b = 9.044 \text{ \AA}$, $c = 10.627 \text{ \AA}$). The inset shows a scanning electron microscopy (SEM) image of $Na_{1.5}VPO_{4.8}F_{0.7}$ after ball-milling and annealing with CB. (b) Galvanostatic charge/discharge curve (5th cycle) and (c) capacity retention for $Na_{1.5}VPO_{4.8}F_{0.7}$ tested as cathode material in Na-ion half-cells. Cells were cycled at room temperature with a current of 64.9 $mA g^{-1}$ (0.5C) in the potential range 2.5–4.3 V vs. Na^+/Na using 1M $NaBF_4$ in EC:PC (1:1 by vol.) as electrolyte. The composition of the electrodes was $Na_{1.5}VPO_{4.8}F_{0.7}$ (72 wt%), CB (18 wt%) and PVdF (10 wt%).

Table 4.3. Rietveld refinement parameters corresponding to the XRD pattern of $Na_{1.5}VPO_{4.8}F_{0.7}$ in Figure 4.11.a. Rietveld refinement was carried out using FullProf Suite (<https://www.ill.eu/sites/fullprof/>).

Pattern				Phase	
Chi2	Rp	Rwp	Rexp	Rbragg	RF-factor
5.69	13.1	10.9	4.57	1.031	1.320

Prior to full-cell experiments, SnSb anodes were cycled vs. elemental Na at a current of 200 $mA g^{-1}$ in the potential range of 0.005–2.0 V for 5 cycles in order to form a stable SEI layer and therefore minimize the charge loss during subsequent cycles. Both charge and discharge capacities were limited to 400 $mA h g^{-1}$ within the potential range of 4.3–1.5 V and the cells were cycled at a current of 200 $mA g^{-1}$. As can be seen in Figure 4.9., the SnSb/ $Na_{1.5}VPO_{4.8}F_{0.7}$ Na-ion full-cell delivers a stable capacity of $\sim 400 \text{ mA h g}^{-1}$ for at least 60 cycles, with an average discharge voltage of 2.7 V (4.10.b).

Based on the anodic capacities obtained for Li- and Na-ion full-cells and the theoretical capacities of the cathode materials (140 mAh g⁻¹ for LiCoO₂ and 129.7 mAh g⁻¹ for Na_{1.5}VPO_{4.8}F_{0.7})⁴⁴ the theoretical cell capacities can be estimated, using $C_{\text{cell}} = C_{\text{anode}}C_{\text{cathode}}/(C_{\text{anode}}+C_{\text{cathode}})$. This cell capacity multiplied by the average discharge voltage yields the theoretical energy density of the cell. In this way, the energy density of the SnSb/Na_{1.5}VPO_{4.8}F_{0.7} full-cell battery developed in this work compares favorably to other recently reported Na-ion full-cells.²⁰³⁻²⁰⁶ Similarly, the SnSb/LiCoO₂ Li-ion full-cell exhibits an energy density of 340 Wh kg⁻¹, comparable to the graphite/LiCoO₂ system. One possible advantage of SnSb over graphite lies in its three-fold higher density compared to graphite (6.9 g cm⁻³ vs. 2.2 g cm⁻³, respectively). This potentially enables higher volumetric energy densities by up to 30%: 1796 Wh L⁻¹ for the SnSb/LiCoO₂ full-cell compared to 1339 Wh L⁻¹ for graphite/LiCoO₂, assuming a density of 5 g cm⁻³ for LiCoO₂.²⁰⁷

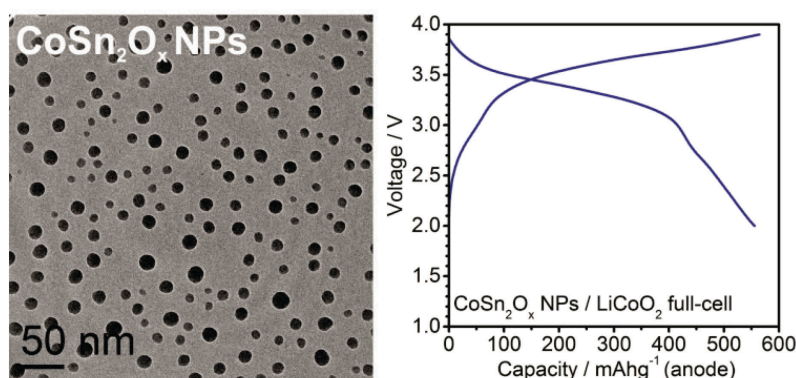
4.4. Conclusion

In summary, an inexpensive and scalable synthesis of SnSb nanocrystals of 10-30 nm in size is reported using metal chlorides as precursors and sodium borohydride as a reducing agent. The important advantages of this method over previous solution syntheses are its nearly quantitative reaction yield and its avoidance of the use of surfactants. The resulting NCs can thus be isolated simply by centrifuging or filtering, and purified by rinsing with water. Li-ion storage in such SnSb NCs is characterized by capacities close to the theoretical maximum, with an average value of 760 mAh g⁻¹ for 100 cycles at a high current density of 1000 mA g⁻¹. For Na-ion storage, lower capacities are obtained, but with higher relative capacity retention upon cycling. The first results from Li-ion and Na-ion full-cell experiments, using LiCoO₂ and Na_{1.5}VPO_{4.8}F_{0.7} as the cathodes, indicate the stable cycling performance of SnSb NCs with specific Li- and Na-ion anodic capacities (average voltage in parentheses) of 600 mAh g⁻¹ (3.0 V) and 400 mAh g⁻¹ (2.7 V), respectively.

Reproduced with modifications from:

M. Walter, S. Doswald and M. V. Kovalenko. *Inexpensive colloidal SnSb nanoalloys as efficient anode materials for lithium- and sodium-ion batteries*. J. Mater. Chem. A, **2016**, 4, 7053-7059. Published by The Royal Society of Chemistry.

Chapter 5. Oxidized Co-Sn nanoparticles as long-lasting anode materials for Li-ion batteries



5.1. Introduction

Despite an intensive research effort to develop new materials for rechargeable Li-ion batteries (LIBs) over the past three decades, graphite remains the most common anode material in commercial devices. This is a surprising circumstance considering the fact that graphite possesses relatively low gravimetric and volumetric capacities (372 mAh g^{-1} and 820 mAh cm^{-3} , respectively) compared to a large number of both alloying- (*e.g.*, Si, Ge, and Sn) and conversion-type materials (*e.g.*, Fe_3O_4 , MoS_2 , and SnSb).^{156, 208} The primary reasons for this are the rapid decline in capacity of many of these alternative anode materials due to massive volume changes during cycling (*e.g.*, $\Delta V = 100\text{-}300\%$) causing mechanical disintegration of the electrodes, and/or due to irreversible reactions during charge and discharge. It has been demonstrated in a variety of case studies that these issues can be mitigated by using nanostructuring strategies in the synthesis of the active anode materials.^{16, 19, 53, 54, 56-58, 63-73, 209} Nevertheless, the commercialization of such high-capacity alloying- and conversion-type anodes has remained hampered for several reasons. In conversion-type anodes, a major fraction of the capacity is often obtained at potentials above 1.0 V vs. Li^+/Li , reducing the voltage of the full-cell and thus the energy density of the corresponding battery. Secondly, the synthesis of nanostructured electrodes is often elaborate and therefore costly. Tin remains among the few materials which are realistic candidates to replace graphite in commercial LIBs, due to its high gravimetric and volumetric capacities (992 mAh g^{-1} and $\sim 7300 \text{ mAh cm}^{-3}$), low delithiation potential (0.2-1.0 V), high electrical

conductivity, low cost and natural abundance. In fact, anodes comprising amorphous Sn-Co-C nanocomposites have indeed been employed in commercial rechargeable batteries (e.g., NexelionTM, Sony Corp., Japan) since at least 2005. The success of this product has triggered further intensive research on Co-Sn-based anodes for LIBs.^{89, 210-227} The superior cycling stability of many Co-Sn-based materials over elemental Sn has been attributed to two factors: 1) the effective buffering of volume changes occurring during the lithiation of Sn by the inactive Co matrix and 2) the prevention of aggregation of Sn particles during delithiation due to the preferred formation of intermetallic Co-Sn phases.⁸⁷⁻⁸⁹ Notable recent examples of nanostructured Co-Sn-based materials include, for instance, CoSnO₃ NPs in a graphene network²²⁸ and Sn-Co NPs encapsulated in carbon spheres,²²⁹ which both exhibit stable capacities over ≥ 100 cycles in a wide potential range of up to 3.0 V vs. Li⁺/Li.

In this chapter, a systematic comparison of well-defined Co-Sn nanoparticle (NP) based materials as anodes for LIBs is presented. A simple synthetic procedure is introduced which can be used to prepare either amorphous Co NPs or crystalline Sn NPs, and subsequently their conversion into crystalline non-oxidized CoSn₂ NPs or oxidized, nearly amorphous CoSn₂O_x NPs, by simple mechanochemical methods is demonstrated. Half-cell electrochemical experiments were carried out to compare pure Sn NPs to both Co-Sn NP systems, indicating superior characteristics of the CoSn₂O_x NPs. Finally, full-cell experiments were carried out on this most promising system using LiCoO₂ as the cathode. Stable cycling with anodic capacities of 576 mAh g⁻¹ for 100 cycles could be demonstrated at a current of 500 mA g⁻¹, with an average discharge voltage of 3.14 V. Note: in the work described herein, “CoSn₂ NPs” is used to refer to the highly crystalline, non-oxidized CoSn₂ material (seen by X-ray diffraction to be phase-pure), while the term “CoSn₂O_x NPs” is used for oxidized and mostly amorphous NPs (with < 5 nm crystal domain sizes).

5.2. Experimental section

Colloidal synthesis of Sn and Co NPs. To prepare Sn NPs, a solution of NaBH₄ (96 mmol, 98%, ACBR) in anhydrous N-methyl-2-pyrrolidone (NMP, 85 mL, 99.5%, Fisher BioReagents) was heated to 60 °C under flowing N₂. Then, a solution of SnCl₂ (1 mmol, $\geq 99\%$, Alfa Aesar) in anhydrous NMP (3 mL) was injected and the reaction mixture was immediately cooled to room temperature using a water-ice bath. To prepare Co NPs, a NaBH₄ solution in anhydrous NMP (32 mmol in 15 mL) was heated to 150 °C under flowing N₂, followed by the injection of CoCl₂ (8 mmol, $\geq 98\%$, Sigma-Aldrich; in 5 mL anhydrous NMP) and immediate cooling to room temperature using a water-ice bath. The obtained Co

NPs and Sn NPs were purified by washing once with dimethyl sulfoxide and then two times with water after separation from the supernatant by centrifugation. Finally, the reaction product was dried under vacuum at room temperature.

Synthesis of crystalline CoSn₂ NPs and oxidized CoSn₂O_x NPs. For the preparation of Co-Sn based NPs, Sn NPs (1.4 mmol) were ball-milled for 4 hours with Co NPs (0.7 mmol) at a frequency of 30 s⁻¹ using a Fritsch Pulverisette 23 mill (10 mL ZrO₂ vessel, loaded with two 10 mm ZrO₂ balls). In order to prepare crystalline CoSn₂ NPs, the vessel was loaded and sealed under nitrogen atmosphere. Oxidized CoSn₂O_x NPs were obtained when the starting materials Co and Sn NPs were loaded in air.

Electrode fabrication, cell assembly and electrochemical measurements. The following battery components were used: carbon black (CB, Super C65, TIMCAL), carboxymethyl cellulose (CMC, Grade: 2200, Daicel Fine Chem Ltd.), fluoroethylene carbonate (FEC, Solvay, battery grade), 1M LiPF₆ in ethylene carbonate: dimethyl carbonate (EC:DMC, 1:1 by volume, Merck, battery grade), glass microfiber separator (GF/D, Whatman), and Cu-foil (9 μm, MTI Corporation). For electrode preparation, aqueous slurries were prepared by mixing the respective NPs (64 wt%) with CB (21 wt%), CMC (15 wt%) and water using a planetary ball-mill (Fritsch Pulverisette 7 mill, 500 rpm, 1 hour), and then coated onto Cu current collectors. The electrodes were then dried at 80 °C under vacuum for 12 hours prior to assembling the cells. Material loadings were ~0.5 mg cm⁻² for half-cell and ~1 mg cm⁻² for full-cell experiments. Electrochemical measurements were conducted in air-tight coin-type cells assembled in an Ar-filled glove box (O₂ < 0.1 ppm, H₂O < 0.1 ppm) using elemental lithium as the counter electrode for half-cells and LiCoO₂ on Al-foil (MTI Corporation, ~20 mg cm⁻²) as the cathode in full-cells. Glass microfiber was used as the separator in all cases. A standard solution of 1M LiPF₆ in EC:DMC with 3% FEC was used as the electrolyte. Galvanostatic cycling tests were performed at room temperature on a MPG2 multi-channel workstation (BioLogic). Anodic capacities were determined corresponding to the mass of the Co-Sn material in both half- and full-cell experiments.

Materials characterization. Transmission electron microscopy (TEM) images were obtained with a Philips CM30 microscope operated at 300 kV, using carbon-coated Cu grids as substrates (Ted-Pella). Energy-dispersive X-ray spectroscopy (EDX) measurements were carried out using a NanoSEM 230 scanning electron microscope. Scanning transmission electron microscopy (STEM) images and EDX spectroscopy maps were collected on a FEI Talos F200X microscope operated at 200 kV. Powder X-ray diffraction (XRD) was measured on a STOE STADI P diffractometer (Cu-Kα₁ irradiation, λ = 1.540598 Å).

5.3. Results and discussion

Inexpensive routes to Co-Sn-based NPs were derived by combining the wet colloidal synthesis of unary metallic Co and Sn NPs with dry mechanochemical reactions between them (Figure 5.1.a), conducted in or without the presence of air.

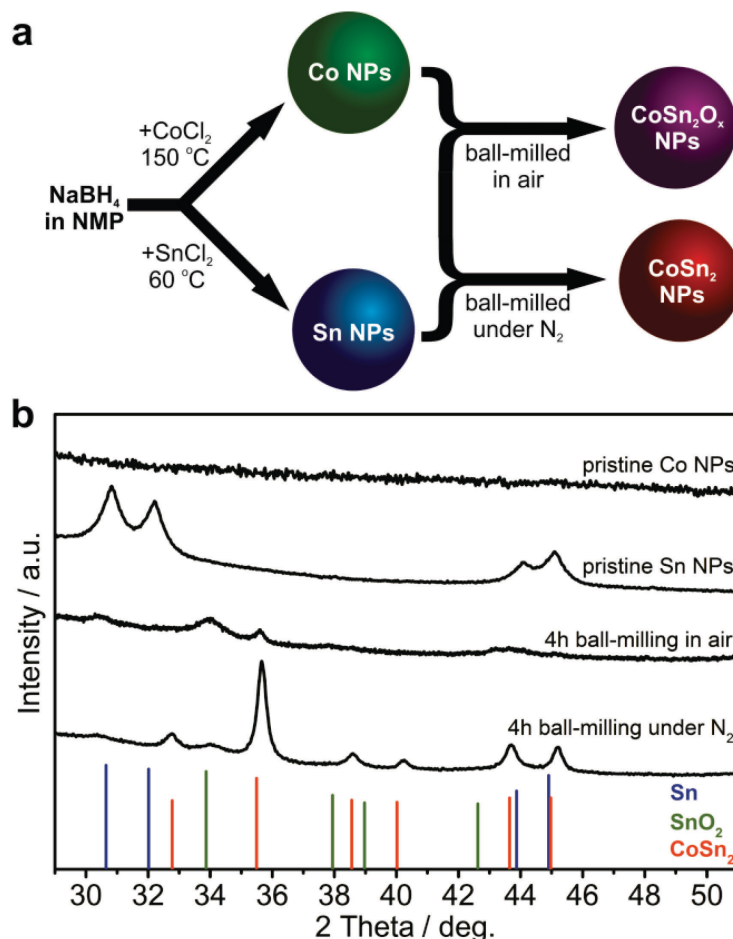


Figure 5.1. (a) Schematic of the preparation of Co-Sn NPs. (b) X-ray diffraction (XRD) patterns of colloiddally synthesized Co and Sn NPs and mechanochemically prepared CoSn_2O_x and crystalline CoSn_2 NPs. Reference patterns: tetragonal SnO_2 , space group $P4_2/mnm$ (136), $a = 4.7391 \text{ \AA}$, $c = 3.1869 \text{ \AA}$, ICDD PDF entry 00-077-0448; tetragonal CoSn_2 , space group $I4/mcm$ (140), $a = 6.363 \text{ \AA}$, $c = 5.456 \text{ \AA}$, ICDD PDF entry 00-025-0256.

Unary metallic NPs of Co (amorphous) and Sn (crystalline) were synthesized by an extension of the method that has been previously reported for Sb NPs²⁶ (also described in Chapter 3) based on the borohydride reduction of metal chlorides in NMP. In contrast to the reduction reactions of SbCl_3 ²⁶ and SnCl_2 which exhibited suitable kinetics at 60°C , a higher temperature of 150°C was required for CoCl_2 . The resulting Co NPs were amorphous (Figure 5.1., see also Figure 5.2.), whereas the Sn NPs were highly crystalline in the form of β -Sn (Figure 5.1.b, indexed as phase-pure tetragonal Sn, space group $I4_1/amd$ (141), $a = 5.831 \text{ \AA}$, $c = 3.182 \text{ \AA}$, ICDD PDF entry No.: 00-004-0673).

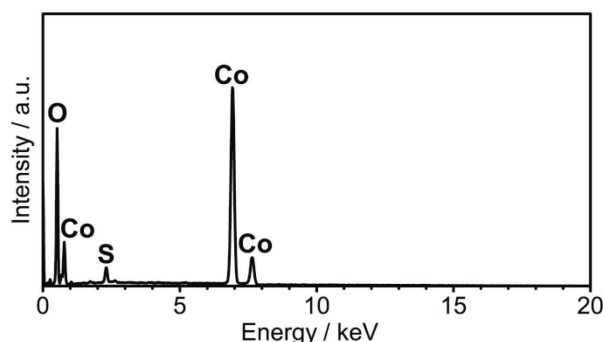


Figure 5.2. EDX spectrum of amorphous Co NPs. The peak denoted as S (corresponding to ~1 wt% of the sample) could be attributed to residual DMSO, left over after washing.

Mixtures of Co and Sn NPs (molar ratio 1:2) were then ball-milled either in air or under nitrogen atmosphere with the intention of intimately mixing and alloying these materials and to study the effects of oxidation. Synthesis in air yielded a largely amorphous/poorly crystalline product, with broad and weak XRD reflections corresponding to SnO_2 and CoSn_2 . For simplicity, the resulting product is denoted as CoSn_2O_x NPs throughout this chapter. In agreement with the XRD results, high-resolution transmission electron microscopy (HR-TEM) investigations indicate the presence of small crystalline domains mainly in the range of < 5 nm. Elemental mapping with energy-dispersive X-ray spectroscopy in scanning TEM (EDX-STEM) studies indicate oxidation throughout the material, with a rather homogeneous distribution of Co, Sn, and O (Figure 5.3.).

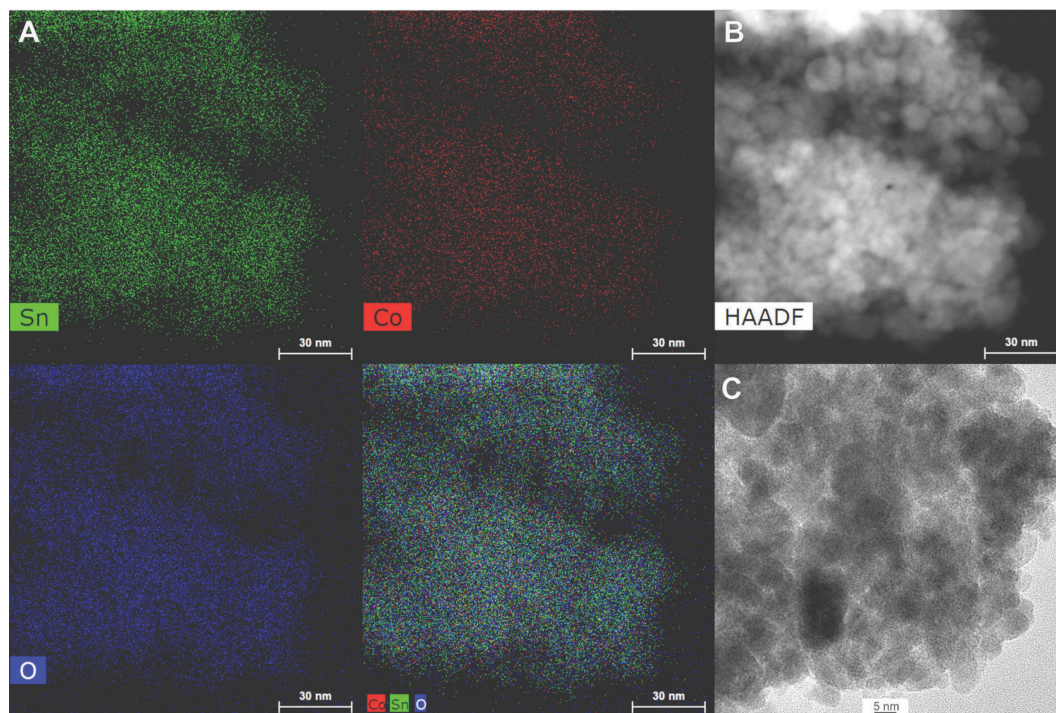


Figure 5.3. (A) Elemental EDX-STEM maps, (B) HAADF-STEM, and (C) HR-TEM images of CoSn_2O_x NPs.

Ball-milling under inert conditions, however, resulted in the formation of highly crystalline CoSn_2 NPs, with only a minor content of SnO_2 . In all cases, the NPs obtained were small: 4-7 nm for Co NPs, 5-10 nm for Sn NPs and 6-20 nm for CoSn_2O_x NPs and CoSn_2 NPs (Figure 5.4.).

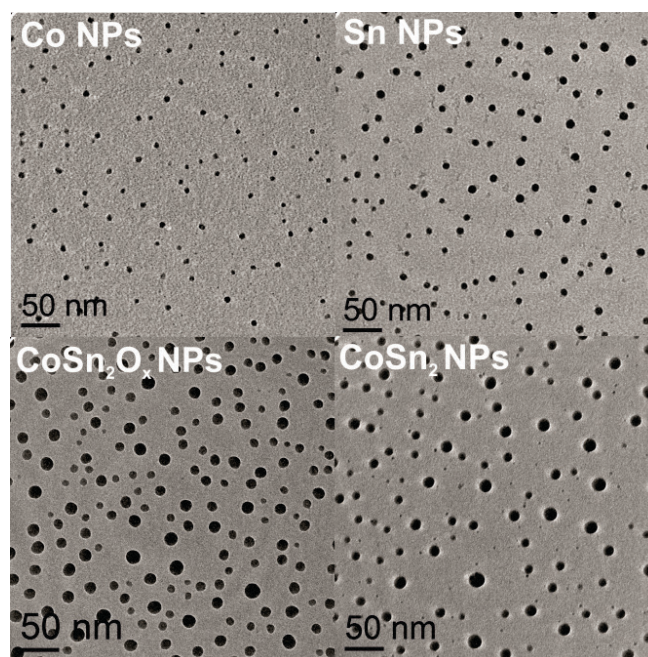


Figure 5.4. Transmission electron microscopy (TEM) images of colloiddally synthesized Co and Sn NPs and mechanochemically prepared CoSn_2O_x and CoSn_2 NPs.

Importantly, as control experiments, attempts to synthesize Co-Sn nanomaterials with commercial microcrystalline powders of Co and Sn did not result in the formation of the CoSn_2 phase (Figure 5.5.).

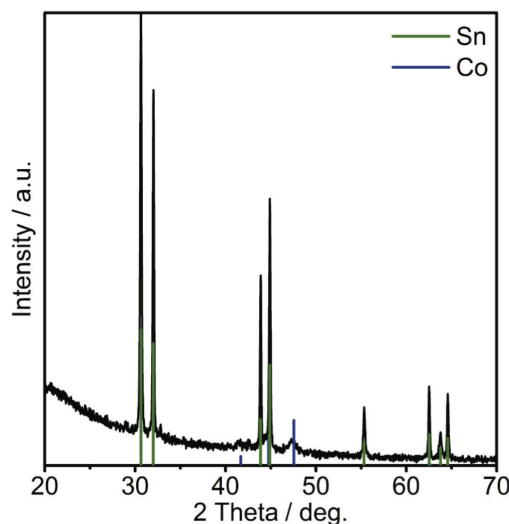


Figure 5.5. XRD pattern of a mixture of bulk Co and Sn powders (molar ratio 1:2) after ball-milling for 4 hours under nitrogen indexed to Sn (ICDD PDF entry No.: 00-004-0673) and Co (ICDD PDF entry No.: 00-005-0727).

Li-ion half-cell experiments. In order to compare the electrochemical properties of Sn, CoSn_2O_x NPs and CoSn_2 NPs, Li-ion half-cells were assembled. Electrodes were composed of NPs, carbon black (CB), and CMC binder (in a ratio of 64:21:15 by weight), and were tested against elemental lithium using 1M LiPF_6 in EC:DMC. FEC was added to the electrolyte to improve cycling stability by forming a stable SEI layer.^{61, 163, 186, 187, 230} All specific capacities and currents presented herein correspond to the combined mass of Sn and Co, excluding CB and CMC. Figure 5.6. shows the capacity retention performance of CoSn_2O_x NPs compared to Sn NPs over 1500 cycles at a high current density of 1984 mA g^{-1} in the potential range of 0.005-1.0 V vs. Li^+/Li .

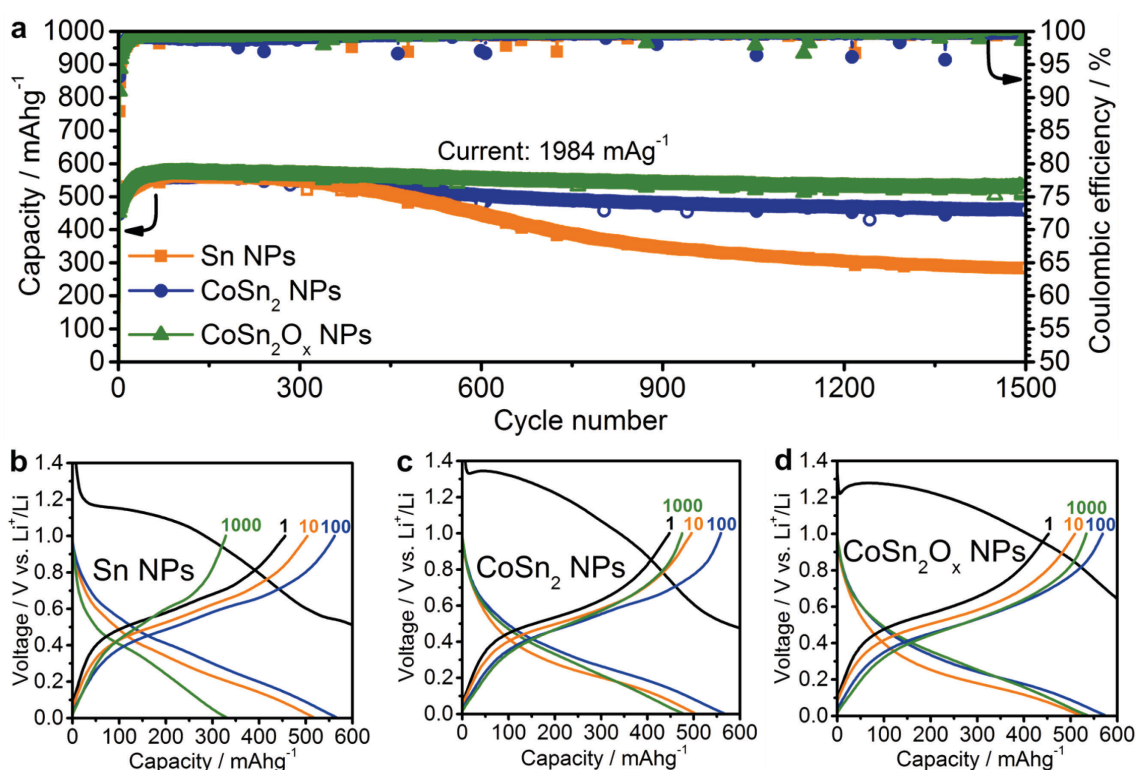


Figure 5.6. (a) Cycling stability measurements of Sn NPs, CoSn₂ NPs and CoSn₂O_x NPs in Li-ion half-cells at a current of 1984 mA g⁻¹ within the potential range of 0.005-1.0 V. Galvanostatic charge/discharge curves for (b) Sn NPs, (c) CoSn₂ NPs, and (d) CoSn₂O_x NPs corresponding to the half-cells in Figure 5.6.a.

Since lithium is reversibly stored in all of the systems studied herein primarily *via* the Sn → Li_{4.4}Sn conversion reaction (theoretical capacity: 992 mAh g⁻¹), a current density of 992 mA g⁻¹ was designated as the 1C rate.²³¹ Assuming that Co does not contribute to any Li-ion capacity, the theoretical capacity of CoSn₂ is 795 mAh g⁻¹. During galvanostatic cycling of the half-cells, the upper cut-off potential was limited to 1.0 V in order to include only the region relevant for full-cells. As can be seen in Figure 5.6., at a high current density of 1984 mA g⁻¹ (“2C”), Sn NPs, CoSn₂O_x NPs, and CoSn₂ NPs initially show similar capacities of 550-600 mAh g⁻¹, with the highest values typically reached after 50-100 cycles. Upon extended cycling, Sn NPs exhibit significant capacity fading after 400 cycles, while Co-Sn-based NPs show a much better retention of their capacity. Specifically, CoSn₂ NPs retain a capacity of 462 mAh g⁻¹ after 1500 cycles (corresponding to a reduction of 18%). CoSn₂O_x NPs exhibit even better cyclability, retaining a capacity of 525 mAh g⁻¹ (a reduction of 8%) after 1500 cycles. It should be noted that for all three systems, the average coulombic efficiency (CE) is 99.6% during cycling. The 1st cycle CE is, however, as low as ~30%, which can be attributed to the formation of solid electrolyte interface (SEI) and the reduction of surface oxides to their corresponding metals with Li₂O as a byproduct.

With such a high cycling stability, the CoSn₂O_x NPs in this work compare favorably to the majority of recently investigated Sn-based Li-ion anode materials (see Table 5.1. for detailed

comparison), especially when considering that the cycling performed herein was restricted to potentials below 1.0 V vs. Li^+/Li in order to obtain values that are truly relevant for full-cells.^{58, 65, 74, 75, 86, 228, 232, 233}

Table 5.1. Comparison of the electrochemical performance of CoSn_2O_x NPs (present work) with other reported systems as anode materials for LIBs.

Anode material	Current density (mA g^{-1})	Initial capacity (mAh g^{-1})	Retained capacity (mAh g^{-1})	Cycle number	Potential range (V vs. Li^+/Li)
CoSn_2O_x NPs (present work)	1984	450 (570 at cycle 100)	525	1500	0.005-1.0 V
$\text{CoSnO}_3@\text{GN}^{228}$	2000	~708	566	1500	0.005-3.0 V
nano Sn-C ⁷⁵	3000	~450 (at cycle 50)	536.5	1000	0.01-2.5 V
nano Sn-C ²³²	4000	~390	410	1000	0.02-3.0 V
nano Sn-C ²³³	200	757	722	200	0.01-2.0 V
Ni_3Sn_2 microcages ⁶⁵	570	~304	~304	1000	0.01-2.0 V
Sn NCs ⁵⁸	1000	~800	550	100	0.005-2.0 V
nano Sn-C ⁸⁶	200	~710	~710	130	0-3.0 V
Sn-carbon/silica ⁷⁴	300	~440	~440	100	0-2.5 V

This superior cycling stability of NPs incorporating Co and Sn compared to pure Sn NCs might be attributable to two effects. Firstly, due to the fact that it does not form lithium alloys, Co can serve as an inactive matrix during cycling and therefore buffer the volume changes caused by the lithiation/delithiation of Sn. Secondly, the presence of Co can prevent Sn NCs from aggregating upon delithiation and therefore further improve the retention of the starting structure of the active anode material.⁸⁷⁻⁸⁹ Further, cyclic voltammetry (CV) measurements indicate a third possible effect: lithiation/delithiation occurs through fewer (most likely amorphous) phase transitions for Co-Sn-based NPs compared to Sn NCs (Figure 5.7.). It is well known that pure Sn forms a multitude of intermediate crystalline phases during lithiation, leading to increased anisotropic strain in the particles during cycling and therefore lower cycling stability.²³¹

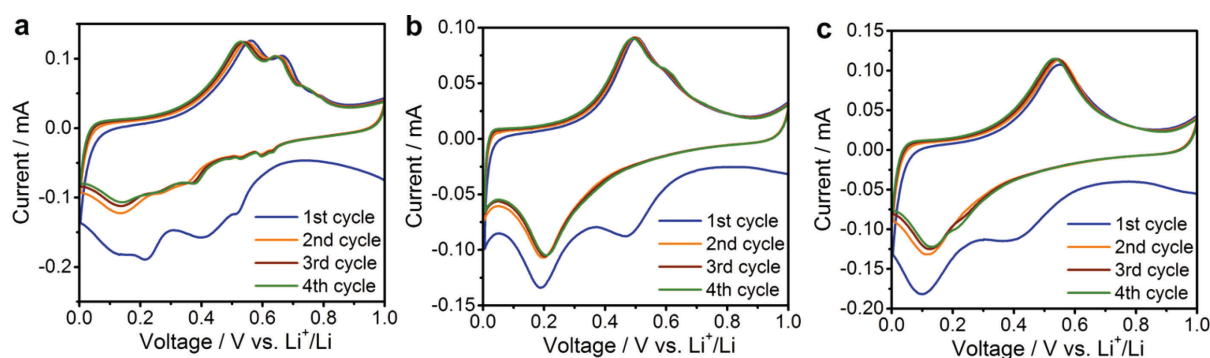


Figure 5.7. Cyclic voltammograms of (a) crystalline Sn NPs, (b) CoSn_2 NPs and (c) CoSn_2O_x NPs in Li-ion half-cells using a scan rate of 0.1 mV s^{-1} in the potential range of 0.005-1.0 V.

The difference between CoSn_2 NPs and CoSn_2O_x NPs in terms of cycling stability might be attributed to the fact that CoSn_2O_x NPs are highly oxidized. The surface oxides are likely converted into Li_2O during the first cycle(s), which is also known to inhibit the sintering of Sn domains during cycling.²³¹ It should be noted that the average delithiation potentials for Sn NCs, CoSn_2 NPs, and CoSn_2O_x NPs are equally low, with an average value of $\sim 0.5 \text{ V}$ vs. Li^+/Li (Figures 5.6.b-d).

Apart from by the mechanical ball-milling of Co and Sn NPs, crystalline CoSn_2 NPs can also be synthesized by the same colloidal method as used herein to synthesize the pure Co and Sn NPs by simultaneous injection of $\text{SnCl}_2/\text{CoCl}_2$ into a solution of NaBH_4 in NMP. However, such a synthesis strategy suffers from an imbalance between the reactivities of the two metal chlorides. A high temperature of 150°C is necessary to reduce Co^{2+} , and the resulting CoSn_2 NPs are larger than 20 nm, which is significantly larger than the Co-Sn based NPs prepared by ball-milling (see Figure 5.8.).

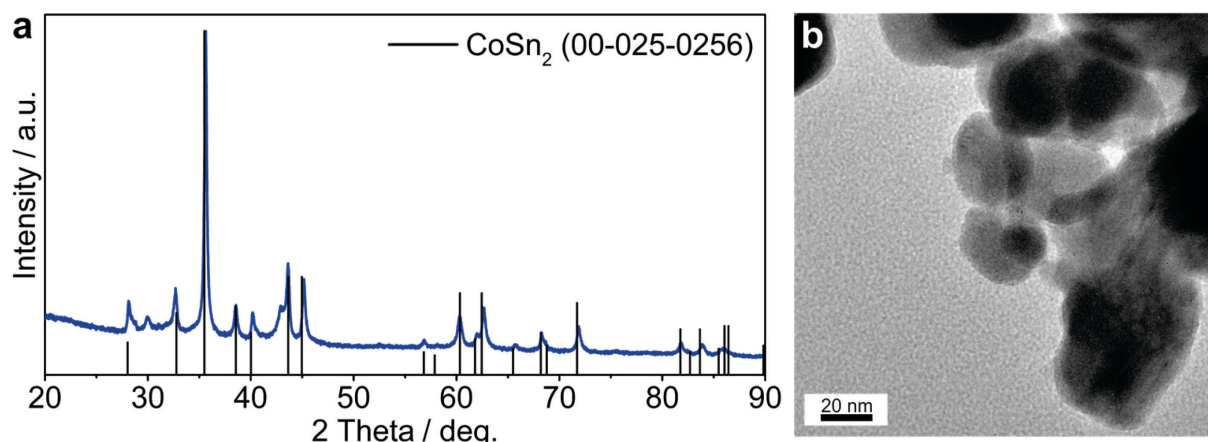


Figure 5.8. (a) XRD pattern and (b) TEM image of CoSn_2 NPs prepared by wet-chemical synthesis. The two unindexed peaks at 30° and 43° might correspond to SnO and CoO . For synthesizing CoSn_2 NPs wet-chemically SnCl_2 (1.33 mmol) and CoCl_2 (0.67 mmol) dissolved in NMP (3 mL) were injected into a solution of NaBH_4 in NMP (16 mmol in 17 mL) at 150°C and kept at this temperature for 1 hour.

Most likely as result of the larger size of colloiddally synthesized CoSn_2 NPs, much poorer capacity retention was observed: the capacity reduced to $< 200 \text{ mAh g}^{-1}$ after 100 cycles (see Figure 5.9.).

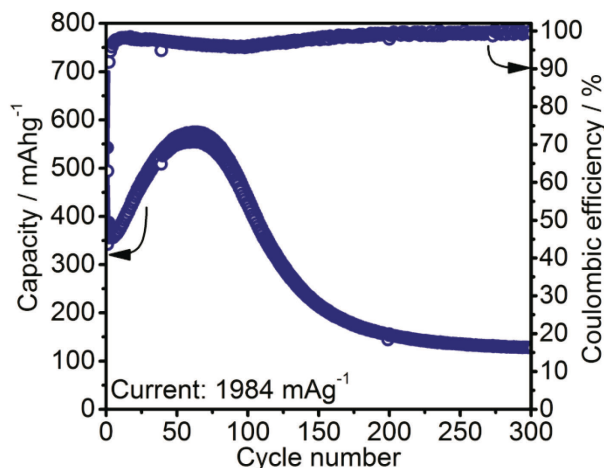


Figure 5.9. Cycling stability of CoSn_2 NPs prepared by wet-chemical synthesis in Li-ion half-cells using a current of 1984 mA g^{-1} in the potential range of 0.005-2.0 V.

To evaluate the rate capability of the Co-Sn based NPs developed in this work, galvanostatic cycling was performed at current rates between 0.2C to 10C (Figure 5.10., 1C = 992 mA g^{-1}). Due to the similar particle sizes of these systems, and therefore similar reaction kinetics in all cases comparable rate capabilities were observed. The only exception was at currents of 0.5C-2C where Sn NPs showed $\sim 50 \text{ mAh g}^{-1}$ lower capacities compared to CoSn_2 NPs. Even at rates as high as 10C, all three materials still retained a capacity of $\sim 350 \text{ mAh g}^{-1}$. Interestingly, it was observed that at such high currents, Li-ion capacities increased during cycling, resulting in the same or even higher capacities during the stepwise decrease of the rate back to 0.2C. Especially for CoSn_2O_x NPs, the slight difference in capacity compared to CoSn_2 NPs initially observed at rates of 0.5C-2C becomes fully diminished during cycling. For comparison, graphite is known to exhibit poorer rate capability,^{234, 235} which was confirmed in this work by control experiments using graphite anodes (TIMCAL) tested under identical conditions (Figure 5.10.b).

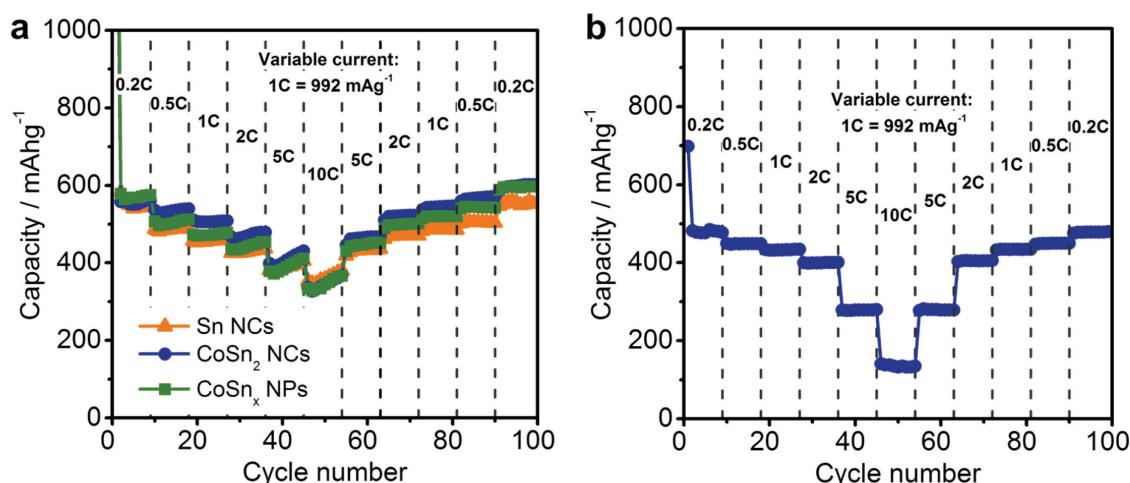


Figure 5.10. Rate capability tests for (a) Sn, CoSn_2 , and CoSn_2O_x NPs and (b) graphite in Li-ion half-cells within the potential range of 0.005-1.0 V.

Li-ion full-cell experiments. In order to investigate the applicability of Co-Sn-based NPs as anode materials for commercial batteries, anode-limited full-cells using LiCoO_2 as the cathode were assembled (Figure 5.11.). Based on the results of the half-cell experiments, CoSn_2O_x NPs were selected for primary investigation in full-cell experiments. Herein, all specific capacities and currents correspond to the mass of CoSn_2O_x NPs.

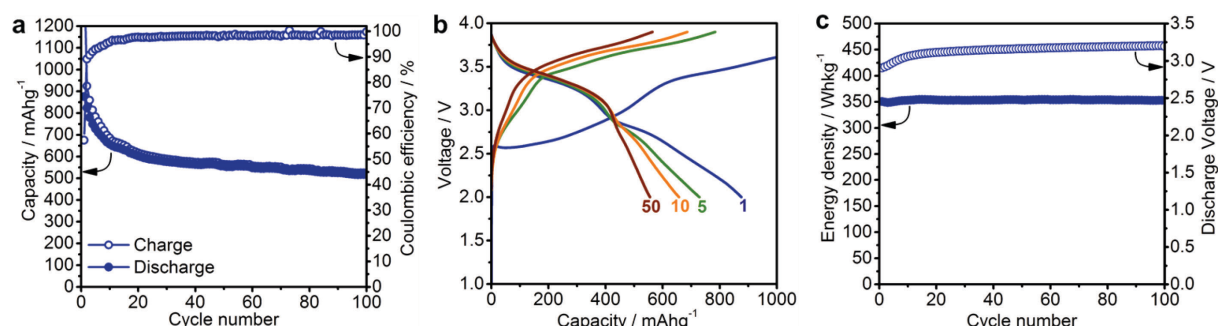


Figure 5.11. Electrochemical performance of a Li-ion full-cell battery with CoSn_2O_x NPs as the anode and LiCoO_2 as the cathode material. (a) Capacity retention and coulombic efficiency. (b) Galvanostatic charge/discharge curves. (c) Specific energy density and discharge voltage. Cells were cycled at a current of 500 mA g^{-1} in the potential range of 2.0-3.9 V. Specific capacities and currents correspond to the mass of CoSn_2O_x NPs.

Full-cells of $\text{CoSn}_2\text{O}_x/\text{LiCoO}_2$ were cycled galvanostatically at a current of 500 mA g^{-1} in the potential range of 2.0-3.9 V. Under such conditions, CoSn_2O_x NPs exhibit an average capacity of 576 mAh g^{-1} upon extended cycling, similar to the values observed in half-cell experiments. Neglecting the excess of cathode material used in this work, the theoretical charge storage capacity of the cell is estimated as 112.6 mAh g^{-1} based on: $C_{\text{cell}} = C_{\text{anode}} C_{\text{cathode}} / (C_{\text{anode}} + C_{\text{cathode}})$. Taking the average discharge voltage of 3.14 V into account, the resulting average specific energy density for the $\text{CoSn}_2\text{O}_x/\text{LiCoO}_2$ cell is

353 Wh kg⁻¹ and, most importantly, it remains stable at this value for 100 cycles. This specific energy density is comparable to that of the state-of-the-art graphite/LiCoO₂ system (~360 Wh kg⁻¹ based on 140 mAh g⁻¹/3.7 V vs. Li⁺/Li for LiCoO₂ and 372 mAh g⁻¹/0.15 V vs. Li⁺/Li for graphite).²³⁶ However, considering the much higher density of bulk β-Sn (7.3 g cm⁻³) and Co (8.9 g cm⁻³) compared to graphite (2.2 g cm⁻³), CoSn₂O_x NPs can theoretically exhibit improved volumetric energy densities by up to ~40%. In fact, for a large variety of portable electronic devices, the importance of volumetric energy density is greater than that of gravimetric energy density.²³⁷ For comparison, the improvement of the volumetric energy density of the Sony NexelionTM battery is 20% over identical cells using graphite anodes.²³⁸

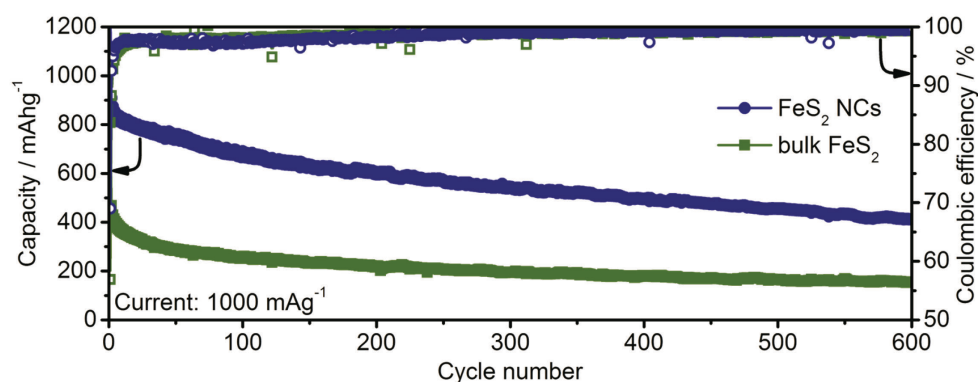
5.4. Conclusion

Co and Sn NPs with diameters of ≤ 10 nm were synthesized *via* the simple reduction of their respective chlorides using NaBH₄ in NMP, and were subsequently converted into intermetallic Co-Sn NPs by ball-milling. The resulting nanostructured materials can be seen as model systems suited for investigating the effects of crystallinity and composition on electrochemical properties upon lithiation/delithiation cycling. Despite the fact that Sn and CoSn₂ NPs show good cycling stability for several hundred cycles, CoSn₂O_x NPs show the most outstanding retention of capacity, losing only 8% of their initial capacity over 1500 cycles at 1984 mA g⁻¹. In addition, in Li-ion full-cell experiments with LiCoO₂ as the cathode material, CoSn₂O_x NPs provide capacities of on average 576 mAh g⁻¹ with an average discharge voltage of 3.14 V. This system therefore exhibits stable specific energy densities comparable to state-of-the-art LIBs based on graphite, and potentially much higher volumetric energy densities due to the higher density of CoSn₂O_x. Considering that high rates were used in both half- and full-cell experiments, the CoSn₂O_x NPs presented herein offer a potential improvement in power density over cells assembled using conventional graphite anodes and also over Sony's commercialized NexelionTM battery which has been designed specifically for low power (*e.g.*, camcorder) devices.²³⁸

Reproduced with modifications from:

M. Walter, S. Doswald, F. Krumeich, N. P. Stadie and M. V. Kovalenko. *Oxidized Co-Sn Nanoparticles as Long-Lasting Anode Materials for Lithium-Ion Batteries*. In preparation.

Chapter 6. Pyrite (FeS_2) nanocrystals as inexpensive high-performance Li-ion cathode and Na-ion anode materials



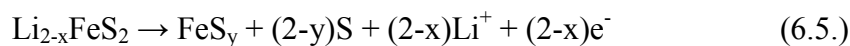
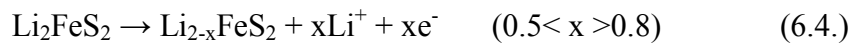
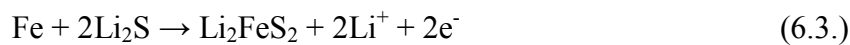
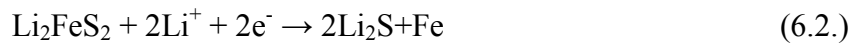
6.1. Introduction

High-performance batteries are increasingly needed for numerous applications such as portable electronics, electric cars or stationary storage systems in tandem with renewable sources of electrical energy.^{134, 177} Due to their high energy density Li-ion batteries (LIBs) are often considered the storage system of choice for such applications. However, in the light of limited abundance and the thereby constantly increasing costs of Li-salts, there is growing interest to develop conceptually identical Na-ion batteries (SIBs) as a potentially less expensive alternative for large-scale applications.^{23-25, 134} Importantly, technology transition from LIBs to SIBs will require not only a (rather obvious) replacement of Li-ions with Na-ions, but also choosing electrode materials composed exclusively of comparably abundant elements. Herein the attention is drawn to pyrite (FeS_2) as a promising low cost, non-toxic rechargeable electrode material for both LIBs and, for the first time, also for SIBs. The quest for new electrode materials is primarily driven by the need to increase the energy density. The latter, in turn, is a product of charge storage capacity and voltage of operation. FeS_2 has a high theoretical specific charge-storage capacity of 894 mAh g^{-1} , assuming full lithiation/sodiation forming $\text{Li}_2\text{S}/\text{Na}_2\text{S}+\text{Fe}$. With these appealing attributes, FeS_2 is already in use as cathode material in commercial primary (non-rechargeable) Li-ion cells produced, for instance, by Energizer®. Yet the development of secondary (rechargeable) LIBs with FeS_2 has been hampered by the poor reversibility of its lithiation/delithiation at room temperature. So far, only several reports have dealt with FeS_2 as a cathode material in

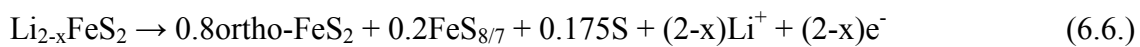
secondary LIBs.²³⁹⁻²⁵¹ For instance, Liu *et al.* demonstrated FeS₂ nanooctahedra with a capacity retention of 495 mAh g⁻¹ after 50 cycles at 0.5C-rate (1C is current density of 894 mA g⁻¹).²⁴⁸ Very little work has so far concerned mechanisms of room-temperature sodiation of FeS₂,²⁵²⁻²⁵⁵ and high-capacity Na-ion storage, at high current densities and long-cycling life are still to be demonstrated.

In this study the aim was to enhance the reaction kinetics and reversibility of Na-ion and Li-ion storage using nanostructured FeS₂. Starting with an inexpensive solution-phase chemical synthesis of nano-sized FeS₂ particles, the performance of nano-FeS₂ as LIB and SIB electrode material is systematically studied and compared to the results with bulk FeS₂. It is found that owing to shorter diffusion path lengths for both electrons and ions, the nanoscopic counterpart exhibits highly reversible insertion of Li- and Na-ions, with near theoretical capacities. The corresponding voltage profiles indicate that nano-FeS₂ has great potential as cathode material for LIBs and as anode material for SIBs. As LIB cathode, FeS₂ NCs exhibit outstanding capacities of 720 and 600 mAh g⁻¹ after 50 cycles at current densities of 200 or 1000 mA g⁻¹, respectively. Further, using FeS₂ NCs for the first time as anode material in SIBs, high cycling stability with capacities of > 500 mAh g⁻¹ for 400 cycles at a high current density of 1000 mA g⁻¹ are demonstrated, making FeS₂ NCs one of the best performing SIB anodes identified so far.

The mechanism of lithiation and delithiation of FeS₂ has been established as:^{247, 251}



More specifically, the final oxidation step was proposed to yield orthorhombic FeS₂ and pyrrhotite Fe₇S₈.²⁵⁶



6.2. Experimental section

Synthesis of FeS_2 NCs. FeS_2 NCs were synthesized by a modified procedure of the synthesis published by Li *et al.*²⁵⁷ FeCl_2 (6.7 mmol, 99.5%, ABCR) was added to oleylamine (160 mL, 80-90%, Acros) and the mixture was kept for 1 hour at 100 °C under vacuum. Then the flask was set under nitrogen, the temperature was increased to 120 °C and elemental sulfur (40 mmol, 99.998%, Sigma-Aldrich) previously dissolved in oleylamine (40 mL) was injected. The resulting black reaction mixture was subsequently heated to 220 °C and kept at this temperature for two hours. After two hours the reaction mixture was cooled to room temperature and the resulting material was washed with chloroform and ethanol. Typically, 0.8 g of FeS_2 NCs were obtained using this procedure corresponding to a relative yield of ca. 99%. The main difference to the procedure of Li *et al.* is in the upscaling of all quantities by a factor of 16. Further, the injection of the S-oleylamine solution was carried out at 120 °C, not at 100 °C, in order to obtain all FeS_2 NCs in 50-100 nm size range. For comparison, at 100 °C Li *et al.* obtained sizes of 150-250 nm.

Synthesis of CoS_2 and NiS_2 NCs. CoS_2 and NiS_2 NCs were synthesized using the same procedure as for FeS_2 NCs, but with CoCl_2 or NiCl_2 instead of FeCl_2 .

Synthesis of PbS NCs. PbS NCs of were provided by Dr. Loredana Protesescu (ETH Zurich/Empa).

Synthesis of SnS , CuS , ZnS and $\text{Cu}_2\text{ZnSnS}_4$ NCs. SnS , CuS , ZnS and $\text{Cu}_2\text{ZnSnS}_4$ NCs were synthesized according to literature-known procedures.²⁵⁸⁻²⁶¹

Electrode fabrication, cell assembly and electrochemical measurements. Prior to electrode preparation the insulating capping ligands were removed by stirring the respective metal sulfide NCs in a 1M solution of hydrazine in acetonitrile (ca. 1 mL per 2 mg sample) for two hours as commonly carried out for quantum dot solids.²⁶² After washing three times with acetonitrile (ca. 20 mL) materials were dried at room temperature for 12 hours under vacuum before electrode preparation. Electrodes were prepared by mixing the respective NC powders (64 wt%) with carbon black (21 wt%, Super C65, TIMCAL), carboxymethyl cellulose (15 wt%, Daicel FineChem Ltd.) and water using a Fritsch Pulverisette 7 planetary ball-mill (500 rpm, 1 hour). The resulting aqueous slurries were coated onto copper current collectors (9 μm , MTI Corporation) and dried for 12 hours at 80 °C under vacuum. Coin-type cells were assembled in an Ar-filled glove box ($\text{O}_2 < 0.1$ ppm, $\text{H}_2\text{O} < 0.1$ ppm) using polished elemental lithium or sodium as the counter and reference electrodes. Glass microfiber (GF/D, Whatman) was used as a separator. A solution of 1M NaClO_4 (98%, Alfa Aesar) in propylene carbonate (battery grade, BASF) with 10% fluoroethylene carbonate (battery grade, Hisunny

Chemical Co.) served as the electrolyte for Na-ion half-cells. For Li-ion half-cells as electrolyte 1M LiPF_6 in ethylene carbonate/dimethyl carbonate (1:1; Merck, battery grade) with 3% fluoroethylene carbonate was used. All galvanostatic cycling tests were carried out at room temperature on an MPG-2 multi-channel workstation (BioLogic). Specific capacities and currents were quantified with respect to the mass of metal sulfide respectively.

Materials characterization. TEM images were obtained with a Philips CM30 TEM microscope at 300 kV using carbon-coated Cu grids as substrates (Ted-Pella). SEM was performed using a NanoSEM 230. Powder XRD was measured on a STOE STADI P powder X-ray diffractometer ($\text{Cu-K}\alpha_1$ irradiation, $\lambda = 1.540598 \text{ \AA}$). Attenuated total reflectance Fourier transform infrared spectroscopy (ATR-FTIR) measurements were carried out on a Nicolet iS5 FTIR spectrometer (Thermo Scientific). For *ex-situ* XRD measurements half-cells were transferred to and opened in an Ar-filled glovebox. The electrode material was removed carefully from the current collector and enclosed between two stripes of adhesive tape.

6.3. Results and discussion

FeS_2 NCs were prepared *via* adaptation of the synthesis proposed by Li *et al.*²⁵⁷ In short, FeCl_2 and elemental S were mixed at 120 °C in oleylamine (OLA), acting as both solvent and surfactant, and reacted at 220 °C for two hours delivering highly crystalline 50-100 nm large FeS_2 NCs (Figure 6.1.) with high reaction yield (99%). No traces of unreacted reagents, marcasite FeS_2 or other iron sulfides of different stoichiometry (FeS or Fe_3S_4) could be detected. Moreover, no traces of oxides were observed, indicating that FeS_2 NCs can be readily handled in air. Based on the low-cost, inexpensive and environmentally benign precursors, scalable heating-up reaction, and recyclable coordinating solvent (OLA), this synthesis can be readily implemented on industrial scale as well.

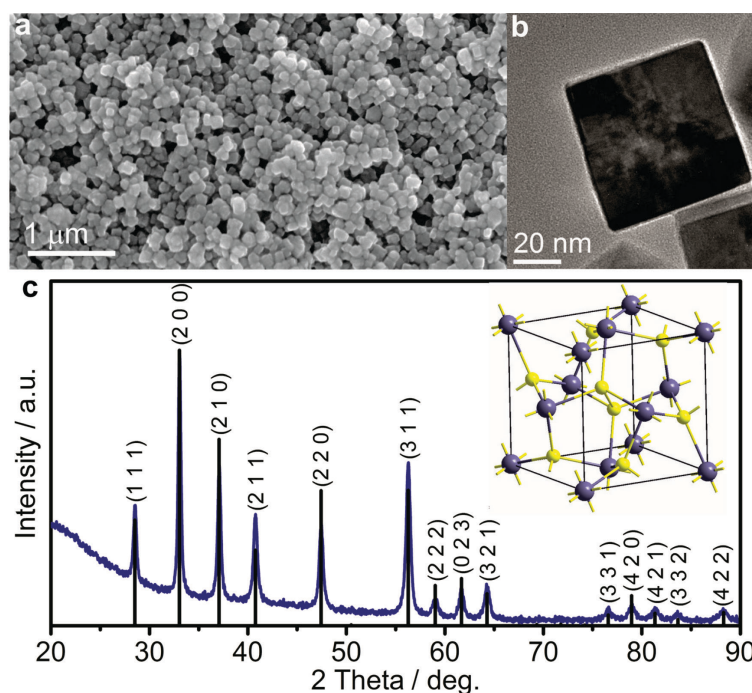


Figure 6.1. Synthesis and characterization of FeS_2 NCs: (a) SEM and (b) TEM images. (c) X-ray diffraction (XRD) pattern indexed to pure-phase pyrite FeS_2 (ICDD database, PDF no.: 00-071-2219; space group $N205$, $Pa3$, $a = 5.4179 \text{ \AA}$) with the schematic representation of the unit cell of pyrite FeS_2 as inset.

The electrochemical properties of the as-synthesized FeS_2 NCs were investigated in air-tight coin type half-cells using either elemental lithium or sodium as both counter- and reference electrodes. The remaining surface-bound OLA molecules were removed from the NC surface by treatment with hydrazine, as commonly applied for colloidal quantum dots for improving their electronic connectivity.²⁶² The removal of ligands was confirmed by ATR-FTIR spectroscopy (Figure 6.2.).

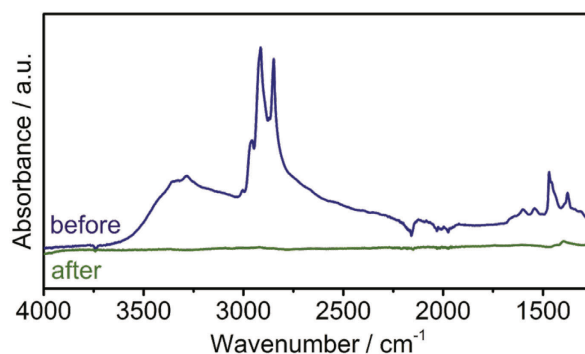


Figure 6.2. ATR-FTIR spectra of FeS_2 NCs before and after hydrazine treatment.

It should be noted that no changes of the XRD pattern were observed upon removal of residual OLA ligands and after electrode preparation (Figure 6.3.). All electrodes containing FeS_2 NCs were prepared by mixing the active material (64 wt%) with carbon black (CB, 21%) as conductive additive and with carboxymethyl cellulose (CMC, 15%) as a binder,

forming a homogeneous aqueous slurry which was coated onto Cu-foil and dried. Fluoroethylene carbonate (FEC) was added to the electrolyte to improve the cycling stability.^{163, 186, 187}

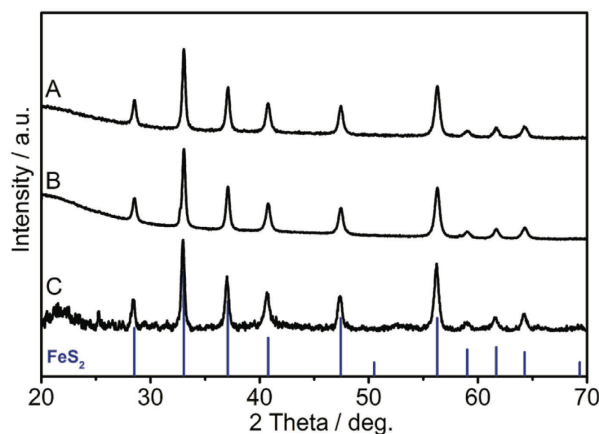


Figure 6.3. XRD pattern of (A) pristine FeS_2 NCs, (B) FeS_2 NCs after ligand removal and (C) electrodes containing FeS_2 NCs (indexed to pure-phase pyrite FeS_2 , ICDD database, PDF no.: 00-071-2219; space group $N205$, $Pa\bar{3}$, $a = 5.4179 \text{ \AA}$).

The results for measurements of FeS_2 NCs as cathode material in Li-ion half cells are shown in Figure 6.4.. Cells were initially discharged to 0.02 V and then cycled in the potential range between 1.0-3.0 V vs. Li^+/Li . The capacities above the theoretical value for the first cycle can be explained by the irreversible formation of the solid electrolyte interface (SEI), seen also as low coulombic efficiency (CE), that is the ratio between charge and discharge capacity, of 75% in the first cycle. Upon subsequent cycling at 200 mA g^{-1} FeS_2 NCs deliver initial capacities close to the theoretical maximum with 800 mAh g^{-1} and show only minor capacity fading during cycling (Figure 6.4.a). Namely, after 100 cycles of charging/discharging FeS_2 NCs still deliver 630 mAh g^{-1} corresponding to capacity retention of 80%. In contrast, bulk FeS_2 shows both significantly lower initial capacities and much faster fading. Despite the fact that the average lithiation potential for FeS_2 NCs is moderately low – 1.73 V (for 1.0-3.0 V range, Figure 6.4.c) or 2.0 V (for 1.5-3.0 V range) – the high capacities result in energy densities more than twice higher than of commercially established LiCoO_2 or LiFePO_4 (Figure 6.4.b, Table 6.1.).

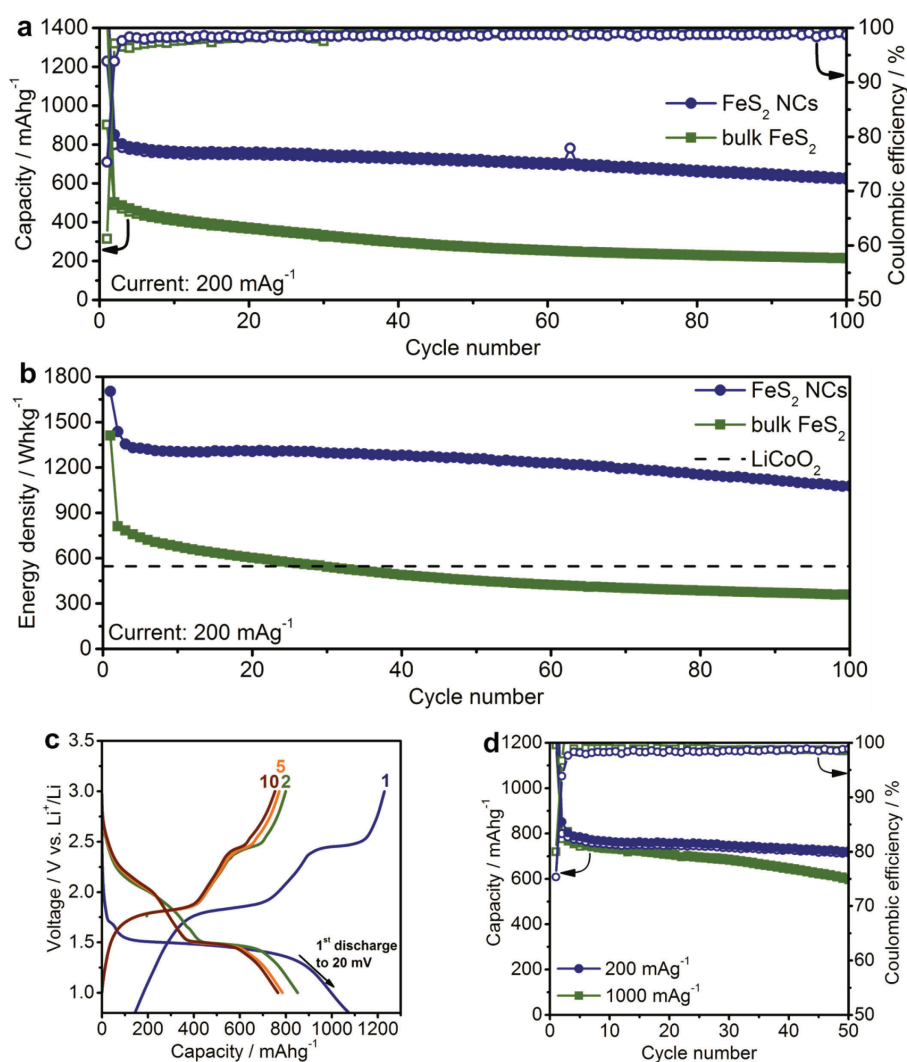


Figure 6.4. Electrochemical performance of FeS_2 NCs tested as cathode material for LIBs. (a) Capacity retention for FeS_2 NCs and bulk FeS_2 . (b) Comparison of the energy density of FeS_2 NCs, bulk FeS_2 and LiCoO_2 . (c) Galvanostatic charge and discharge curves for FeS_2 NCs corresponding to the graph in (a). All cells were cycled with a current rate of 200 mA g^{-1} . (d) Capacity retention for FeS_2 NCs cycled at 1000 or 200 mA g^{-1} . All batteries were measured in the 1.0–3.0 V potential range after initial discharge to 0.02 V. 1M LiPF_6 in a 1 : 1 mixture of ethylene carbonate (EC) and dimethyl carbonate (DMC) with 3% fluoroethylene carbonate (FEC) served as electrolyte for Li-ion half cells.

Table 6.1. Comparison of Li-ion cathodic performance of FeS_2 NCs, with commercial LiCoO_2 and LiFePO_4 materials. Energy density is calculated as product of the specific capacity and average voltage during discharge. For Li-ion full cells the lack of Li in FeS_2 might be compensated by either electrochemical prelithiation of the material or using Li-containing anode materials.²⁶³

Material	Capacity (mAh g^{-1})	Potential (V vs. Li^+/Li)	Energy density (Wh kg^{-1})
FeS_2 NCs	715 (397)	1.73 (2.0)	1237 (794)
LiCoO_2	140	3.9	546
LiFePO_4	170	3.4	578

Even when the current is increased to 1000 mA g^{-1} , more than 600 mAh g^{-1} can be retained for 50 cycles (Figure 6.4.d). At all current rates CE is $\geq 99\%$. This excellent performance in terms of obtaining high capacities at high currents is unprecedented for FeS_2 as cathode in LIBs (for detailed comparison with literature, see Table 6.2.).

Table 6.2. Li-ion cathodic performance of FeS_2 NCs: Comparison of the electrochemical performance of the herein presented FeS_2 NCs with previously reported results by others.

Cathode	Current density (mA g^{-1})	Initial capacity (mAh g^{-1})	Retained capacity (mAh g^{-1})	Cycle number	Reference
FeS_2 NCs	200	800	720	50	Present work
	200	800	630	100	
	1000	800	600	50	
PAN- FeS_2	89.4	729	470	50	²⁵¹
submicron FeS_2	89.4	~600	420	30	²⁴⁶
FeS_2 nanowires	89.4	~400	350	50	²⁴⁷
FeS_2 @C porous nanooctahedra	447	550	495	50	²⁴⁸

Contrary to LIBs, cycling of FeS_2 NCs as cathode material in Na-ion half cells delivers only approximately half the expected capacity and suffers from both faster capacity fading and poorer coulombic efficiency with values ranging from 98 to 96% (Figure 6.5.). Although the performance of such FeS_2 NCs as cathode for SIBs is still superior to previous reports (for detailed comparison with literature, see Table 6.3.),²⁵²⁻²⁵⁵ it shows a drastic difference between Li-ion and Na-ion chemistries.

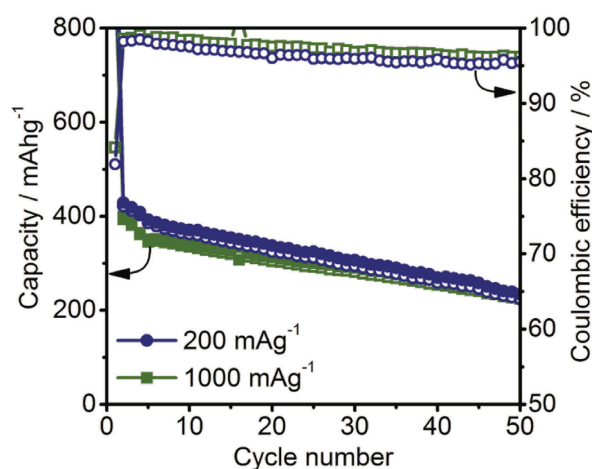


Figure 6.5. Capacity retention for FeS_2 NCs in Na-ion half cells. Cells were cycled in the potential range 1.0-3.0 V, except for the first discharge to 0.02 V.

Table 6.3. Na-ion cathodic performance of FeS_2 NCs: Comparison of the electrochemical performance of the herein presented FeS_2 NCs with previously reported results by others.

Cathode	Current density (mA g^{-1})	Initial capacity (mAh g^{-1})	Retained capacity (mAh g^{-1})	Cycle number	Reference
FeS_2 NCs	200	430	240	50	Present work
	1000	400	240	50	
FeS_2	40	~500	~350	9	²⁵⁵
FeS_2	50	~280	~70	50	²⁵³
FeS_2	50	~450	~85	50	²⁵²

Considering that in case of Na-ion cells a much higher fraction of the charge storage capacity is gained at lower potentials (Figure 6.6.b), galvanostatic cycling measurements in the range 0.02-2.5 V were carried out to analyze the applicability of FeS_2 NCs as an anode material. In particular, it is found that FeS_2 NCs deliver capacities of 600 mAh g^{-1} after 200 cycles at a relatively high current of 1000 mA g^{-1} , and capacity of 500 mAh g^{-1} after 400 cycles (Figure 6.6.a). After 600 cycles, FeS_2 NCs still deliver capacities of 410 mAh g^{-1} , corresponding to 50% of the initial capacity. In contrast electrodes composed of bulk FeS_2 show much lower capacities, presumably due to slower reaction kinetics. Furthermore, for FeS_2 NCs the CE increases from approximately 97% for the first 100 cycles to an average of 99% for the subsequent cycles demonstrating good reversibility of Na-ion storage. Addition of FEC to the electrolyte was found to be crucial, since cells without FEC showed extremely poor CE of 95-83% (Figure 6.6.c). Moreover, cycling tests with limitation of the charge capacity to 500 mAh g^{-1} were carried out to restrict the desodiation to lower potentials, which is a preferred scenario for the full cell as it will retain largest possible potential difference between the cathode and anode and hence the energy density. No capacity fading was observed for 500 cycles at current density of 1000 mA g^{-1} (Figure 6.6.e).

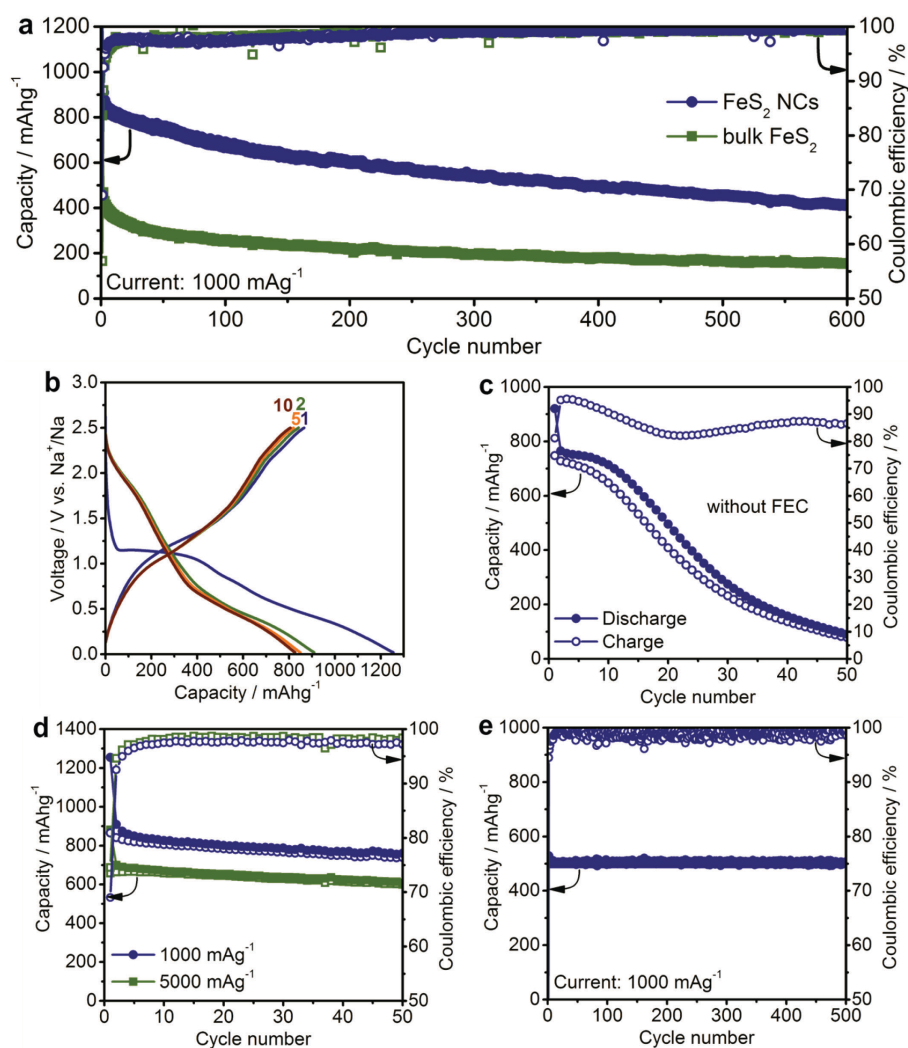


Figure 6.6. Electrochemical performance of FeS_2 NCs tested as anode material for SIBs. (a) Capacity retention for FeS_2 NCs and bulk FeS_2 . (b) Galvanostatic charge and discharge curves for FeS_2 NCs corresponding to the graph in (a). (c) Capacity retention for FeS_2 NCs cycled with the same conditions as in (a) but without the addition of FEC to the electrolyte. (d) Capacity retention for FeS_2 NCs cycled with 5000 or 1000 mA g^{-1} . (e) Capacity retention for FeS_2 NCs cycled with limitation of the charge capacity to 500 mAh g^{-1} . All batteries were measured in the 0.02-2.5 V potential range at a current of 1000 mA g^{-1} unless noted otherwise. 1M NaClO_4 in propylene carbonate (PC) with 10% fluoroethylene carbonate (FEC) served as electrolyte in Na-ion half-cells.

In addition, electrodes with FeS_2 NCs can be cycled with a current as high as 5000 mA g^{-1} and still deliver capacities above 600 mAh g^{-1} for at least 50 cycles corresponding to a retention of 86% of the initial capacity (Figure 6.6.d).

To elucidate the phase evolution during sodiation and desodiation of FeS_2 , *ex-situ* XRD measurements were carried out (Figure 6.7.) at various stages of electrochemical cycling. Starting from the pristine pyrite structure of FeS_2 , no intermediate crystalline phases were observed and no crystalline FeS_2 was restored during charging. It is a possibility that crystalline intermediate phases exist, but cannot be detected due to very small crystallite domain size in the nanometer range.

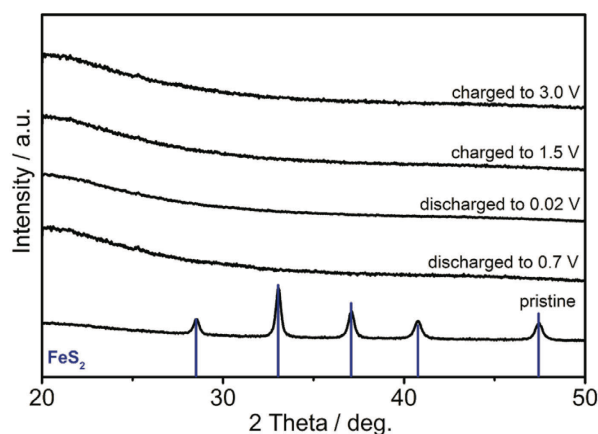
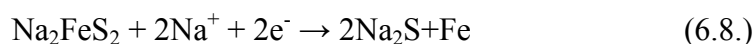


Figure 6.7. Ex-situ XRD measurements for the first discharge and charge cycle of FeS₂ NCs in Na-ion half-cells. Cells were cycled with a current of 200 mA g⁻¹.

Based on the observed capacities close to the theoretical value of 894 mAh g⁻¹ and the aforementioned reports it is assumed that the sodiation of FeS₂ NCs leads to the formation of Na₂S involving most likely only amorphous phases according to the following mechanism:



Amorphous state during cycling may explain the apparently low kinetic restraints for fast charging/discharging and reduced mechanical stress upon expansion and contraction, similarly to the earlier observations with Sb NCs as Na-ion anode material.⁵⁷

The performance of FeS₂ compares very favorably with other metal sulfides reported up to date (for detailed comparison with literature, see Table 6.4.).

Table 6.4. Comparison of the electrochemical performance of the herein presented FeS_2 NCs with previously reported results obtained with metal sulfides as anode in SIBs.

Anode	Current density (mA g^{-1})	Initial capacity (mAh g^{-1})	Retained capacity (mAh g^{-1})	Cycle number	Reference
FeS_2 NCs	1000	820	606	200	Present work
	1000	820	500	400	
	1000	820	410	600	
	5000	700	530	100	
MoS_2 nanosheets	20	~160	~160	100	91
MoS_2/rGO	25	~250	~220	25	92
MoS_2 nanoflowers	50	~230	~350	300	99
	200	~220	~310	600	
	1000	~220	~300	1500	
nano $\text{MoS}_2\text{-C}$	1000	854	484	100	94
nano $\text{TiO}_2\text{-MoS}_2$	100	740	474	30	29
WS_2 @graphene	20	~584	329	500	95
SnS	125	~520	370	30	96
Nano SnS-C	100	486	548	80	97
SnS @graphene	810	~500	492	250	98
$\text{SnS}_2\text{-rGO}$	1000	594	500	400	99
$\text{rGO/Sb}_2\text{S}_3$	50	670	~637	50	100

For the sake of fully objective and unbiased comparison, colloidal NCs of a vast variety of prime metal sulfide candidates for Na-ion storage, composed of earth-abundant elements, such as NiS_2 , CoS_2 , PbS , SnS , CuS , ZnS and $\text{Cu}_2\text{ZnSnS}_4$ were synthesized and carefully studied under identical testing conditions (Figures 6.8., 6.9. and 6.10., see also Experimental Section).

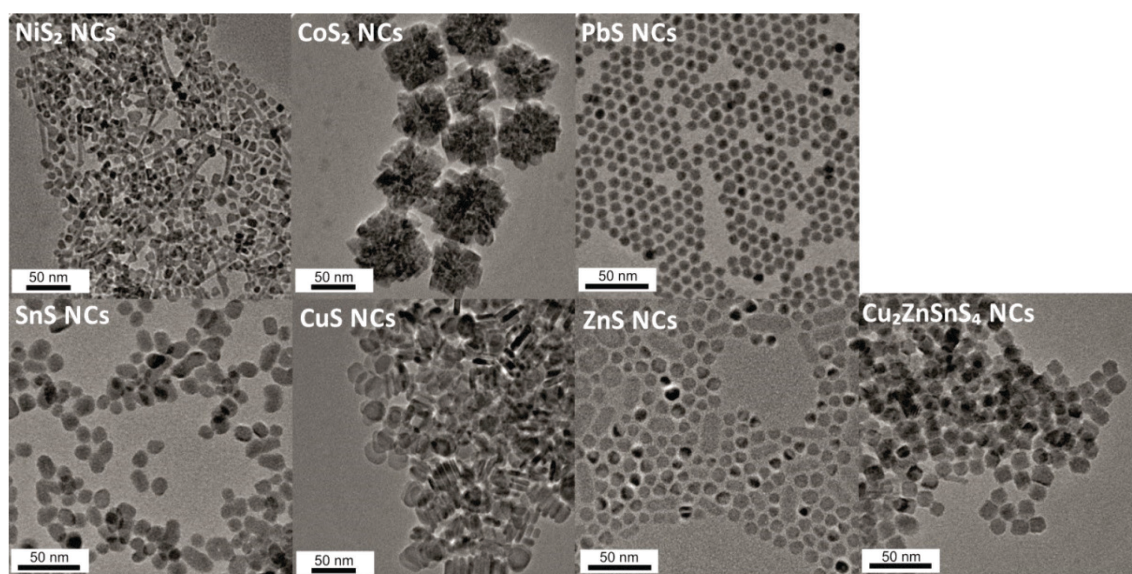


Figure 6.8. TEM-images of various metal sulfide NCs tested as Na-ion anode materials.

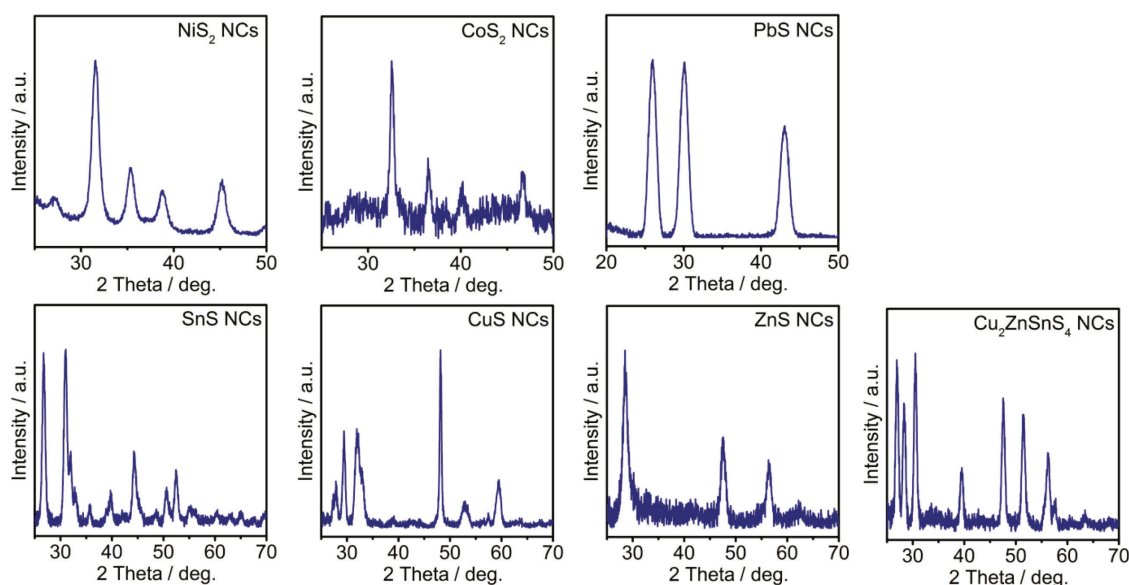


Figure 6.9. XRD patterns of various metal sulfide NCs tested as Na-ion anode materials.

With the exception of SnS all of these sulfides had not been previously tested for Na-ion storage, judging from the available literature. Clearly, in comparison with all these sulfides, FeS_2 shows both higher initial capacity and better long-term cycling stability.

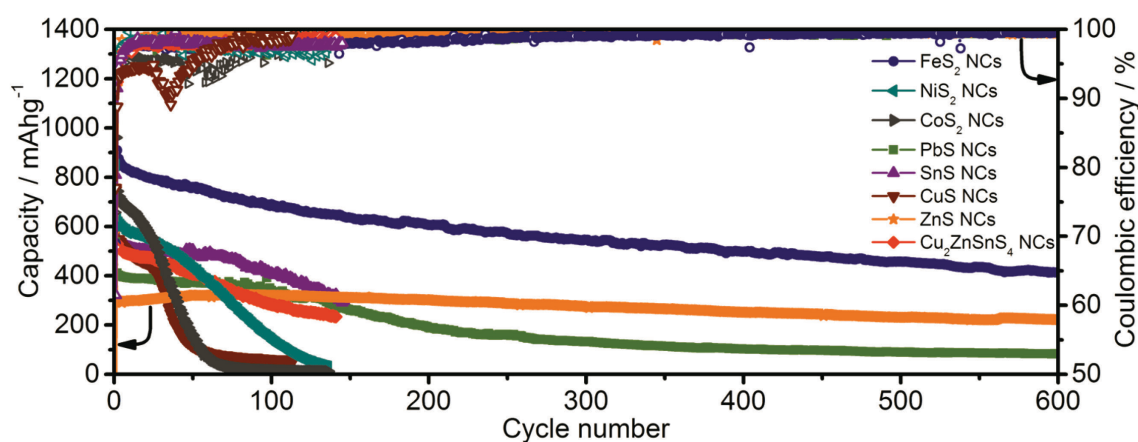


Figure 6.10. Electrochemical performance of various metal sulfide NCs tested as anode material for SIBs. All batteries were measured in the 0.02-2.5 V potential range at a constant current of 1000 mA g^{-1} . 1M NaClO_4 in propylene carbonate (PC) with addition of 10 wt% of fluoroethylene carbonate (FEC) served as electrolyte.

6.4. Conclusion

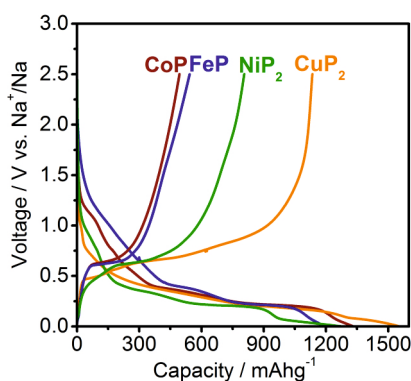
In conclusion, the great potential of FeS_2 NCs as inexpensive, environmentally benign and, most importantly, high-energy-density and long-cycling electrode material for LIB cathodes and SIB anodes was demonstrated, outperforming bulk FeS_2 and other metal chalcogenide NCs under identical testing conditions. Cathodic Li-ion storage by FeS_2 NCs is characterized by high specific capacity of $\geq 630 \text{ mAh g}^{-1}$ for 100 cycles (at a current

of 200 mA g^{-1}), delivering more than twice the energy density of LiCoO_2 or LiFePO_4 . Anodic Na-ion storage exhibits even better overall performance, with capacities of $\geq 500 \text{ mAh g}^{-1}$ retained after 400 cycles at a current density of 1000 mA g^{-1} . It should be noted that very standard, thus possibly suboptimal for nanostructures, testing conditions were used in terms of selected binder, electrolytes and (most simple) electrode formulation. Future work on FeS_2 as electrode material should focus on smart electrode engineering, involving recent specific for alloying or conversion nanostructured anodes developments such as design of three-dimensional nanoarchitectures or elaborate encapsulation of nanoparticles into conductive carbons.²⁶⁴⁻²⁶⁸

Reproduced with modifications from:

M. Walter, T. Zünd and M. V. Kovalenko. *Pyrite (FeS_2) nanocrystals as inexpensive high-performance lithium-ion cathode and sodium-ion anode materials*. *Nanoscale*, **2015**, 7, 9158 - 9163. Published by The Royal Society of Chemistry.

Chapter 7. Evaluation of metal phosphide nanocrystals as anode materials for Na-ion batteries



7.1. Introduction

Li-ion batteries (LIBs) have become the battery technology of choice for applications demanding high energy and power densities, such as portable electronics and mobile vehicles, and also show great promise for the large-scale grid storage of electricity. Yet, the irregular geographic distribution and relatively low natural abundance of lithium salts raise doubts as to the future security and cost of supply. In this regard, conceptually identical Na-ion batteries (SIBs) are a favorable alternative due to the much greater abundance (by a factor of 10^3) and therefore lower price of sodium salts.^{23-25, 134, 269} However, the seemingly simple replacement of the Li-ion with its 50% larger group I neighbor has drastic consequences for the resulting electrochemistry. For instance, both silicon and graphite, which are well-known anode materials with outstanding Li-ion storage properties, show negligible capacities for Na-ions.^{80, 81, 270} Extensive research toward new electrode materials is needed to advance the development of high-performance SIBs.

Of all possible anode materials for SIBs, red phosphorus (P) is probably the most appealing candidate due to its low cost, non-toxicity and, most importantly, extremely high sodium capacity (2596 mAh g⁻¹ for $P \leftrightarrow Na_3P$, one of the highest Na-ion capacities known) at a low desodiation potential (~ 0.6 V vs. Na⁺/Na). However, similarly to other alloying/conversion type materials, P suffers from massive volume changes during sodiation/desodiation ($\Delta V = 291\%$, by molar volume) leading to the mechanical disintegration

of the electrodes and therefore rapid capacity fading due to loss of electrical contact. The other main disadvantage of P is its relatively low electronic conductivity, causing slow reaction kinetics. Although noticeable progress has been demonstrated for P-based SIB anodes,^{26-28, 76, 146, 271} typically very large amounts of conductive carbons are used to provide sufficient conductivity as well as mechanical stability of the electrodes, and often high capacities with good cycling stability can only be achieved at low charge/discharge currents of $< 100 \text{ mA g}^{-1}$ ($< 0.05C$).

This study was motivated by the possibility of addressing the aforementioned issues facing P-based SIB anodes by using metal phosphide nanocrystals (NCs) as the active material. Generally, nanostructured materials often show improved electrochemical performance over their bulk counterparts due to mitigation of the effects caused by volumetric changes and improved ionic and electronic conductivities upon homogeneous mixing with conductive carbon additives.^{16, 19, 54, 56-58, 63-66} Moreover, metallic inclusions, which form *in-situ* upon electrochemical conversion of the transition metal phosphide to alkali metal phosphide, are also expected to improve the electronic connectivity within the electrode. Despite the additional mass of the transition metal, theoretical specific charge-storage capacities of metal phosphides are still extremely high ($900\text{-}1300 \text{ mAh g}^{-1}$), surpassing all of the main alternatives to P such as Sn (847 mAh g^{-1}) and Sb (660 mAh g^{-1}). Herein, the sodium and also lithium storage properties of highly uniform FeP, CoP, NiP₂ and CuP₂ NCs prepared *via* colloidal synthesis methods are presented. It should be noted that, with the exception of a previous study on FeP,¹⁰¹ the work presented in this chapter was the first report on the electrochemical performance of such metal phosphides in SIBs. All of the phosphide NCs investigated in this chapter show high charge-storage capacities, close to the theoretically expected values. In comparison to the corresponding metal sulphide NCs, the phosphides exhibit lower desodiation potentials and are hence better suited as SIB anode materials, but suffer from very fast capacity loss upon cycling. Further work on the optimized formulation of the electrodes and the selection of suitable electrolytes and electrolyte additives is needed to improve long-term cycling stability.

7.2. Experimental section

Synthesis of FeP nanowires (NWs). In a typical experiment, 2.5 g tri-n-octylphosphine oxide (TOPO, 99%, Strem) and 3 mL tri-n-octylphosphine (TOP, $\geq 97\%$, Strem), previously dried at 100 °C under vacuum for 1 hour, were heated to 300 °C under Ar. At 300 °C, 0.5 mL of Fe stock solution, prepared by mixing 1 mL TOP and 0.25 mL $\text{Fe}(\text{CO})_5$ (99.99%, Strem), was injected into the TOP/TOPO mixture. After 30 min, a second injection of 0.5 mL of stock solution was carried out. The reaction was stopped after an additional 30 min. FeP NWs were precipitated by adding hexane and ethanol, separated by centrifugation, and re-dispersed in chloroform containing 1 wt% oleic acid. The second precipitation was induced by adding ethanol. After centrifugation, the FeP nanowires were re-dispersed in chloroform and stored under ambient conditions.

Synthesis of NiP_2 NCs. In a typical experiment, 4.5 mL octadecene (ODE, 90%, Sigma-Aldrich), 6.4 mL oleylamine (OLA, 95%, Strem) and 0.25 g (1 mmol) nickel (II) acetylacetonate ($\geq 98\%$, Merck) were dried at 110 °C under vacuum for 1 hour to remove water and low-boiling point impurities. Then, 2 mL of TOP were added to the flask under Ar and the reaction mixture was heated to 320 °C and held at this temperature for 1 hour. The flask was cooled to 200 °C by flowing air and then 105 mg (3.4 mmol) of red phosphorous ($\geq 97\%$, Sigma-Aldrich) were added. The reaction mixture was then heated again to 330 °C and held at this temperature for 22 hours. NiP_2 NCs were precipitated twice by adding chloroform and ethanol, separated by centrifugation, and re-dispersed again in chloroform. After centrifugation, the NiP_2 NPs were re-dispersed in chloroform and stored under ambient conditions.

Synthesis of CoP NCs. In a typical experiment, 4.5 mL ODE, 6.4 mL OLA and 0.25 g (1 mmol) cobalt (II) acetylacetonate ($\geq 98\%$, Merck) were dried at 110 °C under vacuum for 1 hour to remove water and low-boiling point impurities. Then, 2 mL of TOP were added to the flask under Ar and the reaction mixture was heated to 320 °C for 65 min. The flask was cooled to 200 °C by flowing air and then 105 mg (3.4 mmol) of red phosphorous were added. Then the reaction mixture was heated again to 330 °C and held at this temperature for 22 hours. CoP NCs were isolated and purified identically to the NiP_2 NCs above.

Synthesis of CuP_2 NCs. In a typical experiment, 4.5 mL ODE, 6.4 mL OLA and 0.262 g (1 mmol) copper (II) acetylacetonate ($\geq 97\%$, Sigma-Aldrich) were dried at 110 °C under vacuum for 1 hour to remove water and low-boiling point impurities. Then, 2 mL of TOP were added to the flask under Ar atmosphere and the reaction mixture was heated to 320 °C for 75 min. The flask was cooled to 200 °C by flowing air and then 200 mg (6.4 mmol) of red

phosphorous were added. The reaction mixture was then heated again to 330 °C and was held at this temperature for 22 hours. CuP₂ NCs were isolated and purified identically to the NiP₂ NCs above.

Electrode preparation, cell assembly and electrochemical measurements. In order to evaluate the electrochemical properties of FeP, CoP, NiP₂ and CuP₂ NCs, Na-ion and Li-ion half-cells were assembled. Prior to electrode preparation, organic ligands were removed from the surface of the NCs by stirring them in a 1M solution of hydrazine in acetonitrile for 2 hours at room temperature, as is commonly performed for colloidal quantum dots.²⁶² Electrodes were prepared by mixing the respective metal phosphide NCs (63.75 wt%) with carbon black (21.25 wt%, TIMCAL), carboxymethyl cellulose (CMC, 15 wt%) and water as a solvent using a planetary ball-mill at 500 rpm for 1 hour. The aqueous slurries were coated onto Cu current collectors, which were dried at 80 °C under vacuum overnight prior to cell assembly. For electrochemical testing, coin cells with elemental Na or Li were assembled in an Ar-filled glovebox (O₂ < 0.1 ppm, H₂O < 0.1 ppm) using either 1M NaClO₄ in propylene carbonate (PC) with 10% fluoroethylene carbonate (FEC) or 1M LiPF₆ in a 1:1 mixture of ethylene carbonate (EC) and dimethyl carbonate (DMC) with 3% FEC. FEC was added to the electrolyte in both the Li and Na coin cells to improve capacity retention.^{146, 163, 186, 187, 272} All electrochemical tests were carried out at room temperature and the capacities were reported relative to the mass of the metal phosphide NCs.

Materials Characterization. Transmission electron microscopy (TEM) was performed using a JEOL JEM-2200FS instrument operated at 200 kV, using carbon-coated Cu grids as substrates (Ted-Pella). Powder X-ray diffraction (XRD) was measured using a STOE STADI P diffractometer (with Cu-Kα₁ irradiation, $\lambda = 1.540598$ Å).

7.3. Results and discussion

Synthesis and characterization of metal phosphide nanocrystals. FeP NWs were synthesized according to the procedure reported by Qian *et al.*²⁷³ In order to obtain NiP₂ NCs, a two-step procedure was developed. First, Ni₂P NCs were synthesized according to a known protocol reported by Popczun *et al.*²⁷⁴ A second step was added to the procedure: conversion of the as-prepared Ni₂P NCs into NiP₂ NCs by adding red P to the reaction mixture, followed by heating at 330 °C for 22 hours. Analogously, this two-step approach was also applied in the synthesis of CuP₂ and CoP NCs, simply by replacing nickel (II) acetylacetonate with the respective copper or cobalt salt (for details, see the Experimental Section). Figure 7.1. summarizes the characterization of the metal phosphide NCs obtained by these methods.

FeP NCs were on average ~ 300 nm in length and ~ 7 nm in width. CoP, NiP₂ and CuP₂ NCs exhibited diameters of 25, 10 and 60 nm, respectively. All materials showed phase-pure XRD patterns, indexed according to the standard ICSD files for these compounds.

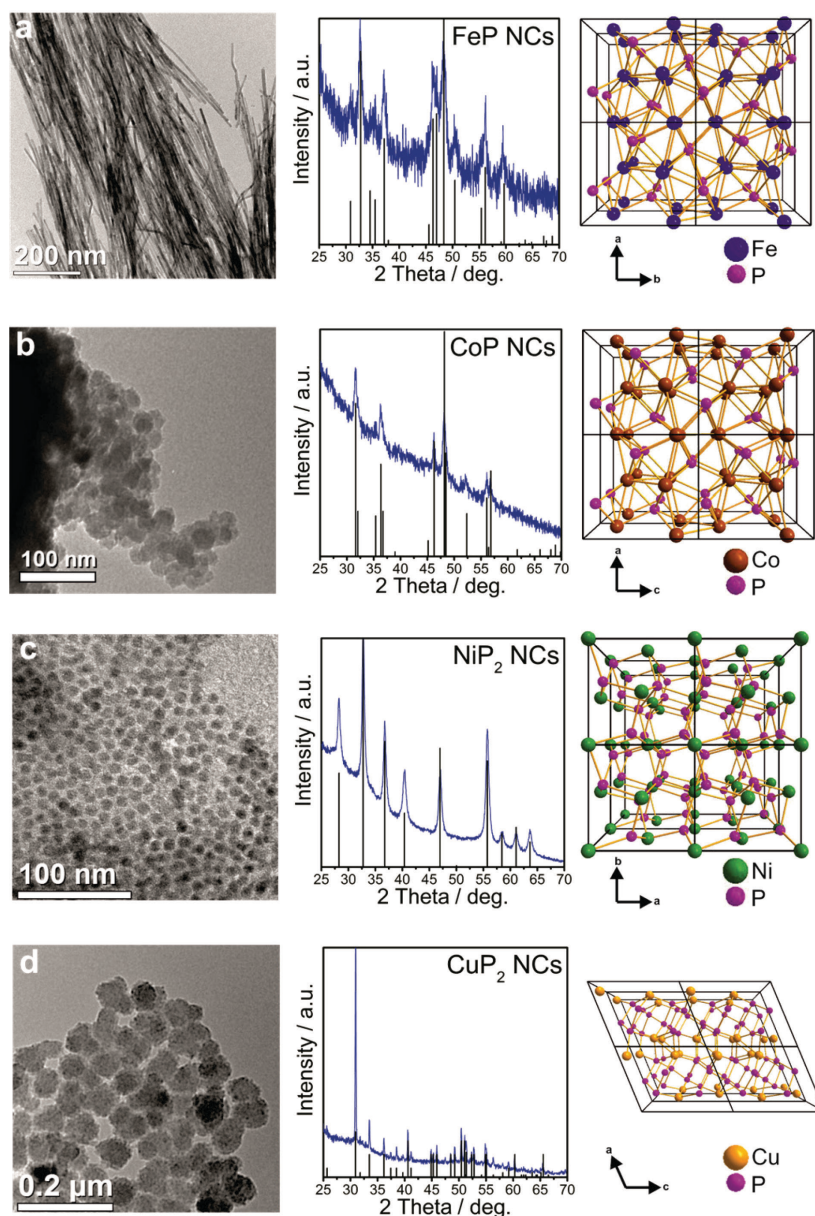


Figure 7.1. Characterization of metal phosphide NCs. Transmission electron microscopy (TEM) images, X-ray diffraction (XRD) patterns and schematic representations of the crystal structures (from left to right) of FeP, CoP, NiP₂ and CuP₂ NCs (a-d). The XRD patterns are indexed according to the ICSD database: to orthorhombic FeP (PDF No.: 00-071-2262, space group $Pna2_1$ (33), $a = 5.193$ Å, $b = 5.792$ Å, $c = 3.099$ Å), orthorhombic CoP (PDF No.: 00-029-0497, space group $Pnma$ (62), $a = 5.077$ Å, $b = 3.281$ Å, $c = 5.587$ Å), cubic NiP₂ (PDF No.: 00-073-0436, space group $Pa\bar{3}$ (205), $a = 5.4706$ Å) and monoclinic CuP₂ (PDF No.: 00-076-1190, space group $P2_1/c$ (14), $a = 5.8004$ Å, $b = 4.8063$ Å, $c = 7.5263$ Å, $\beta = 112.7^\circ$).

Electrochemical performance of metal phosphide nanocrystals. Figure 7.2. shows the electrochemical performance of the metal phosphide NCs in Na-ion and Li-ion half-cells. Na-ion cells were cycled at a current rate of 100 mA g⁻¹ in the potential range of 0.02-2.5 V.

For Li-ion cells, current rates of 300 mA g^{-1} and a potential range of 0.02-2.0 V were used. Assuming the formation of Na_3P or Li_3P via the general conversion reaction $\text{MP}_x + 3\text{x e}^- + 3\text{x A}^+ \leftrightarrow \text{x A}_3\text{P} + \text{M}$ ($\text{M}=\text{Fe, Co, Ni, Cu}$; $\text{A}=\text{Li, Na}$), the metal phosphides FeP , CoP , NiP_2 and CuP_2 have theoretical capacities of 926, 894, 1333 and 1282 mAh g^{-1} respectively. In close agreement, CuP_2 indeed showed the highest capacity in the first cycle. However, the capacities of all studied materials rapidly faded during cycling. The compounds with higher P content, NiP_2 and CuP_2 , showed higher initial capacities but poorer capacity retention. Namely, for CuP_2 NCs the charge capacity decreased from 1140 mAh g^{-1} to 570 mAh g^{-1} within the first 16 cycles. For the FeP , CoP and NiP_2 NCs, the capacities fell below 600 mAh g^{-1} after just the first 10 cycles, and faded to less than 400 mAh g^{-1} during subsequent cycling. Similar observations were made when testing the metal phosphide NCs in Li-ion half-cells (Figure 7.2.b). Due to the high surface area of the nano-sized materials, low coulombic efficiencies (20-70%) were obtained for the first cycle as result of the irreversible decomposition of the electrolyte forming the solid electrolyte interface (SEI) (see Figures 7.2.c and d). Notably, rather poor coulombic efficiencies of 92-95% for Na-ion and 96-98% for Li-ion cells were also obtained during subsequent cycles, indicating continuous deterioration and reformation of the SEI caused by pulverization of the electrode material.

Figures 7.2.e and 7.2.f show the galvanostatic charge and discharge voltage profiles for the first cycle for all tested metal phosphide NCs. For Na-ion storage a desodiation plateau can be identified in all cases at $\sim 0.6 \text{ V vs. Na}^+/\text{Na}$, which is at the same potential as reported for the electrochemical reaction of red P with Na.²⁶ This implies that metal phosphides rather convert into elemental P and that cycling proceeds mainly by the reaction $\text{P} + 3\text{e}^- + 3\text{Na}^+ \leftrightarrow \text{Na}_3\text{P}$, as has been suggested for FeP .¹⁰¹ In Li-ion half-cells the majority of delithiation occurs at a potential of more than 1.0 V showing that metal phosphides are generally better suited as SIB anode materials due to lower voltages of desodiation.

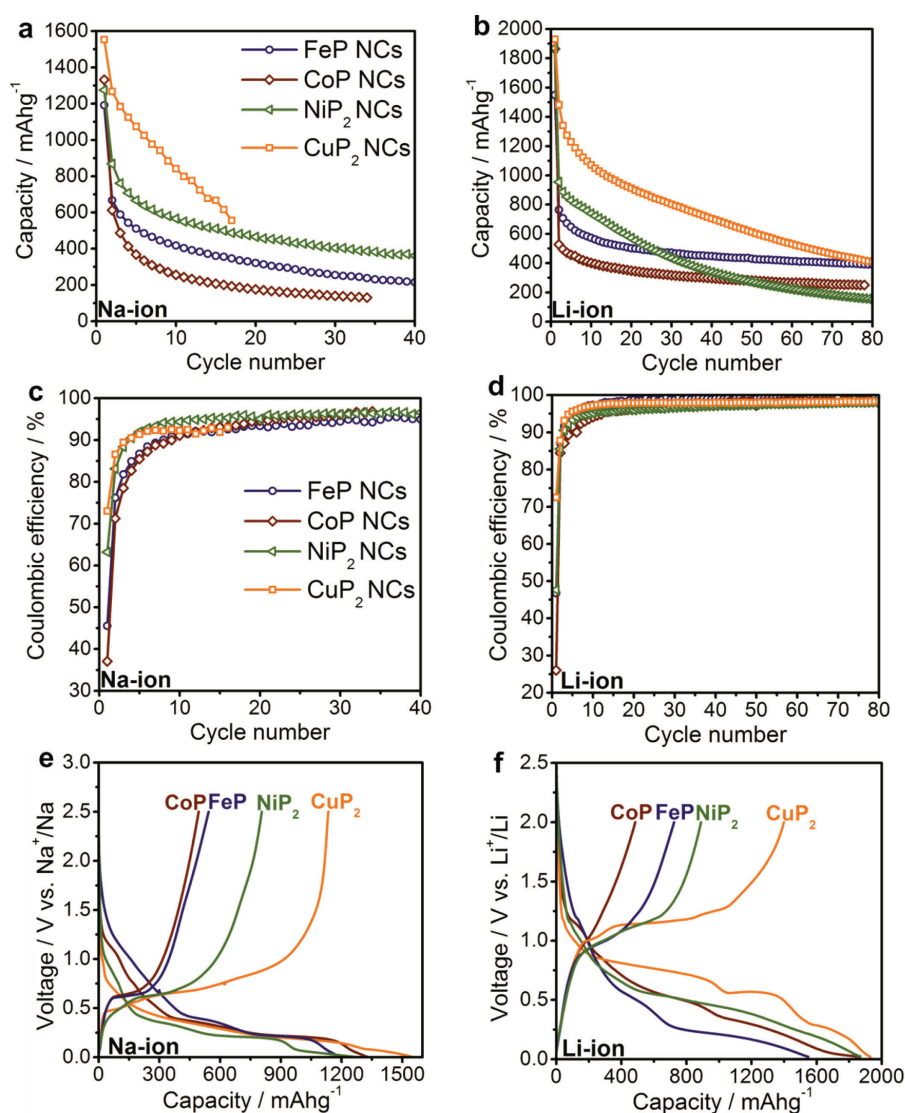


Figure 7.2. Electrochemical performance of metal phosphide nanocrystals. Galvanostatic cycling of metal phosphide NCs in Na-ion (a) and Li-ion half-cells (b) with the respective coulombic efficiency plots (c, d). Galvanostatic charge and discharge curves for the first cycle for Na-ion (e) and Li-ion (f) half-cells. Electrodes were composed of 63.75% metal phosphide NCs, 21.25% CB and 15% CMC. 1M NaClO₄ in PC with 10% FEC served as the electrolyte for Na-ion and 1M LiPF₆ in EC:DMC (1:1) with 3% FEC for Li-ion half-cells. Galvanostatic cycling tests were carried out with a current of 100 mA g⁻¹ in the potential range of 0.02-2.5 V for Na-ion and 300 mA g⁻¹ in the potential range of 0.02-2.0 V for Li-ion half-cells.

Comparison of FeP and FeS₂ NCs as anode materials for Na-ion batteries.

Clearly, from the prospects of low cost and low toxicity, iron-based Na-ion storage electrode materials are the most interesting candidates, in particular when the other chemical constituents of the compound comprise equally abundant elements such as phosphorus and sulfur. Hence, iron sulfides can be seen as a main alternative to phosphides. Similar difficulties with capacity fading have been reported for FeS₂ (pyrite) due to its large (~280%) volume expansion upon Na₂S formation.⁹⁰ In order to compare the electrochemical performance of Fe phosphides and sulfides, pyrite FeS₂ NCs with sizes from 50-100 nm were synthesized and tested under the same conditions as the FeP NCs. The synthesis,

characterization and electrochemical properties of FeS₂ NCs have been detailed in Chapter 6. Assuming the formation of Na₂S, FeS₂ NCs possess a theoretical maximum capacity of 894 mAh g⁻¹, similar to the value for FeP (926 mAh g⁻¹). However, as can be seen in Figure 7.3., the electrochemical performance of FeS₂ and FeP NCs is in fact very different. Whereas FeP NCs show rapid capacity fading upon cycling, FeS₂ NCs exhibit stable capacities of ≥ 800 mAh g⁻¹ (near the theoretical value), clearly demonstrating that the identity of the anion in a conversion-type electrode material plays a critical role in determining its electrochemical properties. The only relevant previous investigation of FeP as a SIB anode material is the recent report by Li *et al.*;¹⁰¹ in that work, anodes prepared by ball-milling FeP showed much faster capacity fading, from 460 mAh g⁻¹ to ~200 mAh g⁻¹ within 40 cycles at a current of 50 mA g⁻¹. Compared to FeP NCs, the only obvious drawback of FeS₂ NCs is the higher desodiation potential (Figures 7.3.b and 7.3.c), that is, however, well compensated by good capacity retention.

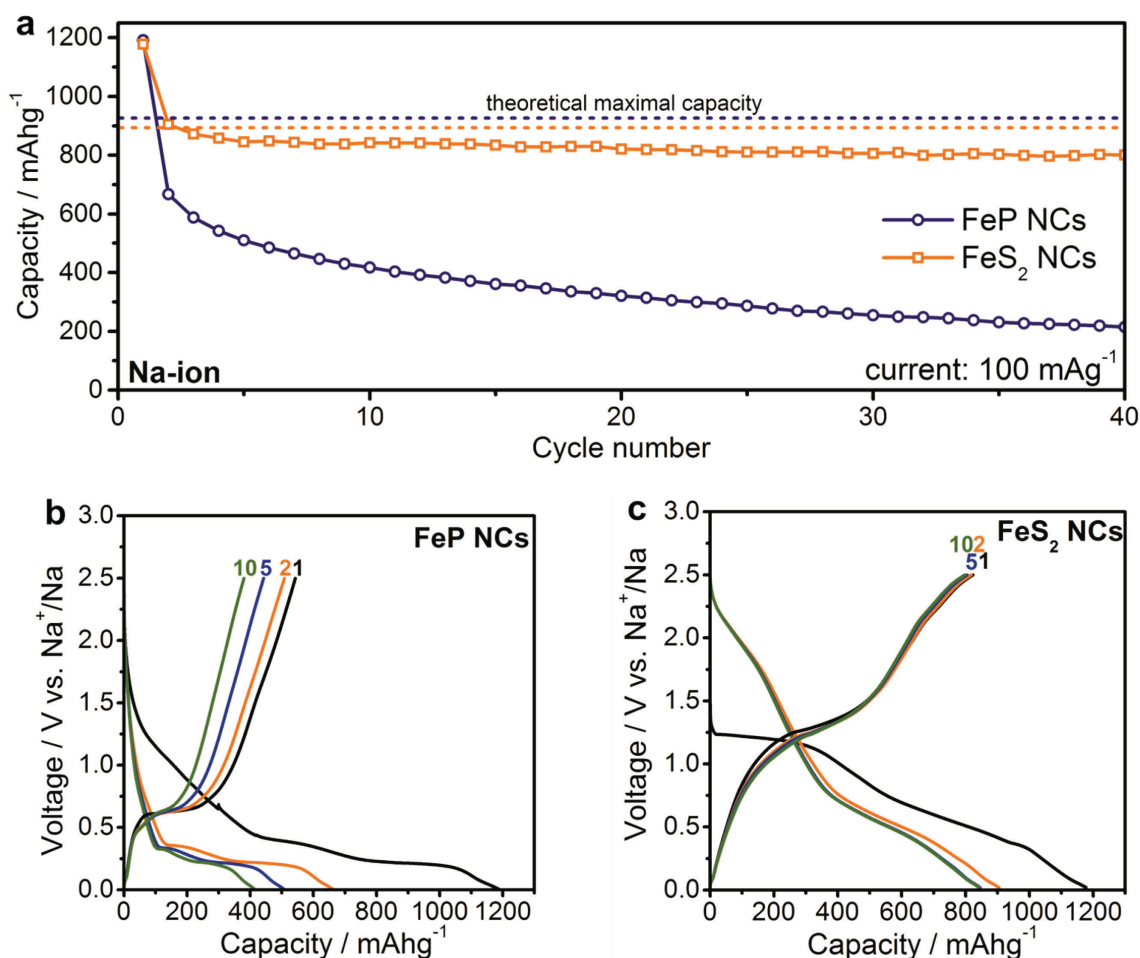


Figure 7.3. Comparison of the electrochemical performance of FeP and FeS₂ NCs. Galvanostatic cycling of FeS₂ and FeP in Na-ion half-cells (a) and the respective charge/discharge curves (b, c). Galvanostatic cycling tests were carried out with a current of 100 mA g⁻¹ in the potential range of 0.02–2.5 V.

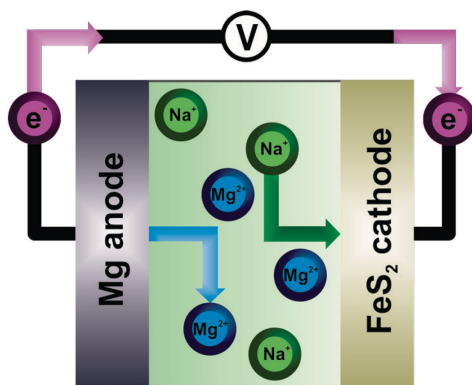
7.4. Conclusion

In conclusion, NCs of FeP, CoP, NiP₂ and CuP₂ were prepared using colloidal synthesis methods. Motivated by their high theoretical capacities, the low electrochemical potentials needed for the anodic side of the battery, and the high natural abundance of their constituting elements, the potential of these nanomaterials as SIB anode materials was explored. Also their sodium storage properties were compared with that of lithium. It is found that with conventionally formulated electrodes (by mixing with amorphous carbon and water-soluble binders), metal phosphide NCs deliver high sodium capacities, but exhibit low capacity retention upon cycling. The direct comparison of FeP and FeS₂ as SIB anode materials indicates the much better cyclability of the latter. Thus, it is concluded that metal phosphides are inherently less stable than their corresponding sulfides and this instability is a combined effect of large volumetric changes and phosphorus-specific processes such as the reactivity of Na₃P towards the electrolyte.¹⁴⁶ Further progress towards high performance phosphide-based electrodes is expected to result from smart electrode engineering by designing secondary structures in which the metal phosphide NPs are encapsulated into conductive carbons,²⁶⁴⁻²⁶⁸ thereby eliminating the direct large-area contact with the electrolyte. Furthermore, a sensible choice of the electrolyte and electrolyte additives might enable the higher stability of the SEI layer in future studies.

Reproduced with modifications from:

M. Walter, M. I. Bodnarchuk, K. V. Kravchyk, and M. V. Kovalenko. *Evaluation of Metal Phosphide Nanocrystals as Anode Materials for Na-ion Batteries*. CHIMIA International Journal for Chemistry, **2015**, 69, 724-728. Copyright©Swiss Chemical Society.

Chapter 8. Efficient and inexpensive Na/Mg hybrid battery



8.1. Introduction

One of the most fundamental challenges for rechargeable lithium (Li)-ion batteries is that their energy densities are still limited by the fact that metallic Li – a lightweight, concentrated and simple source of Li-ions – cannot be safely employed as the negative electrode material (anode).^{9, 10} Due to the formation of dendrites during multiple cycles of electrodeposition/dissolution, which can result in dangerous runaway thermal reactions, metallic Li has been replaced in commercial rechargeable batteries by the safer alternative – graphite – which absorbs Li^+ at similar potentials, but with a 10-fold lower capacity. Analogous issues with dendrite formation have also been encountered with metallic sodium (Na) as an anode material.⁴⁶ Emerging anode materials that alloy with Li or Na (primarily Sn, Si, P and their compounds)^{16, 25, 26, 61, 65, 237, 275-279} suffer from reduced cycling stability due to large volumetric expansion upon alloying ($\Delta V = 100\text{-}400\%$), and often require prohibitively expensive and elaborate synthetic procedures and, for mitigation of volumetric effects, hierarchical nanostructuring methods. In contrast to metallic Li and Na, metallic magnesium (Mg) can be safely employed as an anode material in conceptually analogous rechargeable Mg-ion batteries (MIBs),³⁶⁻⁴⁰ exhibiting both dendrite-free electroplating and, due to less negative redox potential, lower flammability and safer handling. The quest for non-Li-based batteries is further motivated by concerns regarding the future security of the supply of this element and its price development as a result of its geographically uneven natural occurrence.²³ In this regard, Mg-based batteries might become an ideal alternative, owing to the high natural abundance (2.3 wt% in the earth's crust, ~ 1100 times higher than Li)²⁸⁰ and low cost (4 USD kg^{-1} , 15 times lower than Li) of Mg. Significant cost benefits may also arise

from the replacement of copper foils, the standard current collector in commercial Li-ion anodes, by inexpensive aluminum (not suitable for Li-ion anodes due to the formation of Al-Li alloys). Importantly, Mg offers high volumetric (3833 mAh cm^{-3}) and gravimetric capacities (2205 mAh g^{-1}), comparing favorably with metallic Li (2062 mAh cm^{-3} , 3861 mAh g^{-1}) and Na (1128 mAh cm^{-3} , 1166 mAh g^{-1}), as well as a relatively low standard electrode potential ($0.69 \text{ V vs. Li}^+/\text{Li}$ or $0.35 \text{ V vs. Na}^+/\text{Na}$).^{37, 39, 48, 281} In addition, Mg-anodes do not suffer from irreversible capacity loss due to the formation of a solid-electrolyte interface, a common issue facing all emerging Li-ion and Na-ion anode materials arising from the reduction of electrolyte at low anodic potentials. However, despite these advantages, the development of rechargeable MIBs remains hindered by the lack of suitable cathode materials and electrolytes, and overall anode-electrolyte-cathode incompatibilities. Since pioneering work in 2000,³⁶ Chevrel-phase Mo_6S_8 has remained the benchmark cathode material, exhibiting a potential of $\sim 1.1 \text{ V vs. Mg}^{2+}/\text{Mg}$ and practical capacities of $80\text{--}100 \text{ mAh g}^{-1}$ (with a maximal theoretical value of 128 mAh g^{-1} for the $\text{Mo}_6\text{S}_8 + 2\text{Mg}^{2+} + 4\text{e}^- \leftrightarrow \text{Mg}_2\text{Mo}_6\text{S}_8$ insertion reaction). In recent years, theoretical and experimental investigations of novel cathode materials for MIBs have increased tremendously.^{102–110} These studies have shown that the discovery of cathode materials is mainly inhibited by the nature of Mg-ions: their high-charge density (a double charge divided by a small radius of 0.74 \AA) leads to reduced diffusivity within common polar crystalline hosts due to strong Coulomb interactions and causes issues with respect to the electrolyte chemistry,^{37, 39, 40, 282–285} such as the balancing of solvation/desolvation energies for efficient electrodeposition/stripping. For instance, the electrolytes which support reversible stripping and deposition of Mg-ions on the metallic Mg-anode employ highly reducing compounds or solvents, which are then inadvertently oxidized at the cathodic side, restricting the practical operational cathodic voltage to $2 \text{ V vs. Mg}^{2+}/\text{Mg}$.^{37, 51} On the contrary, cheap, conventional electrolytes based on oxidatively stable salts (*e.g.*, $\text{Mg}(\text{ClO}_4)_2$, $\text{Mg}(\text{TFSI})_2$) in an appropriate solvent (*e.g.*, acetonitrile, ionic liquids), cannot be used together with a metallic Mg-anode due to irreversible deposition/stripping of Mg and the formation of a non-conducting passivation layer.²⁸⁶ Only a concerted research and development endeavor on the entire system (metallic Mg-anode, electrolyte and cathode) will determine whether MIBs will reach their expected potential in terms of cost and energy density. An alternative battery concept that takes full advantage of the metallic Mg-anode, but bypasses the need for an efficient Mg-cathode material, is the hybrid Li/Mg battery. This design, incorporating a Li-cathode material and a Mg anode material has been investigated in several recent proof-of-concept reports.^{48, 111–116} An

electrolyte in such a battery comprises one of the common MIB electrolyte formulations with the addition of the suitable Li-salt (*e.g.*, LiCl or LiBH₄). Since the Mg redox potential is higher than that of Li, exclusively Mg-ions are favored to be reduced as well as dissolved during charge and discharge, respectively. The cathode in this type of battery consists of a known Li-ion cathode compound such as TiO₂,¹¹³ TiS₂,^{111, 115} Mo₆S₈,^{112, 116} or LiFePO₄,⁴⁸ providing the benefits of fast, reversible and highly cycleable Li-insertion. For most of these compounds, clear evidence has been presented for the preferred lithiation over magnesiation of the cathode, as expected from the lower charge and higher mobility of Li-ions in metal oxides and sulfides. Overall good reversibility and promising charge-storage capacities of 100-200 mAh g⁻¹ within a potential range of typically 0.4-1.9 V were shown, paving the way for future developments, in particular, on the electrolyte component of the battery with hopes of achieving higher operation voltages.

In order to fully exploit the cost benefits of a metallic Mg-anode for hybrid battery concepts, a shift from Li-electrolyte and Li-cathode chemistries to Na-based alternatives is clearly desirable. With this motivation in mind, herein a hybrid Na-cathode – Mg-anode (Na/Mg) battery is presented that is based exclusively on earth-abundant and inexpensive materials: metallic Mg as the anode, a Na/Mg electrolyte and pyrite (FeS₂) as a Na-ion cathode (see Figure 8.1.a).

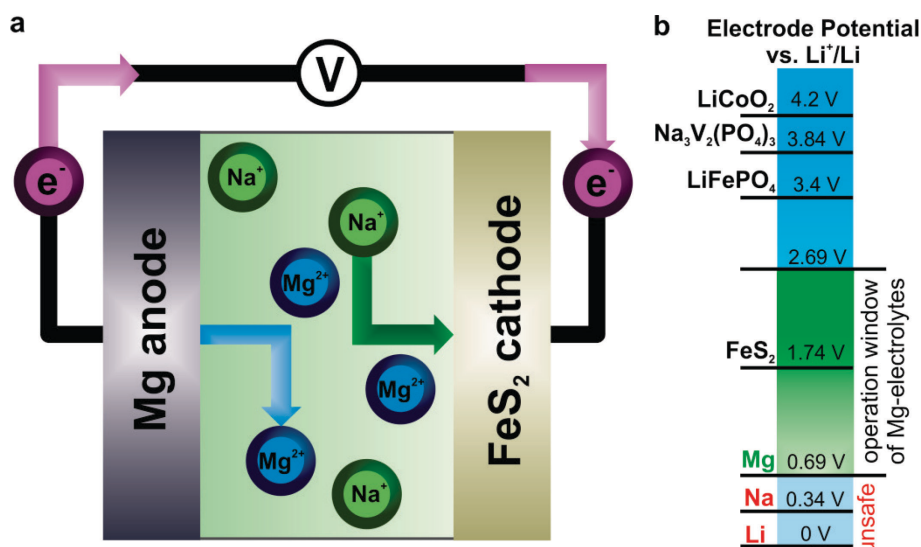


Figure 8.1. (a) Schematic depiction of the working principle of a Na/Mg hybrid battery. During discharge, metallic Mg is oxidized releasing Mg-ions into the electrolyte. Electrons are shuttled through the external electrical circuit from the Mg-anode to the cathode side, where reduction is accompanied by the insertion of Na-ions into FeS₂. Upon charging of the battery, the processes are reversed. (b) Comparison of the electrode potentials vs. Li⁺/Li for positive and negative electrode materials. The operational voltage window of Mg-ion batteries and Na(Li)/Mg-ion batteries is set by the oxidative stability of the electrolyte in which highly efficient electroplating/stripping of metallic Mg can be carried out. Medial discharge potential of FeS₂ falls into this voltage window, while more traditional Li- and Na-ion intercalation cathodes operate at much higher voltages

Similar to the corresponding Li/Mg electrolyte²⁸⁴ the oxidative stability of the chosen electrolyte – 2M NaBH₄ + 0.2M Mg(BH₄)₂ in diglyme – is limited to ~2.3 V vs. Mg²⁺/Mg, as confirmed in control experiments using a stainless steel current collector as a the working electrode in three-electrode glass cells, and does not improve when switching to other metals (Figure 8.2.).

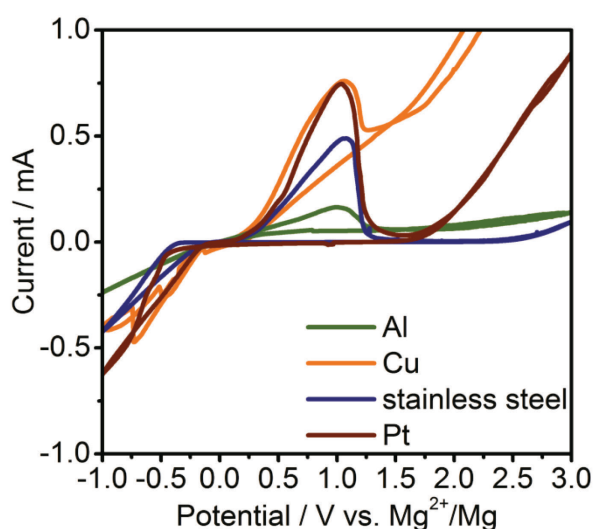


Figure 8.2. Cyclic voltammograms for Mg-plating/stripping tests in three-electrode glass cells using Mg as a quasi-reference and counter electrode with a rate of 5 mV s⁻¹ and 2M NaBH₄ + 0.2M Mg(BH₄)₂ in diglyme as electrolyte.

Other electrolytes which are reported to have higher oxidative stability with Pt electrodes, such as organometallic reagents^{287, 288} or all inorganic compounds⁵¹, do not adequately dissolve Na-salts or, when containing Cl^- , form insoluble NaCl . In other cases, such electrolytes were less attractive due to their either higher cost or highly pyrophoric (*e.g.*, Grignard compounds and other organometallics) and volatile nature (*e.g.*, when THF is used as the solvent).

8.2. Experimental section

Synthesis of FeS_2 NCs. FeS_2 NCs were synthesized according to Li *et al.*²⁵⁷ with slight modifications as described in Chapter 6.

Preparation of CMK-3/sulfur composite. The CMK-3/sulfur composite was reproduced according to the procedure of Ji *et al.* by melt-diffusion of elemental sulfur into CMK-3 (purchased from ACS MATERIAL).²⁶⁴

Mechanochemical preparation of FeS_2 NCs. FeS_2 NCs were prepared by mechanical milling of iron and sulfur powders following the procedure of Chin *et al.*²⁸⁹

Electrode fabrication, cell assembly and electrochemical measurements. Electrodes were prepared by mixing FeS_2 NCs (64 wt%) with carbon black (21 wt%, Super C65, TIMCAL), carboxymethyl cellulose (15 wt%, Daicel FineChem Ltd.) and water using a planetary ball-mill (500 rpm, 1 hour). The resulting aqueous slurries were coated onto stainless steel current collectors and dried for 12 hours at 80 °C under vacuum. Electrode preparation for the CMK-3/S composite was carried out analogously, but using a different composition (84 wt% CMK-3/S, 8 wt% carbon black, 8 wt% PVdF) and cyclopentanone as the solvent following the original procedure of Ji *et al.*²⁶⁴ For electrodes composed of bulk FeS_2 , FeS_2 powders and carbon black (ratio 3:1) were ball-milled prior to slurry preparation for 4 hours. Stainless steel coin-type cells were assembled in an Ar-filled glove box ($\text{O}_2 < 0.1$ ppm, $\text{H}_2\text{O} < 0.1$ ppm) using polished elemental magnesium (99.95%, GalliumSource) as the counter and reference electrodes. Glass microfiber (GF/D, Whatman) was used as a separator. A solution of 2M NaBH_4 (98%, ABCR) and 0.2M $\text{Mg}(\text{BH}_4)_2$ (95%, Sigma-Aldrich) in anhydrous diglyme (99.5%, Sigma-Aldrich) served as the electrolyte, unless noted otherwise. All galvanostatic cycling tests were carried out at room temperature on an MPG-2 multi-channel workstation (BioLogic). Specific capacities and currents were quantified with respect to the mass of FeS_2 . Typical electrode loading was $\sim 0.5 \text{ mg cm}^{-2}$.

Materials characterization. Scanning electron microscopy (SEM) and energy-dispersive X-ray (EDX) spectroscopy measurements were carried out using a NanoSEM 230. Powder X-

ray diffraction (XRD) was measured on a STOE STADI P powder X-ray diffractometer (Cu-K α_1 irradiation, $\lambda = 1.540598 \text{ \AA}$).

8.3. Results and discussion

Choice of Na-ion cathode material. The theoretical (thermodynamic) difference in electrode potentials between Na and Mg, ignoring possible polarization effects, is just 0.35 V (Figure 8.1.b), implying that with the upper electrolyte stability limit of *ca.* 2 V vs. Mg²⁺/Mg, the Na-ion cathode must be chosen from the subset of materials with a standard potential of not more than 2.35 V vs. Na⁺/Na (or 2.69 V vs. Li⁺/Li). The selection of FeS₂ as a cathode material in this proof-of-concept study stems from the previous work in Chapter 6 on its Li-ion and Na-ion storage properties,³² where highly reversible (≥ 100 cycles) insertion of Li- (1.0-3.0 V range) and Na-ions (0.02-2.5 V range) was observed with capacities close to the theoretical value of 894 mAh g⁻¹ (for full transformation into Fe + Li₂S/Na₂S) at high currents of 200-1000 mA g⁻¹. Up to 50% of these capacities lie in the suitable potential range for Na/Mg or Li/Mg batteries. Importantly, such higher capacities were achieved using solution synthesized FeS₂ nanocrystals (NCs), whereas much lower capacities were obtained with bulk micron-sized commercial FeS₂ powders. Therefore, FeS₂ NCs were used in this study to benefit also from their compositional and phase purity, well-defined crystallite sizes (50-100 nm), and facile solution processing for easy miscibility with other electrode components. Alternatively, perhaps more scalable and lower cost methods of nanostructuring of FeS₂ can also be envisioned, such as *via* commonly used high-energy ball-milling methods.²⁹⁰⁻²⁹⁶ FeS₂ has also been investigated as the cathode material for Na-ion batteries by others,^{252-255, 297, 298} wherein high capacities of up to 530 mAh g⁻¹ for 100 cycles at a current of 60 mA g⁻¹²⁹⁸ and outstanding cyclability up to 20000 cycles at a current of 1000 mA g⁻¹ with a capacity of 200 mAh g⁻¹²⁹⁷ have been reported.

In this chapter, FeS₂ NCs were synthesized using a modified procedure based on that of Li *et al.*²⁵⁷ (for details see also Chapter 6). In short, elemental sulfur dissolved in oleylamine was added to a hot solution of iron(II) chloride in oleylamine, and the resulting suspension was held at 220 °C for 2 hours. After the removal of the insulating organic ligands by treatment with a 1M solution of hydrazine in acetonitrile, electrodes were prepared by mixing FeS₂ NCs (64 wt%) with carbon black (21 wt%) and carboxymethyl cellulose binder (15 wt%), followed by coating onto stainless steel current collectors.

Electrochemical properties of the Na/Mg hybrid battery. Figure 8.3. summarizes the electrochemical performance of the resulting Na/Mg hybrid batteries.

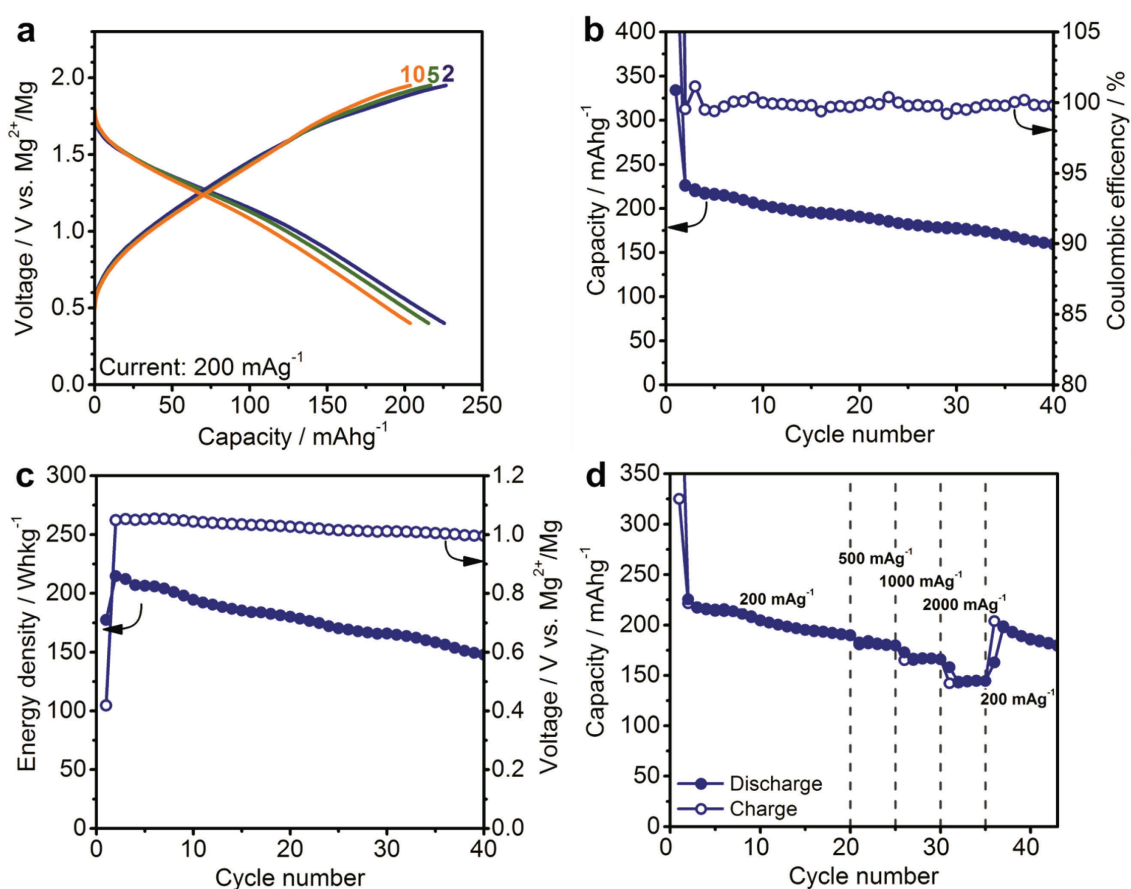


Figure 8.3. Electrochemical performance of Na/Mg hybrid batteries comprised of a Mg-anode and FeS_2 cathode: (a) Galvanostatic charge/discharge curves. (b) Capacity retention and coulombic efficiency over 40 cycle, at a current of 200 mA g^{-1} ($\sim 0.2\text{C}$ -rate). (c) Specific energy density and average discharge voltages over 40 cycles. (d) Rate capability tests. All batteries were cycled in the potential range of 0.4-1.95 V after initial discharge to 0.005 V with 2M NaBH_4 + 0.2M $\text{Mg}(\text{BH}_4)_2$ in diglyme as electrolyte. Specific currents and capacities were determined with respect to the mass of FeS_2 NCs.

Galvanostatic cycling was carried out at a current density of 200 mA g^{-1} in the potential range of 0.4-1.95 V after initial discharge to 0.005 V. Good synergy between the anode, cathode and electrolyte is evidenced by high coulombic efficiency (CE) of on average 99.8%. The FeS_2 cathode provides a high initial capacity of 225 mAh g^{-1} and delivers for 40 cycles an average capacity of 189 mAh g^{-1} (Figures 8.3.b). Taking the capacity of the Mg-anode to be 2205 mAh g^{-1} , the theoretical cell capacity is $C_{\text{cell}} = C_{\text{anode}}C_{\text{cathode}}/(C_{\text{anode}}+C_{\text{cathode}}) = 174.1 \text{ mAh g}^{-1}$. Given the average discharge voltage of 1.03 V, the average energy density of the battery is 179.3 Wh kg^{-1} (Figure 8.3.c). The energy density in the initial cycles is at least 215 Wh kg^{-1} . Even though the energy density (based on active materials only) of the Na/Mg hybrid battery is approximately half the value of the state-of-the-art Li-ion batteries (422 Wh kg^{-1} for graphite/ LiCoO_2 , 362 Wh kg^{-1} for graphite/ LiFePO_4 , 315 Wh kg^{-1} for

graphite/LiMn₂O₄),⁴⁸ it is twice that of the Mg/Mo₆S₈ system, which at room temperature does not exceed 100 Wh kg⁻¹.

Rate capability tests were carried out to further demonstrate that the Na/Mg hybrid battery system shows excellent rate performance (Figure 8.3.d). Cells were initially charged and discharged for 20 cycles with a current of 200 mA g⁻¹, and the current was then increased to 500, 1000 and 2000 mA g⁻¹ for five cycles each. Even at such high rates, FeS₂ NCs deliver stable capacities of 180, 170 and 145 mAh g⁻¹ respectively. Most notably, once the current is decreased again to 200 mA g⁻¹ the capacity returns to the initial level demonstrating that nanostructured FeS₂ is a robust electrode material capable of withstanding high mechanical stress caused by rapid cycling.

Control experiments were carried out to determine whether Na-ions were the species reacting with the FeS₂ cathode (Figure 8.4).

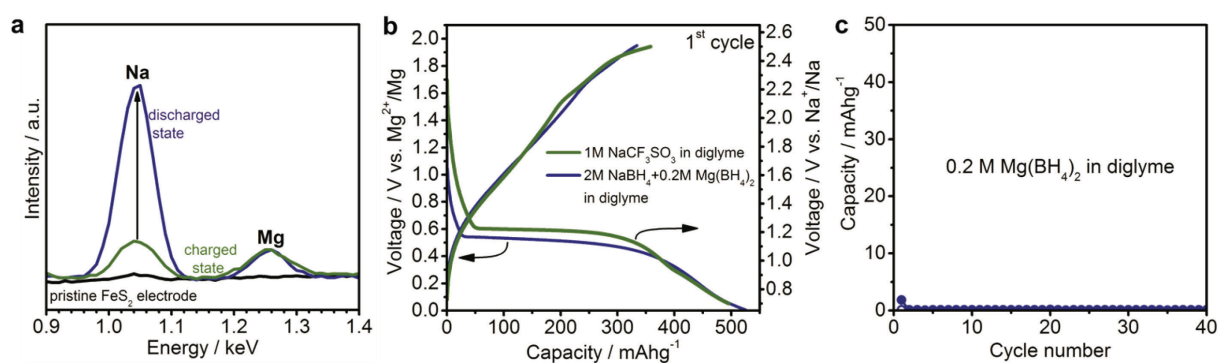


Figure 8.4. (a) Energy-dispersive X-ray (EDX) spectra of pristine, charged, and discharged FeS₂ electrodes cycled in a Na/Mg hybrid battery. (b) Comparison of the 1st cycle galvanostatic charge/discharge curves of FeS₂ NCs cathodes cycled either vs. metallic Na with 1M NaCF₃SO₃ in diglyme as electrolyte or vs. metallic Mg using 2M NaBH₄ + 0.2M Mg(BH₄)₂ in diglyme as electrolyte. All batteries were cycled at a current of 200 mA g⁻¹ (~0.2C-rate). Na-ion cells were cycled in the potential range of 0.7-2.5 V vs Na⁺/Na, whereas Na/Mg hybrid cells were cycled in the range of 0.005-1.95 V vs Mg²⁺/Mg. (c) Electrochemical performance of FeS₂ NCs cycled vs. Mg using 0.2M Mg(BH₄)₂ in diglyme as the electrolyte. Batteries were cycled with a current of 200 mA g⁻¹ in the potential range 0.4-1.95 V after initial discharge to 0.005 V.

When FeS₂ NCs were cycled vs. Na⁺/Na, the rescaled voltage profile perfectly matched that of the Na/Mg hybrid battery system. It should be noted that the voltage curves for Na and Na/Mg cells are shifted by ~0.7 V, approximately twice the value one would expect based on the thermodynamic difference of electrode potentials Na⁺/Na and Mg²⁺/Mg (Figure 8.1.b), most likely due to the relatively large overpotential for Mg-plating/stripping also observed in reference three-electrode cell tests (Figure 8.2.). Moreover, essentially no capacity was observed in cells with a metallic Mg-anode and FeS₂ cathode without the addition of NaBH₄ to the electrolyte (Figure 8.4.c). Elemental analysis of FeS₂ electrodes after 20 cycles using energy-dispersive X-ray (EDX) spectroscopy (Figure 8.4.a) showed that upon switching from

the charged to the discharged state of the FeS_2 cathode, the only compositional change was a 4-fold increase in Na content.

For comparison, analogous Li/Mg hybrid batteries were also assembled, simply by replacing NaBH_4 in the electrolyte with LiBH_4 , and tested under identical electrochemical conditions (Figure 8.5.).

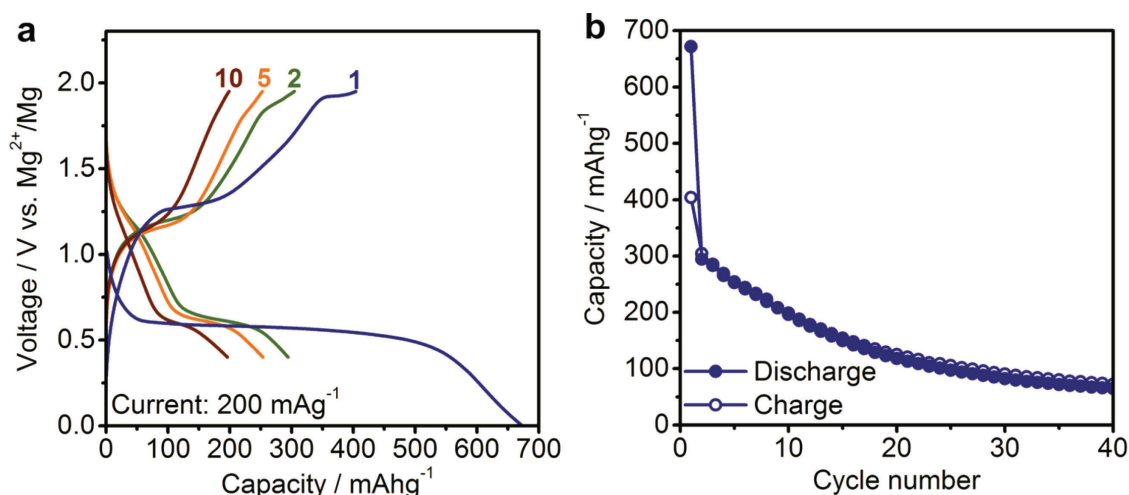
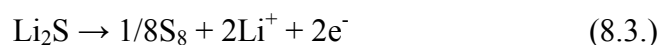
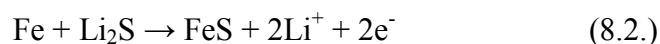
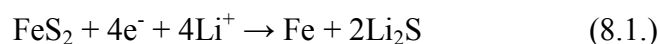


Figure 8.5. (a) Galvanostatic charge/discharge curves and (b) capacity retention for FeS_2 NCs as the cathode in Li/Mg hybrid batteries. Batteries were cycled with a current of 200 mA g^{-1} in the potential range of 0.4–1.95 V after initial discharge to 0.005 V, using 2M LiBH_4 + 0.2M $\text{Mg}(\text{BH}_4)_2$ in diglyme as the electrolyte.

The initial charge/discharge curves exhibit features reported for FeS_2 in Li-ion half-cells,^{32, 248, 251} however, again with notable polarization. Interestingly, Li/Mg dual-salt electrolytes show much faster capacity fading compared to the Na/Mg hybrid battery system, resulting in a decrease of the reversible capacity from 300 mAh g^{-1} to less than 100 mAh g^{-1} within 20 cycles, indicating fundamentally different electrochemistry. The exact mechanism of the Na-ion insertion into FeS_2 at room temperature is not fully established, because only amorphous states can be seen as discussed in Chapter 6. For Li- FeS_2 system, it has been reported that Li/ FeS_2 batteries can essentially be understood as the combination of Li/S and Li/FeS batteries according to the following reaction mechanism:²⁹⁹



To this end, elemental sulfur is known to react with borohydrides forming sulfurated borohydride,³⁰⁰ which might explain the rapid capacity fading observed for Li/Mg hybrid batteries. In a control experiment, a Na/Mg cell was assembled with elemental sulfur embedded into mesoporous carbon (CMK-3, for improving electronic transport, as previously demonstrated for Li-S batteries, Figure 8.6.).²⁶⁴ Very low, rapidly fading capacities of 20-80 mAh g⁻¹ were obtained (Figure 8.6.), presumably due to the aforementioned high reactivity of borohydrides towards elemental sulfur.

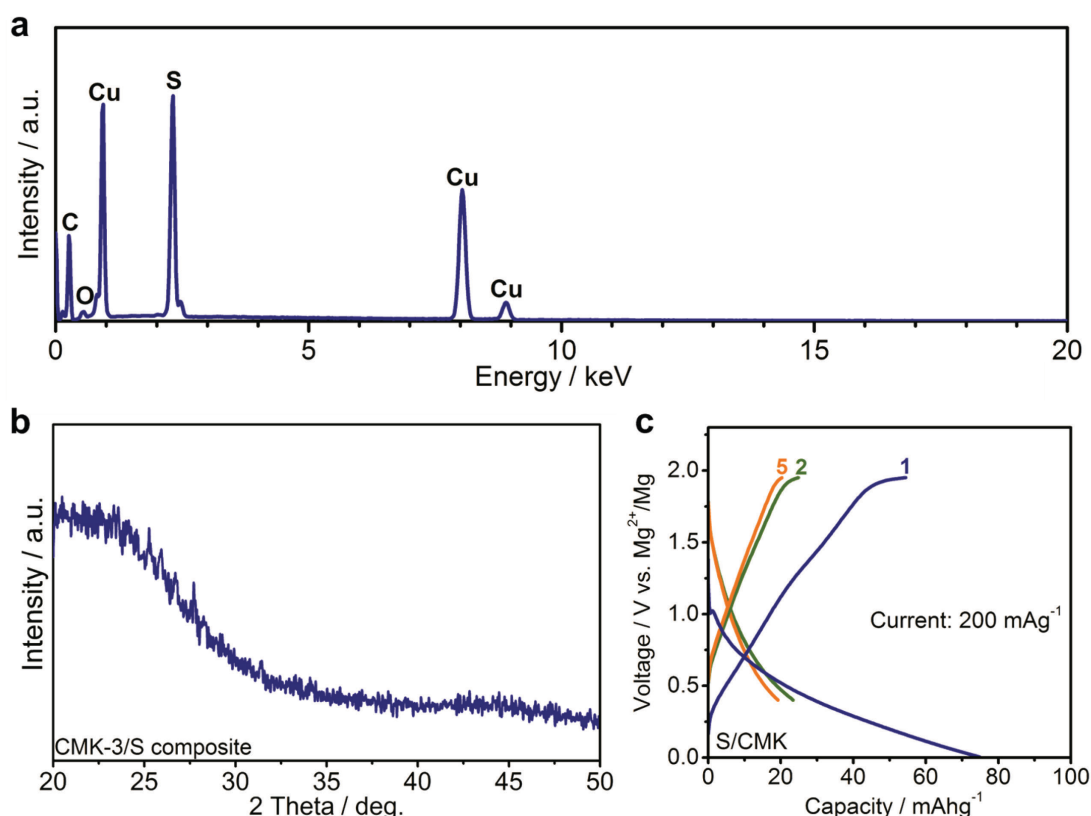


Figure 8.6. (a) EDX spectrum (Cu signal is from the substrate) and (b) XRD pattern of the CMK-3/sulfur composite prepared by melt-diffusion of sulfur into the CMK-3 matrix. (c) Galvanostatic charge/discharge curves for CMK-3/S as the cathode material in Na/Mg hybrid batteries. Batteries were cycled with a current of 200 mA g⁻¹ in the potential range of 0.4-1.95 V after initial discharge to 0.005 V, using 2M NaBH₄ + 0.2M Mg(BH₄)₂ in diglyme as the electrolyte.

8.4. Conclusion

In conclusion, the first demonstration of a Na/Mg hybrid battery was presented, which can be operated with high reversibility and with high coulombic efficiency. With energy densities approaching those of state-of-the-art Li-ion batteries, such batteries may eventually be a system of choice for terawatt-hour-scale grid-level energy storage, where environmentally benign and earth-abundant compositions are crucial and present-day Li-ion batteries are unrealistically expensive. In this regard, it should be noted that further potential

for cost-reduction by switching from the herein colloiddally synthesized FeS_2 NCs to solvent-free dry preparations of FeS_2 nanostructures is fully feasible. Figure 8.7. presents such preliminary tests with FeS_2 nanopowders synthesized by mechanochemical means (see also Figures 8.8. for characterization), *e.g.*, by simple ball-milling of elemental iron and sulfur powders according to the procedure reported by Chin *et al.*²⁸⁹ At least 80% of the capacity of colloidal FeS_2 NCs can be obtained with such inexpensive and high-throughput method. Even electrodes containing grinded bulk FeS_2 show initial capacities of only $\sim 30\%$ lower than colloiddally synthesized FeS_2 NCs, presumably due to slower reaction kinetics.

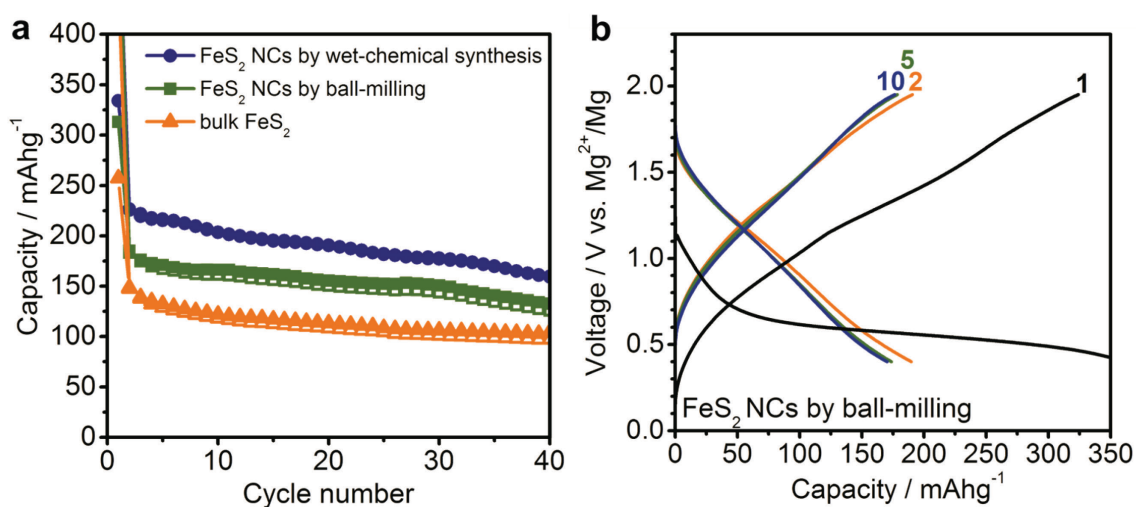


Figure 8.7. (a) Comparison of the electrochemical performance of Na/Mg hybrid batteries using FeS_2 prepared by wet colloidal synthesis, dry mechanochemical synthesis (ball-milling of Fe and S powders, and by coarse grinding of bulk FeS_2). (b) Corresponding charge/discharge curves for FeS_2 NCs prepared by dry mechanochemical synthesis. All batteries were cycled in the potential range of 0.4–1.95 V after initial discharge to 0.005 V at a current of 200 mA g⁻¹ ($\sim 0.2C$ -rate) with 2M NaBH_4 + 0.2M $\text{Mg}(\text{BH}_4)_2$ in diglyme as electrolyte.

In addition, important future work remains in optimizing electrolyte formulations in order to extend the voltage window to harness an even greater proportion of the FeS_2 charge storage capacity. Further economic and safety advantages over borohydride and organometallic-based electrolytes may be achieved by switching to boron-free salts comprising exclusively stable anions such as trifluorosulfonyl imide (TFSI). In fact, preliminary tests (Figure 8.9.) show the full feasibility of operating a boron-free Na/Mg battery with, for instance, a $\text{NaTFSI}/\text{Mg}_2\text{AlCl}_7$ ⁵¹ electrolyte.

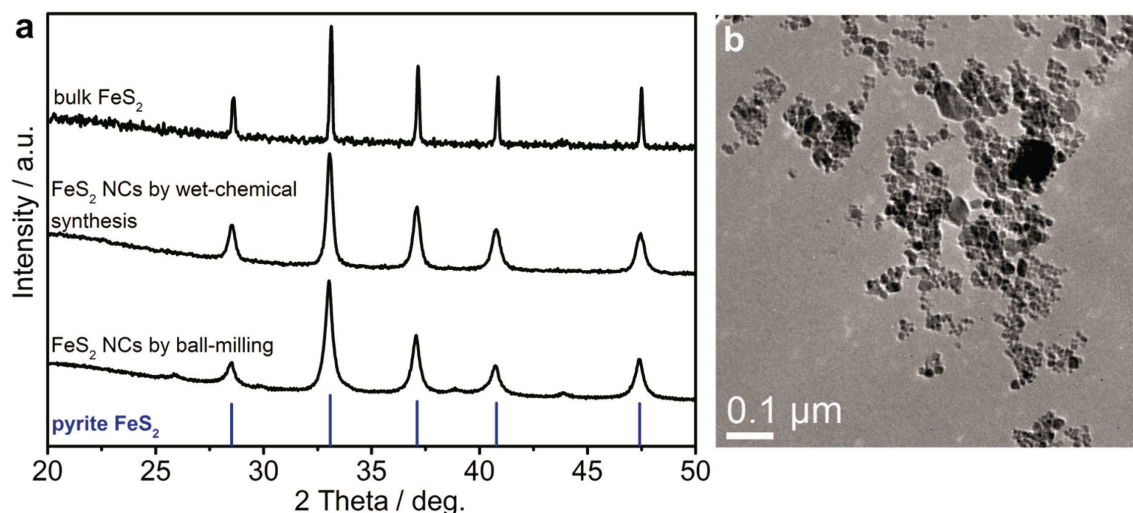


Figure 8.8. (a) XRD patterns of bulk FeS_2 , FeS_2 NCs prepared by wet-chemical (colloidal) synthesis and FeS_2 NCs prepared by dry mechanochemical synthesis (ball-milling of Fe and S powders). (b) TEM-image of mechano-synthesized FeS_2 NCs.

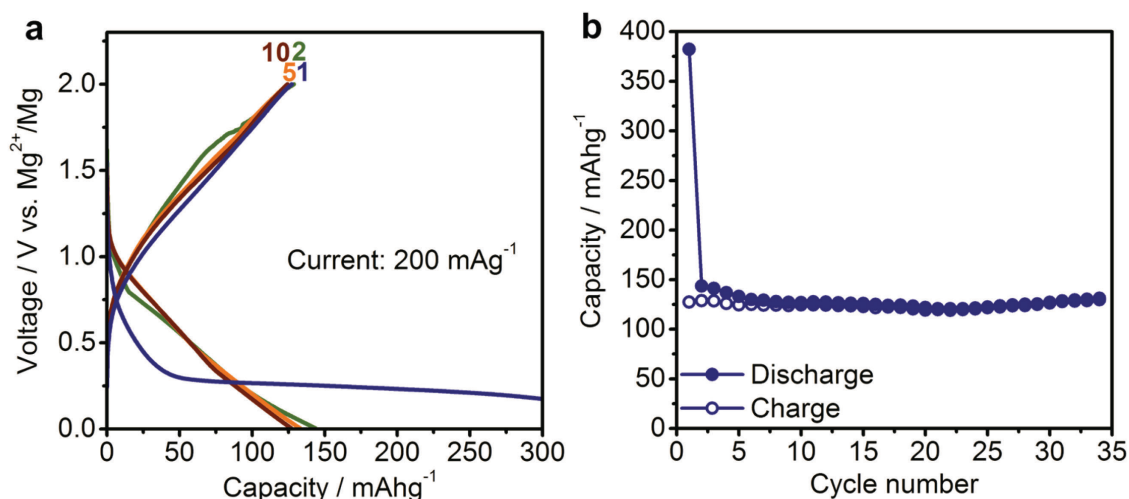
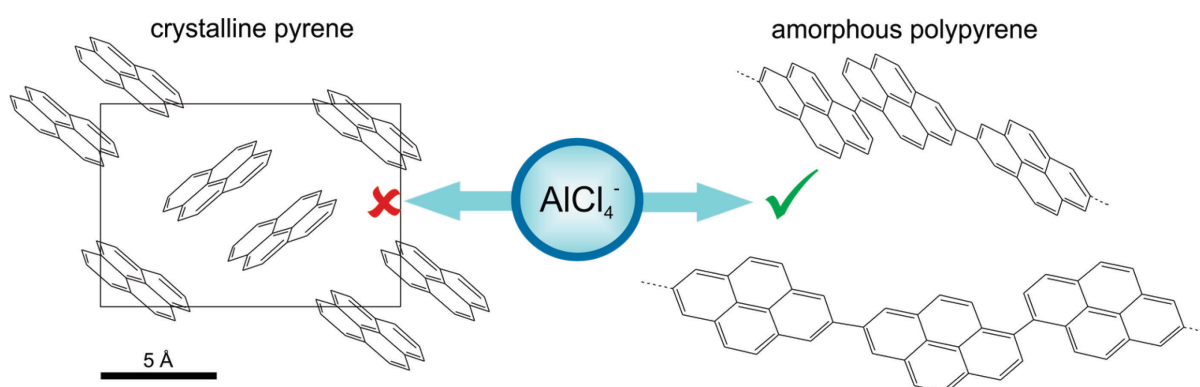


Figure 8.9. (a) Galvanostatic charge/discharge curves and (b) capacity retention for FeS_2 NCs as the cathode. Batteries were cycled with a current of 200 mA g^{-1} in the potential range of 0.005–2.0 V, using 0.5M NaTFSI + 0.27M Mg_2AlCl_7 in THF as the electrolyte.

Adapted with permission from:

M. Walter, K. V. Kravchyk, M. Ibáñez and M. V. Kovalenko. *Efficient and Inexpensive Sodium-Magnesium Hybrid Battery*. Chem. Mater., **2015**, 27, 7452-7458. Copyright 2015 American Chemical Society.

Chapter 9. Pyrene-based polymers as high-performance cathode materials for Al-ion batteries



9.1. Introduction

In order to allow a shift from fossil fuels to renewable energy sources, efficient and inexpensive storage solutions are urgently required.^{134, 177} Despite the fact that lithium-ion batteries outperform any other battery technology in terms of energy and power density, they are rather unsuitable for large scale energy storage due to their relatively high cost, which has triggered the search for more inexpensive battery systems based on earth abundant elements such as sodium-,^{23-28, 30-35, 47, 301, 302} magnesium-,³⁶⁻⁴⁰ sodium/magnesium hybrid-³⁰³ or aluminum-ion batteries^{39, 41}. Aluminum (Al) is especially interesting to use as anode material due to its high abundance (3rd most abundant in the earth's crust)⁴² and hence low cost as well as its extremely high specific (2980 mAh g⁻¹) and volumetric capacity (8046 mAh cm⁻³) higher than metallic lithium (3861 mAh g⁻¹, 2062 mAh cm⁻³) or magnesium (2205 mAh g⁻¹, 3833 mAh cm⁻³).³⁹ Importantly, unlike metallic lithium, aluminum can be safely used as anode material in a rechargeable battery due to smooth, dendrite-free electrodeposition in appropriate electrolytes (typically haloaluminate ionic liquids).³⁹ However, commercialization of Al-ion batteries has been hampered mainly by the difficulty to develop suitable high voltage cathode materials (note that the potential for Al^{3+}/Al is relatively positive with -1.7 V vs. SHE).³⁹ Among the materials that have been explored as potential cathode materials for Al-ion batteries are Mo_6S_8 ,³⁰⁴ V_2O_5 ,^{305, 306} sulphur-based^{307, 308} and graphite-based electrodes.^{41, 309, 310} For graphite electrodes, it has been suggested that during discharge in fact not Al^{3+} -ions are inserted in the cathode material, but AlCl_4^- is removed

accompanied by the reduction of graphite ($C_x^+ + e^- \rightarrow C_x$).⁴¹ Accordingly, the question, which triggered the herein presented work, was, if molecular compounds composed similarly to graphite of sp^2 -hybridized carbons, yet only few condensed aromatic rings, can serve in analogy as cathode material. In particular, the molecule pyrene ($C_{16}H_{10}$) is of interest in monomeric and polymeric form, because of its reported p-type redox-activity at relatively high voltages for lithium- and sodium-ion batteries.^{117, 118} In addition, the theoretical capacity of pyrene, for the formation of the radical cation by extracting one electron from the four condensed aromatic rings, is with 133 mAh g^{-1} comparable to classical cathode materials, for instance $LiCoO_2$ (140 mAh g^{-1}). However, unlike cathode materials based on relatively costly transition metals (*e.g.*, Co, Ni), pyrene is inexpensively available by distillation of coal tar and used already commercially in large quantities for dyes and dye precursors.¹¹⁹ Herein, it is demonstrated that unlike monomeric pyrene, polypyrene and its copolymer with 1-nitropyrene, as example for polycyclic aromatic hydrocarbons, can serve as excellent cathode materials for Al-ion batteries.

9.2. Experimental section

Synthesis of polypyrene and poly(nitropyrene-co-pyrene). Polypyrene was synthesized and purified according to the reported procedure of Li *et al.*³¹¹ For synthesizing poly(nitropyrene-co-pyrene) the same procedure was used with both pyrene and 1-nitropyrene (molar ratio 1:1) as starting materials. The resulting material was additionally purified with acetonitrile and chloroform to remove unreacted 1-nitropyrene completely.

Electrode fabrication, cell assembly and electrochemical measurements. The following battery components were used: carbon black (Super C65, TIMCAL), poly(vinylidene fluoride) (PVdF, Sigma-Aldrich), N-methyl-2-pyrrolidone (NMP, 99%, Sigma-Aldrich), anhydrous $AlCl_3$ (99.99%, ABCR), 1-ethyl-3-methylimidazolium chloride ([EMIm]Cl, 99%, ABCR; additionally dried at 130°C under vacuum), glass microfiber separator (GF/D, Whatman).

Electrodes were prepared by mixing the material with PVdF and NMP using a Fritsch Pulverisette 7 classic planetary mill (500 rpm, 1 hour). The composition of the slurry was 50 wt% pyrene-based polymer, 40 wt% CB and 10 wt% PVdF. Slurries were coated onto tungsten current collectors and were dried at 80°C for 12 hours under vacuum (typical loading $\sim 0.5 \text{ mg cm}^{-2}$). For measurements with pyrene, slurries were prepared using cyclopentanone instead of NMP as solvent and current collectors were dried at room temperature for 12 hours under vacuum. Electrochemical measurements were conducted in

homemade, reusable, air-tight cells assembled in an Ar-filled glove box ($O_2 < 0.1$ ppm, $H_2O < 0.1$ ppm). Aluminum foil was used as both reference and counter electrode. A mixture of [EMIm]Cl and $AlCl_3$ (1:1.3 molar ratio) served as electrolyte. A piece of glass fiber was used as separator. Galvanostatic cycling tests were carried out at room temperature on MPG2 multi-channel workstation (BioLogic). Capacities were normalized by the mass of the respective pyrene-based polymer.

Materials characterization. Powder X-ray diffraction (XRD) was measured on a STOE STADI P powder X-ray diffractometer (Cu- $K\alpha_1$ irradiation, $\lambda = 1.540598$ Å). Scanning electron microscopy (SEM) measurements were carried out using a NanoSEM 230. Attenuated total reflectance Fourier transform infrared (ATR-FTIR) spectroscopy measurements were carried out on a Nicolet iS5 FT-IR spectrometer (Thermo Scientific). Gel permeation chromatography was carried out using Agilent GPC 1100 with tetrahydrofuran as eluent. CHN analysis was carried out using a LECO TruSpec Micro by the Micro-laboratory at ETH Zurich.

9.3. Results and discussion

Polypyrene was synthesized according to the oxidative polymerization procedure reported by Li *et al.*³¹¹ As shown in Figure 9.1.b, the obtained product is almost fully amorphous in contrast to the crystalline pyrene precursor. Polymerization of pyrene is further evidenced by the changes in the Fourier transform infrared (FTIR)-spectra (Figure 9.1.c). In particular, the significantly lower intensity of the signals at 1184, 748 and 706 cm^{-1} , which are mainly associated with C–H deformation, and the C–H stretching vibration at 3040 cm^{-1} , indicate fewer C–H bonds as result of the polymerization.^{133, 311}

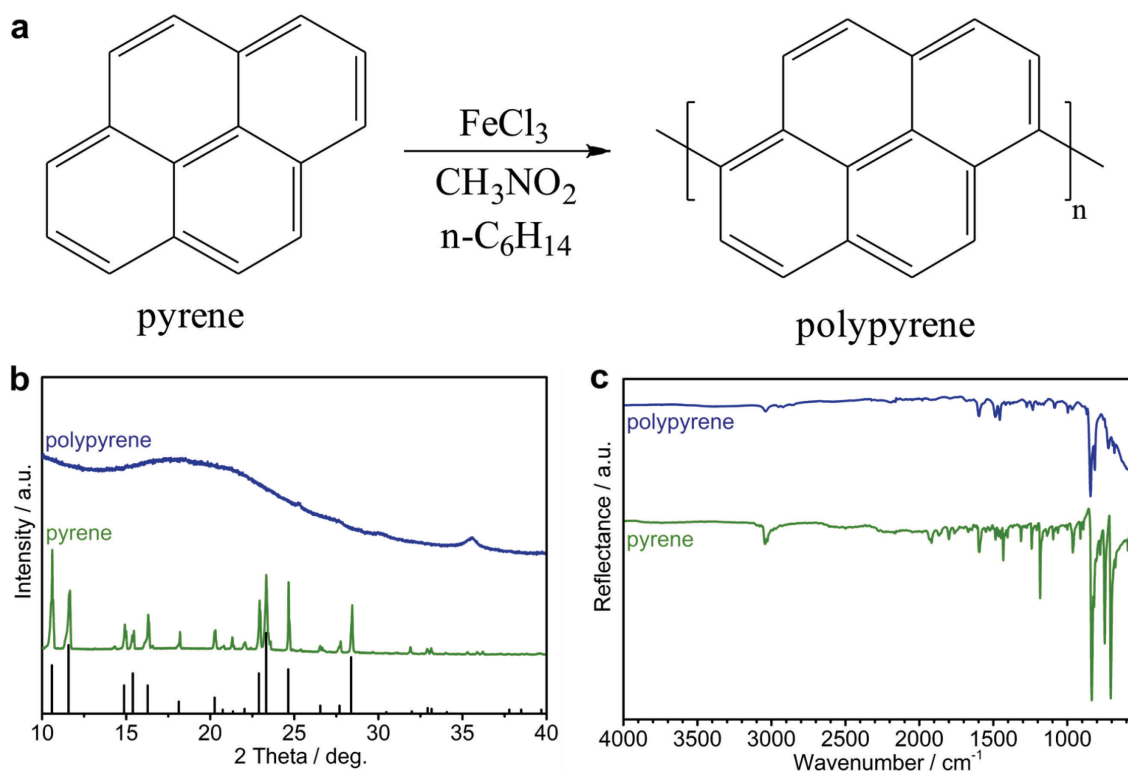


Figure 9.1. (a) Reaction scheme for the synthesis of polypyrene according to Li et al.³¹¹ (b) XRD pattern (indexed to monoclinic pyrene PDF Entry No. 00-024-1855) and (c) FTIR-spectra of pyrene and polypyrene.

For electrochemical tests electrodes were prepared by mixing polypyrene with carbon black (CB), polyvinylidene fluoride (PVdF) and N-methylpyrrolidone (NMP) and casting the resulting slurries on tungsten current collectors. It should be noted that despite the use of NMP as solvent for the binder and a temperature of 80 °C used for drying the current collectors, no crystallization of polypyrene was observed after electrode preparation (Figure 9.2.).

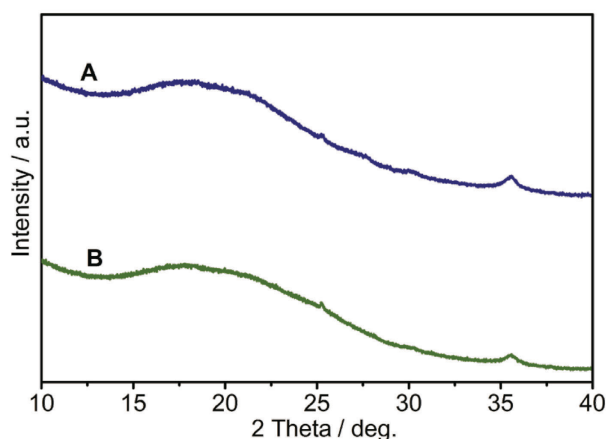


Figure 9.2. Comparison of the XRD-patterns of (A) pristine polypyrene and (B) electrode material containing polypyrene, CB and PVdF prior to battery assembly.

Al-ion batteries were assembled using, in addition to the polypyrene cathode, regular Al-foil as anode material and a chloroaluminate ionic liquid (1:1.3 molar ratio mixture of 1-ethyl-3-methylimidazolium chloride or [EMIm]Cl with AlCl_3) as electrolyte. In such mixture AlCl_3 acts as halide ion acceptor readily forming AlCl_4^- and Al_2Cl_7^- . The working principle of the herein presented Al-ion battery is shown in Figure 9.3.

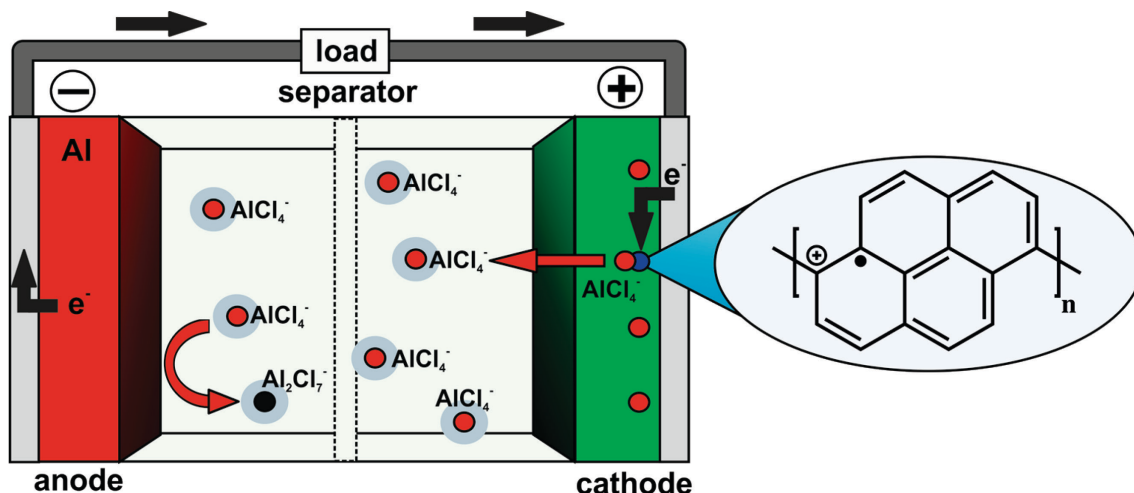
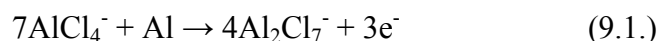


Figure 9.3. Schematic working principle of a rechargeable Al-ion battery with an Al-anode, polypyrene cathode and chloroaluminate ionic liquid electrolyte.

During discharging of the battery the radical cation of polypyrene would be reduced to its pristine neutral state and AlCl_4^- would react with the metallic Al anode forming Al_2Cl_7^- according to:³¹²



Upon charging the processes are then reversed. Figure 9.4. shows the electrochemical performance of electrodes composed of either pyrene or polypyrene as cathode material in Al-ion batteries at a current of 200 mA g^{-1} . In case of polypyrene for 300 cycles a stable capacity of $\sim 70 \text{ mAh g}^{-1}$ is obtained, corresponding to more than half of the theoretical value based on one e^- per pyrene ring (134 mAh g^{-1}). It should be noted that no formation of dendritic structures was observed even after 300 cycles (Figure 9.5.).

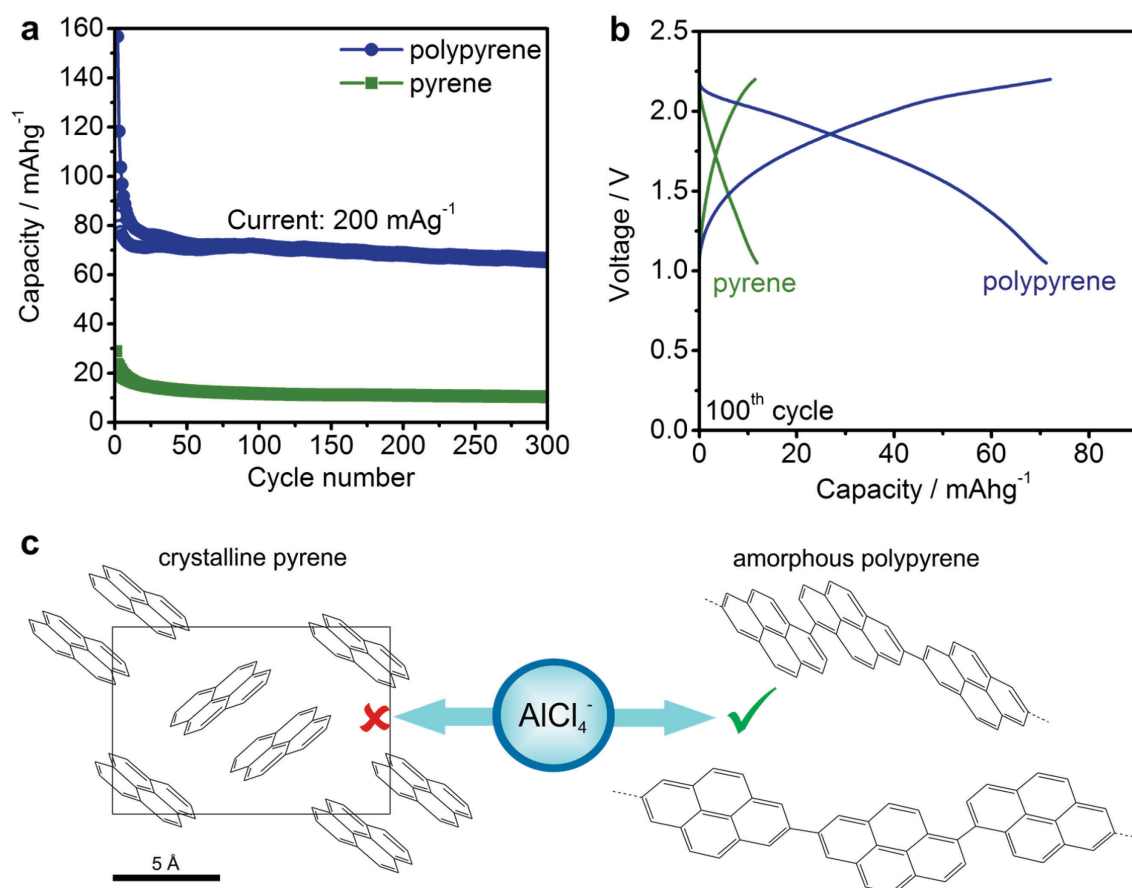


Figure 9.4. Electrochemical performance of Al-ion batteries with pyrene or polypyrene as cathode material: (a) capacity retention and (b) corresponding charge/discharge curves for the 100th cycle. Cells were cycled at room temperature with a current of 200 mA g⁻¹ in the potential range 1.05-2.2 V using Al-foil as anode and [EMIm]Cl : AlCl₃ (molar ratio 1:1.3) as electrolyte. (c) Schematic representation of the structural differences of pyrene and polypyrene possibly leading to different AlCl₄⁻ storage behavior.

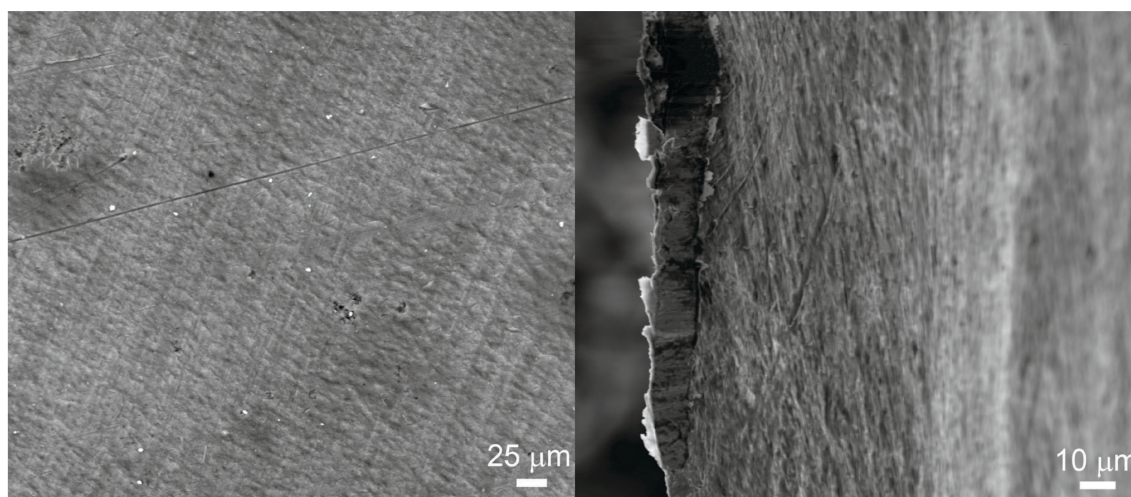


Figure 9.5. SEM images of the Al-anode after cycling for 300 cycles at a current of 200 mA g⁻¹. Cells were cycled at room temperature in the potential range 1.05-2.2 V using [EMIm]Cl : AlCl₃ (molar ratio 1:1.3) as electrolyte.

Galvanostatic charge/discharge curves reveal that the storage capacity corresponds to a relatively high voltage process (on average 1.7 V) (Figure 9.4.b). In comparison to

polypyrene, the performance of monomeric pyrene is very different. In particular, for pyrene the initial discharge capacity is only 20 mAh g⁻¹ and decreases rapidly to values of ~10 mAh g⁻¹. This difference in the electrochemical performance of pyrene and polypyrene can be attributed to several factors. Compared to its polymeric counterpart, pyrene is not only more prone to dissolution in the electrolyte, but also more electronically insulating due to the lack of an extended conjugated π -system. Moreover, insertion is most likely hindered by the simple fact that the intermolecular distances in crystalline pyrene (3.5-4 Å)³¹³ are shorter than the relatively large AlCl₄⁻-ion (diameter of 5.3⁴¹-5.9³¹⁴ Å). In contrast, due to the potentially larger space between disorderly arranged polypyrene chains, AlCl₄⁻-ions can be readily inserted into the amorphous polymer, which is further supported by the relatively porous structure of the latter (Figure 9.6.).

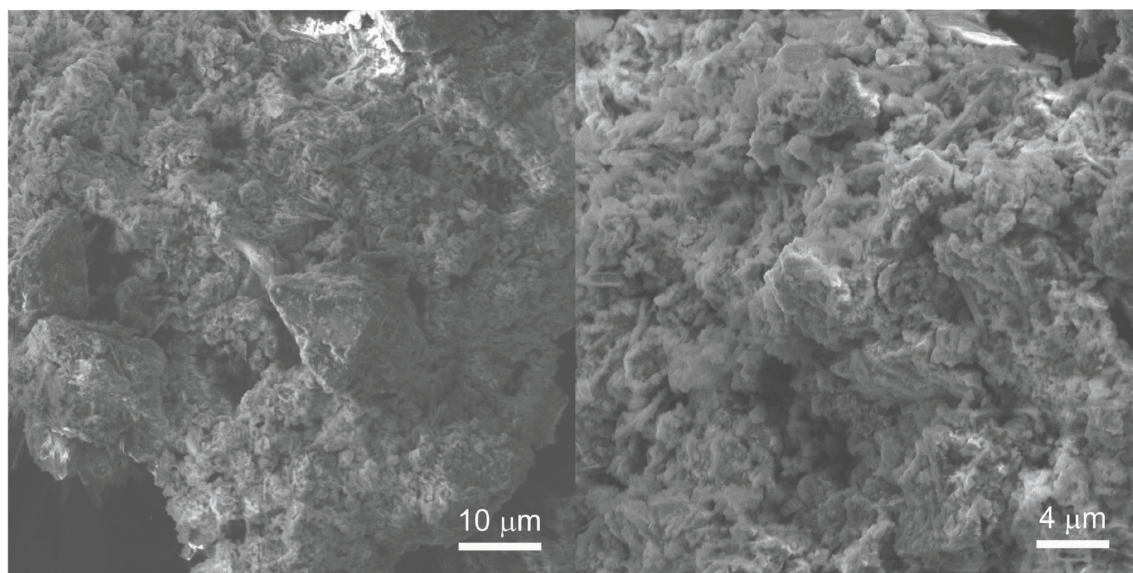


Figure 9.6. SEM images of polypyrene.

Conceptually, the great advantage of polymeric electrode materials are the numerous possibilities to tune the electrochemical properties by smart engineering of chemical composition and structure. In order to evaluate impact of electron withdrawing substituents on the electrochemical performance, a copolymer of 1-nitropyrene and pyrene was synthesized using the aforementioned procedure, but with both compounds as starting materials (molar ratio 1:1). The resulting reaction product is amorphous (Figure 9.7.) and shows almost the same FTIR-spectrum as polypyrene with the main difference being additional vibrations for wavenumbers of ~1510 and 1330 cm⁻¹ (Figure 9.8.). This additional vibrations can be attributed to NO₂-groups, particularly, the N=O asymmetric stretch (typically 1660-1490 cm⁻¹) and N=O symmetric stretch (typically 1390-1260 cm⁻¹)

vibrations³¹⁵ (see also Figure 9.9. for comparison), indicating successful formation of a copolymer of pyrene and 1-nitropyrene.

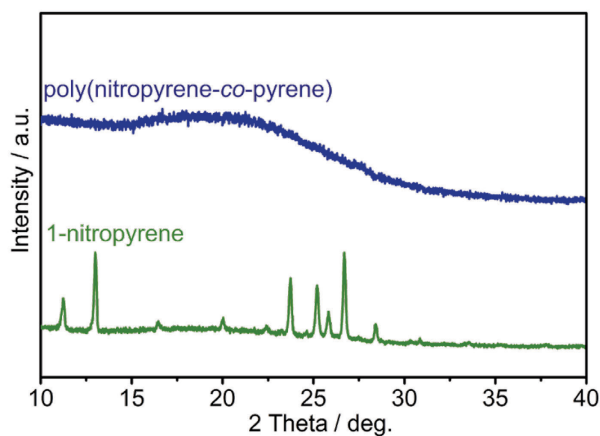


Figure 9.7. Comparison of the XRD patterns of poly(nitropyrene-co-pyrene) and 1-nitropyrene.

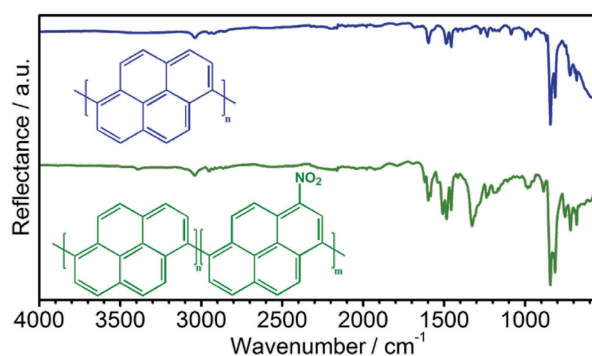


Figure 9.8. FTIR-spectra of polypyrene (blue) and poly(nitropyrene-co-pyrene) (green).

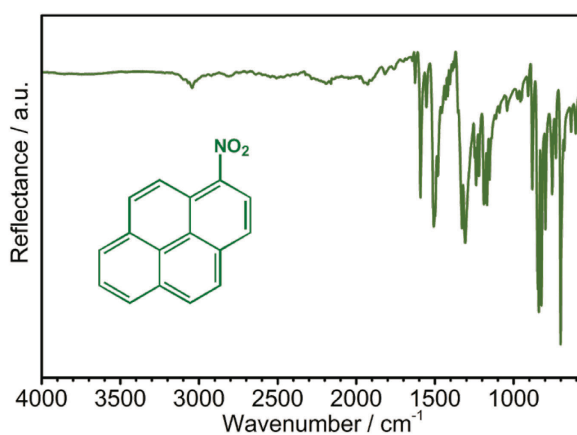


Figure 9.9. FTIR-spectrum of 1-nitropyrene.

CHN analysis delivered an atomic ratio C:N of 45:1 corresponding to approximately three pyrene rings per NO₂-group. Hence, the number of nitropyrene units in the poly(nitropyrene-co-pyrene) is lower than one would expect based on the starting materials,

which were used with a molar ratio of 1:1. With regards to the molecular weight determination it should be noted that similar to polypyrene,³¹¹ the poly(nitropyrene-*co*-pyrene) is only partially soluble in common organic solvents. Gel permeation chromatography (GPC) with tetrahydrofuran (THF) as eluent reveals that both for polypyrene and poly(nitropyrene-*co*-pyrene) the soluble fraction contains mostly oligomeric species with less than 10 repeating units (Figure 9.10.).

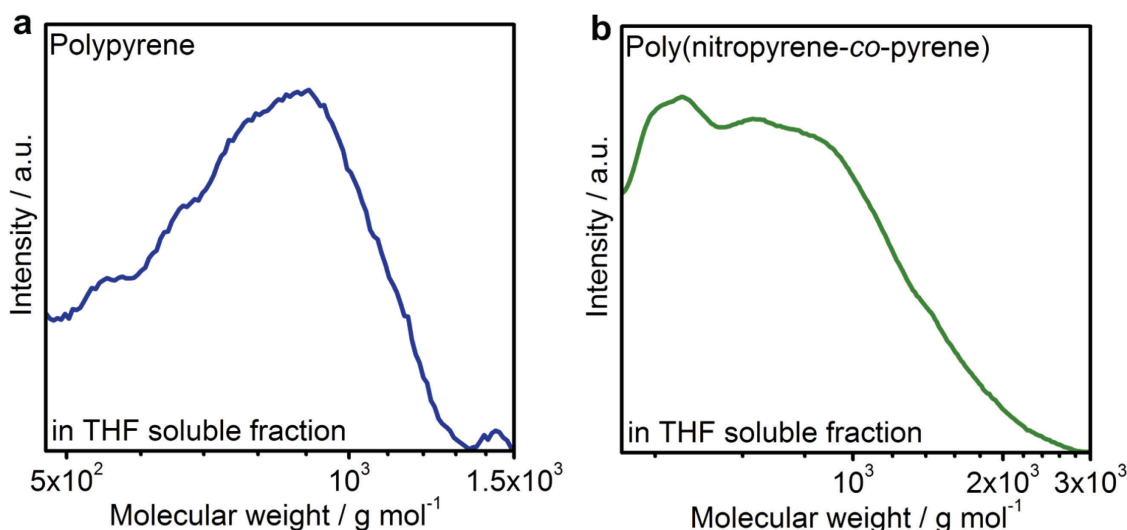


Figure 9.10. Gel permeation chromatography for the in THF soluble fractions of (a) polypyrene and (b) poly(nitropyrene-*co*-pyrene)

Figure 9.11. summarizes the electrochemical tests with poly(nitropyrene-*co*-pyrene) as cathode material in Al-ion batteries carried out at 200 mA g⁻¹ in the potential range 1.05-2.2 V using Al-foil as anode and [EMIm]Cl : AlCl₃ (molar ratio 1:1.3) as electrolyte. Similar to polypyrene almost no capacity fading was observed for 1000 cycles with a stable average discharge voltage of ~1.7 V. Relatively high coulombic and energy efficiencies were observed with values of on average 97% and 86% respectively. For comparison, inorganic cathode materials for Al-ion batteries such as Mo₆S₈³⁰⁴ or V₂O₅,^{305, 306} show much lower energy efficiencies due to drastic voltage hysteresis. Furthermore, even at a high rate of 2000 mA g⁻¹ the poly(nitropyrene-*co*-pyrene) shows only little capacity fading over 500 cycles with an average capacity of ~48 mAh g⁻¹ (Figure 9.12.).

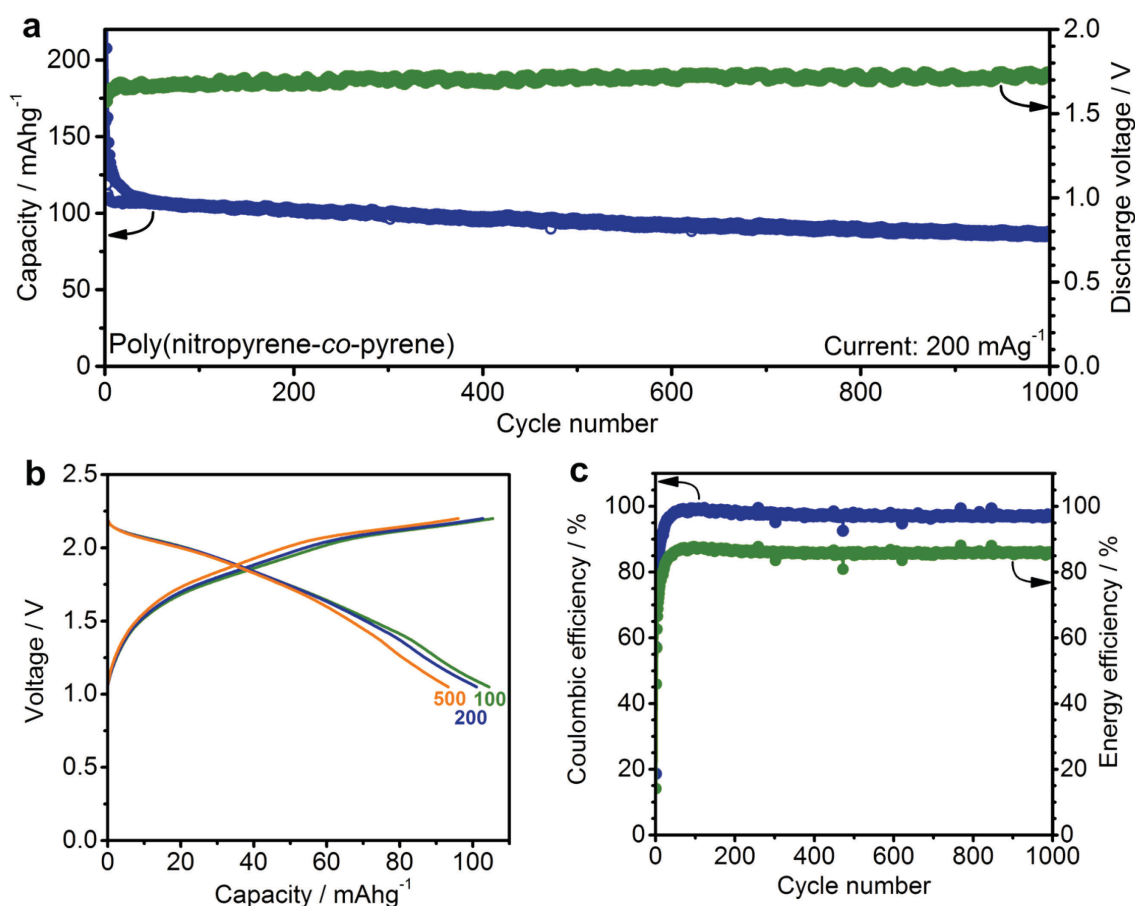


Figure 9.11. Electrochemical performance of Al-ion batteries with poly(nitropyrene-co-pyrene) as cathode material: (a) capacity retention and average discharge voltage, (b) corresponding charge/discharge curves for the 100th, 200th and 500th cycle and (c) coulombic and energy efficiency. Cells were cycled at room temperature with a current of 200 mA g⁻¹ in the potential range 1.05–2.2 V using Al-foil as anode and [EMIm]Cl : AlCl₃ (molar ratio 1:1.3) as electrolyte.

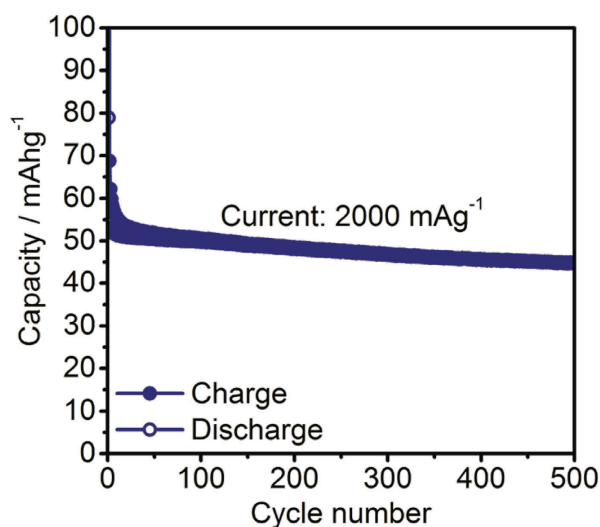


Figure 9.12. Capacity retention of poly(nitropyrene-co-pyrene) as cathode material in Al-ion batteries. Cells were cycled at room temperature with a current of 2000 mA g⁻¹ in the potential range 1.05–2.2 V using Al-foil as anode and [EMIm]Cl : AlCl₃ (molar ratio 1:1.3) as electrolyte.

Interestingly, the poly(nitropyrene-*co*-pyrene) shows significantly higher capacities than the polypyrene sample, yet the profile of the galvanostatic charge and discharge curves remains almost the same (Figure 9.11.b) indicating that the introduction of NO₂-groups is possibly not significant enough to affect the overall redox potential. Possible explanations for the higher observed capacity are that the poly(nitropyrene-*co*-pyrene) shows better dispersibility in NMP than the homopolymer and therefore potentially better contact with the conductive additive carbon black or structural differences between homo- and copolymer (*e.g.*, space between polymer chains) that lead to utilization of a higher fraction of active material. However, it should be noted that much poorer battery performance was observed for materials obtained by polymerization of 1-nitropyrene only (Figure 9.13.). In the presently only other report on polymers as cathode materials for Al-ion batteries, namely polythiophene and polypyrrole,³¹⁶ poorer performance compared to poly(nitropyrene-*co*-pyrene) was reported in terms of discharge voltage, cycle number and rate performance (see Table 9.1. for detailed comparison).

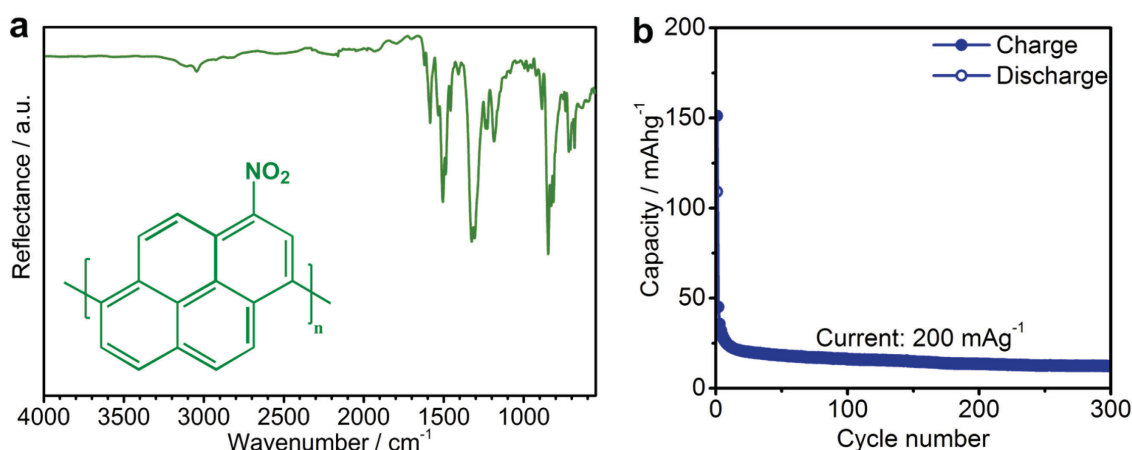


Figure 9.13. (a) FTIR-spectrum and (b) capacity retention for polynitropyrene prepared using the same conditions as for polypyrene and poly(nitropyrene-*co*-pyrene) with only 1-nitropyrene as starting material. Cells were cycled at room temperature with a current of 200 mA g⁻¹ in the potential range 1.05-2.2 V using Al-foil as anode and [EMIm]Cl : AlCl₃ (molar ratio 1:1.3) as electrolyte.

Table 9.1. Comparison of the electrochemical performance of the herein presented polypyrene and with other polymeric materials reported as cathode materials for Al-ion batteries.

Cathode material	Current density (mA g ⁻¹)	Average capacity (mA g ⁻¹)	Cycle number	Average discharge voltage (V)
Poly(nitropyrene- <i>co</i> -pyrene) (present work)	200	~100 ~94	500 1000	~1.7
Polypyrrole ³¹⁶	20	~55	100	~1.2
Polythiophene ³¹⁶	16	~75	100	~1.4

Further, the energy density of the cathode was estimated roughly as product of average discharge capacity (94 mAh g^{-1}) and voltage (1.70 V) leading to values of approximately 160 Wh kg^{-1} , which is higher than the state-of-the-art cathode material for Al-ion batteries pyrolytic graphite ($\sim 132 \text{ Wh kg}^{-1}$ based on 66 mAh g^{-1} as capacity and 2.0 V discharge voltage),⁴¹ exemplifying the great utility of polymeric materials, and, in particular, copolymers, as cathode materials for Al-ion batteries. In fact, polycyclic aromatic carbons in general offer numerous possibilities to tune the electrochemical properties such as redox potential and conductivity thanks to extensive studies on these materials for organic electronics.^{119, 317} In addition, general technological and economic advantages over classical inorganic compounds as cathode materials for Al-ion batteries, are their better processability, lower cost due to absence of expensive transition metals and non-essentiality for high-temperature annealing, since high crystallinity is not an requirement.³¹⁸

9.4. Conclusion

In summary, a proof-of-concept high-performance Al-ion battery was demonstrated with inexpensive pyrene-based polymers as cathode materials. Whereas, crystalline monomeric pyrene shows insignificant capacities, good electrochemical performance was obtained for amorphous polypyrene as cathode material in Al-ion batteries, which could be improved further by using a copolymer of pyrene and nitropyrene. In particular, stable cycling with an average capacity of 94 mAh g^{-1} and a discharge voltage of 1.70 V for 1000 cycles at a current of 200 mA g^{-1} was demonstrated for poly(nitropyrene-*co*-pyrene) with high coulombic (97-98%) and energy efficiencies (86%). In light of the vast possibilities polymeric compounds, in particular polymeric aromatic hydrocarbons, offer in terms of compositional and structural tunability, this work illustrates the great utility of such compounds as electrode materials for emerging electrochemical energy storage solutions.

Reproduced with modifications from:

M. Walter, C. Böfer, K. V. Kravchyk, and M. V. Kovalenko. *Pyrene-based polymers as high-performance cathode materials for Al-ion batteries*. In preparation.

Chapter 10. Conclusions and outlook



10.1. Conclusions

This dissertation encompassed seven different projects, with three focusing mainly on the development of simple synthetic procedures for metallic and intermetallic nanostructured anode materials for Li- and Na-ion storage (Chapters 3-5) and two on the evaluation metal sulfide and phosphide nanocrystals as potential Na-ion anode materials (Chapters 6-7). In the last two chapters conceptually very novel battery systems were explored with the first demonstration of a Na/Mg hybrid battery (Chapter 8) and a high-performance Al-ion battery enabled by a polymeric cathode material (Chapter 9). The main results are the following:

- (1) Sb NCs can be inexpensively synthesized with high reaction yield by simple reduction of the metal chloride with NaBH_4 in NMP and subsequent purification with water. Such Sb NCs show outstanding rate performance and cycling stability as Na-ion anode material with capacities close to the theoretical value of 660 mAh g^{-1} . The typically poor cycling stability of red P was significantly improved by devising a P/Sb/Cu composite *via* simple mechanic mixing of Sb NCs with “bulk” red P and Cu NWs with capacities resulting in capacities of $> 1300 \text{ mAh g}^{-1}$ for 30 cycles and $> 1100 \text{ mAh g}^{-1}$ after 50 cycles at 125 mA g^{-1} .
- (2) The same inexpensive, surfactant-free procedure to synthesize Sb NCs can be adopted for the synthesis of intermetallic SnSb nanoalloys, notably with the same short reaction time and very moderate reaction temperature of 60°C . Such SnSb NCs deliver stable capacities close to the theoretical capacity for Li-ion storage with a value of 760 mAh g^{-1} for 100 cycles at a high rate of 1000 mA g^{-1} . For Na-ion storage lower capacities are obtained, most likely due to the incomplete sodiation of Sn phases, however, the relative capacity retention is at high rates even better than for Li-ion storage. Full cell experiments show generally better

performance of the Li-ion cells (with LiCoO_2 as cathode) compared to the Na-ion counterparts (with $\text{Na}_{1.5}\text{VPO}_{4.8}\text{F}_{0.7}$ as the cathode) with an anodic capacity of 600 mAh g^{-1} and discharge voltage of 3.0 V .

(3) To evaluate Co-Sn based NPs as anode material for LIBs, it was shown that NPs of Co and Sn with diameters of $\leq 10 \text{ nm}$ can be synthesized *via* simple reduction of their respective chlorides using NaBH_4 in NMP and subsequently converted into intermetallic Co-Sn NPs by ball-milling. CoSn_2O_x NPs prepared by ball-milling in air show outstanding cycling stability as anode material tested in Li-ion half-cells with only 8% capacity loss over 1500 cycles at a high cycling rate of 1984 mA g^{-1} . In Li-ion full-cells with LiCoO_2 as cathode material CoSn_2O_x NPs provide a capacity of $\sim 580 \text{ mAh g}^{-1}$ with an average discharge voltage of 3.14 V .

(4) Pyrite FeS_2 NCs were investigated for the first time as potential inexpensive, high-capacity anode material for Na-ion batteries. Whereas also very high specific capacities of $\geq 630 \text{ mAh g}^{-1}$ for 100 cycles (at a current of 200 mA g^{-1}) were obtained for testing FeS_2 NCs as Li-ion cathode material, even higher capacities were obtained as Na-ion anode material with capacities of $\geq 500 \text{ mAh g}^{-1}$ retained after 400 cycles at a current density of 1000 mA g^{-1} . Notably, FeS_2 NCs not only surpass bulk FeS_2 in terms of capacity level, but also numerous other nanostructured metal sulfides such as NiS_2 , CoS_2 , PbS , SnS , CuS , ZnS and $\text{Cu}_2\text{ZnSnS}_4$.

(5) Based on the very high theoretical capacities ($\sim 1000 \text{ mAh g}^{-1}$) the first row transition metal phosphides FeP , CoP , NiP_2 and CuP_2 were investigated as potential anode materials for Na-ion batteries in form of colloidal NCs. Despite high initial capacities, rather poor capacity retention was obtained. The direct comparison of the FeP and FeS_2 NCs, which have similar theoretical capacities, illustrates the generally better cyclability of the metal sulfide. Most likely the large volume changes occurring during sodiation and reactivity of the carbonate-based electrolyte towards the discharge product $\text{Na}_3\text{P}^{146}$ explain the relatively poor cycling stability of the metal phosphide NCs.

(6) For the first time a proof-of-concept Na/Mg hybrid battery was presented using metallic magnesium as anode material, FeS_2 NCs as cathode material and an electrolyte containing both Na- and Mg-ions. FeS_2 NCs as cathode material deliver an average discharge capacity of $\sim 190 \text{ mAh g}^{-1}$ with a discharge voltage of $\sim 1.0 \text{ V}$ and high coulombic efficiency

of ~99.8% in this hybrid battery. Based on earth-abundant elements only such Na/Mg hybrid battery can potentially be an option in the future for applications requiring rather low cost than high energy density such as large-scale energy storage.

(7) A proof-of-concept high-performance Al-ion battery with an inexpensive polypyrene-based cathode material was presented to demonstrate the great utility of such compounds as electrode materials for emerging electrochemical energy storage solutions. Compared to monomeric crystalline pyrene, amorphous polypyrene shows significantly improved electrochemical properties, which can be further tuned by using a copolymer of pyrene and 1-nitropyrene. In particular, the electrochemical properties of poly(nitropyrene-*co*-pyrene) are characterized by a high discharge voltage of ~1.7 V, a stable capacity of ~100 mAh g⁻¹ and energy efficiency of ~85% for at least 1000 cycles at a current of 200 mA g⁻¹.

10.2. Outlook

In light of the numerous requirements batteries need to fulfill in terms of performance, cost and safety, predicting, which type of battery might be commercialized in the future, is almost impossible, especially for such technologically immature systems such as Na-, Mg- or Al-ion batteries. In case of the inexpensively synthesized metallic and intermetallic NPs (Chapters 3-5), which also resulted in two patent applications, upscaling of the procedure and electrochemical testing is currently carried out by Belenos Clean Power Holding Ltd. in order to evaluate, if the higher capacity and high rate performance can be translated to practical cells. A major remaining challenge in this regard, and for nanomaterials in general, will be to find solutions for the large irreversible charge loss caused by the SEI formation in the first cycle(s).

As potential anode materials for Na-ion batteries numerous different materials ranging from metallic nanocrystals to metal sulfides and metal phosphides have been investigated (Chapters 3-4, 6-7). Particularly, in case of metal phosphides and phosphorus containing composites, the cycling stability is not sufficient requiring the development of superior electrolytes. However, it should also be noted that for practical applications concerns regarding toxicity of phosphorus containing materials for practical cells exist, since in the charged state phosphorus is converted into Na₃P, which would in case of cell breakage readily react with water to form highly toxic and flammable PH₃. An important consideration for future work on anode materials must also be the overall cost of the entire system, since conceptually the only advantage of Na-ion batteries lies in the lower cost of sodium-salts and

the fact that cheaper aluminum-current collectors can be used on the anode side (because sodium unlike lithium does not alloy with aluminum). Hence, in order to have an overall economic advantage the employed electrode materials must not be more expensive than their Li-ion counterparts. In case of Sb-based materials, which were shown to be excellent anode materials for Na-ion storage, a future question will be, if this material is truly a good choice as commercial anode material, since it is geographically just as unequally distributed as lithium-salts (with China holding the main reserves). In terms of economic and environmental considerations “fool’s gold” FeS₂ NCs of Chapter 6 are probably the most promising anode materials for Na-ion storage presented in this thesis. Despite the very high capacity and rate capability of FeS₂ NCs a future question will be, if this material can be useful for practical cells due to its relatively high desodiation voltage.

In fact, as low-cost batteries for large-scale energy storage possibly the herein presented proof-of-concept Na/Mg hybrid battery (Chapter 8) or Al-ion battery (Chapter 9) might emerge as more viable candidates than Na-ion batteries. However, both of these battery systems are still in their infancy and require much more extensive work with regards to electrolyte formulations and high-loading electrodes. Particularly, the development of electrolytes with higher oxidative stability is ultimately the key to improve both Na/Mg hybrid and Al-ion batteries in terms of energy density, since it will allow the use of materials with higher operating voltages. In light of the significant interest the work on Na/Mg hybrid batteries³⁰³ has received (highlighted in > 20 news outlets including *NZZ*, *Blick*, *American Chemical Society News*; among Top 20 most downloaded *Chemistry of Materials* articles for the previous 12 months as of May 2016), further exploration and evaluation of this novel battery type is expected in the future.

References

1. R. Korthauer, *Handbuch Lithium-Ionen-Batterien*, Springer, 2013.
2. B. Dunn, H. Kamath and J.-M. Tarascon, *Science*, 2011, **334**, 928-935.
3. G. L. Soloveichik, *Annu. Rev. Chem. Biomol. Eng.*, 2011, **2**, 503-527.
4. O. Gröger, H. A. Gasteiger and J.-P. Suchsland, *J. Electrochem. Soc.*, 2015, **162**, A2605-A2622.
5. P. W. Atkins and J. de Paula, *Physikalische Chemie*, WILEY-VCH Verlag GmbH & Co. KGaA, 2006.
6. V. S. Bagotsky, in *Fundamentals of Electrochemistry*, John Wiley & Sons, Inc., 2005, DOI: 10.1002/047174199X.ch3, pp. 33-50.
7. C. Lefrou, P. Fabry and J.-C. Poignet, *Electrochemistry: the basics, with examples*, Springer Science & Business Media, 2012.
8. V. S. Bagotsky, in *Fundamentals of Electrochemistry*, John Wiley & Sons, Inc., 2005, DOI: 10.1002/047174199X.ch19, pp. 343-360.
9. J. M. Tarascon and M. Armand, *Nature*, 2001, **414**, 359-367.
10. Z. Li, J. Huang, B. Yann Liaw, V. Metzler and J. Zhang, *J. Power Sources*, 2014, **254**, 168-182.
11. K. Brandt, *Solid State Ionics*, 1994, **69**, 173-183.
12. J. B. Goodenough, *Acc. Chem. Res.*, 2013, **46**, 1053-1061.
13. J. B. Goodenough and K.-S. Park, *J. Am. Chem. Soc.*, 2013, **135**, 1167-1176.
14. K. Xu, *Chem. Rev.*, 2004, **104**, 4303-4418.
15. M. Zou, M. Yoshio, S. Gopukumar and J.-i. Yamaki, *Chem. Mater.*, 2003, **15**, 4699-4702.
16. M. F. Oszejca, M. I. Bodnarchuk and M. V. Kovalenko, *Chem. Mater.*, 2014, **26**, 5422-5432.
17. K. M. Abraham, *J. Phys. Chem. Lett.*, 2015, **6**, 830-844.
18. L. L. Gaines and R. M. Cuenca, Costs of lithium-ion batteries for vehicles, <http://ntl.bts.gov/lib/14000/14700/14729/DE00761281.pdf>, (accessed 07.06.2016).
19. M. R. Palacin, *Chem. Soc. Rev.*, 2009, **38**, 2565-2575.
20. P. Dvorak, Battery stores 40 MW for Fairbanks, Alaska emergencies, <http://www.windpowerengineering.com/design/electrical/battery-stores-40-mw-for-ankorage-emergencies/>, (accessed 02.06.2016).
21. *Overview on global battery markets*, Frost & Sullivan, 2009.
22. M. Ehsani, Y. Gao and A. Emadi, *Modern electric, hybrid electric, and fuel cell vehicles: fundamentals, theory, and design*, CRC press, 2009.
23. H. Pan, Y.-S. Hu and L. Chen, *Energy Environ. Sci.*, 2013, **6**, 2338-2360.
24. M. D. Slater, D. Kim, E. Lee and C. S. Johnson, *Angew. Chem. Int. Ed.*, 2013, **23**, 947-958.
25. V. Palomares, P. Serras, I. Villaluenga, K. B. Hueso, J. Carretero-Gonzalez and T. Rojo, *Energy Environ. Sci.*, 2012, **5**, 5884-5901.
26. M. Walter, R. Erni and M. V. Kovalenko, *Sci. Rep.*, 2015, **5**, 08418.
27. J. Qian, X. Wu, Y. Cao, X. Ai and H. Yang, *Angew. Chem. Int. Ed.*, 2013, **52**, 4633-4636.
28. Y. Kim, Y. Park, A. Choi, N.-S. Choi, J. Kim, J. Lee, J. H. Ryu, S. M. Oh and K. T. Lee, *Adv. Mater.*, 2013, **25**, 3045-3049.
29. W.-H. Ryu, J.-W. Jung, K. Park, S.-J. Kim and I.-D. Kim, *Nanoscale*, 2014, **6**, 10975-10981.
30. B. Farbod, K. Cui, W. P. Kalisvaart, M. Kupsta, B. Zahiri, A. Kohandehghan, E. M. Lotfabad, Z. Li, E. J. Lubner and D. Mitlin, *ACS Nano*, 2014, **8**, 4415-4429.

31. E. M. Lotfabad, J. Ding, K. Cui, A. Kohandehghan, W. P. Kalisvaart, M. Hazelton and D. Mitlin, *ACS Nano*, 2014, **8**, 7115-7129.
32. M. Walter, T. Zund and M. V. Kovalenko, *Nanoscale*, 2015, **7**, 9158-9163.
33. M. Pasta, C. D. Wessells, N. Liu, J. Nelson, M. T. McDowell, R. A. Huggins, M. F. Toney and Y. Cui, *Nat. Commun.*, 2014, **5**.
34. Y. You, X.-L. Wu, Y.-X. Yin and Y.-G. Guo, *Energy Environ. Sci.*, 2014, **7**, 1643-1647.
35. L. Wang, Y. Lu, J. Liu, M. Xu, J. Cheng, D. Zhang and J. B. Goodenough, *Angew. Chem., Int. Ed.*, 2013, **52**, 1964-1967.
36. D. Aurbach, Z. Lu, A. Schechter, Y. Gofer, H. Gizbar, R. Turgeman, Y. Cohen, M. Moshkovich and E. Levi, *Nature*, 2000, **407**, 724-727.
37. H. D. Yoo, I. Shterenberg, Y. Gofer, G. Gershtinsky, N. Pour and D. Aurbach, *Energy Environ. Sci.*, 2013, **6**, 2265-2279.
38. M.-S. Park, J.-G. Kim, Y.-J. Kim, N.-S. Choi and J.-S. Kim, *Isr. J. Chem.*, 2015, **55**, 570-585.
39. J. Muldoon, C. B. Bucur and T. Gregory, *Chem. Rev.*, 2014, **114**, 11683-11720.
40. I. Shterenberg, M. Salama, Y. Gofer, E. Levi and D. Aurbach, *MRS Bull.*, 2014, **39**, 453-460.
41. M.-C. Lin, M. Gong, B. Lu, Y. Wu, D.-Y. Wang, M. Guan, M. Angell, C. Chen, J. Yang, B.-J. Hwang and H. Dai, *Nature*, 2015, **520**, 324-328.
42. L. Tan and Y. Chi-lung, *Int. Geol. Rev.*, 1970, **12**, 778-786.
43. R. Berthelot, D. Carlier and C. Delmas, *Nat. Mater.*, 2011, **10**, 74-80.
44. Y. U. Park, D. H. Seo, H. S. Kwon, B. Kim, J. Kim, H. Kim, I. Kim, H. I. Yoo and K. Kang, *J. Am. Chem. Soc.*, 2013, **135**, 13870-13878.
45. M. Nose, H. Nakayama, K. Nobuhara, H. Yamaguchi, S. Nakanishi and H. Iba, *J. Power Sources*, 2013, **234**, 175-179.
46. M. Jäckle and A. Groß, *J. Chem. Phys.*, 2014, **141**, 174710.
47. B. Jache and P. Adelhelm, *Angew. Chem. Int. Ed.*, 2014, **53**, 10169-10173.
48. S. Yagi, T. Ichitsubo, Y. Shirai, S. Yanai, T. Doi, K. Murase and E. Matsubara, *J. Mater. Chem. A*, 2014, **2**, 1144-1149.
49. J. Muldoon, C. B. Bucur, A. G. Oliver, T. Sugimoto, M. Matsui, H. S. Kim, G. D. Allred, J. Zajicek and Y. Kotani, *Energy Environ. Sci.*, 2012, **5**, 5941-5950.
50. J. Song, E. Sahadeo, M. Noked and S. B. Lee, *J. Phys. Chem. Lett.*, 2016, **7**, 1736-1749.
51. R. E. Doe, R. Han, J. Hwang, A. J. Gmitter, I. Shterenberg, H. D. Yoo, N. Pour and D. Aurbach, *Chem. Commun.*, 2014, **50**, 243-245.
52. K. T. Lee and J. Cho, *Nano Today*, 2011, **6**, 28-41.
53. L. Ji, Z. Lin, M. Alcoutlabi and X. Zhang, *Energy Environ. Sci.*, 2011, **4**, 2682-2699.
54. C. Liu, F. Li, L.-P. Ma and H.-M. Cheng, *Adv. Mater.*, 2010, **22**, E28-E62.
55. C. Jiang, E. Hosono and H. Zhou, *Nano Today*, 2006, **1**, 28-33.
56. P. G. Bruce, B. Scrosati and J.-M. Tarascon, *Angew. Chem. Int. Ed.*, 2008, **47**, 2930-2946.
57. M. He, K. Kravchyk, M. Walter and M. V. Kovalenko, *Nano Lett.*, 2014, **14**, 1255-1262.
58. K. Kravchyk, L. Protesescu, M. I. Bodnarchuk, F. Krumeich, M. Yarema, M. Walter, C. Guntlin and M. V. Kovalenko, *J. Am. Chem. Soc.*, 2013, **135**, 4199-4202.
59. C. K. Chan, H. Peng, G. Liu, K. McIlwrath, X. F. Zhang, R. A. Huggins and Y. Cui, *Nat. Nanotechnol.*, 2008, **3**, 31-35.
60. W.-J. Zhang, *J. Power Sources*, 2011, **196**, 13-24.
61. Y. Kim, K.-H. Ha, S. M. Oh and K. T. Lee, *Chem. - Eur. J.*, 2014, **20**, 11980-11992.

-
62. N. Liu, Z. Lu, J. Zhao, M. T. McDowell, H. W. Lee, W. Zhao and Y. Cui, *Nat. Nanotechnol.*, 2014, **9**, 187-192.
 63. A. Magasinski, P. Dixon, B. Hertzberg, A. Kvit, J. Ayala and G. Yushin, *Nat. Mater.*, 2010, **9**, 353-358.
 64. M. He, M. Walter, K. V. Kravchyk, R. Erni, R. Widmer and M. V. Kovalenko, *Nanoscale*, 2015, **7**, 455-459.
 65. J. Liu, Y. Wen, P. A. van Aken, J. Maier and Y. Yu, *Nano Lett.*, 2014, **14**, 6387-6392.
 66. A. Jahel, C. M. Ghimbeu, L. Monconduit and C. Vix-Guterl, *Adv. Energy Mater.*, 2014, **4**, 1400025.
 67. C. Guo, L. Wang, Y. Zhu, D. Wang, Q. Yang and Y. Qian, *Nanoscale*, 2015, 10123-10129.
 68. G. Zeng, N. Shi, M. Hess, X. Chen, W. Cheng, T. Fan and M. Niederberger, *ACS Nano*, 2015, **9**, 4227-4235.
 69. J. Zhang, K. Wang, Q. Xu, Y. Zhou, F. Cheng and S. Guo, *ACS Nano*, 2015, **9**, 3369-3376.
 70. X.-Y. Yu, H. Hu, Y. Wang, H. Chen and X. W. Lou, *Angew. Chem. Int. Ed.*, 2015, 7395-7398.
 71. J. Zhou, J. Qin, X. Zhang, C. Shi, E. Liu, J. Li, N. Zhao and C. He, *ACS Nano*, 2015, **9**, 3837-3848.
 72. H. Hwang, H. Kim and J. Cho, *Nano Lett.*, 2011, **11**, 4826-4830.
 73. J. S. Cho, Y. J. Hong and Y. C. Kang, *ACS Nano*, 2015, **9**, 4026-4035.
 74. J. Hwang, S. H. Woo, J. Shim, C. Jo, K. T. Lee and J. Lee, *ACS Nano*, 2013, **7**, 1036-1044.
 75. X. Huang, S. Cui, J. Chang, P. B. Hallac, C. R. Fell, Y. Luo, B. Metz, J. Jiang, P. T. Hurley and J. Chen, *Angew. Chem. Int. Ed.*, 2015, **54**, 1490-1493.
 76. Y. Zhu, Y. Wen, X. Fan, T. Gao, F. Han, C. Luo, S.-C. Liou and C. Wang, *ACS Nano*, 2015, **9**, 3254-3264.
 77. X. H. Liu, L. Zhong, S. Huang, S. X. Mao, T. Zhu and J. Y. Huang, *ACS Nano*, 2012, **6**, 1522-1531.
 78. C. Delmas, J.-J. Braconnier, C. Fouassier and P. Hagenmuller, *Solid State Ionics*, 1981, **3**, 165-169.
 79. L. W. Shacklette, T. R. Jow and L. Townsend, *J. Electrochem. Soc.*, 1988, **135**, 2669-2674.
 80. P. Ge, *Solid State Ionics*, 1988, **28-30**, 1172-1175.
 81. S. Komaba, Y. Matsuura, T. Ishikawa, N. Yabuuchi, W. Murata and S. Kuze, *Electrochem. Commun.*, 2012, **21**, 65-68.
 82. A. Darwiche, C. Marino, M. T. Sougrati, B. Fraisse, L. Stievano and L. Monconduit, *J. Am. Chem. Soc.*, 2012, **134**, 20805-20811.
 83. W. M. Zhang, J. S. Hu, Y. G. Guo, S. F. Zheng, L. S. Zhong, W. G. Song and L. J. Wan, *Adv. Mater.*, 2008, **20**, 1160-1165.
 84. G. Derrien, J. Hassoun, S. Panero and B. Scrosati, *Adv. Mater.*, 2007, **19**, 2336-2340.
 85. M. Wachtler, J. O. Besenhard and M. Winter, *J. Power Sources*, 2001, **94**, 189-193.
 86. Y. Xu, Q. Liu, Y. Zhu, Y. Liu, A. Langrock, M. R. Zachariah and C. Wang, *Nano Lett.*, 2013, **13**, 470-474.
 87. N. Tamura, Y. Kato, A. Mikami, M. Kamino, S. Matsuta and S. Fujitani, *J. Electrochem. Soc.*, 2006, **153**, A1626-A1632.
 88. C. M. Ionica-Bousquet, P. E. Lippens, L. Aldon, J. Olivier-Fourcade and J. C. Jumas, *Chem. Mater.*, 2006, **18**, 6442-6447.
 89. S.-I. Lee, S. Yoon, C.-M. Park, J.-M. Lee, H. Kim, D. Im, S.-G. Doo and H.-J. Sohn, *Electrochim. Acta*, 2008, **54**, 364-369.
-

-
90. F. Klein, B. Jache, A. Bhide and P. Adelhelm, *Phys. Chem. Chem. Phys.*, 2013, **15**, 15876-15887.
 91. G. S. Bang, K. W. Nam, J. Y. Kim, J. Shin, J. W. Choi and S.-Y. Choi, *ACS Appl. Mater. Interfaces*, 2014, **6**, 7084-7089.
 92. L. David, R. Bhandavat and G. Singh, *ACS Nano*, 2014, **8**, 1759-1770.
 93. Z. Hu, L. Wang, K. Zhang, J. Wang, F. Cheng, Z. Tao and J. Chen, *Angew. Chem. Int. Ed.*, 2014, **53**, 12794-12798.
 94. C. Zhu, X. Mu, P. A. van Aken, Y. Yu and J. Maier, *Angew. Chem. Int. Ed.*, 2014, **53**, 2152-2156.
 95. D. Su, S. Dou and G. Wang, *Chem. Commun.*, 2014, **50**, 4192-4195.
 96. P. K. Dutta, U. K. Sen and S. Mitra, *RSC Adv.*, 2014, **4**, 43155-43159.
 97. L. Wu, H. Lu, L. Xiao, J. Qian, X. Ai, H. Yang and Y. Cao, *J. Mater. Chem. A*, 2014, **2**, 16424-16428.
 98. T. Zhou, W. K. Pang, C. Zhang, J. Yang, Z. Chen, H. K. Liu and Z. Guo, *ACS Nano*, 2014, **8**, 8323-8333.
 99. B. Qu, C. Ma, G. Ji, C. Xu, J. Xu, Y. S. Meng, T. Wang and J. Y. Lee, *Adv. Mater.*, 2014, **26**, 3854-3859.
 100. D. Y. Yu, P. V. Prihodchenko, C. W. Mason, S. K. Batabyal, J. Gun, S. Sladkevich, A. G. Medvedev and O. Lev, *Nat. Commun.*, 2013, **4**, 2922.
 101. W.-J. Li, S.-L. Chou, J.-Z. Wang, H.-K. Liu and S.-X. Dou, *Chem. Commun.*, 2015, **51**, 3682-3685.
 102. P. Saha, M. K. Datta, O. I. Velikokhatnyi, A. Manivannan, D. Alman and P. N. Kumta, *Prog. Mater. Sci.*, 2014, **66**, 1-86.
 103. L. Jiao, H. Yuan, Y. Wang, J. Cao and Y. Wang, *Electrochem. Commun.*, 2005, **7**, 431-436.
 104. K. W. Nam, S. Kim, S. Lee, M. Salama, I. Shterenberg, Y. Gofer, J.-S. Kim, E. Yang, C. S. Park, J.-S. Kim, S.-S. Lee, W.-S. Chang, S.-G. Doo, Y. N. Jo, Y. Jung, D. Aurbach and J. W. Choi, *Nano Lett.*, 2015, **15**, 4071-4079.
 105. R. Y. Wang, C. D. Wessells, R. A. Huggins and Y. Cui, *Nano Lett.*, 2013, **13**, 5748-5752.
 106. G. Gershinsky, H. D. Yoo, Y. Gofer and D. Aurbach, *Langmuir*, 2013, **29**, 10964-10972.
 107. B. Liu, T. Luo, G. Mu, X. Wang, D. Chen and G. Shen, *ACS Nano*, 2013, **7**, 8051-8058.
 108. Y. NuLi, Y. Zheng, F. Wang, J. Yang, A. I. Minett, J. Wang and J. Chen, *Electrochem. Commun.*, 2011, **13**, 1143-1146.
 109. S. Rasul, S. Suzuki, S. Yamaguchi and M. Miyayama, *Solid State Ionics*, 2012, **225**, 542-546.
 110. S. H. Lee, R. A. DiLeo, A. C. Marschilok, K. J. Takeuchi and E. S. Takeuchi, *ECS Electrochem. Lett.*, 2014, **3**, A87-A90.
 111. H. D. Yoo, Y. Liang, Y. Li and Y. Yao, *ACS Appl. Mater. Interfaces*, 2015, **7**, 7001-7007.
 112. Y. Cheng, Y. Shao, J.-G. Zhang, V. L. Sprenkle, J. Liu and G. Li, *Chem. Commun.*, 2014, **50**, 9644-9646.
 113. S. Su, Z. Huang, Y. NuLi, F. Tuerxun, J. Yang and J. Wang, *Chem. Commun.*, 2015, **51**, 2641-2644.
 114. T. Ichitsubo, S. Okamoto, T. Kawaguchi, Y. Kumagai, F. Oba, S. Yagi, N. Goto, T. Doi and E. Matsubara, *J. Mater. Chem. A*, 2015, **3**, 10188-10194.
 115. T. Gao, F. Han, Y. Zhu, L. Suo, C. Luo, K. Xu and C. Wang, *Adv. Energy Mater.*, 2015, **5**, 1401507.
-

116. J.-H. Cho, M. Aykol, S. Kim, J.-H. Ha, C. Wolverton, K. Y. Chung, K.-B. Kim and B.-W. Cho, *J. Am. Chem. Soc.*, 2014, **136**, 16116-16119.
117. J. C. Bachman, R. Kavian, D. J. Graham, D. Y. Kim, S. Noda, D. G. Nocera, Y. Shao-Horn and S. W. Lee, *Nat. Commun.*, 2015, **6**.
118. S. C. Han, E. G. Bae, H. Lim and M. Pyo, *J. Power Sources*, 2014, **254**, 73-79.
119. T. M. Figueira-Duarte and K. Müllen, *Chem. Rev.*, 2011, **111**, 7260-7314.
120. C. B. Murray, D. J. Norris and M. G. Bawendi, *J. Am. Chem. Soc.*, 1993, **115**, 8706-8715.
121. S. G. Kwon and T. Hyeon, *Small*, 2011, **7**, 2685-2702.
122. N. T. K. Thanh, N. Maclean and S. Mahiddine, *Chem. Rev.*, 2014, **114**, 7610-7630.
123. Y. Yin and A. P. Alivisatos, *Nature*, 2005, **437**, 664-670.
124. D. B. Williams and C. B. Carter, in *Transmission Electron Microscopy: A Textbook for Materials Science*, Springer US, Boston, MA, 1996, DOI: 10.1007/978-1-4757-2519-3_1, pp. 3-17.
125. A. E. Vladár and M. T. Postek, *Handbook of Charged Particle Optics*, 2008, 437.
126. J. I. Goldstein, D. E. Newbury, P. Echlin, D. C. Joy, C. E. Lyman, E. Lifshin, L. Sawyer and J. R. Michael, in *Scanning Electron Microscopy and X-ray Microanalysis: Third Edition*, Springer US, Boston, MA, 2003, DOI: 10.1007/978-1-4615-0215-9_6, pp. 271-296.
127. W. L. Bragg, *Proc. R. Soc. London, Ser. A*, 1913, **89**, 248-277.
128. W. Massa, *Kristallstrukturbestimmung*, Springer, 2007.
129. P. Scherrer, *Bestimmung der inneren Struktur und der Größe von Kolloidteilchen mittels Röntgenstrahlen*, Springer, 1912.
130. A. Miranda and A. R. Barron, Attenuated Total Reflectance-Fourier Transform Infrared Spectroscopy, <http://cnx.org/contents/1051014e-cbb8-45a7-a744-29dcad4cb522@2>, (accessed 06.06.2016).
131. B. C. Smith, in *Fundamentals of Fourier Transform Infrared Spectroscopy, Second Edition*, CRC Press, 2011, DOI: doi:10.1201/b10777-5, pp. 87-146.
132. B. C. Smith, in *Fundamentals of Fourier Transform Infrared Spectroscopy, Second Edition*, CRC Press, 2011, DOI: doi:10.1201/b10777-2, pp. 1-17.
133. S. Califano and G. Abbondanza, *J. Chem. Phys.*, 1963, **39**, 1016-1023.
134. R. Van Noorden, *Nature*, 2014, **507**, 26-28.
135. D. Yuan, W. He, F. Pei, F. Wu, Y. Wu, J. Qian, Y. Cao, X. Ai and H. Yang, *J. Mater. Chem. A*, 2013, **1**, 3895-3899.
136. D. Buchholz, L. G. Chagas, M. Winter and S. Passerini, *Electrochim. Acta*, 2013, **110**, 208-213.
137. D. Buchholz, A. Moretti, R. Kloepsch, S. Nowak, V. Siozios, M. Winter and S. Passerini, *Chem. Mater.*, 2012, **25**, 142-148.
138. N. Yabuuchi, M. Kajiyama, J. Iwatate, H. Nishikawa, S. Hitomi, R. Okuyama, R. Usui, Y. Yamada and S. Komaba, *Nat. Mater.*, 2012, **11**, 512-517.
139. W. Huang, J. Zhou, B. Li, J. Ma, S. Tao, D. Xia, W. Chu and Z. Wu, *Sci. Rep.*, 2014, **4**, 4188; DOI:10.1038/srep04188.
140. Y. H. Lu, L. Wang, J. G. Cheng and J. B. Goodenough, *Chem. Commun.*, 2012, **48**, 6544-6546.
141. Y. Wen, K. He, Y. Zhu, F. Han, Y. Xu, I. Matsuda, Y. Ishii, J. Cumings and C. Wang, *Nat. Commun.*, 2014, **5**, 4033.
142. L. M. Wu, D. Buchholz, D. Bresser, L. G. Chagas and S. Passerini, *J. Power Sources*, 2014, **251**, 379-385.
143. Y. Wang, X. Yu, S. Xu, J. Bai, R. Xiao, Y. S. Hu, H. Li, X. Q. Yang, L. Chen and X. Huang, *Nat. Commun.*, 2013, **4**, 2365.

-
144. Y. Sun, L. Zhao, H. Pan, X. Lu, L. Gu, Y. S. Hu, H. Li, M. Armand, Y. Ikuhara, L. Chen and X. Huang, *Nat. Commun.*, 2013, **4**, 1870.
145. Y. M. Lin, P. R. Abel, A. Gupta, J. B. Goodenough, A. Heller and C. B. Mullins, *ACS Appl. Mater. Interfaces*, 2013, **5**, 8273-8277.
146. N. Yabuuchi, Y. Matsuura, T. Ishikawa, S. Kuze, J.-Y. Son, Y.-T. Cui, H. Oji and S. Komaba, *ChemElectroChem*, 2014, **1**, 580-589.
147. L. Xiao, Y. Cao, J. Xiao, W. Wang, L. Kovarik, Z. Nie and J. Liu, *Chem. Commun.*, 2012, **48**, 3321-3323.
148. A. Darwiche, M. T. Sougrati, B. Fraisse, L. Stievano and L. Monconduit, *Electrochem. Commun.*, 2013, **32**, 18-21.
149. Y. Zhu, X. Han, Y. Xu, Y. Liu, S. Zheng, K. Xu, L. Hu and C. Wang, *ACS Nano*, 2013, **7**, 6378-6386.
150. X. Zhou, Z. Dai, J. Bao and Y.-G. Guo, *J. Mater. Chem. A*, 2013, **1**, 13727-13731.
151. D. H. Nam, K. S. Hong, S. J. Lim and H. S. Kwon, *J. Power Sources*, 2014, **247**, 423-427.
152. L. Wu, X. Hu, J. Qian, F. Pei, F. Wu, R. Mao, X. Ai, H. Yang and Y. Cao, *Energy Environ. Sci.*, 2014, **7**, 323-328.
153. C. Nithya and S. Gopukumar, *J. Mater. Chem. A*, 2014, **2**, 10516-10525.
154. W.-J. Li, S.-L. Chou, J.-Z. Wang, H.-K. Liu and S.-X. Dou, *Nano Lett.*, 2013, **13**, 5480-5484.
155. J. B. Goodenough and Y. Kim, *Chem. Mater.*, 2009, **22**, 587-603.
156. N. Nitta and G. Yushin, *Part. Part. Syst. Char.*, 2014, **31**, 317-336.
157. Y.-S. Hu, R. Demir-Cakan, M.-M. Titirici, J.-O. Müller, R. Schlögl, M. Antonietti and J. Maier, *Angew. Chem. Int. Ed.*, 2008, **47**, 1645-1649.
158. Y. Yao, M. T. McDowell, I. Ryu, H. Wu, N. Liu, L. Hu, W. D. Nix and Y. Cui, *Nano Lett.*, 2011, **11**, 2949-2954.
159. H. Wu, G. Zheng, N. Liu, T. J. Carney, Y. Yang and Y. Cui, *Nano Lett.*, 2012, **12**, 904-909.
160. C. K. Chan, X. F. Zhang and Y. Cui, *Nano Lett.*, 2007, **8**, 307-309.
161. M.-H. Park, M. G. Kim, J. Joo, K. Kim, J. Kim, S. Ahn, Y. Cui and J. Cho, *Nano Lett.*, 2009, **9**, 3844-3847.
162. T. D. Bogart, D. Oka, X. Lu, M. Gu, C. Wang and B. A. Korgel, *ACS Nano*, 2013, **8**, 915-922.
163. A. M. Chockla, K. C. Klavetter, C. B. Mullins and B. A. Korgel, *Chem. Mater.*, 2012, **24**, 3738-3745.
164. A. M. Chockla, J. T. Harris, V. A. Akhavan, T. D. Bogart, V. C. Holmberg, C. Steinhagen, C. B. Mullins, K. J. Stevenson and B. A. Korgel, *J. Am. Chem. Soc.*, 2011, **133**, 20914-20921.
165. K. C. Klavetter, S. M. Wood, Y. M. Lin, J. L. Snider, N. C. Davy, A. M. Chockla, D. K. Romanovicz, B. A. Korgel, J. W. Lee, A. Heller and C. B. Mullins, *J. Power Sources*, 2013, **238**, 123-136.
166. S. D. Beattie, D. Larcher, M. Morcrette, B. Simon and J. M. Tarascon, *J. Electrochem. Soc.*, 2008, **155**, 158-163.
167. I. Kovalenko, B. Zdyrko, A. Magasinski, B. Hertzberg, Z. Milicev, R. Burtovyy, I. Luzinov and G. Yushin, *Science*, 2011, **333**, 75-79.
168. H. Guo, N. Lin, Y. Chen, Z. Wang, Q. Xie, T. Zheng, N. Gao, S. Li, J. Kang, D. Cai and D.-L. Peng, *Sci. Rep.*, 2013, **3**, 2323.
169. M. Heß and P. Novák, *Electrochim. Acta*, 2013, **106**, 149-158.
170. K. Nakahara, R. Nakajima, T. Matsushima and H. Majima, *J. Power Sources*, 2003, **117**, 131-136.
171. C.-M. Park, J.-H. Kim, H. Kim and H.-J. Sohn, *Chem. Soc. Rev.*, 2010, **39**, 3115-3141.
-

-
172. S. Li, Y. Chen, L. Huang and D. Pan, *Inorg. Chem.*, 2014, **53**, 4440-4444.
173. M. I. Bodnarchuk, K. V. Kravchyk, F. Krumeich, S. Wang and M. V. Kovalenko, *ACS Nano*, 2014, **8**, 2360-2368.
174. M. Zhang, Z. H. Wang, G. C. Xi, D. K. Ma, R. Zhang and Y. T. Qian, *J. Cryst. Growth*, 2004, **268**, 215-221.
175. G. Kieslich, C. S. Birkel, A. Stewart, U. Kolb and W. Tremel, *Inorg. Chem.*, 2011, **50**, 6938-6943.
176. Y. W. Wang, B. H. Hong, J. Y. Lee, J.-S. Kim, G. H. Kim and K. S. Kim, *J. Phys. Chem. B*, 2004, **108**, 16723-16726.
177. D. Larcher and J. M. Tarascon, *Nat. Chem.*, 2015, **7**, 19-29.
178. S. Fan, T. Sun, X. Rui, Q. Yan and H. H. Hng, *J. Power Sources*, 2012, **201**, 288-293.
179. L. Ji, M. Gu, Y. Shao, X. Li, M. H. Engelhard, B. W. Arey, W. Wang, Z. Nie, J. Xiao, C. Wang, J.-G. Zhang and J. Liu, *Adv. Mater.*, 2014, **26**, 2901-2908.
180. Y. Wang and J. Y. Lee, *Angew. Chem. Int. Ed.*, 2006, **45**, 7039-7042.
181. L. Fan, J. Zhang, Y. Zhu, X. Zhu, J. Liang, L. Wang and Y. Qian, *RSC Adv.*, 2014, **4**, 62301-62307.
182. D. Sun, B. An, B. Zhang, Q. Ru, X. Hou and S. Hu, *J. Solid State Electrochem.*, 2014, **18**, 2573-2579.
183. Y.-U. Park, D.-H. Seo, B. Kim, K.-P. Hong, H. Kim, S. Lee, R. A. Shakoor, K. Miyasaka, J.-M. Tarascon and K. Kang, *Sci. Rep.*, 2012, **2**, 00704.
184. L. Li, K. H. Seng, D. Li, Y. Xia, H. K. Liu and Z. Guo, *Nano Res.*, 2014, **7**, 1466-1476.
185. J. Xie, W. Song, Y. Zheng, S. Liu, T. Zhu, G. Cao and X. Zhao, *Int. J. Smart Nano Mater.*, 2011, **2**, 261-271.
186. V. Etacheri, O. Haik, Y. Goffer, G. A. Roberts, I. C. Stefan, R. Fasching and D. Aurbach, *Langmuir*, 2011, **28**, 965-976.
187. S. Komaba, T. Ishikawa, N. Yabuuchi, W. Murata, A. Ito and Y. Ohsawa, *ACS Appl. Mater. Interfaces*, 2011, **3**, 4165-4168.
188. Y. F. Zhukovskii, P. Balaya, E. A. Kotomin and J. Maier, *Phys. Rev. Lett.*, 2006, **96**, 058302.
189. Y.-Y. Hu, Z. Liu, K.-W. Nam, O. J. Borkiewicz, J. Cheng, X. Hua, M. T. Dunstan, X. Yu, K. M. Wiaderek, L.-S. Du, K. W. Chapman, P. J. Chupas, X.-Q. Yang and C. P. Grey, *Nat. Mater.*, 2013, **12**, 1130-1136.
190. S. Laruelle, S. Grugeon, P. Poizot, M. Dollé, L. Dupont and J.-M. Tarascon, *J. Electrochem. Soc.*, 2002, **149**, A627-A634.
191. J.-C. Kim and D.-W. Kim, *Electrochem. Commun.*, 2014, **46**, 124-127.
192. M.-S. Park, S. A. Needham, G.-X. Wang, Y.-M. Kang, J.-S. Park, S.-X. Dou and H.-K. Liu, *Chem. Mater.*, 2007, **19**, 2406-2410.
193. S. Chen, P. Chen, M. Wu, D. Pan and Y. Wang, *Electrochem. Commun.*, 2010, **12**, 1302-1306.
194. R. Yang, J. Huang, W. Zhao, W. Lai, X. Zhang, J. Zheng and X. Li, *J. Power Sources*, 2010, **195**, 6811-6816.
195. X. Niu, H. Zhou, Z. Li, X. Shan and X. Xia, *J. Alloys Compd.*, 2015, **620**, 308-314.
196. L. Baggetto, H.-Y. Hah, J.-C. Jumas, C. E. Johnson, J. A. Johnson, J. K. Keum, C. A. Bridges and G. M. Veith, *J. Power Sources*, 2014, **267**, 329-336.
197. P. K. Allan, J. M. Griffin, A. Darwiche, O. J. Borkiewicz, K. M. Wiaderek, K. W. Chapman, A. J. Morris, P. J. Chupas, L. Monconduit and C. P. Grey, *J. Am. Chem. Soc.*, 2016, DOI: 10.1021/jacs.5b13273.
198. L. D. Ellis, T. D. Hatchard and M. N. Obrovac, *J. Electrochem. Soc.*, 2012, **159**, A1801-A1805.
199. Z. Li, J. Ding and D. Mitlin, *Acc. Chem. Res.*, 2015, **48**, 1657-1665.
-

-
200. M. K. Datta, R. Epur, P. Saha, K. Kadakia, S. K. Park and P. N. Kumta, *J. Power Sources*, 2013, **225**, 316-322.
201. Y. Xu, Y. Zhu, Y. Liu and C. Wang, *Adv. Energy Mater.*, 2013, **3**, 128-133.
202. H. Zhu, Z. Jia, Y. Chen, N. Weadock, J. Wan, O. Vaaland, X. Han, T. Li and L. Hu, *Nano Lett.*, 2013, **13**, 3093-3100.
203. P. R. Kumar, Y. H. Jung, K. K. Bharathi, C. H. Lim and D. K. Kim, *Electrochim. Acta*, 2014, **146**, 503-510.
204. S.-M. Oh, S.-T. Myung, C. S. Yoon, J. Lu, J. Hassoun, B. Scrosati, K. Amine and Y.-K. Sun, *Nano Lett.*, 2014, **14**, 1620-1626.
205. S. Guo, H. Yu, P. Liu, Y. Ren, T. Zhang, M. Chen, M. Ishida and H. Zhou, *Energy Environ. Sci.*, 2015, **8**, 1237-1244.
206. J. Ming, H. Ming, W. Yang, W.-J. Kwak, J.-B. Park, J. Zheng and Y.-K. Sun, *RSC Adv.*, 2015, **5**, 8793-8800.
207. Y.-C. Lu, B. M. Gallant, D. G. Kwabi, J. R. Harding, R. R. Mitchell, M. S. Whittingham and Y. Shao-Horn, *Energy Environ. Sci.*, 2013, **6**, 750-768.
208. J. Cabana, L. Monconduit, D. Larcher and M. R. Palacín, *Adv. Mater.*, 2010, **22**, E170-E192.
209. L. Wang, J. Liang, Y. Zhu, T. Mei, X. Zhang, Q. Yang and Y. Qian, *Nanoscale*, 2013, **5**, 3627-3631.
210. A. D. W. Todd, R. E. Mar and J. R. Dahn, *J. Electrochem. Soc.*, 2007, **154**, A597-A604.
211. P. P. Ferguson, A. D. W. Todd and J. R. Dahn, *Electrochem. Commun.*, 2008, **10**, 25-31.
212. P. P. Ferguson, M. L. Martine, A. E. George and J. R. Dahn, *J. Power Sources*, 2009, **194**, 794-800.
213. Z. Chen, J. Qian, X. Ai, Y. Cao and H. Yang, *J. Power Sources*, 2009, **189**, 730-732.
214. X.-Y. Fan, F.-S. Ke, G.-Z. Wei, L. Huang and S.-G. Sun, *J. Alloys Compd.*, 2009, **476**, 70-73.
215. L. Huang, J.-S. Cai, Y. He, F.-S. Ke and S.-G. Sun, *Electrochem. Commun.*, 2009, **11**, 950-953.
216. F. Nacimiento, R. Alcántara and J. L. Tirado, *J. Electrochem. Soc.*, 2010, **157**, A666-A671.
217. J. He, H. Zhao, J. Wang, J. Wang and J. Chen, *J. Alloys Compd.*, 2010, **508**, 629-635.
218. X.-L. Wang, W.-Q. Han, J. Chen and J. Graetz, *ACS Appl. Mater. Interfaces*, 2010, **2**, 1548-1551.
219. F. Nacimiento, P. Lavela, J. Tirado and J. Jiménez-Mateos, *J. Solid State Electrochem.*, 2012, **16**, 953-962.
220. G. Ferrara, L. Damen, C. Arbizzani, R. Inguanta, S. Piazza, C. Sunseri and M. Mastragostino, *J. Power Sources*, 2011, **196**, 1469-1473.
221. Z. Du and S. Zhang, *J. Phys. Chem. C*, 2011, **115**, 23603-23609.
222. L.-J. Xue, Y.-F. Xu, L. Huang, F.-S. Ke, Y. He, Y.-X. Wang, G.-Z. Wei, J.-T. Li and S.-G. Sun, *Electrochim. Acta*, 2011, **56**, 5979-5987.
223. M.-Y. Li, C.-L. Liu, M.-R. Shi and W.-S. Dong, *Electrochim. Acta*, 2011, **56**, 3023-3028.
224. D.-H. Nam, R.-H. Kim, C.-L. Lee and H.-S. Kwon, *J. Electrochem. Soc.*, 2012, **159**, A1822-A1826.
225. G. Ferrara, C. Arbizzani, L. Damen, M. Guidotti, M. Lazzari, F. G. Vergottini, R. Inguanta, S. Piazza, C. Sunseri and M. Mastragostino, *J. Power Sources*, 2012, **211**, 103-107.
226. R. M. Gnanamuthu, Y. N. Jo and C. W. Lee, *J. Alloys Compd.*, 2013, **564**, 95-99.
-

-
227. J. R. Gonzalez, F. Nacimiento, R. Alcantara, G. F. Ortiz and J. L. Tirado, *CrystEngComm*, 2013, **15**, 9196-9202.
228. C. Wu, J. Maier and Y. Yu, *Adv. Funct. Mater.*, 2015, **25**, 3488-3496.
229. B. Zhang, X.-S. Li, C.-L. Liu, Z.-H. Liu and W.-S. Dong, *RSC Adv.*, 2015, **5**, 53586-53591.
230. Z. Yang, A. A. Gewirth and L. Trahey, *ACS Appl. Mater. Interfaces*, 2015, **7**, 6557-6566.
231. I. A. Courtney and J. R. Dahn, *J. Electrochem. Soc.*, 1997, **144**, 2045-2052.
232. N. Zhang, Q. Zhao, X. Han, J. Yang and J. Chen, *Nanoscale*, 2014, **6**, 2827-2832.
233. Z. Zhu, S. Wang, J. Du, Q. Jin, T. Zhang, F. Cheng and J. Chen, *Nano Lett.*, 2014, **14**, 153-157.
234. S. R. Sivakkumar, J. Y. Nerkar and A. G. Pandolfo, *Electrochim. Acta*, 2010, **55**, 3330-3335.
235. F. Ding, W. Xu, D. Choi, W. Wang, X. Li, M. H. Engelhard, X. Chen, Z. Yang and J.-G. Zhang, *J. Mater. Chem.*, 2012, **22**, 12745-12751.
236. P. Gevorkian, *Large-Scale Solar Power Systems: Construction and Economics*, Cambridge University Press, 2012.
237. M. N. Obrovac and V. L. Chevrier, *Chem. Rev.*, 2014, **114**, 11444-11502.
238. D. Foster, J. Wolfenstine, J. Read and J. L. Allen, *Performance of Sony's Alloy Based Li-Ion Battery*, DTIC Document, 2008.
239. E. Strauss, D. Golodnitsky and E. Peled, *Electrochem. Solid-State Lett.*, 1999, **2**, 115-117.
240. E. Strauss, D. Golodnitsky and E. Peled, *Electrochim. Acta*, 2000, **45**, 1519-1525.
241. Y. Shao-Horn, S. Osmialowski and Q. C. Horn, *J. Electrochem. Soc.*, 2002, **149**, A1547-A1555.
242. Y. Shao-Horn, S. Osmialowski and Q. C. Horn, *J. Electrochem. Soc.*, 2002, **149**, A1499-A1502.
243. E. Strauss, D. Golodnitsky, K. Freedman, A. Milner and E. Peled, *J. Power Sources*, 2003, **115**, 323-331.
244. J.-W. Choi, G. Cheruvally, H.-J. Ahn, K.-W. Kim and J.-H. Ahn, *J. Power Sources*, 2006, **163**, 158-165.
245. X. Feng, X. He, W. Pu, C. Jiang and C. Wan, *Ionics*, 2007, **13**, 375-377.
246. D. Zhang, J. P. Tu, J. Y. Xiang, Y. Q. Qiao, X. H. Xia, X. L. Wang and C. D. Gu, *Electrochim. Acta*, 2011, **56**, 9980-9985.
247. L. Li, M. Caban-Acevedo, S. N. Girard and S. Jin, *Nanoscale*, 2014, **6**, 2112-2118.
248. J. Liu, Y. Wen, Y. Wang, P. A. van Aken, J. Maier and Y. Yu, *Adv. Mater.*, 2014, **26**, 6025-6030.
249. T. Evans, D. M. Piper, S. C. Kim, S. S. Han, V. Bhat, K. H. Oh and S.-H. Lee, *Adv. Mater.*, 2014, **26**, 7386-7392.
250. T. S. Yoder, M. Tussing, J. E. Cloud and Y. Yang, *J. Power Sources*, 2015, **274**, 685-692.
251. S. B. Son, T. A. Yersak, D. M. Piper, S. C. Kim, C. S. Kang, J. S. Cho, S. S. Suh, Y. U. Kim, K. H. Oh and S. H. Lee, *Adv. Energy Mater.*, 2014, **4**, 1300961.
252. T. B. Kim, J. W. Choi, H. S. Ryu, G. B. Cho, K. W. Kim, J. H. Ahn, K. K. Cho and H. J. Ahn, *J. Power Sources*, 2007, **174**, 1275-1278.
253. T. B. Kim, W. H. Jung, H. S. Ryu, K. W. Kim, J. H. Ahn, K. K. Cho, G. B. Cho, T. H. Nam, I. S. Ahn and H. J. Ahn, *J. Alloys Compd.*, 2008, **449**, 304-307.
254. A. Kitajou, J. Yamaguchi, S. Hara and S. Okada, *J. Power Sources*, 2014, **247**, 391-395.
255. Z. Shadike, Y.-N. Zhou, F. Ding, L. Sang, K.-W. Nam, X.-Q. Yang and Z.-W. Fu, *J. Power Sources*, 2014, **260**, 72-76.
-

-
256. T. A. Yersak, H. A. Macpherson, S. C. Kim, V.-D. Le, C. S. Kang, S.-B. Son, Y.-H. Kim, J. E. Trevey, K. H. Oh, C. Stoldt and S.-H. Lee, *Adv. Energy Mater.*, 2013, **3**, 120-127.
257. W. Li, M. Dobliger, A. Vaneski, A. L. Rogach, F. Jackel and J. Feldmann, *J. Mater. Chem.*, 2011, **21**, 17946-17952.
258. L. Hongtao, L. Yan, W. Zan and H. Ping, *Nanotechnology*, 2010, **21**, 105707.
259. A. Ghezelbash and B. A. Korgel, *Langmuir*, 2005, **21**, 9451-9456.
260. J. Joo, H. B. Na, T. Yu, J. H. Yu, Y. W. Kim, F. Wu, J. Z. Zhang and T. Hyeon, *J. Am. Chem. Soc.*, 2003, **125**, 11100-11105.
261. X. Yu, A. Shavel, X. An, Z. Luo, M. Ibáñez and A. Cabot, *J. Am. Chem. Soc.*, 2014, **136**, 9236-9239.
262. D. V. Talapin and C. B. Murray, *Science*, 2005, **310**, 86-89.
263. S. Iwamura, H. Nishihara, Y. Ono, H. Morito, H. Yamane, H. Nara, T. Osaka and T. Kyotani, *Sci. Rep.*, 2015, **5**, 08085.
264. X. Ji, K. T. Lee and L. F. Nazar, *Nat. Mater.*, 2009, **8**, 500-506.
265. X. W. Lou, C. M. Li and L. A. Archer, *Adv. Mater.*, 2009, **21**, 2536-2539.
266. H. Zhang, X. Yu and P. V. Braun, *Nat. Nanotechnol.*, 2011, **6**, 277-281.
267. Y. Yu, L. Gu, C. Wang, A. Dhanabalan, P. A. van Aken and J. Maier, *Angew. Chem. Int. Ed.*, 2009, **48**, 6485-6489.
268. N. Liu, H. Wu, M. T. McDowell, Y. Yao, C. Wang and Y. Cui, *Nano Lett.*, 2012, **12**, 3315-3321.
269. N. Yabuuchi, K. Kubota, M. Dahbi and S. Komaba, *Chem. Rev.*, 2014, **114**, 11636-11682.
270. L. D. Ellis, B. N. Wilkes, T. D. Hatchard and M. N. Obrovac, *J. Electrochem. Soc.*, 2014, **161**, A416-A421.
271. J. Song, Z. Yu, M. L. Gordin, S. Hu, R. Yi, D. Tang, T. Walter, M. Regula, D. Choi, X. Li, A. Manivannan and D. Wang, *Nano Lett.*, 2014, **14**, 6329-6335.
272. L. O. Vogt, M. El Kazzi, E. Jämstorp Berg, S. Pérez Villar, P. Novák and C. Villevieille, *Chem. Mater.*, 2015, **27**, 1210-1216.
273. C. Qian, F. Kim, L. Ma, F. Tsui, P. Yang and J. Liu, *J. Am. Chem. Soc.*, 2004, **126**, 1195-1198.
274. E. J. Popczun, J. R. McKone, C. G. Read, A. J. Biacchi, A. M. Wiltrout, N. S. Lewis and R. E. Schaak, *J. Am. Chem. Soc.*, 2013, **135**, 9267-9270.
275. S. Goriparti, E. Miele, F. De Angelis, E. Di Fabrizio, R. Proietti Zaccaria and C. Capiglia, *J. Power Sources*, 2014, **257**, 421-443.
276. N. Nitta, F. Wu, J. T. Lee and G. Yushin, *Mater. Today*, 2015, **18**, 252-264.
277. M. Dahbi, N. Yabuuchi, K. Kubota, K. Tokiwa and S. Komaba, *Phys. Chem. Chem. Phys.*, 2014, **16**, 15007-15028.
278. S.-W. Kim, D.-H. Seo, X. Ma, G. Ceder and K. Kang, *Adv. Energy Mater.*, 2012, **2**, 710-721.
279. D. Kundu, E. Talaie, V. Duffort and L. F. Nazar, *Angew. Chem. Int. Ed.*, 2015, **54**, 3431-3448.
280. J. Emsley, *Nature's Building Blocks: An A-Z Guide to the Elements*, OUP Oxford, 2011.
281. R. Mohtadi and F. Mizuno, *Beilstein J. Nanotechnol.*, 2014, **5**, 1291-1311.
282. R. E. Doe, G. E. Blomgren and K. A. Persson, 2011, US20110159381.
283. O. Tutusaus and R. Mohtadi, *ChemElectroChem*, 2015, **2**, 51-57.
284. Y. Shao, T. Liu, G. Li, M. Gu, Z. Nie, M. Engelhard, J. Xiao, D. Lv, C. Wang, J.-G. Zhang and J. Liu, *Sci. Rep.*, 2013, **3**, 03130.
285. G. Vardar, A. E. S. Sleightholme, J. Naruse, H. Hiramatsu, D. J. Siegel and C. W. Monroe, *ACS Appl. Mater. Interfaces*, 2014, **6**, 18033-18039.
-

286. L. P. Lossius and F. Emmenegger, *Electrochim. Acta*, 1996, **41**, 445-447.
287. D. Aurbach, H. Gizbar, A. Schechter, O. Chusid, H. E. Gottlieb, Y. Gofer and I. Goldberg, *J. Electrochem. Soc.*, 2002, **149**, A115-A121.
288. C. Liao, N. Sa, B. Key, A. K. Burrell, L. Cheng, L. A. Curtiss, J. T. Vaughey, J.-J. Woo, L. Hu, B. Pan and Z. Zhang, *J. Mater. Chem. A*, 2015, **3**, 6082-6087.
289. P. P. Chin, J. Ding, J. B. Yi and B. H. Liu, *J. Alloys Compd.*, 2005, **390**, 255-260.
290. M. N. Obrovac, O. Mao and J. R. Dahn, *Solid State Ionics*, 1998, **112**, 9-19.
291. F. Gillot, S. Boyanov, L. Dupont, M. L. Doublet, M. Morcrette, L. Monconduit and J. M. Tarascon, *Chem. Mater.*, 2005, **17**, 6327-6337.
292. J. Hassoun, G. Mulas, S. Panero and B. Scrosati, *Electrochem. Commun.*, 2007, **9**, 2075-2081.
293. S.-M. Oh, S.-W. Oh, C.-S. Yoon, B. Scrosati, K. Amine and Y.-K. Sun, *Adv. Funct. Mater.*, 2010, **20**, 3260-3265.
294. S.-O. Kim and A. Manthiram, *J. Mater. Chem. A*, 2015, **3**, 2399-2406.
295. F. Badway, N. Pereira, F. Cosandey and G. G. Amatucci, *J. Electrochem. Soc.*, 2003, **150**, A1209-A1218.
296. L. Wu, X. Hu, J. Qian, F. Pei, F. Wu, R. Mao, X. Ai, H. Yang and Y. Cao, *J. Mater. Chem. A*, 2013, **1**, 7181-7184.
297. Z. Hu, Z. Zhu, F. Cheng, K. Zhang, J. Wang, C. Chen and J. Chen, *Energy Environ. Sci.*, 2015, **8**, 1309-1316.
298. Y. Zhu, L. Suo, T. Gao, X. Fan, F. Han and C. Wang, *Electrochem. Commun.*, 2015, **54**, 18-22.
299. S. S. Zhang, *J. Mater. Chem. A*, 2015, **3**, 7689-7694.
300. J. Lalancette, A. Freche, J. Brindle and M. Laliberté, *Synthesis*, 1972, **1972**, 526-532.
301. M. Walter, S. Doswald and M. V. Kovalenko, *J. Mater. Chem. A*, 2016, **4**, 7053-7059.
302. M. Walter, M. I. Bodnarchuk, K. V. Kravchyk and M. V. Kovalenko, *CHIMIA International Journal for Chemistry*, 2015, **69**, 724-728.
303. M. Walter, K. V. Kravchyk, M. Ibáñez and M. V. Kovalenko, *Chem. Mater.*, 2015, **27**, 7452-7458.
304. L. Geng, G. Lv, X. Xing and J. Guo, *Chem. Mater.*, 2015, **27**, 4926-4929.
305. N. Jayaprakash, S. K. Das and L. A. Archer, *Chem. Commun.*, 2011, **47**, 12610-12612.
306. M. Chiku, H. Takeda, S. Matsumura, E. Higuchi and H. Inoue, *ACS Appl. Mater. Interfaces*, 2015, **7**, 24385-24389.
307. G. Cohn, L. Ma and L. A. Archer, *J. Power Sources*, 2015, **283**, 416-422.
308. S. Xia, X.-M. Zhang, K. Huang, Y.-L. Chen and Y.-T. Wu, *J. Electroanal. Chem.*, 2015, **757**, 167-175.
309. P. R. Gifford and J. B. Palmisano, *J. Electrochem. Soc.*, 1988, **135**, 650-654.
310. J. V. Rani, V. Kanakaiah, T. Dadmal, M. S. Rao and S. Bhavanarushi, *J. Electrochem. Soc.*, 2013, **160**, A1781-A1784.
311. X.-G. Li, Y.-W. Liu, M.-R. Huang, S. Peng, L.-Z. Gong and M. G. Moloney, *Chem. - Eur. J.*, 2010, **16**, 4803-4813.
312. S. Zein El Abedin, *J. Solid State Electrochem.*, 2012, **16**, 775-783.
313. J. M. Robertson and J. G. White, *J. Chem. Soc.*, 1947, DOI: 10.1039/JR9470000358, 358-368.
314. H. D. B. Jenkins and K. P. Thakur, *J. Chem. Educ.*, 1979, **56**, 576.
315. E. Pretsch, P. Bühlmann, C. Affolter, E. Pretsch, P. Bühlmann and C. Affolter, *Structure determination of organic compounds*, Springer, 2009.
316. N. S. Hudak, *J. Phys. Chem. C*, 2014, **118**, 5203-5215.
317. C. Wang, H. Dong, W. Hu, Y. Liu and D. Zhu, *Chem. Rev.*, 2012, **112**, 2208-2267.
318. Z. Song and H. Zhou, *Energy Environ. Sci.*, 2013, **6**, 2280-2301.

Appendix A. Abbreviation list

<i>Abbreviation</i>	<i>Full name</i>
<i>AIB</i>	<i>Al-ion battery</i>
<i>ATR</i>	<i>attenuated total reflectance</i>
<i>CB</i>	<i>carbon black</i>
<i>CE</i>	<i>coulombic efficiency</i>
<i>CMC</i>	<i>carboxymethyl cellulose</i>
<i>CNT</i>	<i>carbon nanotube</i>
<i>COD</i>	<i>Crystallography Open Database</i>
<i>CTI</i>	<i>Commission for Technology and Innovation</i>
<i>CV</i>	<i>cyclic voltammetry</i>
<i>DMC</i>	<i>dimethyl carbonate</i>
<i>EC</i>	<i>ethylene carbonate</i>
<i>EDX</i>	<i>energy dispersive X-ray (spectroscopy)</i>
<i>EMIm</i>	<i>1-ethyl-3-methylimidazolium</i>
<i>FEC</i>	<i>fluoroethylene carbonate</i>
<i>FTIR</i>	<i>Fourier transform infrared (spectroscopy)</i>
<i>HAADF</i>	<i>high angle annular dark field</i>
<i>HR</i>	<i>high-resolution</i>
<i>ICDD</i>	<i>International Centre for Diffraction Data</i>
<i>LIB</i>	<i>Li-ion battery</i>
<i>MH</i>	<i>metal hydride</i>
<i>MIB</i>	<i>Mg-ion battery</i>
<i>NC</i>	<i>nanocrystal</i>
<i>NMP</i>	<i>N-methyl-2-pyrrolidone</i>
<i>NP</i>	<i>nanoparticle</i>
<i>NW</i>	<i>nanowire</i>
<i>ODE</i>	<i>octadecene</i>
<i>OLA</i>	<i>oleylamine</i>
<i>PVdF</i>	<i>polyvinylidene fluoride</i>
<i>PC</i>	<i>propylene carbonate</i>
<i>rpm</i>	<i>revolutions per minute</i>
<i>SEI</i>	<i>solid electrolyte interface</i>
<i>SEM</i>	<i>scanning electron microscope</i>
<i>SHE</i>	<i>standard hydrogen electrode</i>
<i>SIB</i>	<i>Na-ion battery</i>
<i>STEM</i>	<i>scanning transmission electron microscope</i>
<i>TEM</i>	<i>transmission electron microscope</i>
<i>TFSI</i>	<i>bis((trifluoro)sulfonyl)-imide</i>
<i>THF</i>	<i>tetrahydrofuran</i>
<i>TOP</i>	<i>trioctylphosphine</i>
<i>TOPO</i>	<i>trioctylphosphine oxide</i>
<i>XRD</i>	<i>X-ray diffraction</i>

Appendix B. Curriculum Vitae

Name: Marc Dominik Walter

Nationality: German

Education

Since 2013	Doctoral studies in Chemistry under the supervision of Prof. Dr. Maksym Kovalenko, ETH Zurich and Empa-Swiss Federal Laboratories for Materials Science and Technology, Switzerland
2011-2013	M.Sc. studies in Chemistry, ETH Zurich, Switzerland Master thesis at Bayer Technology Services, Leverkusen, Germany
2008-2011	B.Sc. studies in Chemistry, University of Bonn, Germany
1999-2008	Gymnasium Lohmar (secondary school), Germany

Awards

2015 SCNAT-SCS Travel Award

2013-2009 Scholarship of the German National Academic Foundation

2011 Prize of the German Chemical Society for outstanding performance in the bachelor exam at the University of Bonn

2008 High-school Prize of the German Chemical Society as best graduating student in chemistry at Gymnasium Lohmar

Appendix C. List of publications

12. **M. Walter**, S. Doswald, and M.V. Kovalenko.

Inexpensive Colloidal SnSb nanoalloys as efficient anode materials for lithium- and sodium-ion batteries.

J. Mater. Chem. A, **2016**, 4, 7053-7059.

11. P. Kitschke, **M. Walter**, T. Rüffer, H. Lang, M.V. Kovalenko, and M. Mehring.

From molecular germanates to microporous Ge@C via twin polymerization.

Dalton Trans., **2016**, 45, 5741-5751.

10. P. Kitschke, **M. Walter**, T. Rüffer, A. Seifert, F. Speck, T. Seyller, S. Spange, H. Lang, A.A. Auer, M.V. Kovalenko, and M. Mehring.

Porous Ge@C materials via twin polymerization of germanium(II) salicyl alcoholates for Li-ion batteries.

J. Mater. Chem. A, **2016**, 4, 2705-2719.

9. **M. Walter**,* M.I. Bodnarchuk,* (*contributed equally) K.V. Kravchyk, and M.V. Kovalenko.

Evaluation of Metal Phosphide Nanocrystals as Anode Materials for Na-ion Batteries.

CHIMIA International Journal for Chemistry, **2015**, 69, 724-728.

8. **M. Walter**, K. V. Kravchyk, M. Ibáñez and M.V. Kovalenko.

Efficient and Inexpensive Sodium-Magnesium Hybrid Battery.

Chem. Mater., **2015**, 27, 7452-7458.

7. M.F. Oszajca, K. V. Kravchyk, **M. Walter**, F. Krieg, M.I. Bodnarchuk, and M.V. Kovalenko.

Colloidal BiF₃ nanocrystals: a bottom-up approach to conversion-type Li-ion cathodes.

Nanoscale, **2015**, 7, 16601-16605.

6. **M. Walter**, T. Zünd, and M.V. Kovalenko.

Pyrite (FeS₂) nanocrystals as inexpensive high-performance lithium-ion cathode and sodium-ion anode material.

Nanoscale, **2015**, 7, 9158-9163.

5. **M. Walter**, R. Erni, and M.V. Kovalenko.

Inexpensive Antimony Nanocrystals and Their Composites with Red Phosphorus as High-Performance Anode Materials for Na-ion Batteries.

Sci. Rep., **2015**, 5, 8418.

4. M. He,* **M. Walter**,* K.V. Kravchyk,* (*contributed equally) R. Erni, R. Widmer, and M.V. Kovalenko.

Monodisperse SnSb Nanocrystals for Li-ion and Na-ion Battery Anodes: Synergy and Dissonance Between Sn and Sb.

Nanoscale, **2015**, 7, 455-459.

3. L. Protesescu, A. J. Rossini, D. Kriegner, M. Valla, A. de Kergommeaux, **M. Walter**, K.V. Kravchyk, M. Nachttegaal, J. Stangl, B. Malaman, P. Reiss, A. Lesage, L. Emsley, C. Copéret, and M.V. Kovalenko.

Unraveling the core-shell structure of ligand-capped Sn/SnO_x nanoparticles by surface enhanced nuclear magnetic resonance, Mössbauer and X-ray absorption spectroscopies.

ACS Nano, **2014**, 8, 2639-2648.

2. M. He, K.V. Kravchyk, **M. Walter**, and M.V. Kovalenko.

Monodisperse Antimony Nanocrystals for High-Rate Li-ion and Na-ion Battery Anodes: Nano vs. Bulk.

Nano Lett., **2014**, 14, 1255-1262.

1. K.V. Kravchyk, L. Protesescu, M.I. Bodnarchuk, F. Krumeich, M. Yarema, **M. Walter**, C. Guntlin, and M.V. Kovalenko.

Monodisperse and inorganically capped Sn and Sn/SnO₂ nanocrystals for high performance Li-ion battery anodes.

J. Am. Chem. Soc., **2013**, 135, 4199-4202.

Appendix D. List of patents

3. M.V. Kovalenko, **M. Walter** (filed by Belenos Clean Power Holding Ltd.).

Method for the production of MSn_x nanoparticles as anode materials for a rechargeable battery.

Filing date 30/07/2015, Application number EP15179106.8-1353.

2. M.V. Kovalenko, **M. Walter** (filed by Belenos Clean Power Holding Ltd.).

Sb nanocrystals or Sb-alloy nanocrystals for fast charge/discharge Li- and Na-ion battery anodes.

Filing date 23/06/2014, Publication number EP2959989.

1. M.V. Kovalenko, M. He, K. Kravchyk, **M. Walter** (filed by Belenos Clean Power Holding Ltd.).

Antimony based anode material for rechargeable batteries and preparation method.

Filing date 28/11/2013, Publication number EP2879211.

Appendix E. List of presentations

Oral presentations

8. **1st International Symposium on Magnesium Batteries**, Blaubeuren/Germany, July 2016
7. **2016 MRS Spring Meeting**, Phoenix/USA, March/April 2016
6. **Empa PhD Students' Symposium 2015**, Dübendorf/Switzerland, December 2015
5. **Colloquium on Natural Resources and Pollutants + Energy**, Dübendorf/Switzerland, December 2014
4. **From Graduation to Innovation**, Chemnitz/Germany, June 2014
3. **Nanoforum 2014**, Linz/Austria, June 2014
2. **NaNaX6 – Nanoscience with Nanocrystals**, Bad Hofgastein/Austria, May 2014
1. **Swiss Chemical Society Fall Meeting**, Lausanne/Switzerland, September 2013

Poster presentations

7. **2016 MRS Spring Meeting**, Phoenix/USA, March/April 2016
6. **The SCCER Heat and Electricity Storage 3rd Symposium “Storing Renewable Energy for Future Mobility”**, Villigen/Switzerland, October 2015
5. **LiBD 2015 Lithium Battery Discussions – Electrode Materials**, Arcachon/France, June 2015
4. **ETH Industry Day 2014**, Zurich/Switzerland, August 2014
3. **ETH Industry Day 2013**, Zurich/Switzerland, September 2013
2. **Swiss Nanoconvention**, Basel/Switzerland, May 2013
1. **Nanoevent “NextNanoStars”**, Basel/Switzerland, March 2013